Computation of Probability of Positioning Failure: A Method for Positioning Safety Assessment in Safety-Critical Applications

Ciuban, S.

DOI
10.4233/uuid:611abcd2-60cb-4d47-be3a-ee4809f145b7

Publication date
2025

Document Version
Final published version

Citation (APA)
Ciuban, S. (2025). *Computation of Probability of Positioning Failure: A Method for Positioning Safety Assessment in Safety-Critical Applications*. [Dissertation (TU Delft), Delft University of Technology]. https://doi.org/10.4233/uuid:611abcd2-60cb-4d47-be3a-ee4809f145b7

Important note
To cite this publication, please use the final published version (if applicable).
Please check the document version above.

Computation of Probability of Positioning Failure: A Method for Positioning Safety Assessment in Safety-Critical Applications

Sebastian Ciuban

Computation of Probability of Positioning Failure: A Method for Positioning Safety Assessment in Safety-Critical Applications

Computation of Probability of Positioning Failure: A Method for Positioning Safety Assessment in Safety-Critical Applications

Dissertation

for the purpose of obtaining the degree of doctor
at Delft University of Technology, The Netherlands,
by the authority of the Rector Magnificus prof. dr. ir. T.H.J.J. van der Hagen,
chair of the Board of Doctorates,
to be defended publicly on
18th of December 2025 at 15.00

by

Sebastian CIUBAN

Master of Science in Aerospace Engineering,
École Nationale de l'Aviation Civile, France,
born in Baia Mare, Romania.

This dissertation has been approved by the promotors.

Promotor: Prof. dr. ir. P.J.G. Teunissen
Copromotor: Dr. ir. C.C.J.M. Tiberius

Composition of the doctoral committee:

Rector Magnificus,	chairperson
Prof. dr. ir. P.J.G. Teunissen,	Delft University of Technology, promotor
Dr. ir. C.C.J.M. Tiberius,	Delft University of Technology, copromotor
Independent members:	
Prof. dr. ir. M. Mulder,	Delft University of Technology.
Prof. dr. ir. R.F. Hanssen,	Delft University of Technology.
Dr. ir. Z. Perkó,	Delft University of Technology/Radformation, U.S.A.
Dr. P. Thevenon,	École Nationale de l'Aviation Civile, France
Prof. Dr-Ing. S. Schön,	Leibniz University Hannover, Germany

This research was funded by the Dutch Research Council (NWO) under Grant 18305 "I-GNSS Positioning for Assisted and Automated Driving".

Keywords: Detection Identification and Adaptation (DIA), Probability of positioning failure, Rare event simulation, Safety-critical applications

Printed by: Ipskamp Printing

Style: TU Delft House Style, with modifications by Moritz Beller
`https://github.com/Inventitech/phd-thesis-template`

ISBN 978-94-6536-009-6

An electronic version of this dissertation is available at
`http://repository.tudelft.nl/`.

"A ship in a harbour is safe but that is not what ships are built for."

John A. Shedd

Contents

Summary

Satellite-based Positioning, Navigation, and Timing (PNT) technologies, including Global Navigation Satellite Systems (GNSS) and emerging Low Earth Orbit (LEO) constellations, alongside Terrestrial Networked Positioning Systems (TNPS) and various other sensors for positioning (e.g., inertial measurement units, cameras, LiDAR), are used and of interest for safety-critical applications across automotive, aviation, rail, and maritime domains. An important positioning safety criterion for these applications is represented by the probability of positioning failure, defined as the probability that a position estimator falls outside an application-specific safety-region. Rigorous quantification of this probability, denoted $\mathbb{P}_{\mathcal{F}}$, is essential to verify compliance with safety requirements and to support the design and evaluation of positioning algorithms and systems.

This thesis addresses the challenges associated with computing $\mathbb{P}_{\mathcal{F}}$ when the position estimator results from a combined parameter estimation and statistical hypothesis testing procedure for model misspecifications in the positioning model. A key challenge is posed by the multimodality of the probability density function (PDF) of the position estimator, which renders analytical integration methods intractable. Another key challenge is represented by the stringent requirements that $\mathbb{P}_{\mathcal{F}}$ must satisfy for safety-critical applications (e.g., below 10^{-5}), which implies that the event of positioning failure $\mathcal{F}$ must be rare—rendering standard Monte Carlo techniques computationally too expensive. Therefore, a novel method is developed in this thesis which addresses these challenges and is grounded in rare event simulation techniques, specifically Importance Sampling and the Cross-Entropy method. This method enables the construction of a 'failure-tree' that decomposes $\mathbb{P}_{\mathcal{F}}$ into components conditioned on the hypothesis testing decisions, thereby supporting rigorous positioning safety analyses during the design stage of positioning algorithms, and systems, for safety-critical applications.

The positioning safety is assessed in several representative scenarios. The importance of accounting for estimation–testing dependence is emphasized in a scenario involving cooperative positioning of automated vehicles, where neglecting this dependence results in probabilities of positioning failure being underestimated by an order of magnitude. Furthermore, positioning safety analyses for Unmanned Aerial Vehicles (UAVs) across multiple European airspace regions reveal substantial variability in the probabilities of positioning failure due to changes in receiver-satellite geometry over time, highlighting the importance of comprehensive simulation-based assessments. Additionally, an example is shown in which the probability of positioning failure is computed while accounting for multidimensional model misspecifications (e.g., multiple simultaneous outliers, or faults, in the observations). Collectively, the contributions and findings of this thesis highlight a rigorous approach to computing probabilities of positioning failure and conducting positioning safety analyses.

Samenvatting

Op satellieten gebaseerde plaatsbepalings-, navigatie- en tijdsbepalings (PNT), waaronder wereldwijde navigatiesatellietsystemen (GNSS) en opkomende Low Earth Orbit (LEO) constellaties, naast terrestrische netwerk plaatsbepalingssystemen (TNPS) en verschillende andere sensoren voor plaatsbepaling (zoals traagheidsnavigatie, camera's, LiDAR), worden gebruikt en zijn van belang voor veiligheidskritische toepassingen in de auto-, luchtvaart-, spoorweg- en maritieme sector. Een belangrijk veiligheidscriterium voor plaatsbepaling in deze toepassingen is de kans op falen van de plaatsbepaling, gedefinieerd als de kans dat een positieschatter buiten een toepassingsspecifieke veiligheidszone valt. Rigoureuze kwantificering van deze kans, aangeduid als $\mathbb{P}_{\mathcal{F}}$, is essentieel om te controleren of aan de veiligheidsvereisten wordt voldaan en om het ontwerp en de evaluatie van plaatsbepalingsalgoritmen en -systemen te ondersteunen.

In deze dissertatie worden de uitdagingen behandeld die gepaard gaan met het berekenen van $\mathbb{P}_{\mathcal{F}}$ wanneer de positieschatter het resultaat is van een gecombineerde parameterschatting en statistische hypothesetoetsprocedure voor modelmispecificaties in het plaatsbepalingsmodel. Een belangrijke uitdaging wordt gevormd door de multimodaliteit van de kansdichtheidsfunctie van de positieschatter, waardoor analytische integratiemethoden onuitvoerbaar zijn. Een andere belangrijke uitdaging wordt gevormd door de strenge eisen waaraan $\mathbb{P}_{\mathcal{F}}$ moet voldoen voor veiligheidskritische toepassingen (bijv. lager dan 10^{-5}), wat inhoudt dat een plaatsbepalingsfout $\mathcal{F}$ zeldzaam moet zijn, waardoor standaard Monte Carlo-technieken rekentechnisch te duur zijn. Daarom is in dit proefschrift een nieuwe methode ontwikkeld om deze uitdagingen aan te gaan. Deze methode is gebaseerd op simulatietechnieken voor zeldzame gebeurtenissen, met name Importance Sampling en de Cross-Entropy methode. Deze methode maakt het mogelijk om een 'faalboom' te construeren die de $\mathbb{P}_{\mathcal{F}}$ ontbindt in componenten die afhankelijk zijn van de hypothesetoetsbeslissingen, waardoor rigoureuze veiligheidsanalyses van plaatsbepaling tijdens de ontwerpfase van plaatsbepalingsalgoritmen en -systemen voor veiligheidskritische toepassingen ondersteund worden.

De plaatsbepalingsveiligheid wordt beoordeeld in verschillende representatieve scenario's. Het belang van het meenemen van schattings-toetsafhankelijkheid wordt benadrukt in een scenario met coöperatieve plaatsbepaling van geautomatiseerde voertuigen, waar het verwaarlozen van deze afhankelijkheid resulteert in een onderschatting van de waarschijnlijkheid van falende plaatsbepaling met een orde van grootte. Verder laten veiligheidsanalyses van plaatsbepaling voor onbemande luchtvaartuigen (UAV's) in meerdere Europese luchtruimregio's zien dat de kans op falen van de plaatsbepaling aanzienlijk varieert door veranderingen in satellietgeometrie. Daarnaast wordt een voorbeeld getoond waarin de waarschijnlijkheid van falende plaatsbepaling wordt berekend terwijl rekening wordt gehouden met meerdimensionale modelspecificaties (bijv. meerdere gelijktijdige

uitschieters of fouten in de waarnemingen). Gezamenlijk benadrukken de bijdragen en bevindingen van dit proefschrift een rigoureuze aanpak voor het berekenen van kansen op falen van plaatsbepaling en het uitvoeren van veiligheidsanalyses voor plaatsbepaling.

1 Introduction

1.1 Background

Satellite-based Positioning, Navigation, and Timing (PNT), including conventional Global Navigation Satellite Systems (GNSS) and emerging Low Earth Orbit (LEO) systems, together with Terrestrial Networked Positioning Systems (TNPS) and other sensors for positioning (e.g., inertial measurement units, cameras, LiDAR), is widely used and of growing interest in various safety-critical applications, including automotive, aviation, rail, and maritime domains [1–3]. Based on these positioning technologies a vehicle's position estimator $\underline{\mathrm{x}} \in \mathbb{R}^n$ can be formulated and its statistical probability density function (PDF) $f_{\underline{\mathrm{x}}}(x)$ can be obtained. Given an application specific safety-region $\mathcal{B} \subset \mathbb{R}^n$ for the vehicle, one can then pose the following question:

"What is the probability that the position estimator $\underline{\mathrm{x}} \in \mathbb{R}^n$ falls outside the designated safety-region $\mathcal{B} \subset \mathbb{R}^n$?".

Quantifying this probability enables its comparison against application-specific requirements, or guidelines, to determine whether they are satisfied (e.g., for automotive [4], or for aviation [5]). It can also support studies aimed at defining or refining such requirements. Furthermore, this probabilistic characterization is valuable at the design stage of positioning algorithms, where decisions must be made regarding (i) measurement models, (ii) parameter estimation methods for the position vector, (iii) statistical hypothesis testing procedures to accommodate model misspecifications (e.g., multiple simultaneous faults and outliers in measurements), and (iv) positioning scenarios for vehicles, among other factors. This probability can be interpreted as a positioning 'safety indicator' for the application of interest. The aforementioned probability corresponds to the event of *positioning failure*, defined as $\mathcal{F} = \{\underline{\mathrm{x}} \notin \mathcal{B}\}$ [5], and is expressed as

$$\mathbb{P}_{\mathcal{F}} = \mathsf{P}(\underline{\mathrm{x}} \notin \mathcal{B}) = \int_{\mathcal{B}^c} f_{\underline{\mathrm{x}}}(x)\, dx, \tag{1.1}$$

where $\mathcal{B}^c \subset \mathbb{R}^n$ is the complement of the safety-region $\mathcal{B} \subset \mathbb{R}$ (i.e., the $\mathbb{R}^n$ space without the safety-region $\mathcal{B}$). The computation and analysis of (1.1) align with the scenario-based safety

1

assessment framework used for automated and autonomous vehicles [6–8]. Moreover, a wide range of other applications also base their safety analyses on the probability of failure with respect to (w.r.t.) the events of interest, including nuclear power plants, aerospace systems, and structural safety [9–11].

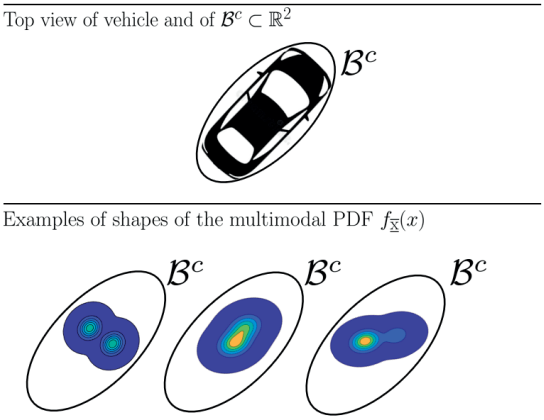

Figure 1.1: Examples of multimodal shapes that the PDF $f_{\underline{X}}(x)$ can have in the context of positioning for an automated (or autonomous) vehicle with the safety-region $\mathcal{B} \subset \mathbb{R}^2$ as the area inside the ellipse and $\mathcal{B}^c \subset \mathbb{R}^2$ being the complement of the safety-region. The PDF $f_{\underline{X}}(x)$ is visualized as a contour plot using a blue-to-yellow color scale, where blue indicates low probability density and yellow indicates high probability density. The image of the vehicle has been adapted from [12].

It is important to highlight that the PDF $f_{\underline{X}}(x)$ is generally *multimodal* (see Figure 1.1). The multimodal structure of $f_{\underline{X}}(x)$ arises because the position estimator $\underline{\hat{x}} \in \mathbb{R}^n$, typically, results from a combined parameter estimation and statistical hypothesis testing procedure, designed to accommodate model misspecifications. Teunissen captured the interplay between these two statistical inference concepts in the theoretical framework introduced in [13], and later extended it in [14]. To account for such model misspecifications, one can assume a positioning model that is valid under nominal conditions (the null hypothesis $\mathcal{H}_0$) and formulate alternative positioning models under multiple alternative hypotheses $\mathcal{H}_{i\neq 0}$ with $i \in \{1, ..., k\}$. For example, in the case of satellite-based positioning, one can define positioning models under the $\mathcal{H}_{i\neq 0}$'s to account for the presence of one or multiple simultaneous outliers (or faults) in the code-based observables, cycle slips in the phase-based observables, satellite failures, unmodelled atmospheric delays, etc. Then the objective is to select, based on the observables $\underline{y} \in \mathbb{R}^m$, the most likely hypothesis and use the corresponding positioning model to provide the position estimator $\underline{\hat{x}}_i \in \mathbb{R}^n$ for $i \in \{0, ..., k\}$ (see an illustrative example in Figure 1.2). Figure 1.2 shows that the position estimator $\underline{\hat{x}} \in \mathbb{R}^n$ is a function of the individual estimators $\underline{\hat{x}}_i \in \mathbb{R}^n$ and the statistical hypothesis testing procedure used to select these estimators (e.g., Detection Identification and Adaptation-DIA procedure [15–17] or a Fault Detection and Exclusion-FDE procedure [18–20]).

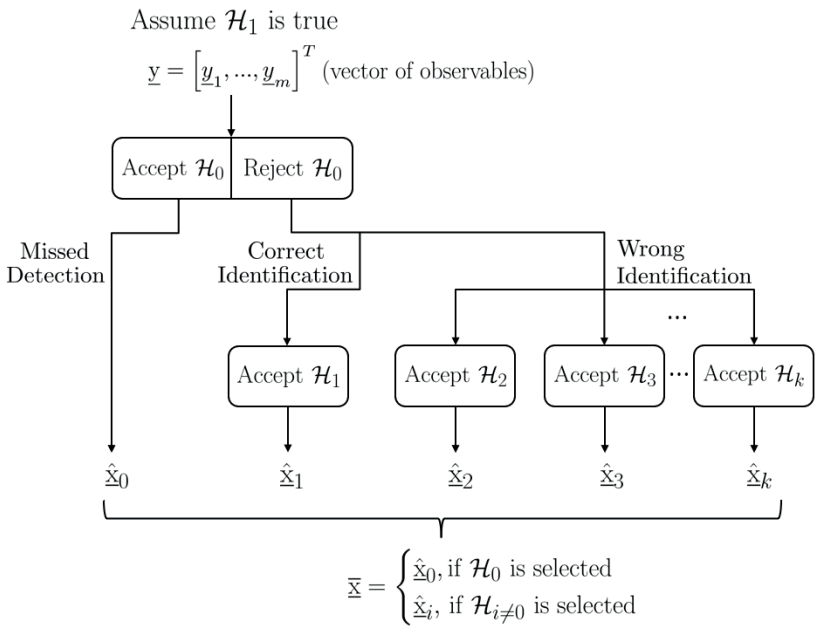

Figure 1.2: Schematic representation of a combined parameter estimation and a multiple statistical hypothesis testing procedure given a vector of m-observables $\underline{y} = \left[\underline{y}_1, \ldots, \underline{y}_m\right]^T$. The example illustrates probable outcomes of the combined procedure, assuming hypothesis $\mathcal{H}_1$ is true (e.g., simultaneous outliers in observables $\underline{y}_1$ and $\underline{y}_2$). The probable outcomes of the decision logic are captured by the estimator $\overline{\underline{x}} \in \mathbb{R}^n$.

The expression of $f_{\overline{\underline{x}}}(x)$ provides additional insights into its dependencies [13]

$$f_{\overline{\underline{x}}}(x) = \sum_{i=0}^{k} \int_{\mathbb{R}^r} f_{\hat{\underline{x}}_i, \underline{t}}(x, t) p_i(t) dt, \tag{1.2}$$

where $f_{\hat{\underline{x}}_i, \underline{t}}(x, t)$ is the joint PDF of the individual estimators $\hat{\underline{x}}_i \in \mathbb{R}^n$ and the vector of misclosures $\underline{t} \in \mathbb{R}^r$ used to construct statistical tests for selecting the most likely hypothesis $\mathcal{H}_i$ for $i \in \{0, ..., k\}$, and $p_i(t)$ is an indicator function that equals 1 if $\mathcal{H}_i$ is selected and 0 otherwise. The vector of misclosures has the dimension of the measurement redundancy, denoted r, and it contains all the available information from the observables useful for testing the validity of the positioning model under $\mathcal{H}_0$. From the expression of $f_{\overline{\underline{x}}}(x)$ in (1.2), it follows that the probability of positioning failure $\mathbb{P}_{\mathcal{F}}$ from (1.1) depends on the $k+1$ hypotheses, the dimension n of the to-be-estimated parameter vector, and the dimension r of the misclosure vector. Furthermore, $\hat{\underline{x}}_i \in \mathbb{R}^n$ and $\underline{t} \in \mathbb{R}^r$ are *dependent* for $i \neq 0$, which means that the joint PDF cannot be expressed as a product of the marginals PDFs (i.e., $f_{\hat{\underline{x}}_i, \underline{t}}(x, t) \neq f_{\hat{\underline{x}}_i}(x) f_{\underline{t}}(t)$ for $i \neq 0$).

In the following subsection, the research objectives are presented. These objectives are centered around the challenges that arise when computing the probability of positioning

1

failure $\mathbb{P}_{\mathcal{F}}$ for *any* type of combined parameter estimation and statistical hypothesis testing procedure within the frameworks introduced in [13, 14].

1.2 Research objectives

The computation of $\mathbb{P}_{\mathcal{F}}$ in (1.1) is challenging primarily due to two factors: (i) the PDF $f_{\underline{x}}(x)$ is generally multimodal, and its integration over the complement of the application-specific, multi-dimensional, safety-region $\mathcal{B}^c \subset \mathbb{R}^n$ is non-trivial (i.e., analytical integration methods are intractable); and (ii) the event of positioning failure $\mathcal{F} = \{\underline{x} \notin \mathcal{B}\}$ must be *rare* in safety-critical applications (e.g., requiring $\mathbb{P}_{\mathcal{F}} < 10^{-7}$ for automated and autonomous driving [4]). Addressing these challenges enables rigorous positioning safety analyses, at the design stage of positioning algorithms, that are broadly applicable across a range of safety-critical domains, including automotive, civil aviation, rail, and maritime.

The starting point is the decomposition of the probability of positioning failure $\mathbb{P}_{\mathcal{F}}$ into conditional components based on the statistical testing decisions: Correct Acceptance (CA) when $\mathcal{H}_0$ is accepted and $\mathcal{H}_0$ is valid; False Alarm (FA_i) when $\mathcal{H}_{i\neq 0}$ is accepted and $\mathcal{H}_0$ is valid; Missed Detection (MD_i) when $\mathcal{H}_0$ is accepted and $\mathcal{H}_{i\neq 0}$ is valid; Correct Identification (CI_i) when $\mathcal{H}_{i\neq 0}$ is accepted and that $\mathcal{H}_{i\neq 0}$ is indeed valid; Wrong Identification (WI_j) when $\mathcal{H}_j$ is accepted and $\mathcal{H}_{i\neq 0}$ is valid for $j \notin \{0, i\}$. This decomposition is conceptualized as a 'failure-tree' in Figure 1.3.

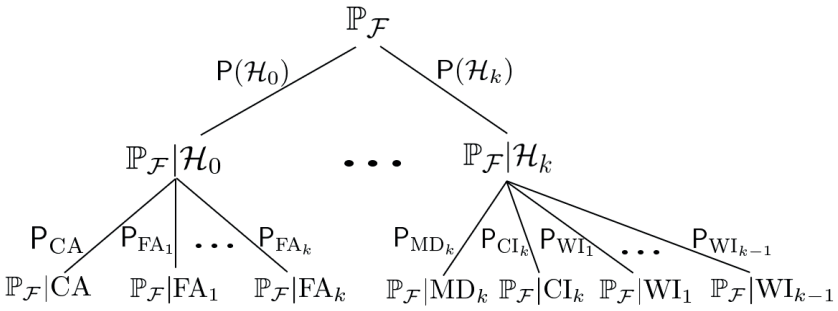

Figure 1.3: Representation of the probability of positioning failure $\mathbb{P}_{\mathcal{F}}$ as a 'failure-tree' based on (1.3) and (1.4) .

The equations that describe the branches and connections in Figure 1.3 are the following

$$\begin{aligned}
\mathsf{P}(\mathcal{H}_0)\mathbb{P}_{\mathcal{F}}|\mathcal{H}_0 &= \mathsf{P}(\mathcal{H}_0)\left(\mathsf{P}_{\text{CA}}\mathbb{P}_{\mathcal{F}}|\text{CA} + \sum_{i=1}^{k} \mathsf{P}_{\text{FA}_i}\mathbb{P}_{\mathcal{F}}|\text{FA}_i\right), \\
\mathsf{P}(\mathcal{H}_i)\mathbb{P}_{\mathcal{F}}|\mathcal{H}_i &= \mathsf{P}(\mathcal{H}_i)\left(\mathsf{P}_{\text{MD}_i}\mathbb{P}_{\mathcal{F}}|\text{MD}_i + \mathsf{P}_{\text{CI}_i}\mathbb{P}_{\mathcal{F}}|\text{CI}_i + \sum_{j\notin\{0,i\}}^{k} \mathsf{P}_{\text{WI}_j}\mathbb{P}_{\mathcal{F}}|\text{WI}_j\right),
\end{aligned} \tag{1.3}$$

where $\mathsf{P}(\mathcal{H}_0)$ and $\mathsf{P}(\mathcal{H}_i)$, for $i \in \{1, ..., k\}$, are the apriori probabilities of the hypotheses $\mathcal{H}_0$ and $\mathcal{H}_{i\neq 0}$, $\mathbb{P}_{\mathcal{F}}|\mathcal{E}$ is the probability of positioning failure conditioned on the statistical testing decision $\mathcal{E} \in \{\text{CA}, \text{FA}_i, \text{MD}_i, \text{CI}_i, \text{WI}_j\}$, and $\mathsf{P}_{\mathcal{E}}$ is the probability of the event of the

statistical decision $\mathcal{E}$. The expressions from (1.3) can then be used to formulate the total $\mathbb{P}_{\mathcal{F}}$ as

$$\mathbb{P}_{\mathcal{F}} = \mathsf{P}(\mathcal{H}_0)\mathbb{P}_{\mathcal{F}}|\mathcal{H}_0 + \sum_{i=1}^{k} \mathsf{P}(\mathcal{H}_i)\mathbb{P}_{\mathcal{F}}|\mathcal{H}_i. \tag{1.4}$$

With the components in (1.3) one can fully characterize the probability of positioning failure $\mathbb{P}_{\mathcal{F}}$, thereby providing all the necessary information to support a rigorous safety analysis—particularly for the design and evaluation of positioning systems in safety-critical applications. To the best of the thesis author's knowledge, no methods are currently available that enable the construction of the failure-tree illustrated in Figure 1.3, and thus facilitate positioning safety analyses based on such a structure. Therefore, the objectives of the research presented in this thesis are stated as follows:

- To develop a method for computing the probability of positioning failure and its conditional components.
- To analyze the impact of neglecting estimation–testing dependence on positioning safety, expressed in terms of the probability of positioning failure, using a representative scenario relevant to automated and autonomous vehicle applications.
- To perform positioning safety analyses in terms of the probability of positioning failure over time windows (e.g., 24 hours), capturing variability resulting from changes in the functional and stochastic models used for positioning (e.g., of Unmanned Aerial Vehicles-UAVs).
- To assess the probability of positioning failure under multidimensional model misspecifications, such as multiple simultaneous outliers in observations.

1

1.3 Thesis outline

The structure of this thesis aligns with the stated research objectives in Section 1.2. Each chapter is based on a peer-reviewed journal article, reflecting the progression and contributions of the research.

Chapter 2: Method to compute the probability of positioning failure
This chapter presents the method developed to construct the 'failure-tree' in Figure 1.3. The method is based on rare event simulation principles, specifically Importance Sampling and the Cross-Entropy method. An example is shown in which it is applied to a satellite-based positioning simulation scenario relevant for automated or autonomous vehicles, demonstrating how it enables rigorous positioning safety analyses. The chapter is based on the following journal article:

- *S. Ciuban, P.J.G. Teunissen, and C.C.J.M. Tiberius. "A Method to Compute the Probability of Positioning Failure for Vehicles in the Context of Dependence Between Parameter Estimation and Statistical Hypothesis Testing", IEEE Transactions on Vehicular Technologies, 74(10):15238 - 15253, 2025.*

Chapter 3: Positioning safety analysis for automated/autonomous vehicles
The impact of neglecting the dependence between parameter estimation and statistical hypothesis testing on positioning safety—expressed in terms of the probability of positioning failure—is studied for a simulation scenario relevant for automated and autonomous vehicles. The probability of positioning failure and its components are computed using an Extended Kalman Filter (EKF) combined with the Detection, Identification, and Adaptation (DIA) method. By comparing results with and without accounting for the estimation–testing dependence, the analysis reveals that overlooking this dependence can lead to overly optimistic safety assessments. The chapter is based on the following journal article:

- *S. Ciuban, P.J.G. Teunissen, and C.C.J.M. Tiberius. "Dependence Between Parameter Estimation and Statistical Hypothesis Testing: Positioning Safety Analysis for Automated/Autonomous Vehicles", IEEE Transactions on Intelligent Transportation Systems, 26(4):5509 - 5521, 2025.*

Chapter 4: Probability of positioning failure for UAVs in multiple authorized European airspace regions
Positioning safety for Unmanned Aerial Vehicles (UAVs) is assessed by computing the probability of positioning failure across multiple regulated European airspace regions. The simulation-based analysis is performed over 24-hour operational periods with real GPS satellite orbit data and UAV receiver settings comparable to Technical Standard Order (TSO)-certified equipment. Results are evaluated against integrity requirements for Specific Assurance and Integrity Levels (SAIL) 3 and 4, supporting use cases such as positioning algorithm verification and requirement development. The chapter is based on the following journal article:

- *S. Ciuban, C. Yin, P.J.G. Teunissen, and C.C.J.M. Tiberius. "Probability of Positioning Failure for UAVs in Multiple Authorized European Airspace Regions", IEEE Transactions on Vehicular Technologies, Submitted.*

Chapter 5: DIA-estimator and multidimensional model misspecifications
This chapter focuses on evaluating positioning safety in the presence of multidimensional model misspecifications, such as multiple simultaneous outliers in the observations, and a transparent approach is described on how multiple simultaneous outliers should be considered for safety analyses. The probability of positioning failure and its conditional components are quantified under these conditions. A representative UAV simulation scenario is analyzed using real GPS satellite data, both for a fixed satellite geometry and across a 24-hour period, offering insight into how model misspecifications influence positioning safety. The chapter is based on the following journal article:

- *S. Ciuban, P.J.G. Teunissen, and C.C.J.M. Tiberius. "DIA-Estimator and Multidimensional Model Misspecifications: GNSS-based Positioning Safety Analysis for UAVs", GPS Solutions, Submitted.*

Chapter 6: Conclusions and recommendations
This chapter presents the main conclusions of the research conducted in this thesis. It summarizes the key findings, per chapter, and the insights gained from the work. Additionally, several recommendations for future work are provided.

1

BIBLIOGRAPHY

[1] P. J. G. Teunissen and O. Montenbruck, editors. *Handbook of Global Navigation Satellite Systems*. Springer, 2017.

[2] Y. T. J. Morton et al., editors. *Position, Navigation, and Timing Technologies in the 21st Century: Integrated Satellite Navigation, Sensor Systems, and Civil Applications*. Wiley, IEEE Press, 2020.

[3] J. C. J. Koelemeij et al. A hybrid optical-wireless network for decimetre-level terrestrial positioning. *Nature*, 611(7936):473–478, November 2022.

[4] T. G. R. Reid et al. Localization Requirements for Autonomous Vehicles. *SAE International Journal of Connected and Automated Vehicles*, 2019.

[5] RTCA-Special Committee 159. Minimum Operational Performance Standards (MOPS) for Global Positioning System/Satellite-Based Augmentation System Airborne Equipment. DO-229F, Radio Technical Commission for Aeronautics, 2020.

[6] S. Riedmaier et al. Survey on Scenario-Based Safety Assessment of Automated Vehicles. *IEEE Access*, 8:87456–87477, 2020.

[7] U.N.E.C.E. New Assessment/Test Method for Automated Driving (NATM) Guidelines for Validating Automated Driving Systems (ADS). Report, United Nations Economic Commission for Europe - Inland Transport Committee, 2023.

[8] E. de Gelder et al. TNO Street Wise: Scenario-Based Safety Assessment of Automated Driving Systems. White paper, Netherlands Organisation for Applied Scientific Research (TNO), 2024.

[9] K. Jin et al. An approach to constructing effective training data for a classification model to evaluate the reliability of a passive safety system. *Reliability Engineering and System Safety*, 222:1–10, 2022.

[10] V. Chabridon et al. Evaluation of failure probability under parameter epistemic uncertainty: Application to aerospace system reliability assessment. *Aerospace Science and Technology*, 69:526–537, 2017.

[11] M. Shinozuka. Basic analysis of structural safety. *Journal of Structural Engineering*, 109(3):721–740, 1983.

[12] Wikimedia Commons. Citroen C3, top. Available at `https://commons.wikimedia.org/wiki/File:C3top.png#file`.

[13] P. J. G. Teunissen. Distributional theory for the DIA method. *Journal of Geodesy*, 92(1):59–80, 2018.

[14] P. J. G. Teunissen. On the Optimality of DIA-Estimators: Theory and Applications. *Journal of Geodesy*, 98(43):1–26, 2024.

[15] W. Baarda. A Testing Procedure for Use in Geodetic Networks. *Netherlands Geodetic Commission, Publications on Geodesy*, 2(5):1–97, 1968.

[16] I. Gillissen and I. A. Elema. Test results of DIA: A real-time adaptive integrity monitoring procedure, used in an integrated navigation system. *International Hydrographic Review*, 73(1):75–103, 1996.

[17] P. J. G. Teunissen. Batch and Recursive Model Validation. In P. J. G. Teunissen and O. Montenbruck, editors, *Springer Handbook of Global Navigation Satellite Systems*, pages 687–720. Springer, 2017.

[18] P. T. Hwang and R. G. Brown. RAIM-FDE Revisited: A New Breakthrough in Availability Performance With nioRAIM (Novel Integrity-Optimized RAIM). *NAVIGATION*, 53(1):41–51, 2006.

[19] L. Yang, Y. Li, and C. Rizos. An enhanced MEMS-INS/GNSS integrated system with fault detection and exclusion capability for land vehicle navigation in urban areas. *GPS Solutions*, 18(4):593–603, 2013.

[20] J. Blanch et al. Baseline Advanced RAIM User Algorithm and Possible Improvements. *IEEE Transactions on Aerospace and Electronic Systems*, 51(1):713–732, 2015.

2

Method to compute the probability of positioning failure

Positioning technologies are widely used in automotive, aviation, rail, and maritime safety-critical applications. Therefore, the computation of the probability of positioning failure for vehicles, which is the probability that the position estimator is outside a safety region, is of interest for positioning safety analyses. Since parameter estimation and statistical hypothesis testing for model misspecifications are commonly employed in positioning algorithms, the resulting position estimator is conditioned on the statistical hypothesis testing outcome. Hence, the probability density function (PDF) of the vehicle position estimator that accounts for the dependence between the two inference concepts should be used in the computations. In this contribution, we propose a method to compute the probability of positioning failure using the PDF of the vehicle position estimator, which accounts for the aforementioned dependence and is based on rare event simulation techniques, specifically Importance Sampling and the Cross-Entropy method. We apply the proposed method to a satellite-based positioning scenario, in decimeter precision, of an automated vehicle. The results show that the proposed method enables extensive positioning safety-analyses giving insights that can be used in the development of positioning algorithms and deciding whether safety targets and/or requirements are met. Finally, we discuss some limitations of the method and propose several further improvements.

This chapter is based on the journal article *S. Ciuban, P.J.G. Teunissen, and C.C.J.M. Tiberius. "A Method to Compute the Probability of Positioning Failure for Vehicles in the Context of Dependence Between Parameter Estimation and Statistical Hypothesis Testing", IEEE Transactions on Vehicular Technologies, 74(10):15238 - 15253, 2025.*

2.1 Introduction

Positioning via Global Navigation Satellite Systems (GNSS) and/or Terrestrial Networked Positioning Systems (TNPS) is widely used and of interest, along with other sensors (inertial measurement units, cameras, LiDAR, etc.), across several safety-critical applications, such as automotive, aviation, rail, and maritime [1–5]. Based on these positioning technologies a vehicle's position estimator $\underline{\hat{x}} \in \mathbb{R}^n$ can be formulated and its probability density function (PDF) $f_{\underline{\hat{x}}}(x)$ can be obtained. Positioning safety analyses often have the objective to quantify the probability of the event of positioning failure $\mathcal{F} = \{\underline{\hat{x}} \in \mathcal{B}^c\}$ with $\mathcal{B}^c \subset \mathbb{R}^n$ being the complement of a chosen safety-region $\mathcal{B} \subset \mathbb{R}^n$ [6]. The *probability of positioning failure* is expressed as

$$\mathbb{P}_{\mathcal{F}} = \mathsf{P}(\underline{\hat{x}} \in \mathcal{B}^c) = \int_{\mathcal{B}^c} f_{\underline{\hat{x}}}(x)\, dx. \tag{2.1}$$

Based on (2.1), positioning safety analyses can be performed, and the obtained probability can be used to check compliance with application-specific requirements or guidelines (e.g., for automotive [7], or for aviation [6]). Moreover, there is a wide range of applications where safety analyses are also based on the probability of failure, with respect to (w.r.t.) the events of interest, such as safety analyses for nuclear power plants, aerospace systems, and structural safety [8–10].

The computation and analysis of (2.1) align with the scenario-based safety assessment framework used for automated and autonomous vehicles [11–13]. In accordance with the principles of this framework, positioning safety analyses can be conducted at the design stage of the positioning algorithms, where decisions are to be made regarding (i) measurement models, (ii) parameter estimation methods for the position vector, (iii) statistical hypothesis testing procedures to accommodate for model misspecifications (e.g., outliers or faults in measurements), and (iv) positioning scenarios for vehicles, among other factors. Since the vehicle's position estimator $\underline{\hat{x}} \in \mathbb{R}^n$ is often an outcome of parameter estimation and statistical hypothesis testing for model misspecifications [14–17], it is critical to account for the *dependence* between the two statistical inference concepts in the PDF $f_{\underline{\hat{x}}}(x)$. Teunissen has introduced a theoretical framework that rigorously treats this dependence and gives access to $f_{\underline{\hat{x}}}(x)$ in the distributional theory for the Detection, Identification, and Adaptation (DIA) method [18]. Failing to account for the dependence between parameter estimation and statistical hypothesis testing, the computation of (2.1) can lead to unrepresentative results (e.g., overly-optimistic [19–21]). These type of implications have been recognized in various other disciplines such as mathematical statistics, biometrics, econometrics, and signal processing [22–27].

To perform positioning safety analyses, one must compute (2.1), which is challenging mainly because the PDF $f_{\underline{\hat{x}}}(x)$ is generally *multimodal* and its integration over the region $\mathcal{B}^c \subset \mathbb{R}^n$ for $n \geq 1$ is non-trivial. Existing methods in the GNSS positioning literature primarily focus on analytical upper-bounding techniques of $\mathbb{P}_{\mathcal{F}}$ based on univariate PDFs (i.e., when $n = 1$), which have been developed for civil aviation applications where the vertical component of the position estimator is of main interest [28–30]. Furthermore, recent research explored upper-bounding approaches in the framework of Bayesian statistics and extreme value theory [31–33]. In the context of positioning safety for automotive

applications, the extent to which upper-bounding $\mathbb{P}_{\mathcal{F}}$ overestimates its actual value when $n > 1$ (e.g., for a two-dimensional position vector) is still unclear or not specifically addressed [34–36]. Therefore, we turn our attention to numerical integration techniques, such as Monte Carlo methods, to compute $\mathbb{P}_{\mathcal{F}}$ directly without upper-bounding it, which is a reasonable decision in the context of scenario-based safety assessments. However, if $\mathbb{P}_{\mathcal{F}}$ is required to be 'small' (e.g., $\mathbb{P}_{\mathcal{F}} < 10^{-7}$) then the standard Monte Carlo method becomes computationally inefficient due to the large pseudo-random samples needed to be generated from the PDF of interest $f_{\underline{x}}(x)$ [37]. In this situation one can apply principles from rare-event simulation [37, 38]. To the best of our knowledge, there is currently a lack of methods for computing (2.1) that address the aforementioned challenges and shortcomings, specifically accounting for the dependence between parameter estimation and statistical hypothesis testing. Therefore, we propose a method to compute (2.1) which: (i) exploits the structure of $f_{\underline{x}}(x)$ by operating on its conditional components [18] while allowing the position vector to have a dimension $n \geq 1$, (ii) uses principles from rare-event simulation, specifically Importance Sampling (IS) and the Cross-Entropy (CE) method, for computing 'small' probabilities [38, 39], and (iii) quantifies the simulation uncertainty of the obtained results. We demonstrate the applicability of the method in the context of a GNSS-based decimetre precision level positioning scenario of an automated vehicle. The chosen scenario serves as an example and is not restricted to GNSS-based positioning as other positioning technologies can also be used (e.g., TNPS [2]). The methodological framework presented in this contribution is applicable beyond the automotive field, such as civil aviation, shipping, and rail. Thus, an extensive and component-wise positioning safety-analysis is made possible for multivariate position estimators of vehicles while accounting for the dependence between parameter estimation and statistical hypothesis testing in their PDFs.

This contribution is organized as follows: In Section 2.2 we briefly review the main principles of the distributional theory for the DIA method to arrive at the expression of the estimator $\overline{\underline{x}} \in \mathbb{R}^n$ which captures the aforementioned dependence (called the DIA-estimator) and at the expression of its PDF $f_{\overline{\underline{x}}}(x)$. In the first part of Section 2.3, we formulate the probability of positioning failure based on $f_{\overline{\underline{x}}}(x)$ and treat it as a rare event simulation problem. The second part of Section 2.3 describes the proposed method for the computation of (2.1) based on the principles of IS and the CE method. In Section 2.4 we apply the proposed method to carry out a positioning safety analysis for an automated vehicle which position vector is determined, at decimetre level, based on GNSS. The probability of positioning failure is computed for a worst-case scenario, at a single-epoch (snapshot) and as a function of the vehcile's orientation, based on which conclusions can be drawn whether the safety targets or requirements are met. Also in Section 2.4 we discuss the limitations and potential improvements of the proposed method. Section 2.5 contains a summary and conclusions of this contributions while suggesting several directions for future work.

Throughout the paper we make use of the following notation: an underscore denotes a random quantity (e.g., the random vector $\underline{x} \in \mathbb{R}^n$), $f_{\underline{x}}(x)$ is the PDF of $\underline{x}$, $\mathsf{E}_{f_{\underline{x}}}(\underline{x})$ is the expectation operator, and $\mathsf{D}_{f_{\underline{x}}}(\underline{x})$ is the dispersion or variance operator. The joint PDF of two random vectors $\underline{x} \in \mathbb{R}^n$ and $\underline{t} \in \mathbb{R}^r$ is denoted $f_{\underline{x},\underline{t}}(x,t)$. The PDF of a random vector $\underline{x}$

conditioned on an event $\mathcal{E}$ is denoted $f_{\underline{x}|\mathcal{E}}(x|\mathcal{E})$. The probability of an event $\mathcal{E}$ is denoted $\mathsf{P}_{\mathcal{E}} = \mathsf{P}(\mathcal{E})$. A projection matrix is denoted as $\mathbf{\Pi}_{\mathrm{A}}$ and it projects orthogonally (w.r.t. some metric) onto the range space of the matrix $\mathrm{A} \in \mathbb{R}^{m\times n}$ ($\mathcal{R}(\mathrm{A})$). For the weighted squared norm of a vector we use the notation $\|.\|^2_{\mathrm{Q}} = (.)^T\mathrm{Q}^{-1}(.)$. If the squared norm is w.r.t. the identity matrix then it is denoted $\|.\|^2$.

2.2 Parameter estimation and statistical hypothesis testing

In this section we review the main principles of the distributional theory for the Detection, Identification, and Adaptation (DIA) method [18]. Based on these principles, the PDF of the DIA-estimator, which accounts for the statistical dependence between parameter estimation and statistical hypothesis testing, is obtained. This PDF is then used to formulate the probability of positioning failure in Section 2.3.

Let us assume a random vector of observables (e.g., based on the (pseudo)range measurements from a positioning system) $\underline{\mathrm{y}} \in \mathbb{R}^m$ which is normally distributed

$$\underline{\mathrm{y}} \sim \mathcal{N}\left(\mathrm{Ax}, \mathrm{Q}_{\mathrm{yy}}\right), \tag{2.2}$$

where $\mathrm{A} \in \mathbb{R}^{m\times n}$ is the design matrix with $\mathrm{rank}(\mathrm{A}) = n$, $\mathrm{x} \in \mathbb{R}^n$ is the vector of unknown parameters, and $\mathrm{Q}_{\mathrm{yy}} \in \mathbb{R}^{m\times m}$ is the symmetric positive definite variance-covariance matrix of $\underline{\mathrm{y}} \in \mathbb{R}^m$. We consider model misspecifications of the mean of $\underline{\mathrm{y}}$ (e.g., due to outliers in the observables) as these are the most common in practice [40]. The following multiple statistical hypothesis testing problem is formulated,

$$\mathcal{H}_0 : \mathsf{E}_{f_{\underline{\mathrm{y}}}}\left(\underline{\mathrm{y}}\right) = \mathrm{Ax} \quad \text{vs.} \quad \mathcal{H}_{i\neq 0} : \mathsf{E}_{f_{\underline{\mathrm{y}}}}\left(\underline{\mathrm{y}}\right) = \mathrm{Ax} + \mathrm{C}_i\mathrm{b}_i \tag{2.3}$$

for $i \in \{0, ..., k\}$, where $\mathrm{C}_i \in \mathbb{R}^{m\times q_i}$ models the type of model misspecification, $\mathrm{rank}([\mathrm{A}, \mathrm{C}_i]) = n + q_i$, and $\mathrm{b}_i \in \mathbb{R}^{q_i}$ is the model misspecification (e.g., outlier). The redundancy of $\mathcal{H}_0$ is $r = m - \mathrm{rank}(\mathrm{A})$. The statistical testing procedure can be designed using the vector of misclosures

$$\underline{\mathrm{t}} = \mathrm{B}^T\underline{\mathrm{y}}, \quad \mathrm{Q}_{\mathrm{tt}} = \mathrm{B}^T\mathrm{Q}_{\mathrm{yy}}\mathrm{B}, \tag{2.4}$$

where $\mathrm{B} \in \mathbb{R}^{m\times r}$ is a basis matrix of $\mathcal{R}(\mathrm{A})^{\perp}$ (i.e., $\mathrm{B}^T\mathrm{A} = 0_{r\times n}$). The vector of misclosures provides a measure of inconsistency between the model under $\mathcal{H}_0$ and the observations, and has its dimension equal to the redundancy r. Furthermore, it is possible to link the Best Linear Unbiased Estimators (BLUEs) of $\mathrm{x} \in \mathbb{R}^n$ under the $\mathcal{H}_{i\neq 0}$'s and $\mathcal{H}_0$ using $\underline{\mathrm{t}} \in \mathbb{R}^r$ as follows [18]

$$\begin{bmatrix}\underline{\hat{\mathrm{x}}}_i \\ \underline{\mathrm{t}}\end{bmatrix} = \underbrace{\begin{bmatrix}\mathrm{I}_n & -\mathrm{L}_i \\ 0_{r\times n} & \mathrm{I}_r\end{bmatrix}}_{\mathrm{V}_i}\begin{bmatrix}\underline{\hat{\mathrm{x}}}_0 \\ \underline{\mathrm{t}}\end{bmatrix}, \text{ with } \mathrm{L}_i = \begin{cases} 0_{n\times r} & , i = 0 \\ \mathrm{A}^{+}\mathrm{C}_i\mathrm{C}_{\mathrm{t}_i}^{+} & , i > 0 \end{cases} \tag{2.5}$$

where $\underline{\hat{\mathrm{x}}}_0 = \mathrm{A}^{+}\underline{\mathrm{y}}$ and $\mathrm{A}^{+} = (\mathrm{A}^T\mathrm{Q}_{\mathrm{yy}}^{-1}\mathrm{A})^{-1}\mathrm{A}^T\mathrm{Q}_{\mathrm{yy}}^{-1}$ from the normal equations defined by $(\mathrm{A}^T\mathrm{Q}_{\mathrm{yy}}^{-1}\mathrm{A})\underline{\hat{\mathrm{x}}}_0 = \mathrm{A}^T\mathrm{Q}_{\mathrm{yy}}^{-1}\underline{\mathrm{y}}$. The BLUE-inverse of $\mathrm{C}_{\mathrm{t}_i} = \mathrm{B}^T\mathrm{C}_i$ is $\mathrm{C}_{\mathrm{t}_i}^{+} = (\mathrm{C}_{\mathrm{t}_i}^T\mathrm{Q}_{\mathrm{tt}}^{-1}\mathrm{C}_{\mathrm{t}_i})^{-1}\mathrm{C}_{\mathrm{t}_i}^T\mathrm{Q}_{\mathrm{tt}}^{-1}$.

Note that the transformation in (2.5) is in block-triangular form and its inverse is simply $\mathrm{V}_i^{-1} = \begin{bmatrix} \mathrm{I}_n & \mathrm{L}_i \\ 0_{r\times n} & \mathrm{I}_r \end{bmatrix}$. The PDF of $\left[\underline{\hat{\mathrm{x}}}_i^T \ \underline{\mathrm{t}}^T\right]^T$, under a $\mathcal{H}_a$, is

$$\mathcal{H}_a : \begin{bmatrix} \underline{\hat{\mathrm{x}}}_i \\ \underline{\mathrm{t}} \end{bmatrix} \sim \mathcal{N}\left(\begin{bmatrix} \mathrm{x} + \mathrm{A}^{+}\mathrm{R}_i\mathrm{C}_a\mathrm{b}_a \\ \mathrm{B}^T\mathrm{C}_a\mathrm{b}_a \end{bmatrix}, \begin{bmatrix} \mathrm{Q}_{\hat{\mathrm{x}}_0\hat{\mathrm{x}}_0} + \mathrm{L}_i\mathrm{Q}_{\mathrm{tt}}\mathrm{L}_i^T & -\mathrm{L}_i\mathrm{Q}_{\mathrm{tt}} \\ -\mathrm{Q}_{\mathrm{tt}}\mathrm{L}_i^T & \mathrm{Q}_{\mathrm{tt}} \end{bmatrix} \right), \tag{2.6}$$

where $\mathrm{R}_i = \mathrm{I}_m - \mathrm{C}_i\left(\mathrm{B}^T\mathrm{C}_i\right)^{+}\mathrm{B}^T$ projects along $\mathcal{R}(\mathrm{C}_i)$ and onto $\mathcal{R}(\mathrm{A}, \mathrm{Q}_{\mathrm{yy}}\mathrm{B}(\mathrm{B}^T\mathrm{C}_i)^{\perp})$ with $(\mathrm{B}^T\mathrm{C}_i)^{\perp}$ being a basis matrix of the null space of $\mathrm{C}_i^T\mathrm{B}$ [18]. The variance-covariance $\mathrm{Q}_{\hat{\mathrm{x}}_0\hat{\mathrm{x}}_0} = (\mathrm{A}^T\mathrm{Q}_{\mathrm{yy}}^{-1}\mathrm{A})^{-1}$ is the one of $\underline{\hat{\mathrm{x}}}_0$. For a given $\mathcal{H}_a$, we emphasize the following two-cases for the joint PDF of $\left[\underline{\hat{\mathrm{x}}}_i^T \ \underline{\mathrm{t}}^T\right]^T$,

$$f_{\underline{\hat{\mathrm{x}}}_i,\underline{\mathrm{t}}}(x,t) \begin{cases} = f_{\underline{\hat{\mathrm{x}}}_0}(x) f_{\underline{\mathrm{t}}}(t) & , \text{ if } i = 0 \\ \neq f_{\underline{\hat{\mathrm{x}}}_i}(x) f_{\underline{\mathrm{t}}}(t) & , \text{ if } i > 0, \end{cases} \tag{2.7}$$

which shows that, for $i > 0$, the BLUEs $\underline{\hat{\mathrm{x}}}_i$ and the misclosure vector $\underline{\mathrm{t}}$ are *dependent*.

2.2.1 Partitioning of misclosure vector space

Partitioning principles are applied to the misclosure vector space $\mathbb{R}^r$ to 'map' the hypothesis testing problem (2.3) to a partitioning problem. A partitioning of $\mathbb{R}^r$ can be formulated based on $\mathcal{P}_i \subset \mathbb{R}^r$, for $i \in \{0,...,k\}$ such that $\cup_{i=0}^{k}\mathcal{P}_i = \mathbb{R}^r$ and $\mathcal{P}_i \cap \mathcal{P}_l = \{0\}$ for $i \neq l$. The hypothesis $\mathcal{H}_i$, for $i \in \{0,...,k\}$, is selected as the most likely one if and only if $\underline{\mathrm{t}} \in \mathcal{P}_i$, leading to the result of the procedure: $\underline{\hat{\mathrm{x}}}_i$. The partitions can be defined as follows

$$\begin{aligned} \mathcal{P}_0 &= \left\{ t \in \mathbb{R}^r \mid \|t\|^2_{\mathrm{Q}_{\mathrm{tt}}} \leq \chi^2_{\alpha}(r,0) \right\}, \\ \mathcal{P}_{i\neq 0} &= \left\{ t \in \mathbb{R}^r \mid t \notin \mathcal{P}_0,\ \check{\mathrm{T}}_i = \max_{l\in\{1,...,k\}} \mathrm{T}_l \right\}, \end{aligned} \tag{2.8}$$

where $\|\underline{\mathrm{t}}\|^2_{\mathrm{Q}_{\mathrm{tt}}}$ is the overall model test statistic, $\chi^2_{\alpha}(r,0)$ is the critical value for a level of significance α, and $\underline{\mathrm{T}}_l$ is the result of the following transformation [40, 41]

$$\underline{\mathrm{T}}_l = \mathrm{CDF}_{\chi^2(q_l,0)}\left(\|\mathbf{\Pi}_{\mathrm{C}_{\mathrm{t}_l}}\underline{\mathrm{t}}\|^2_{\mathrm{Q}_{\mathrm{tt}}} \right), \tag{2.9}$$

where $\mathrm{CDF}_{\chi^2(q_l,0)}(.)$ is the cumulative distribution function (CDF) of $\chi^2(q_l,0)$, $\|\mathbf{\Pi}_{\mathrm{C}_{\mathrm{t}_l}}\underline{\mathrm{t}}\|^2_{\mathrm{Q}_{\mathrm{tt}}} \overset{\mathcal{H}_0}{\sim} \chi^2(q_l,0)$, $\mathbf{\Pi}_{\mathrm{C}_{\mathrm{t}_l}} = \mathrm{C}_{\mathrm{t}_l}\mathrm{C}^{+}_{\mathrm{t}_l}$, and $\underline{\mathrm{T}}_l$ has a uniform distribution on the interval $[0,1]$ under $\mathcal{H}_0$. In this way all $\underline{\mathrm{T}}_l$'s will have the same PDF under $\mathcal{H}_0$, as the dimension of the model misspecification $\mathrm{b}_l \in \mathbb{R}^{q_l}$ would generally differ across the alternative hypotheses. Therefore, the maximum among them ($\underline{\check{\mathrm{T}}}_i$) corresponds to the most likely $\mathcal{H}_{i\neq 0}$ [40]. Note that if the dimension of the model misspecification is the same across the alternative hypotheses, then the transformation step in (2.9) is not needed and the maximum across $\|\mathbf{\Pi}_{\mathrm{C}_{\mathrm{t}_l}}\underline{\mathrm{t}}\|^2_{\mathrm{Q}_{\mathrm{tt}}}$ can be found directly to obtain $\underline{\check{\mathrm{T}}}_i$. Fig. 2.1(a) shows partitions obtained for a simple example. For other types of partitions (e.g., inclusion of undecided regions when discriminating between hypotheses is challenging), we refer to [42]. We also mention that the statistical hypothesis testing procedure can be formulated, equally, based on the BLUE's residual vector $\underline{\hat{\mathrm{e}}}_0 = \underline{\mathrm{y}} - \mathrm{A}\underline{\hat{\mathrm{x}}}_0$, which gives $\underline{\hat{\mathrm{e}}}_0 = \mathrm{Q}_{\mathrm{yy}}\mathrm{B}\,\mathrm{Q}_{\mathrm{tt}}^{-1}\underline{\mathrm{t}}$ leading to the equality of the quadratic forms $\|\underline{\hat{\mathrm{e}}}_0\|^2_{\mathrm{Q}_{\mathrm{yy}}} = \|\underline{\mathrm{t}}\|^2_{\mathrm{Q}_{\mathrm{tt}}} \overset{\mathcal{H}_0}{\sim} \chi^2(r,0)$.

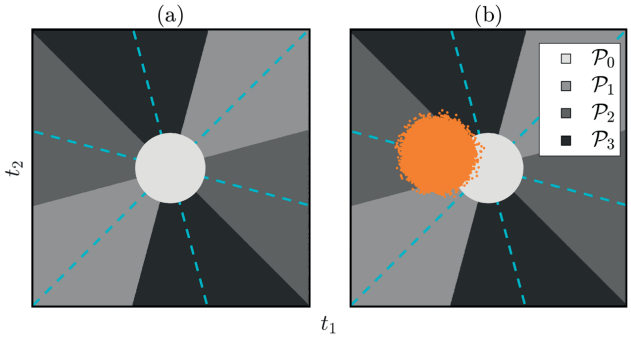

Figure 2.1: (a) Partition of $\mathbb{R}^{r=2}$ when $\mathrm{A} = [1\ 1\ 1]^T$, $\mathrm{x} \in \mathbb{R}$, $\mathrm{Q_{yy}} = \mathrm{I}_3$, and $\mathrm{C}_i = \mathrm{c}_i$'s are the canonical unit vectors for $i = \{1,2,3\}$. The dashed lines (in cyan) are the spans of the vectors $\mathrm{B}^T\mathrm{c}_i$. (b) Partition of $\mathbb{R}^{r=2}$ along with pseudo-random samples ('dots' coloured in orange) generated from $f_{\underline{\mathrm{t}}}(t|\mathcal{H}_2)$ (as an example). Under $\mathcal{H}_2$, the samples from $f_{\underline{\mathrm{t}}}(t|\mathcal{H}_2)$ are shifted away from the origin along the vector span of $\mathrm{B}^T\mathrm{c}_2$.

2.2.2 Statistical hypothesis testing decisions and their probabilities

The decision outcome in statistical hypothesis testing is determined by where the misclosure vector $\underline{\mathrm{t}}$ lands in $\mathbb{R}^r$ with partitions $\mathcal{P}_i \subset \mathbb{R}^r$, for $i \in \{0,..,k\}$. Under $\mathcal{H}_0$, the decision outcomes are: (i) Correct Acceptance (CA) of $\mathcal{H}_0$ when $\underline{\mathrm{t}} \in \mathcal{P}_0$, and (ii) False Alarm (FA) when $\underline{\mathrm{t}} \notin \mathcal{P}_0$, or specifically the FA per alternative hypothesis when $\underline{\mathrm{t}} \in \mathcal{P}_i$ for $i > 0$. The probabilities of these decisions are given by

$$\mathsf{P}_{\mathrm{CA}} = \mathsf{P}(\underline{\mathrm{t}} \in \mathcal{P}_0|\mathcal{H}_0), \quad \mathsf{P}_{\mathrm{FA}} = \sum_{i=1}^{k} \mathsf{P}(\underline{\mathrm{t}} \in \mathcal{P}_i|\mathcal{H}_0), \tag{2.10}$$

where $\mathsf{P}(\underline{\mathrm{t}} \in \mathcal{P}_i|\mathcal{H}_0) = \mathsf{P}_{\mathrm{FA}_i}$, $\mathsf{P}_{\mathrm{FA}} = \sum_{i=1}^{k} \mathsf{P}_{\mathrm{FA}_i} = \alpha$ is the level of significance, and $\mathsf{P}_{\mathrm{CA}} + \mathsf{P}_{\mathrm{FA}} = 1$. Similarly, under $\mathcal{H}_a$, for $a > 0$, the outcomes of the decisions are: (i) missed detection (MD) when $\underline{\mathrm{t}} \in \mathcal{P}_0$, (ii) Correct Identification (CI) when $\underline{\mathrm{t}} \in \mathcal{P}_a$, and (iii) Wrong Identification (WI) $\underline{\mathrm{t}} \in \mathcal{P}_i$ for $i \notin \{0, a\}$ (see Fig. 2.1(b)). The probabilities of these decisions are given by

$$\begin{aligned} \mathsf{P}_{\mathrm{MD}_a} &= \mathsf{P}(\underline{\mathrm{t}} \in \mathcal{P}_0|\mathcal{H}_a), \quad \mathsf{P}_{\mathrm{CI}_a} = \mathsf{P}(\underline{\mathrm{t}} \in \mathcal{P}_a|\mathcal{H}_a), \\ \mathsf{P}_{\mathrm{WI}} &= \sum_{i \neq 0,a}^{k} \mathsf{P}(\underline{\mathrm{t}} \in \mathcal{P}_i|\mathcal{H}_a), \end{aligned} \tag{2.11}$$

where $\mathsf{P}(\underline{\mathrm{t}} \in \mathcal{P}_i|\mathcal{H}_a) = \mathsf{P}_{\mathrm{WI}_i}$ and the decision outcome of Correct Detection (CD) is given by $\mathsf{P}_{\mathrm{CD}_a} = \mathsf{P}_{\mathrm{CI}_a} + \mathsf{P}_{\mathrm{WI}}$ fulfilling $\mathsf{P}_{\mathrm{MD}_a} + \mathsf{P}_{\mathrm{CD}_a} = 1$. The probabilities in (2.11) depend on the unknown model misspecification $\mathrm{b}_a \in \mathbb{R}^{q_a}$ since $f_{\underline{\mathrm{t}}}(t|\mathcal{H}_a) = \mathcal{N}\left(\mathrm{B}^T\mathrm{C}_a\mathrm{b}_a, \mathrm{Q_{tt}}\right)$.

2.2.3 DIA-estimator and its PDF

The *combined* parameter estimation and statistical hypothesis testing procedure, in the forms discussed previously, can be captured by the Detection (D) Identification (I) and

Adaptation (A) procedure, summarized as follows

$$\begin{cases} \text{if } \underline{t} \in \mathcal{P}_0 \text{ (no D)} \rightarrow \text{ output } \hat{\underline{x}}_0, \\ \text{if } \underline{t} \notin \mathcal{P}_0 \text{ (D)} \rightarrow \underline{t} \in \mathcal{P}_{i\neq 0} \text{ (I)} \rightarrow \text{ output } \hat{\underline{x}}_i \text{ (A)}. \end{cases} \tag{2.12}$$

The procedure in (2.12), or any procedure of similar form (e.g., [28]), can be expressed in terms of the DIA-estimator

$$\overline{\underline{x}} = \begin{cases} \hat{\underline{x}}_0, & \text{if } \underline{t} \in \mathcal{P}_0 \\ \hat{\underline{x}}_i, & \text{if } \underline{t} \in \mathcal{P}_{i\neq 0} \end{cases} \xrightarrow{\text{compact form}} \overline{\underline{x}} = \sum_{i=0}^{k} \hat{\underline{x}}_i \, p_i(\underline{t}) \,, \tag{2.13}$$

where the indicator function $p_i(\underline{t}) = 1$ if $\underline{t} \in \mathcal{P}_i$ and 0 otherwise. The PDF of $\overline{\underline{x}}$ follows from Theorem 1 in [18]

$$f_{\overline{\underline{x}}}(x) = \sum_{i=0}^{k} \int_{\mathcal{P}_i} f_{\hat{\underline{x}}_i, \underline{t}}(x, t)\, dt, \tag{2.14}$$

which, in general, is a multimodal PDF. The conditional components of $f_{\overline{\underline{x}}}(x)$ on the testing decisions of CA, FA_i, MD_a, CI_a, and WI_i can be obtained from $f_{\overline{\underline{x}}}(x|\mathcal{H}_0)$ and $f_{\overline{\underline{x}}}(x|\mathcal{H}_a)$ for $a \neq 0$. The probability of positioning failure and its conditional components are formulated in Section 2.3, based on (2.14), together with the proposed method to compute them.

2.2.4 Remarks on the dimensions of vector spaces

In this subsection we provide several remarks about the dimensionality of the unknown parameter $\mathrm{x} \in \mathbb{R}^n$ and of the misclosure vector $\underline{t} \in \mathbb{R}^r$ for GNSS-based positioning applications. One may not be interested in the complete parameter vector $\mathrm{x} \in \mathbb{R}^n$, but only in the components corresponding to the 1D, 2D, or 3D position. The linear transformation that gives the desired position components can be expressed as $\theta = \mathrm{H}^T \mathrm{x} \in \mathbb{R}^p$ with $p < n$. Further developments are done in terms of $\mathrm{x} \in \mathbb{R}^n$, however a similar route would apply also for $\theta \in \mathbb{R}^p$ [18].

The redundancy under $\mathcal{H}_0$, and therefore the dimension of the misclosure vector $\underline{t} \in \mathbb{R}^r$, depends on the chosen positioning technology, like for example GNSS. In this case it depends on: the number of observed GNSS satellites, type of observables, from how many frequencies these observables are obtained, the number of parameters to be estimated, etc [43]. As we will see in Section 2.4, in the case of a GNSS receiver which obtains code-based pseudoranges from 15 GNSS satellites of two constellations (e.g., 8 GPS and 7 Galileo satellites) at a single-epoch (snapshot), on a single-frequency, with the objective to estimate the 3D position vector and the receiver clock bias, then (i) $r = 15 - 4 - 1 = 10$ if the Inter System Bias (ISB) is considered unknown, or (ii) $r = 15 - 4 = 11$ if the ISB is considered known [43]. If more than two GNSS constellations are considered, under similar assumptions, r could reach values around 40.

2.3 Method to compute the probability of positioning failure and its components

In this section we present the expression of the probability of positioning failure, its conditional components, and introduce a method developed to compute them. The starting point is the probability of positioning failure re-expressed from (2.1)

$$\mathbb{P}_{\mathcal{F}}(\mathbf{b}) = \int_{\mathcal{B}^c} f_{\underline{\mathrm{x}}}(x)\, dx, \tag{2.15}$$

where the dependence on the model misspecifications is accounted in the notation with $\mathbf{b} = \{\mathrm{b}_1, ..., \mathrm{b}_k\}$ for $i > 0$, and $\mathcal{B}^c = \mathbb{R}^n / \mathcal{B}$ is the complement of the safety-region $\mathcal{B} \subset \mathbb{R}^n$. Applying the law of total probability to (2.15) yields

$$\mathbb{P}_{\mathcal{F}}(\mathbf{b}) = \mathsf{P}(\mathcal{H}_0) \underbrace{\left(\int_{\mathcal{B}^c} f_{\underline{\mathrm{x}}}(x|\mathcal{H}_0)\, dx \right)}_{\mathbb{P}_{\mathcal{F}}|\mathcal{H}_0} + \sum_{i=1}^{k} \mathsf{P}(\mathcal{H}_i) \underbrace{\left(\int_{\mathcal{B}^c} f_{\underline{\mathrm{x}}}(x|\mathcal{H}_i)\, dx \right)}_{\mathbb{P}_{\mathcal{F}}|\mathcal{H}_i(\mathrm{b}_i)}, \tag{2.16}$$

with $\mathsf{P}(\mathcal{H}_0)$ and $\mathsf{P}(\mathcal{H}_i)$, for $i > 0$, denote the apriori probabilities of the hypotheses. Combining (2.14) and (2.16), it follows that

$$\mathbb{P}_{\mathcal{F}}(\mathbf{b}) = \mathsf{P}(\mathcal{H}_0) \left(\sum_{j=0}^{k} \mathsf{E}_{f_{\underline{\hat{\mathrm{x}}}_j, \underline{\mathrm{t}}}} \left(\mathbb{1}_j(\underline{\mathrm{x}}, \underline{\mathrm{t}}) | \mathcal{H}_0 \right) \right) + \sum_{i=1}^{k} \mathsf{P}(\mathcal{H}_i) \left(\sum_{j=0}^{k} \mathsf{E}_{f_{\underline{\hat{\mathrm{x}}}_j, \underline{\mathrm{t}}}} \left(\mathbb{1}_j(\underline{\mathrm{x}}, \underline{\mathrm{t}}) | \mathcal{H}_i \right) \right), \tag{2.17}$$

where the 'joint' indicator function $\mathbb{1}_j(\underline{\mathrm{x}}, \underline{\mathrm{t}}) = 1$ if $[\underline{\mathrm{x}}^T \ \underline{\mathrm{t}}^T]^T \in \left(\mathcal{B}^c \cap \mathcal{P}_j \right)$, and 0 otherwise. The two summations of joint probabilities in parentheses in (2.17) are rewritten below, explicitly incorporating the statistical testing decisions into the notation,

$$\begin{aligned} \sum_{j=0}^{k} \mathsf{E}_{f_{\underline{\hat{\mathrm{x}}}_j, \underline{\mathrm{t}}}} \left(\mathbb{1}_j(\underline{\mathrm{x}}, \underline{\mathrm{t}}) | \mathcal{H}_0 \right) &= \mathbb{P}_{\mathcal{F}}|\mathrm{CA}\, \mathsf{P}_{\mathrm{CA}} + \sum_{j=1}^{k} \mathbb{P}_{\mathcal{F}}|\mathrm{FA}_j\, \mathsf{P}_{\mathrm{FA}_j}, \\ \sum_{j=0}^{k} \mathsf{E}_{f_{\underline{\hat{\mathrm{x}}}_j, \underline{\mathrm{t}}}} \left(\mathbb{1}_j(\underline{\mathrm{x}}, \underline{\mathrm{t}}) | \mathcal{H}_i \right) &= \mathbb{P}_{\mathcal{F}}|\mathrm{MD}_i\, \mathsf{P}_{\mathrm{MD}_i} + \mathbb{P}_{\mathcal{F}}|\mathrm{CI}_i\, \mathsf{P}_{\mathrm{CI}_i} + \sum_{j \neq 0, i}^{k} \mathbb{P}_{\mathcal{F}}|\mathrm{WI}_j\, \mathsf{P}_{\mathrm{WI}_j}\ . \end{aligned} \tag{2.18}$$

where $\mathbb{P}_{\mathcal{F}}|\mathcal{E}$ is the probability of positioning failure conditioned on the testing decision $\mathcal{E} \in \{\mathrm{CA}, \mathrm{FA}_j, \mathrm{MD}_i, \mathrm{CI}_i, \mathrm{WI}_j\}$. These decompositions are schematically illustrated as a 'failure-tree' in Fig. 2.2, where Level 1 corresponds to (2.18) and Level 2 corresponds to (2.16)
The objective of our proposed method is to construct the 'failure-tree' in Fig. 2.2 by computing all of the components from Levels 1 and 2.

2.3.1 Computation of Level 1 Components

To illustrate the computational steps for an arbitrary component from Level 1, we introduce the following generic notation

$$\mathbb{P}_{\mathcal{F}}|\mathcal{H} = \begin{cases} \mathbb{P}_{\mathcal{F}}|\mathcal{H}_0, & \text{if } \mathcal{H} = \mathcal{H}_0 \\ \mathbb{P}_{\mathcal{F}}|\mathcal{H}_i(\mathrm{b}_i), & \text{if } \mathcal{H} = \mathcal{H}_i \text{ for } i \in \{1, ..., k\}\,. \end{cases} \tag{2.19}$$

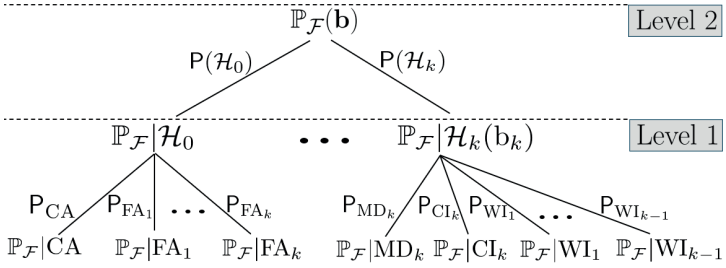

Figure 2.2: Representation of $\mathbb{P}_{\mathcal{F}}(\mathbf{b})$ as a 'failure-tree'. Level 1 corresponds to (2.18) and Level 2 to (2.16).

From (2.17) it follows that

$$\mathbb{P}_{\mathcal{F}}|\mathcal{H} = \sum_{j=0}^{k} \underbrace{\mathsf{E}_{f_{\underline{\hat{x}}_j,\underline{t}}}\left(\mathbb{1}_j(\underline{x},\underline{t})|\mathcal{H}\right)}_{\mathcal{X}_j}, \tag{2.20}$$

where $\mathcal{X}_j$ denotes the j^{th} joint-probability component of the sum. The first step is to reparametrize the components $\mathcal{X}_j$, noting that the number of distributional parameters defining each $f_{\underline{\hat{x}}_j,\underline{t}}(x,t|\mathcal{H})$ increases quadratically, up to $[(n+r)+(n+r)(n+r+1)/2]$, primarily due to the variance-covariance matrix. To mitigate this quadratic increase in dimensionality we start from

$$\underline{s}_j = \begin{bmatrix} \underline{\hat{x}}_j \\ \underline{t} \end{bmatrix}, \quad Q_{s_j s_j} = \begin{bmatrix} Q_{\hat{x}_0\hat{x}_0} + L_j Q_{tt} L_j^T & -L_j Q_{tt} \\ -Q_{tt} L_j^T & Q_{tt} \end{bmatrix}. \tag{2.21}$$

An approach is to apply a change of variable to the expected values in (2.20) such that they are expressed w.r.t. PDFs which have simpler forms (e.g., identity variance-covariance matrices) [44]. Suppose an invertible linear transformation defined by $U_j : \mathbb{R}^{(n+r)} \to \mathbb{R}^{(n+r)}$ applied to (2.21), which gives the following pair

$$\underline{z}_j = U_j \underline{s}_j, \quad \underline{s}_j = U_j^{-1} \underline{z}_j \,. \tag{2.22}$$

One could make use of the *readily-available* transformation in the block-triangular form V_j in (2.5) and its inverse to set

$$U_j = \begin{bmatrix} I_n & L_j \\ 0_{r\times n} & I_r \end{bmatrix} \to Q_{z_j z_j} = \begin{bmatrix} Q_{\hat{x}_0\hat{x}_0} & 0_{n\times r} \\ 0_{r\times n} & Q_{tt} \end{bmatrix}, \tag{2.23}$$

or proceed with a *one-time* Cholesky decomposition of $Q_{\hat{x}_0\hat{x}_0} = G_{\hat{x}_0} G_{\hat{x}_0}^T$ and of $Q_{tt} = G_t G_t^T$ to set

$$U_j = \begin{bmatrix} G_{\hat{x}_0}^{-1} & G_{\hat{x}_0}^{-1} L_j \\ 0_{r\times n} & G_t^{-1} \end{bmatrix} \to Q_{z_j z_j} = \begin{bmatrix} I_n & 0_{n\times r} \\ 0_{r\times n} & I_r \end{bmatrix}, \tag{2.24}$$

where $G_{\hat{x}_0}^{-1}$ is already obtained by solving the system of normal equations from (2.5) by making use of $A^T Q_{yy}^{-1} A = Q_{\hat{x}_0\hat{x}_0}^{-1} = G_{\hat{x}_0}^{-T} G_{\hat{x}_0}^{-1}$. The option in (2.24) is preferred for moderate

to high dimension of $\underline{s}_j \in \mathbb{R}^{(n+r)}$ (e.g., > 5). Applying the change of variable from (2.24) to (2.20) we obtain

$$\mathbb{P}_{\mathcal{F}}|\mathcal{H} = \sum_{j=0}^{k} \underbrace{\mathsf{E}_{f_{\underline{z}_j}}\left(\mathbb{1}_j\left(\mathrm{U}_j^{-1}\underline{z}\right)|\mathcal{H}\right)}_{\mathcal{S}_j}, \tag{2.25}$$

where $\mathrm{U}_j^{-1} = \begin{bmatrix} \mathrm{G}_{\hat{\mathrm{x}}_0} & -\mathrm{L}_j\mathrm{G}_{\mathrm{t}} \\ 0_{r\times n} & \mathrm{G}_{\mathrm{t}} \end{bmatrix}$ and the number of distributional parameters of $f_{\underline{z}_j}(z|\mathcal{H})$ is $2(n+r)$. Note that the dimensionality of the components $\mathcal{S}_j$ now increases *linearly* rather than quadratically, as was the case for $\mathcal{X}_j$ in (2.20). It is the expression in (2.25) that is used in the further developments and analysis.

The second step is to generate N_j independent and identically distributed (i.i.d.) pseudo-random samples from $f_{\underline{z}_j}(z|\mathcal{H})$ to compute (2.25) via standard Monte Carlo (MC) [37],

$$\underline{\mathbb{P}}_{\mathcal{F}}|\mathcal{H} = \sum_{j=0}^{k} \underbrace{\left[\frac{1}{N_j}\sum_{\ell=1}^{N_j} \mathbb{1}_j\left(\mathrm{U}_j^{-1}\underline{z}^{(\ell)}\right)\right]}_{\underline{\mathcal{S}}_j}. \tag{2.26}$$

where the underscores in $\underline{\mathbb{P}}_{\mathcal{F}}|\mathcal{H}$ and in $\underline{\mathcal{S}}_j$ indicate that the quantities have been numerically computed and thus includes simulation-related uncertainty. For simplicity we consider $N_j = N$ for all $j \in \{0, ..., k\}$. The component-wise mean and simulation variance (dispersion) are [45]

$$\mathsf{E}_f\left(\underline{\mathcal{S}}_j|\mathcal{H}\right) = \mathcal{S}_j, \;\; \mathsf{D}_f\left(\underline{\mathcal{S}}_j|\mathcal{H}\right) = \frac{\mathcal{S}_j\left(1-\mathcal{S}_j\right)}{N}. \tag{2.27}$$

The results of $\mathsf{E}_f(.)$ and $\mathsf{D}_f(.)$ correspond to the Bernoulli distribution. If the objective is to compute a target value $\mathcal{S}_j = 10^{-9}$ with $\sqrt{\mathsf{D}_f\left(\underline{\mathcal{S}}_j|\mathcal{H}\right)} = 10^{-10}$, then the required number of pseudo-random samples would be $N \approx 10^{11}$. This illustrates the main challenge in rare-event simulation: the requirement for an extremely large number of pseudo-random samples to achieve a desired simulation standard deviation. To tackle this problem, a different approach from the standard MC method is needed.

Importance Sampling (IS) is a reasonable candidate to be considered as it can achieve simulation variance reduction without a significant increase of the required pseudo-random samples [38]. It has found applicability across a wide area of safety-critical applications, such as reliability analyses for structures, nuclear power plants, and for computation of probabilities of collision events in aviation [46–48]. Based on the principles of IS, the expected values in (2.25) can be re-expressed as

$$\mathbb{P}_{\mathcal{F}}|\mathcal{H} = \sum_{j=0}^{k} \underbrace{\mathsf{E}_{\tilde{f}_j}\left(\mathbb{1}_j\left(\mathrm{U}_j^{-1}\underline{z}\right)\tilde{\mathcal{L}}_j(\underline{z})|\mathcal{H}\right)}_{\tilde{\mathcal{S}}_j}, \tag{2.28}$$

where $\tilde{\mathcal{L}}_j(\underline{z}) = \dfrac{f_{\underline{z}_j}(\underline{z}|\mathcal{H})}{\tilde{f}_j(\underline{z})}$. The newly introduced PDFs $\tilde{f}_j(z)$ are called IS densities, auxiliar densities, or proposal densities [45, 49]. A necessary condition for the IS densities is $\mathbb{1}_j(\mathrm{U}_j^{-1}z)\tilde{f}_j(z) \neq 0$ whenever $\mathbb{1}_j(\mathrm{U}_j^{-1}z)f_{\underline{z}_j}(z|\mathcal{H}) \neq 0$ [49]. Given $\tilde{N}_j = \tilde{N}$, for all $j \in \{0, ..., k\}$, i.i.d. pseudo-random samples generated from the IS densities $\tilde{f}_j(z)$, then (2.28) can be computed as

$$\underline{\mathbb{P}}_{\mathcal{F}}|\mathcal{H} = \sum_{j=0}^{k} \underbrace{\left[\frac{1}{\tilde{N}} \sum_{\ell=1}^{\tilde{N}} \mathbb{1}_j\left(\mathrm{U}_j^{-1}\underline{\mathrm{z}}^{(\ell)}\right) \tilde{\mathcal{L}}_j\left(\underline{\mathrm{z}}^{(\ell)}\right)\right]}_{\underline{\tilde{S}}_j}, \tag{2.29}$$

where $\underline{\mathbb{P}}_{\mathcal{F}}|\mathcal{H}$ is an unbiased estimator of $\mathbb{P}_{\mathcal{F}}(\mathbf{b})$ if the conditions for the IS densities are met [45, 49]. The simulation variance of the numerically computed j^{th} component $\underline{\tilde{S}}_j$ is

$$\mathsf{D}_{\tilde{f}_j}\left(\underline{\tilde{S}}_j|\mathcal{H}\right) = \frac{\left[\mathsf{E}_{\tilde{f}_j}\left(\mathbb{1}_j\left(\mathrm{U}_j^{-1}\underline{\mathrm{z}}\right)\tilde{\mathcal{L}}_j^2(\underline{\mathrm{z}})|\mathcal{H}\right) - \tilde{S}_j^2\right]}{\tilde{N}}, \tag{2.30}$$

which can be used as criteria for the choices of the IS densities to achieve variance reduction. One can notice from (2.30) that the following IS densities are giving *exactly* zero variances [38]

$$\tilde{f}_j^*(z) = \frac{\mathbb{1}_j\left(\mathrm{U}_j^{-1}z\right) f_{\underline{z}_j}(z|\mathcal{H})}{\tilde{S}_j}. \tag{2.31}$$

These theoretically optimal IS densities are the best in a minimum variance sense. However, as they depend on the unknown quantities of interest, their use is not feasible in practice. Instead, one could search within a parametric family of PDFs (e.g., exponential family) and find the one that minimizes (2.30) [45]. We account for the distributional parameters in the notation of $\tilde{f}_j(z;\tilde{\Theta}_j)$ and formulate the following variance minimization problem [50]

$$\underline{\tilde{\Theta}}_j = \underset{\tilde{\Theta}_j}{\arg\min}\, \mathsf{E}_{\tilde{f}_j}\left(\mathbb{1}_j\left(\mathrm{U}_j^{-1}\underline{\mathrm{z}}\right)\frac{f_{\underline{z}_j}^2(\underline{\mathrm{z}}|\mathcal{H})}{\tilde{f}_j^2\left(\underline{\mathrm{z}};\tilde{\Theta}_j\right)}\right). \tag{2.32}$$

Typically there are no analytical solutions to the minimization problems in (2.32), and this can lead to time consuming optimization algorithms [39]. In [39], Rubinstein proposes an alternative which is based on finding the IS densities which minimizes the cross-entropy, or Kullback-Leibler (KL) divergence, w.r.t. the theoretically optimal IS densities in (2.31). The KL divergences are defined as [51]

$$\mathcal{D}\left(\tilde{f}_j^*, \tilde{f}_j\right) = \mathsf{E}_{\tilde{f}_j^*}\left(\ln \tilde{f}_j^*(\underline{\mathrm{z}})\right) - \mathsf{E}_{\tilde{f}_j^*}\left(\ln \tilde{f}_j(\underline{\mathrm{z}};\tilde{\Theta}_j)\right). \tag{2.33}$$

Using the expressions of the theoretically optimal IS densities from (2.31), the minimization problem of (2.33) w.r.t. $\tilde{\Theta}_j$ becomes

$$\underline{\tilde{\Theta}}_j = \underset{\tilde{\Theta}_j}{\arg\min}\, -\mathsf{E}_{f_{\underline{z}_j}}\left(\mathbb{1}_j\left(\mathrm{U}_j^{-1}\underline{\mathrm{z}}\right)\ln \tilde{f}_j\left(\underline{\mathrm{z}};\tilde{\Theta}_j\right)|\mathcal{H}\right). \tag{2.34}$$

Note that the expected values in (2.34) are now expressed w.r.t. the original PDFs $f_{\underline{z}_j}(z|\mathcal{H})$, which means that the minimization problems may be too computationally expensive to be carried out in the context of rare events since $\mathbb{1}_j\left(\mathrm{U}_j^{-1}\underline{z}\right)=0$ too often. To circumvent this issue, the expected values can be expressed with respect to newly introduced IS densities $\acute{f}_j(z;\acute{\Theta}_j)$ (assumed to be known a-priori) [39]

$$\underline{\tilde{\Theta}}_j=\underset{\tilde{\Theta}_j}{\arg\max}\,\mathsf{E}_{\acute{f}_j}\left(\mathbb{1}_j\left(\mathrm{U}_j^{-1}\underline{z}\right)\frac{f_{\underline{z}_j}(\underline{z}|\mathcal{H})}{\acute{f}_j(\underline{z};\acute{\Theta}_j)}\ln\tilde{f}_j\left(\underline{z};\tilde{\Theta}_j\right)\right). \tag{2.35}$$

The stochastic counterpart of (2.35) can be formulated given access $\acute{N}_j$ pseudo-random samples from the a-priori IS densities $\acute{f}_j(z;\acute{\Theta}_j)$,

$$\underline{\tilde{\Theta}}_j=\underset{\tilde{\Theta}_j}{\arg\max}\frac{1}{\acute{N}_j}\sum_{\ell=1}^{\acute{N}_j}\mathbb{1}_j\left(\mathrm{U}_j^{-1}\underline{z}^{(\ell)}\right)\acute{\mathcal{L}}_j(\underline{z}^{(\ell)})\ln\tilde{f}_j\left(\underline{z}^{(\ell)};\tilde{\Theta}_j\right), \tag{2.36}$$

$\acute{\mathcal{L}}_j(\underline{z}^{(\ell)})=\dfrac{f_{\underline{z}_j}(\underline{z}^{(\ell)})}{\acute{f}_j(\underline{z}^{(\ell)};\acute{\Theta}_j)}$. If the objective functions in (2.36) are convex and differentiable $\tilde{\Theta}_j$, the solutions may be obtained analytically by setting the gradients to zero [39, 45]. A procedure, known as the Cross-Entropy (CE) method, can be used to carry out the maximization problems in (2.36) as described in [52, 53]. Once $\underline{\tilde{\Theta}}_j$ are obtained, then $\tilde{N}$ i.i.d. pseudo-random samples can be generated from $\tilde{f}_j(z;\underline{\tilde{\Theta}}_j)$ to compute (2.29).

The third step quantifies the uncertainty related to the simulation. This is achieved by repeating the computations of the second step N_{sim} times, each time with a different set of i.i.d. pseudo-random samples. The results are the mean values of the components $\underline{\tilde{\mathcal{M}}}_j=(1/N_{\text{sim}})\sum_{h=1}^{N_{\text{sim}}}\underline{\tilde{S}}_j^{(h)}$, and the empirical standard deviations $\tilde{\sigma}_j$, based on which $\overline{\mathbb{P}}_{\mathcal{F}}|\mathcal{H}=\sum_{j=0}^{k}\underline{\tilde{\mathcal{M}}}_j$ and its σ_{sim} are obtained. Some common example values for N_{sim} are 50, 100 [54, 55]. The three-step procedure to compute the Level 1 components in Fig. 2.2 is summarized in Fig. 2.3 (next page).

2.3.2 Computation of Level 2 Component

Once the Level 1 entries $\overline{\mathbb{P}}_{\mathcal{F}}|\mathcal{H}_0,\ldots,\overline{\mathbb{P}}_{\mathcal{F}}|\mathcal{H}_k(\mathrm{b}_k)$ and their simulation standard deviations are obtained, one needs to make assumptions or have knowledge of the a priori probabilities of occurrences of the hypotheses $\mathsf{P}(\mathcal{H}_0),\ldots,\mathsf{P}(\mathcal{H}_k)$. Assuming access to their values, then the total probability of positioning failure can be computed

$$\overline{\mathbb{P}}_{\mathcal{F}}(\mathbf{b})=\mathsf{P}(\mathcal{H}_0)\overline{\mathbb{P}}_{\mathcal{F}}|\mathcal{H}_0+\sum_{i=1}^{k}\mathsf{P}(\mathcal{H}_i)\overline{\mathbb{P}}_{\mathcal{F}}|\mathcal{H}_i(\mathrm{b}_i) \tag{2.37}$$

and its simulation standard deviation propagated accordingly. For positioning safety analyses, the maximum of (2.37) can be compared against an application specific requirement to decide whether the requirement is met,

$$\max_{\mathbf{b}}\overline{\mathbb{P}}_{\mathcal{F}}(\mathbf{b})=\mathsf{P}(\mathcal{H}_0)\overline{\mathbb{P}}_{\mathcal{F}}|\mathcal{H}_0+\max_{\mathrm{b}_1,\ldots,\mathrm{b}_k}\sum_{i=1}^{k}\mathsf{P}(\mathcal{H}_i)\overline{\mathbb{P}}_{\mathcal{F}}|\mathcal{H}_i(\mathrm{b}_i). \tag{2.38}$$

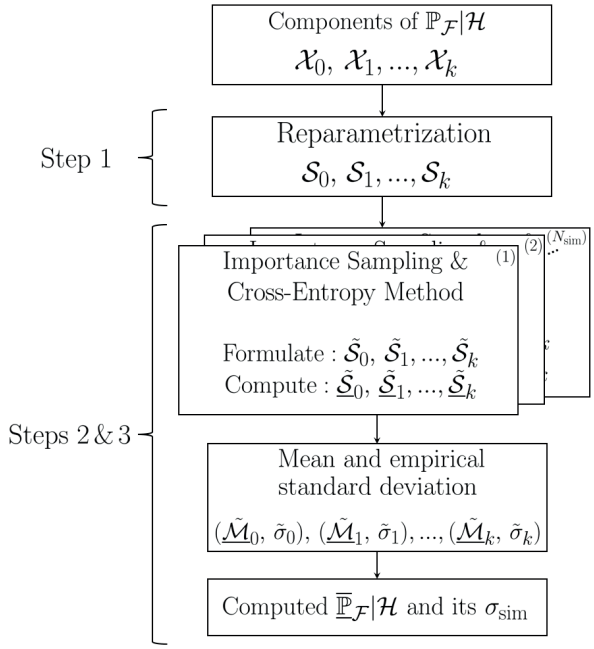

Figure 2.3: Summary of procedure to compute Level 1 components in Fig. 2.2.

2.3.3 Remarks on the family of PDFs to consider for the IS densities

When choosing the parametric family of PDFs for determining the IS densities using the CE method, a reasonable choice is to use the same parametric family as the original PDFs [52]. For instance, if $f_{\underline{\hat{x}}_0}(x)$ and $f_{\underline{z}_i}(z)$ for $i > 0$ are Gaussian PDFs, then choosing $\tilde{f}_0(x;\tilde{\Theta}_0)$ and $\tilde{f}_i(z;\tilde{\Theta}_i)$ to be Gaussian PDFs is reasonable as well. However, additional criteria should be taken into account when choosing the parametric family of PDFs for the IS densities, such as: the dimensionality of the vectors of interest (e.g., $\underline{x} \in \mathbb{R}^n$, $\underline{t} \in \mathbb{R}^r$), the characteristics of the safety (or failure)-regions (e.g., unimodal or multimodal), simulation time budget [56–58] etc. The detailed analysis of these aspects is beyond the scope of this contribution. In Section 2.4, we choose the parametric family of Gaussian PDFs for the IS densities, considering that $f_{\underline{\hat{x}}_0}(x)$ and $f_{\underline{z}_i}(z)$, for $i > 0$, are also Gaussian PDFs.

2.4 Positioning safety analysis for an automated vehicle

As an example, to demonstrate the working of the method we carry out a positioning safety analysis for an automated vehicle which coordinates, in a local East-North-Up (ENU) coordinate system, are determined using single-frequency (code)pseudorange observables in a Differential GNSS (DGNSS) setting. The GNSS constellations we consider are GPS (G) and Galileo (E), at L1/E1 radio-frequency (1575.42 MHz). A reference receiver is stationed at an accurately known position which determines the pseudorange corrections (PRCs) that are transmitted to the automated vehicle's rover receiver using a Networked Transport of RTCM via Internet Protocol (NTRIP) [59]. Depending on the distance between the reference and the rover receiver, decimeter-level positioning precision of the rover receiver is achievable [60]. An illustration of the DGNSS setup is presented in Fig. 2.4. The index '$*$' is used to indicate the GNSS constellation (G or E).

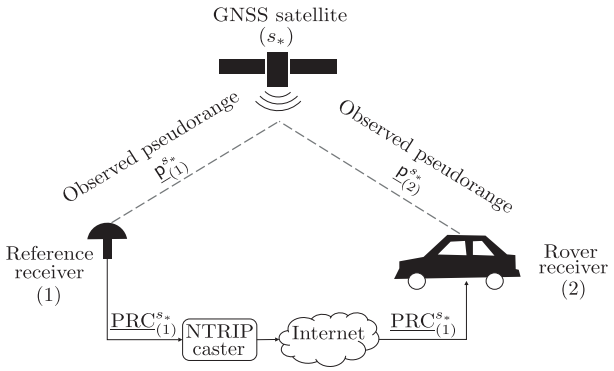

Figure 2.4: Pseudorange corrections are determined at the reference receiver $\underline{\mathrm{PRC}}^{s_*}_{(1)} = \rho^{s_*}_{(1)} - \underline{\mathrm{p}}^{s_*}_{(1)}$, where $\rho^{s_*}_{(1)}$ is the Euclidean distance. The $\underline{\mathrm{PRC}}^{s_*}_{(1)}$'s are collected by an NTRIP caster which are then distributed to the automated vehicle's rover receiver to be applied to $\underline{\mathrm{p}}^{s_*}_{(2)}$. Source: Adapted from [61].

The corresponding linear(ized) DGNSS model is given by [43]

$$\underbrace{\mathsf{E}_{f_{\Delta\underline{\mathrm{y}}}}\left(\begin{bmatrix}\Delta\underline{\mathrm{y}}_{\mathrm{G}}\\ \Delta\underline{\mathrm{y}}_{\mathrm{E}}\end{bmatrix}\right)}_{\Delta\underline{\mathrm{y}}} = \underbrace{\begin{bmatrix}\mathrm{M}_{\mathrm{G}} & \mathbf{u}_{\mathrm{G}}\\ \mathrm{M}_{\mathrm{E}} & \mathbf{u}_{\mathrm{E}}\end{bmatrix}}_{\mathrm{J_A}}\underbrace{\begin{bmatrix}\Delta\mathbf{r}\\ \mathrm{c}\,\Delta\mathbf{t}\end{bmatrix}}_{\Delta\mathrm{x}}, \quad \mathrm{Q}_{\Delta\mathrm{y}\Delta\mathrm{y}} = \mathrm{blkdiag}[\mathrm{Q}_{\Delta\mathrm{y_G}\Delta\mathrm{y_G}}, \mathrm{Q}_{\Delta\mathrm{y_E}\Delta\mathrm{y_E}}], \tag{2.39}$$

where $\Delta\underline{\mathrm{y}} \sim \mathcal{N}(\mathsf{E}_{f_{\Delta\underline{\mathrm{y}}}}(\Delta\underline{\mathrm{y}}), \mathrm{Q}_{\Delta\mathrm{y}\Delta\mathrm{y}})$ and $\mathrm{J_A} \in \mathbb{R}^{m\times n}$ is the Jacobian of the vector function A(.) which links the unknowns of interest to the nonlinear (code)pseudorange observables. The components of $\Delta\underline{\mathrm{y}}_* \in \mathbb{R}^{m_*}$ are the observed pseudoranges from which the Euclidean distances between an appropriately chosen linearization point and the satellites are subtracted, and the PRCs are applied via addition. The PRCs remove most of the satellite orbit errors, the satellite clock error and satellite code hardware bias, while the differential delays due to the troposphere and ionosphere are considered negligible for distances between the reference and rover receiver up to 10 km [62]. Both the reference and rover receivers have calibrated

the GPS-Galileo Inter System Bias (ISB) by applying it as an additional correction to their pseudoranges [43]. The rows of $\mathrm{M}_* \in \mathbb{R}^{m_* \times 3}$ contain the unit direction vectors between the rover receiver and the satellites, while $\mathbf{u}_* \in \mathbb{R}^{m_*}$ is the vector of ones. The unknown parameters are the rover's ENU coordinate increments $\Delta\mathbf{r} \in \mathbb{R}^3$ and $\Delta\mathbf{t} \in \mathbb{R}$ which represents the combined differential receiver clock and hardware delay. The c term is the speed of light in a vacuum. The Jacobian $\mathrm{J_A} \in \mathbb{R}^{m \times n}$ has $\mathrm{rank}(\mathrm{J_A}) = 4$. The variance-covariance matrix $\mathrm{Q}_{\Delta \mathrm{y}_* \Delta \mathrm{y}_*} = 2\sigma^2_{\mathrm{y}_*} \mathrm{W}_*^{-1} \in \mathbb{R}^{m_* \times m_*}$ is diagonal where $\mathrm{W}_* = \mathrm{diag}[\omega_{1_*}, ..., \omega_{m_*}] \in \mathbb{R}^{m_* \times m_*}$ is the weight matrix which components are the elevation-dependent weighting functions based on [63]. In $\mathrm{Q}_{\Delta \mathrm{y}_* \Delta \mathrm{y}_*}$, σ_{y_*} is the standard deviation of the pseudorange observables, in [m], and the factor 2 is due to the application of the PRCs to the observed pseudoranges by the rover receiver (assuming the same σ_{y_*} at both reference and rover receivers [64]). In this scenario, we aim for a horizontal positioning precision of approximately 0.5 meters, specified as the 95% circular probability radius. To achieve this, we set $\sqrt{2}\sigma_{\mathrm{y_G}} = 0.3$ m and $\sqrt{2}\sigma_{\mathrm{y_E}} = 0.2$ m, which correspond to positioning precisions attainable with DGNSS [60].

The model in (2.39) has a total number of $m = m_\mathrm{G} + m_\mathrm{E}$ observables and $n = 4$ unknowns. The redundancy follows to be $r = m - \mathrm{rank}(\mathrm{J_A}) = m - 4$. The estimate $\hat{\mathrm{x}}$ is obtained from a Gauss-Newton iteration scheme once the stop criterion is met for $\Delta\hat{\mathrm{x}}$ [65]. Given that $r \geq 2$, we account for individual outliers in the observations (e.g., due to signal reflections by local environment near the rover receiver) and assume that only one observation outlier occurs at a time. This is the case of datasnooping [66, 67]. The following statistical hypothesis testing problem is defined

$$\mathcal{H}_0 : \mathsf{E}_{f_{\underline{\Delta \mathrm{y}}}}\left(\underline{\Delta \mathrm{y}}\right) = \mathrm{J_A}\Delta\mathrm{x} \quad \text{vs.} \quad \mathcal{H}_i : \mathsf{E}_{f_{\underline{\Delta \mathrm{y}}}}\left(\underline{\Delta \mathrm{y}}\right) = \mathrm{J_A}\Delta\mathrm{x} + \mathrm{c}_i \mathrm{b}_i \tag{2.40}$$

for $i \in \{1, ..., k\}$, where $k = m$, $\mathrm{c}_i \in \mathbb{R}^m$ is the canonical unit vector having one as its i^{th} element and zero elsewhere, $\mathrm{b}_i \in \mathbb{R}$ is the unknown outlier with its size in [m], and $\mathrm{rank}([\mathrm{J_A}, \mathrm{c}_i]) = 4 + 1 = 5$. Given the misclosure vector $\underline{\mathrm{t}} = \mathrm{B}^T \underline{\Delta \mathrm{y}}$ with $\mathrm{B}^T \mathrm{J_A} = 0_{r \times n}$, the resulting partitions of $\mathbb{R}^r$ for datasnooping, given a level of significance $\alpha = \mathsf{P}_{\mathrm{FA}}$ are

$$\mathcal{P}_0 = \left\{ t \in \mathbb{R}^r \mid ||t||^2_{\mathrm{Q_{tt}}} \leq \chi^2_\alpha(r, 0) \right\}, \tag{2.41}$$

$$\mathcal{P}_{i \neq 0} = \left\{ t \in \mathbb{R}^r \mid t \notin \mathcal{P}_0,\ |w_i| = \max_{j \in \{1,...,k\}} |w_j| \right\}, \tag{2.42}$$

where $|\underline{w}_j| = ||\mathbf{\Pi}_{\mathrm{c_t}_j} \underline{\mathrm{t}}||_{\mathrm{Q_{tt}}}$ is the w-test statistic [68].

We consider the skyplot in Fig. 2.5 which shows the positions of the satellites, as observed by the rover receiver, expressed in terms of their azimuth (w.r.t. the North direction) and elevation angles (w.r.t. the horizontal plane). The satellite geometry contains $m_\mathrm{G} = 8$ GPS satellites (blue) and $m_\mathrm{E} = 7$ Galileo satellites (orange) with an elevation cut-off angle of 10°. The redundancy is $r = 11$ and the analysis focuses on the 2D position of the vehicle as the horizontal domain is most relevant. The 2D position vector is defined as $\overline{\underline{\theta}} = \mathrm{H}^T \overline{\underline{\mathrm{x}}}$ where $\mathrm{H}^T = \begin{bmatrix} \mathrm{I}_2 & 0_{2\times 2} \end{bmatrix}$ and $\overline{\underline{\mathrm{x}}} = \sum_{i=0}^{k=15} \hat{\underline{\mathrm{x}}}_i p_i(\underline{\mathrm{t}})$ captures the estimation and statistical hypothesis

testing problem defined in (2.40)–(2.42). The PDF of $\underline{\hat{\theta}}$ can be expressed as [18]

$$\begin{aligned} f_{\underline{\hat{\theta}}}(\theta) &= \sum_{i=0}^{k=15} \int_{\mathcal{P}_i} f_{\underline{\hat{\theta}}_i, \underline{t}}(x,t)\, dt \\ &= \sum_{i=0}^{k=15} \mathsf{E}_{f_{\underline{t}}} \left(f_{\underline{\hat{\theta}}_0} \left(\theta + \mathrm{H}^T \mathrm{L}_i \underline{t} \right) p_i(\underline{t}) \right), \end{aligned} \tag{2.43}$$

where the second equality will be used for the visual interpretation of the PDFs. Based on (2.43), the 2D probability of positioning failure is formulated with the objective of computing it using the proposed method from Section 2.3

$$\mathbb{P}_{\mathcal{F}}(\mathbf{b}) = \int_{\mathcal{B}^c} f_{\underline{\hat{\theta}}}(\theta)\, d\theta, \tag{2.44}$$

for a given safety region $\mathcal{B}$ and its complement $\mathcal{B}^c$.

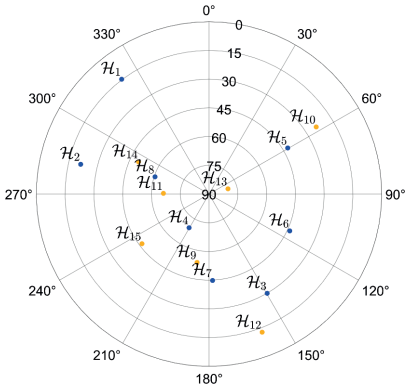

Figure 2.5: Skyplot view of the rover receiver (vehicle)-satellite geometry. The eight blue dots are representing the GPS satellites, while the seven orange ones represents the Galileo satellites and the corresponding $\mathcal{H}_i$'s, for $i > 0$.

2.4.1 Probability of positioning failure for fixed vehicle and safety-region orientation

In determining the shape and size of the safety region $\mathcal{B} \subset \mathbb{R}^2$, several factors should be considered, such as: (i) the vehicle's dimensions; (ii) the road geometry to ensure that all points $\theta \in \mathbb{R}^2$ within the set $\mathcal{B}$ correspond to the vehicle staying within its lane; (iii) the minimum required braking distance depending on the vehicle's speed; (iv) the proximity to other traffic participants, among other considerations. Various studies have proposed different shapes for the safety region that encompasses the vehicle, such as elliptical or rectangular forms [7, 69, 70]. For consistency with existing approaches in the literature, we choose an ellipse to inscribe the shape of the vehicle which has a length of 4.5 [m], a width of 1.8 [m], and the orientation w.r.t. the vertical axis is 45° (as an example). For a single-epoch in time the safety-region can be defined as (see Fig. 2.6),

$$\mathcal{B} = \{\theta \in \mathbb{R}^2 \mid ||\theta - \theta_{\text{true}}||^2_{Q_{\mathcal{B}}} \leq 1\}, \tag{2.45}$$

where $Q_{\mathcal{B}}^{-1} = \begin{bmatrix} 0.358 & -0.259 \\ -0.259 & 0.358 \end{bmatrix}$ [m^{-2}] and $\theta_{\text{true}} \in \mathbb{R}^2$ is the true location of the vehicle (set at $0_{2\times1}$ for this example). The major-axis of $\mathcal{B}$ has a length of 6.36 [m] with an orientation w.r.t. the horizontal axis of 45°, and the minor-axis has a length of 2.55 [m].

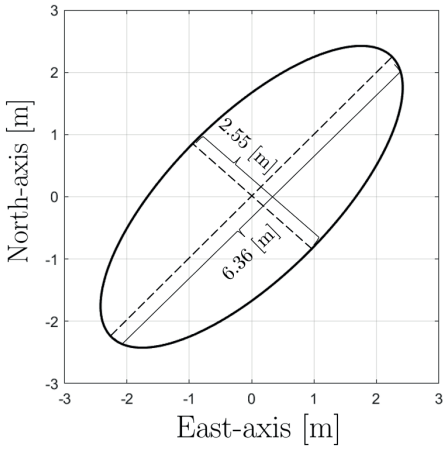

Figure 2.6: Safety-region $\mathcal{B} \subset \mathbb{R}^2$ inscribing the vehicle (at a single-epoch) defined in (2.45).

In the following sub-sections (A.1 and A.2) we present results from computing the Level 1 components of $\overline{\mathbb{P}}_{\mathcal{F}}|\mathcal{H}_0$ and of $\overline{\mathbb{P}}_{\mathcal{F}}|\mathcal{H}_{14}$ as illustrative examples. A similar approach is followed for the remaining fourteen Level 1 entries $\overline{\mathbb{P}}_{\mathcal{F}}|\mathcal{H}_i$ for $i \notin \{0, 14\}$. In sub-section (A.3) the resulting total probability of positioning failure is obtained and discussed.

A.1 Computation of Level 1 Components of $\mathbb{P}_{\mathcal{F}}|\mathcal{H}_0$

First, we are providing an analysis of the conditional components of the PDF $f_{\overline{\underline{\theta}}}(\theta|\mathcal{H}_0)$ (i.e., $f_{\overline{\underline{\theta}}|\text{CA}}(\theta|\text{CA})$ and $f_{\overline{\underline{\theta}}|\text{FA}_i}(\theta|\text{FA}_i)$ for $i \in \{1, ..., 15\}$). Under the event of a CA testing decision, the PDF $f_{\overline{\underline{\theta}}|\text{CA}}(\theta|\text{CA}) = f_{\hat{\underline{\theta}}_0}(\theta|\mathcal{H}_0)$ is a normal distribution, with the precision of the horizontal position components $\sigma_{\hat{\theta}_{0,\text{east}}} = 0.18$ [m], $\sigma_{\hat{\theta}_{0,\text{north}}} = 0.20$ [m], and the correlation coefficient is $\rho_{\hat{\theta}_0} = 0.01$. Hence, the contours of $f_{\overline{\underline{\theta}}|\text{CA}}(\theta|\text{CA})$ are nearly circular. The conditional PDFs $f_{\overline{\underline{\theta}}|\text{FA}_i}(\theta|\text{FA}_i)$ are obtained from the averaged shifted functions $f_{\hat{\underline{\theta}}_0}\left(\theta + \text{H}^T\text{L}_i\,\underline{\text{t}}|\mathcal{H}_0\right)$ for $\underline{\text{t}} \in \mathcal{P}_i$, which account for the outcome of statistical testing (see (2.43)). A closer look into the shifting term $\text{H}^T\text{L}_i\,\underline{\text{t}}$ will give better insights about the features of $f_{\overline{\underline{\theta}}|\text{FA}_i}(\theta|\text{FA}_i)$ (e.g., orientation, multimodality). We re-express the shifting term, for $i > 0$, as

$$\text{H}^T\text{L}_i\,\underline{\text{t}} = \text{H}^T Q_{\hat{\text{x}}_0\hat{\text{x}}_0} \text{J}_\text{A}^T Q_{\Delta\text{y}\Delta\text{y}}^{-1} \text{c}_i (\text{c}_{\text{t}_i}^+\,\underline{\text{t}}) = \text{g}_i(\text{c}_{\text{t}_i}^+\,\underline{\text{t}}), \tag{2.46}$$

where $\text{g}_i \in \mathbb{R}^2$ and $(\text{c}_{\text{t}_i}^+\,\underline{\text{t}}) \in \mathbb{R}$. The angle of $\mathcal{R}(\text{g}_i)$ w.r.t. the horizontal axis is driven by the design matrix J_A and by $Q_{\Delta\text{y}_*\Delta\text{y}_*}$ through $Q_{\hat{\text{x}}_0\hat{\text{x}}_0}$. The rows of $(\text{H}^T Q_{\hat{\text{x}}_0\hat{\text{x}}_0}) \in \mathbb{R}^{2\times n}$ (variances of the components on East and North directions, the covariance between them, and their covariances with the Up component and $\Delta\mathbf{t}$) are influencing the orientation of $\mathcal{R}(\text{g}_i)$ by transforming the scaled rows of J_A obtained from $(\text{J}_\text{A}^T Q_{\Delta\text{y}\Delta\text{y}}^{-1} \text{c}_i) \in \mathbb{R}^n$. In turn, $\mathcal{R}(\text{g}_i)$ drives the orientation of $f_{\overline{\underline{\theta}}|\text{FA}_i}(\theta|\text{FA}_i)$.

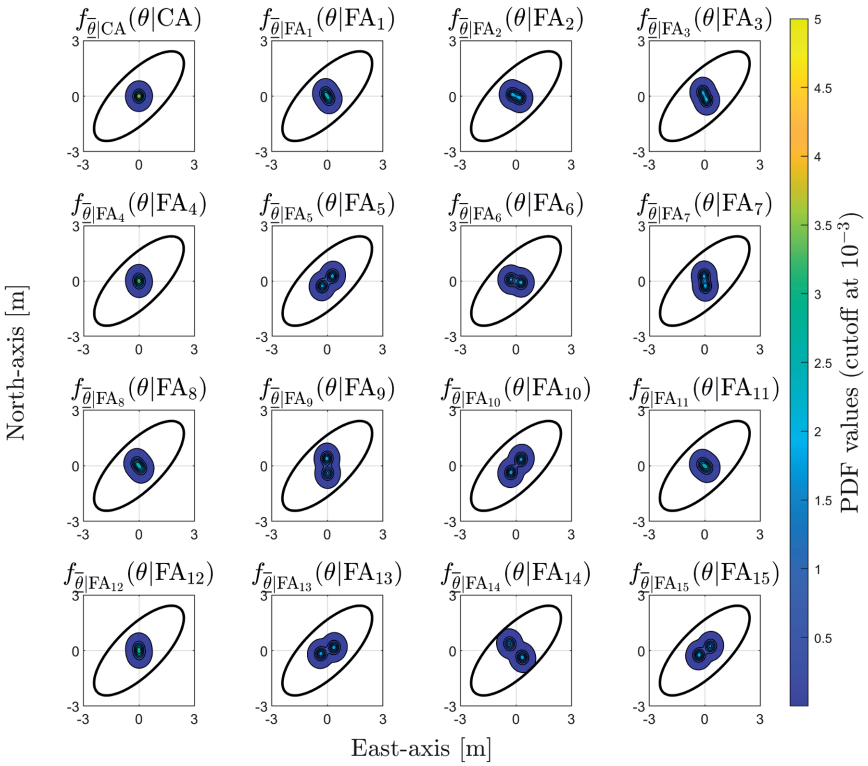

Figure 2.7: Components of $f_{\underline{\theta}}(\theta|\mathcal{H}_0)$ for $\mathrm{P_{FA}} = 10^{-3}$ and $N_t = 10^7$ i.i.d. pseudo-random samples drawn from $f_{\underline{t}}(t|\mathcal{H}_0)$. The ellipse represents the safety-region $\mathcal{B} \subset \mathbb{R}^2$ from (2.45) in relation with each conditional component of $f_{\underline{\theta}}(\theta|\mathcal{H}_0)$ (i.e., $f_{\underline{\theta}|\mathrm{CA}}(\theta|\mathrm{CA})$ and $f_{\underline{\theta}|\mathrm{FA}_i}(\theta|\mathrm{FA}_i)$ for $i \in \{1, ..., 15\}$.

One can relate the satellite geometry from Fig. 2.5 with the components in Fig. 2.7 to identify which ones present similarities (e.g., in orientation and shape). As examples, the following 'pairs' of components show similarities: $f_{\underline{\theta}|\mathrm{FA}_5}(\theta|\mathrm{FA}_5)$ and $f_{\underline{\theta}|\mathrm{FA}_{10}}(\theta|\mathrm{FA}_{10})$, $f_{\underline{\theta}|\mathrm{FA}_8}(\theta|\mathrm{FA}_8)$ and $f_{\underline{\theta}|\mathrm{FA}_{11}}(\theta|\mathrm{FA}_{11})$, $f_{\underline{\theta}|\mathrm{FA}_7}(\theta|\mathrm{FA}_7)$ and $f_{\underline{\theta}|\mathrm{FA}_9}(\theta|\mathrm{FA}_9)$, etc. The way $(\mathrm{c}_{\mathrm{t}_i}^{+}\,\underline{\mathrm{t}})$ varies across $\mathcal{R}(\mathrm{g}_i)$, for $\underline{\mathrm{t}} \in \mathcal{P}_i$, determines the multimodality of $f_{\underline{\theta}|\mathrm{FA}_i}(\theta|\mathrm{FA}_i)$. Take, for example, $f_{\underline{\theta}|\mathrm{FA}_1}(\theta|\mathrm{FA}_1)$ and $f_{\underline{\theta}|\mathrm{FA}_{12}}(\theta|\mathrm{FA}_{12})$ as they do not show multimodality due to the reduced influence of the low-elevation satellites 1 and 12 on the 2D positioning (via the elevation-based weighting in $\mathrm{Q}_{\Delta\mathrm{y}_*\Delta\mathrm{y}_*}$). The components $f_{\underline{\theta}|\mathrm{FA}_4}(\theta|\mathrm{FA}_4)$, $f_{\underline{\theta}|\mathrm{FA}_8}(\theta|\mathrm{FA}_8)$, and $f_{\underline{\theta}|\mathrm{FA}_{11}}(\theta|\mathrm{FA}_{11})$ do not show multimodality, despite satellites 4, 8, and 11 being at a rather high elevation, because of their reduced contribution to the east and north directions. The rest of the components show multimodality as the corresponding satellites' contribution to the 2D positioning is larger due to the rover receiver-satellite geometry and due to the elevation weighting. By relating the shape of the safety-region $\mathcal{B}$ with these components (see Fig. 2.7) it is possible to identify which ones have a small or large amount of probability density outside $\mathcal{B}$. For instance, $f_{\underline{\theta}|\mathrm{FA}_{14}}(\theta|\mathrm{FA}_{14})$ is closely aligned with the minor-axis of $\mathcal{B}$ and its modes are the

furthest apart, which indicates that it is one of the components with the largest amount of probability density outside $\mathcal{B}$.

Secondly, we compute the Level 1 components corresponding to $\mathcal{H}_0$ using the procedure in Fig. 2.3

$$\overline{\mathbb{P}}_{\mathcal{F}}|\mathcal{H}_0 = \sum_{i=0}^{k=15} \underline{\tilde{\mathcal{M}}}_i|\mathcal{H}_0 = \mathsf{P}_{\mathrm{CA}}\underline{\tilde{\mathbb{P}}}_{\mathcal{F}}|\mathrm{CA} + \sum_{i=1}^{k=15} \underline{\tilde{\mathsf{P}}}_{\mathrm{FA}_i}\underline{\tilde{\mathbb{P}}}_{\mathcal{F}}|\mathrm{FA}_i, \tag{2.47}$$

where P_{CA} is known, since $\mathsf{P}_{\mathrm{CA}} = 1 - \mathsf{P}_{\mathrm{FA}} = 1 - 10^{-3}$. The results are obtained over $N_{\mathrm{sim}} = 100$ displayed in Table 2.1.

Table 2.1: Level 1 Components of $\overline{\mathbb{P}}_{\mathcal{F}}|\mathcal{H}_0$ for $\mathsf{P}_{\mathrm{FA}} = 10^{-3}$ and $\tilde{N}_i = 10^5$ i.i.d. pseudo-random samples drawn from IS densities. Results are obtained over $N_{\mathrm{sim}} = 100$.

Comp.	Value	Std.
$\mathsf{P}_{\mathrm{CA}}\underline{\tilde{\mathbb{P}}}_{\mathcal{F}}\|\mathrm{CA}$	$2.51 \cdot 10^{-11}$	$6.39 \cdot 10^{-14}$
$\underline{\tilde{\mathsf{P}}}_{\mathrm{FA}_1}\underline{\tilde{\mathbb{P}}}_{\mathcal{F}}\|\mathrm{FA}_1$	$4.63 \cdot 10^{-13}$	$1.04 \cdot 10^{-14}$
$\underline{\tilde{\mathsf{P}}}_{\mathrm{FA}_2}\underline{\tilde{\mathbb{P}}}_{\mathcal{F}}\|\mathrm{FA}_2$	$1.29 \cdot 10^{-12}$	$2.80 \cdot 10^{-14}$
$\underline{\tilde{\mathsf{P}}}_{\mathrm{FA}_3}\underline{\tilde{\mathbb{P}}}_{\mathcal{F}}\|\mathrm{FA}_3$	$2.55 \cdot 10^{-12}$	$5.42 \cdot 10^{-14}$
$\underline{\tilde{\mathsf{P}}}_{\mathrm{FA}_4}\underline{\tilde{\mathbb{P}}}_{\mathcal{F}}\|\mathrm{FA}_4$	$1.73 \cdot 10^{-14}$	$7.76 \cdot 10^{-16}$
$\underline{\tilde{\mathsf{P}}}_{\mathrm{FA}_5}\underline{\tilde{\mathbb{P}}}_{\mathcal{F}}\|\mathrm{FA}_5$	$2.20 \cdot 10^{-15}$	$9.42 \cdot 10^{-17}$
$\underline{\tilde{\mathsf{P}}}_{\mathrm{FA}_6}\underline{\tilde{\mathbb{P}}}_{\mathcal{F}}\|\mathrm{FA}_6$	$4.48 \cdot 10^{-12}$	$7.25 \cdot 10^{-14}$
$\underline{\tilde{\mathsf{P}}}_{\mathrm{FA}_7}\underline{\tilde{\mathbb{P}}}_{\mathcal{F}}\|\mathrm{FA}_7$	$2.56 \cdot 10^{-12}$	$4.40 \cdot 10^{-14}$
$\underline{\tilde{\mathsf{P}}}_{\mathrm{FA}_8}\underline{\tilde{\mathbb{P}}}_{\mathcal{F}}\|\mathrm{FA}_8$	$4.82 \cdot 10^{-13}$	$1.04 \cdot 10^{-14}$
$\underline{\tilde{\mathsf{P}}}_{\mathrm{FA}_9}\underline{\tilde{\mathbb{P}}}_{\mathcal{F}}\|\mathrm{FA}_9$	$2.76 \cdot 10^{-11}$	$3.19 \cdot 10^{-13}$
$\underline{\tilde{\mathsf{P}}}_{\mathrm{FA}_{10}}\underline{\tilde{\mathbb{P}}}_{\mathcal{F}}\|\mathrm{FA}_{10}$	$1.56 \cdot 10^{-14}$	$3.54 \cdot 10^{-16}$
$\underline{\tilde{\mathsf{P}}}_{\mathrm{FA}_{11}}\underline{\tilde{\mathbb{P}}}_{\mathcal{F}}\|\mathrm{FA}_{11}$	$2.38 \cdot 10^{-13}$	$6.29 \cdot 10^{-15}$
$\underline{\tilde{\mathsf{P}}}_{\mathrm{FA}_{12}}\underline{\tilde{\mathbb{P}}}_{\mathcal{F}}\|\mathrm{FA}_{12}$	$6.82 \cdot 10^{-14}$	$2.20 \cdot 10^{-15}$
$\underline{\tilde{\mathsf{P}}}_{\mathrm{FA}_{13}}\underline{\tilde{\mathbb{P}}}_{\mathcal{F}}\|\mathrm{FA}_{13}$	$7.95 \cdot 10^{-14}$	$3.81 \cdot 10^{-15}$
$\underline{\tilde{\mathsf{P}}}_{\mathrm{FA}_{14}}\underline{\tilde{\mathbb{P}}}_{\mathcal{F}}\|\mathrm{FA}_{14}$	$4.86 \cdot 10^{-9}$	$4.36 \cdot 10^{-11}$
$\underline{\tilde{\mathsf{P}}}_{\mathrm{FA}_{15}}\underline{\tilde{\mathbb{P}}}_{\mathcal{F}}\|\mathrm{FA}_{15}$	$5.29 \cdot 10^{-15}$	$1.37 \cdot 10^{-16}$
$\overline{\mathbb{P}}_{\mathcal{F}}\|\mathcal{H}_0$	$4.95 \cdot 10^{-9}$	$4.36 \cdot 10^{-11}$

The Most Impactful Component (MIC) of $\overline{\mathbb{P}}_{\mathcal{F}}|\mathcal{H}_0$ is $\underline{\tilde{\mathsf{P}}}_{\mathrm{FA}_{14}}\underline{\tilde{\mathbb{P}}}_{\mathcal{F}}|\mathrm{FA}_{14} = 4.86 \cdot 10^{-9}$ due to two main reasons: (i) the principal axis of $f_{\underline{\theta}|\mathrm{FA}_{14}}(\theta|\mathrm{FA}_{14})$ is the most aligned with the minor-axis of $\mathcal{B}$ (see Fig. 2.7), and (ii) the two modes of $f_{\underline{\theta}|\mathrm{FA}_{14}}(\theta|\mathrm{FA}_{14})$ are most far apart from each other along the principal axis leading to the most probability density outside $\mathcal{B}$. Conversely, the principal axes of $f_{\underline{\theta}|\mathrm{FA}_5}(\theta|\mathrm{FA}_5)$ and $f_{\underline{\theta}|\mathrm{FA}_{15}}(\theta|\mathrm{FA}_{15})$ are the most aligned with the major-axis of $\mathcal{B}$ which leads to the Least Impactful Components (LICs): $\underline{\tilde{\mathsf{P}}}_{\mathrm{FA}_5}\underline{\tilde{\mathbb{P}}}_{\mathcal{F}}|\mathrm{FA}_5 = 2.20 \cdot 10^{-15}$ and $\underline{\tilde{\mathsf{P}}}_{\mathrm{FA}_{15}}\underline{\tilde{\mathbb{P}}}_{\mathcal{F}}|\mathrm{FA}_{15} = 5.29 \cdot 10^{-15}$.

A.2 Computation of Level 1 Components of $\mathbb{P}_{\mathcal{F}}|\mathcal{H}_{14}(\mathrm{b}_{14})$

We show the results obtained after computing the components of $\overline{\mathbb{P}}_{\mathcal{F}}|\mathcal{H}_{14}(\mathrm{b}_{14}) = \sum_{i=0}^{k=15} \underline{\tilde{\mathcal{M}}}_i|\mathcal{H}_{14}$

for $N_{\text{sim}} = 100$ and a range of values for the size of b_{14} to find the maximum (worst-case size of the outlier). We re-express $\overline{\mathbb{P}}_{\mathcal{F}}|\mathcal{H}_{14}(\mathrm{b}_{14})$ in terms of its computed components

$$\overline{\mathbb{P}}_{\mathcal{F}}|\mathcal{H}_{14}(\mathrm{b}_{14}) = \mathsf{P}_{\mathrm{MD}_{14}}\underline{\tilde{\mathbb{P}}}_{\mathcal{F}}|\mathrm{MD}_{14} + \underline{\tilde{\mathsf{P}}}_{\mathrm{CI}_{14}}\underline{\tilde{\mathbb{P}}}_{\mathcal{F}}|\mathrm{CI}_{14} + \sum_{i\neq 0,14}^{k=15} \underline{\tilde{\mathsf{P}}}_{\mathrm{WI}_i}\underline{\tilde{\mathbb{P}}}_{\mathcal{F}}|\mathrm{WI}_i. \tag{2.48}$$

where $\mathsf{P}_{\mathrm{MD}_{14}}$ can be computed exactly. The range of values is chosen between 0 and 2.5 [m] (negative values need not be considered due to the symmetry of the results). The objectives in this sub-section are to compute the components of $\overline{\mathbb{P}}_{\mathcal{F}}|\mathcal{H}_{14}(\mathrm{b}_{14})$, determine the maximum $\overline{\mathbb{P}}_{\mathcal{F}}|\mathcal{H}_{14}(\mathrm{b}_{14})$, and the corresponding magnitude of b_{14}. As an example, Fig. 2.8(a) shows the individual probabilities $\mathsf{P}_{\mathrm{MD}_{14}}$ and $\underline{\tilde{\mathbb{P}}}_{\mathcal{F}}|\mathrm{MD}_{14}$ as a function of b_{14}. As the outlier b_{14} increases, the probability density of $f_{\underline{\theta}|\mathrm{MD}_{14}}(\theta|\mathrm{MD}_{14})$ increases in $\mathcal{B}^c$, while $\mathsf{P}_{\mathrm{MD}_{14}}$ decreases. Fig. 2.8(b) shows that after $\mathsf{P}_{\mathrm{MD}_{14}}\underline{\tilde{\mathbb{P}}}_{\mathcal{F}}|\mathrm{MD}_{14}$ reaches its maximum at $9.42\cdot 10^{-4}$ for $\mathrm{b}_{14} = 1.70$ [m], the decrease is driven by $\mathsf{P}_{\mathrm{MD}_{14}}$ as its values are significantly smaller than those of $\underline{\tilde{\mathbb{P}}}_{\mathcal{F}}|\mathrm{MD}_{14}$.

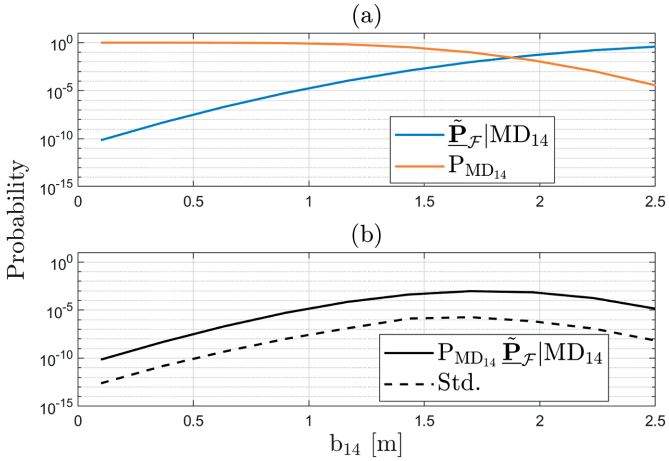

Figure 2.8: (a) Individual probabilities $\mathsf{P}_{\mathrm{MD}_{14}}$ and $\underline{\tilde{\mathbb{P}}}_{\mathcal{F}}|\mathrm{MD}_{14}$; (b) Component $\mathsf{P}_{\mathrm{MD}_{14}}\underline{\tilde{\mathbb{P}}}_{\mathcal{F}}|\mathrm{MD}_{14}$ and its simulation standard deviation (Std.) as a function of b_{14}.

The behavior of all of the components from (2.48) is presented in Fig. 2.9. For instance, Fig. 2.9(a) shows that in the case of the event of CI_{14}, as b_{14} increases, the component $\underline{\tilde{\mathsf{P}}}_{\mathrm{CI}_{14}}\underline{\tilde{\mathbb{P}}}_{\mathcal{F}}|\mathrm{CI}_{14}$ exhibits low variation. While b_{14} increases, $\underline{\tilde{\mathsf{P}}}_{\mathrm{CI}_{14}}$ goes toward 1, and $\underline{\tilde{\mathbb{P}}}_{\mathcal{F}}|\mathrm{CI}_{14}$ stabilizes on the order of 10^{-8} for b_{14} larger than 1.2 [m]. An interesting aspect is that $\underline{\tilde{\mathsf{P}}}_{\mathrm{CI}_{14}}\underline{\tilde{\mathbb{P}}}_{\mathcal{F}}|\mathrm{CI}_{14} > \mathsf{P}_{\mathrm{MD}_{14}}\underline{\tilde{\mathbb{P}}}_{\mathcal{F}}|\mathrm{MD}_{14}$ when $\mathrm{b}_{14} < 0.46$ [m] despite $\underline{\tilde{\mathsf{P}}}_{\mathrm{CI}_{14}} < \mathsf{P}_{\mathrm{MD}_{14}}$. Furthermore, this example shows that $\underline{\tilde{\mathsf{P}}}_{\mathrm{CI}_{14}}\underline{\tilde{\mathbb{P}}}_{\mathcal{F}}|\mathrm{CI}_{14}$ is the MIC of $\overline{\mathbb{P}}_{\mathcal{F}}|\mathcal{H}_{14}(\mathrm{b}_{14})$ for $\mathrm{b}_{14} < 0.46$ [m], while for $\mathrm{b}_{14} > 0.46$ [m] the MIC is $\mathsf{P}_{\mathrm{MD}_{14}}\underline{\tilde{\mathbb{P}}}_{\mathcal{F}}|\mathrm{MD}_{14}$ until $\underline{\tilde{\mathsf{P}}}_{\mathrm{CI}_{14}}\underline{\tilde{\mathbb{P}}}_{\mathcal{F}}|\mathrm{CI}_{14}$ and $\mathsf{P}_{\mathrm{MD}_{14}}\underline{\tilde{\mathbb{P}}}_{\mathcal{F}}|\mathrm{MD}_{14}$ cross again as $\mathrm{b}_{14} \to \infty$.

In Fig. 2.9(b) one can observe that the components under WI_4 and WI_5 have the lowest values (relative to the curves in the top and bottom plots of Fig. 2.9(b)). The main reasons are: (i) the correlation coefficients between the corresponding w-test statistics

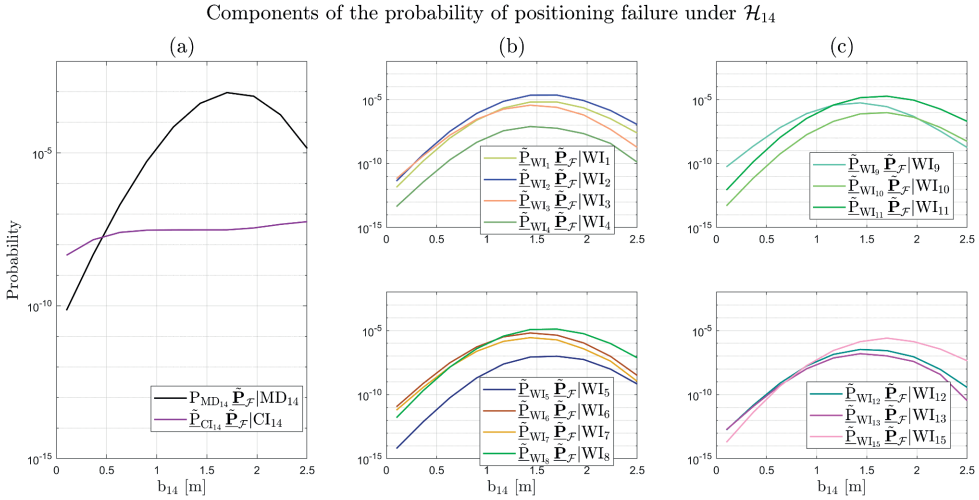

Figure 2.9: Level 1 components of $\underline{\overline{P}}_{\mathcal{F}}|\mathcal{H}_{14}(b_{14})$ for range of outliers $b_{14} \in [0.0,\ 2.5]$ in meters, $P_{FA} = 10^{-3}$ and 10^5 i.i.d. pseudo-random samples generated from IS densities. Curves are mean values obtained based on $N_{sim} = 100$. Mean values of components are: (a) under MD_{14} and CI_{14}; (b) under WI_i corresponding to GPS satellites (for $i \in \{1, ..., 8\}$); (c) under WI_i corresponding to Galileo satellites (for $i \in \{9, 10, 11, 12, 13, 15\}$).

$|\rho_{w_{14},w_4}| = 0.021$ and $|\rho_{w_{14},w_5}| = 0.088$ are the smallest among all, determining the locations of the main modes of $f_{\underline{\theta}|WI_4}(\theta|WI_4)$ and $f_{\underline{\theta}|WI_5}(\theta|WI_5)$ to vary slowest as b_{14} increases; (ii) the least probability density of $f_{\underline{\theta}|WI_4}(\theta|WI_4)$ and $f_{\underline{\theta}|WI_5}(\theta|WI_5)$ outside $\mathcal{B}$. For $b_{14} < 1$ [m] the separation between the components $\underline{\tilde{P}}_{WI_i}\underline{\tilde{P}}_{\mathcal{F}}|WI_i$ for $i \in \{1, 2, 3, 6, 7, 8\}$ is not significant. This is due to the probability density of the corresponding conditional PDFs not varying significantly outside $\mathcal{B}$, and the separation of the $\underline{\tilde{P}}_{WI_i}$'s not being substantial. On the other hand, the components under WI_1, WI_2, and WI_8 show together a dominant behavior for $b_{14} > 1.5$ [m] due to: (i) the correlation coefficients between the corresponding w-test statistics being the largest, and (ii) the probability density of the corresponding conditional PDFs being the highest in $\mathcal{B}^c$. The same type of reasoning applies for the components in Fig. 2.9(c).

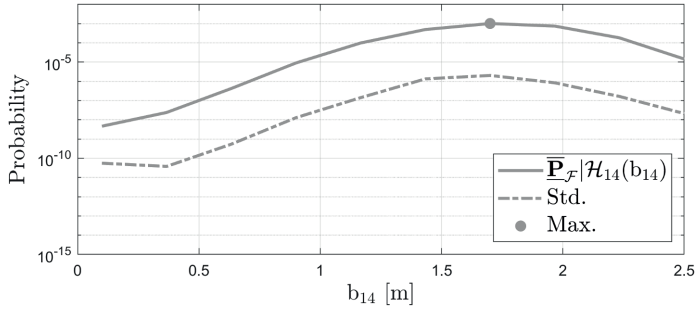

Figure 2.10: Obtained $\underline{\overline{P}}_{\mathcal{F}}|\mathcal{H}_{14}(b_{14})$ as a function of $b_{14} \in [0.0,\ 2.5]$ in meters, its simulaton standard deviation (Std.), and its maximum (max.) at $1.02 \cdot 10^{-3}$.

The Level 1 components in Fig. 2.9 are then used to compute the function $\overline{\underline{\mathbb{P}}}_{\mathcal{F}}|\mathcal{H}_{14}(\mathrm{b}_{14})$ from (2.48). This function, along with its simulation standard deviation and maximum (gray dot), is shown in Fig. 2.10. The maximum occurs at $1.02 \cdot 10^{-3}$ for $\mathrm{b}_{14} = 1.7$ [m], with its MIC being $\mathsf{P}_{\mathrm{MD}_{14}}\tilde{\overline{\underline{\mathbb{P}}}}_{\mathcal{F}}|\mathrm{MD}_{14}$. A similar approach is followed for the computation of other Level 1 components $\overline{\underline{\mathbb{P}}}_{\mathcal{F}}|\mathcal{H}_i(\mathrm{b}_i)$ for $i \neq \{0, 14\}$.

A.3 Computation of the Level 2 component $\mathbb{P}_{\mathcal{F}}(\mathbf{b})$ for a worst-case scenario

The maximum values of $\overline{\underline{\mathbb{P}}}_{\mathcal{F}}|\mathcal{H}_i(\mathrm{b}_i)$ for $i > 0$ have been determined and the results are presented in Table 2.2. The largest three maximum values are given by (in ascending order) $\overline{\underline{\mathbb{P}}}_{\mathcal{F}}|\mathcal{H}_{11}(\mathrm{b}_{11})$, $\overline{\underline{\mathbb{P}}}_{\mathcal{F}}|\mathcal{H}_2(\mathrm{b}_2)$, $\overline{\underline{\mathbb{P}}}_{\mathcal{F}}|\mathcal{H}_{14}(\mathrm{b}_{14})$ as the corresponding PDFs $f_{\underline{\overline{\theta}}}(\theta|\mathcal{H}_i)$, for $i \in \{11, 2, 14\}$, have the largest probability density outside $\mathcal{B}$.

Finally, to compute the worst-case scenario $\underline{\mathbb{P}}_{\mathcal{F}}(\mathbf{b})$ from (2.38), some assumptions are needed for the a priori $\mathsf{P}(\mathcal{H}_i)'s$ for $i \in \{0, ..., 15\}$. Since alternative hypotheses account for outliers in the pseudoranges at the rover receiver (automated vehicle), it is reasonable to assume that they primarily occur due to different signal reflections caused by the surrounding environment (e.g., buildings) [71]. For this analysis, we make three sets of assumptions ranging from more conservative cases to more optimistic ones: (Case 1) $\mathsf{P}(\mathcal{H}_0) = 0.8500$ and $\mathsf{P}(\mathcal{H}_i) = 10^{-2}$ for $\forall i > 0$, (Case 2) $\mathsf{P}(\mathcal{H}_0) = 0.9850$ and $\mathsf{P}(\mathcal{H}_i) = 10^{-3}$ for $\forall i > 0$, (Case 3) $\mathsf{P}(\mathcal{H}_0) = 0.9985$ and $\mathsf{P}(\mathcal{H}_i) = 10^{-4}$ for $\forall i > 0$. The results of the worst-case $\overline{\underline{\mathbb{P}}}_{\mathcal{F}}(\mathbf{b})$ for these three assumptions are shown in Table 2.3.

Table 2.2: Obtained $\overline{\underline{\mathbb{P}}}_{\mathcal{F}}|\mathcal{H}_0$ and $\overline{\underline{\mathbb{P}}}_{\mathcal{F}}|\mathcal{H}_i(\mathrm{b}_i)$ for $i > 0$, their maximum value, standard deviation (std.), and the size of the model outlier where the maximum occurs.

Comp.	Max. Value	Std.	b_i [m]
$\overline{\underline{\mathbb{P}}}_{\mathcal{F}}\|\mathcal{H}_0$	$4.95 \cdot 10^{-9}$	$4.36 \cdot 10^{-11}$	-
$\overline{\underline{\mathbb{P}}}_{\mathcal{F}}\|\mathcal{H}_1(\mathrm{b}_1)$	$3.56 \cdot 10^{-6}$	$1.94 \cdot 10^{-8}$	5.32
$\overline{\underline{\mathbb{P}}}_{\mathcal{F}}\|\mathcal{H}_2(\mathrm{b}_2)$	$1.54 \cdot 10^{-5}$	$7.92 \cdot 10^{-8}$	3.66
$\overline{\underline{\mathbb{P}}}_{\mathcal{F}}\|\mathcal{H}_3(\mathrm{b}_3)$	$2.34 \cdot 10^{-6}$	$1.23 \cdot 10^{-8}$	2.54
$\overline{\underline{\mathbb{P}}}_{\mathcal{F}}\|\mathcal{H}_4(\mathrm{b}_4)$	$2.67 \cdot 10^{-8}$	$2.02 \cdot 10^{-10}$	1.34
$\overline{\underline{\mathbb{P}}}_{\mathcal{F}}\|\mathcal{H}_5(\mathrm{b}_5)$	$2.18 \cdot 10^{-8}$	$2.86 \cdot 10^{-10}$	1.65
$\overline{\underline{\mathbb{P}}}_{\mathcal{F}}\|\mathcal{H}_6(\mathrm{b}_6)$	$3.99 \cdot 10^{-6}$	$2.87 \cdot 10^{-8}$	1.99
$\overline{\underline{\mathbb{P}}}_{\mathcal{F}}\|\mathcal{H}_7(\mathrm{b}_7)$	$2.31 \cdot 10^{-6}$	$9.55 \cdot 10^{-9}$	1.88
$\overline{\underline{\mathbb{P}}}_{\mathcal{F}}\|\mathcal{H}_8(\mathrm{b}_8)$	$7.44 \cdot 10^{-6}$	$2.37 \cdot 10^{-8}$	1.71
$\overline{\underline{\mathbb{P}}}_{\mathcal{F}}\|\mathcal{H}_9(\mathrm{b}_9)$	$6.94 \cdot 10^{-6}$	$5.08 \cdot 10^{-8}$	1.32
$\overline{\underline{\mathbb{P}}}_{\mathcal{F}}\|\mathcal{H}_{10}(\mathrm{b}_{10})$	$2.76 \cdot 10^{-7}$	$8.03 \cdot 10^{-10}$	2.60
$\overline{\underline{\mathbb{P}}}_{\mathcal{F}}\|\mathcal{H}_{11}(\mathrm{b}_{11})$	$9.83 \cdot 10^{-6}$	$3.62 \cdot 10^{-8}$	1.21
$\overline{\underline{\mathbb{P}}}_{\mathcal{F}}\|\mathcal{H}_{12}(\mathrm{b}_{12})$	$1.16 \cdot 10^{-7}$	$5.23 \cdot 10^{-10}$	3.39
$\overline{\underline{\mathbb{P}}}_{\mathcal{F}}\|\mathcal{H}_{13}(\mathrm{b}_{13})$	$6.47 \cdot 10^{-8}$	$3.76 \cdot 10^{-10}$	1.21
$\overline{\underline{\mathbb{P}}}_{\mathcal{F}}\|\mathcal{H}_{14}(\mathrm{b}_{14})$	$1.02 \cdot 10^{-3}$	$2.03 \cdot 10^{-6}$	1.70
$\overline{\underline{\mathbb{P}}}_{\mathcal{F}}\|\mathcal{H}_{15}(\mathrm{b}_{15})$	$6.93 \cdot 10^{-7}$	$5.61 \cdot 10^{-9}$	1.38

Table 2.3: Maximum values of $\underline{\overline{\mathbb{P}}}_{\mathcal{F}}(\mathbf{b})$ and their standard deviations (std.).

Cases	$\mathsf{P}(\mathcal{H}_0)$	Max. $\underline{\overline{\mathbb{P}}}_{\mathcal{F}}(\mathbf{b})$	Std.
1	0.8500	$1.07 \cdot 10^{-5}$	$2.03 \cdot 10^{-8}$
2	0.9850	$1.08 \cdot 10^{-6}$	$2.03 \cdot 10^{-9}$
3	0.9985	$1.12 \cdot 10^{-7}$	$2.74 \cdot 10^{-10}$

In the case of the most conservative assumption ($\mathsf{P}(\mathcal{H}_0) = 0.8500$), the maximum $\underline{\overline{\mathbb{P}}}_{\mathcal{F}}(\mathbf{b}) = 1.07 \cdot 10^{-5} \pm 2.03 \cdot 10^{-8}$ can be considered rather large compared to what would be desired from the precision of positioning at the decimeter level (e.g. [7]). However, we emphasize that the present positioning safety analysis is restricted to single-epoch (snapshot) GNSS-only positioning and it does not consider a sensor suite for positioning.

A.4 Verification of the results

Using the direct simulation approach based on the standard MC, as described in the appendix of [72], we verify the results of Tables 2.2 and 2.3 using 10^6 i.i.d. pseudo-random samples and $N_{\text{sim}} = 100$. The results are presented below in Tables 2.4 and 2.5 and they agree with the ones from Tables 2.2 and 2.3 (the relative differences are $< 20\%$). A dash '–' in Table 2.4 indicates that the target value is around or below 10^{-8} and it could not be computed reliably with 10^6 i.i.d. pseudo-random samples and $N_{\text{sim}} = 100$. Therefore, they are also not taken into account in the generation of Table 2.5. To generate these results for verification, we have used computational resources from the Delft High Performance Computing Center (DHPC)[73].

Table 2.4: Verification of results in Table 2.2 based on standard MC approach in Appendix of [72].

Comp.	Max. Value	Std.	b_i [m]
$\underline{\overline{\mathbb{P}}}_{\mathcal{F}}\|\mathcal{H}_0$	-	-	-
$\underline{\overline{\mathbb{P}}}_{\mathcal{F}}\|\mathcal{H}_1(\mathrm{b}_1)$	$3.75 \cdot 10^{-6}$	$2.00 \cdot 10^{-7}$	5.32
$\underline{\overline{\mathbb{P}}}_{\mathcal{F}}\|\mathcal{H}_2(\mathrm{b}_2)$	$1.54 \cdot 10^{-5}$	$4.21 \cdot 10^{-7}$	3.66
$\underline{\overline{\mathbb{P}}}_{\mathcal{F}}\|\mathcal{H}_3(\mathrm{b}_3)$	$2.27 \cdot 10^{-6}$	$1.48 \cdot 10^{-7}$	2.54
$\underline{\overline{\mathbb{P}}}_{\mathcal{F}}\|\mathcal{H}_4(\mathrm{b}_4)$	-	-	-
$\underline{\overline{\mathbb{P}}}_{\mathcal{F}}\|\mathcal{H}_5(\mathrm{b}_5)$	-	-	-
$\underline{\overline{\mathbb{P}}}_{\mathcal{F}}\|\mathcal{H}_6(\mathrm{b}_6)$	$4.60 \cdot 10^{-6}$	$2.20 \cdot 10^{-7}$	1.99
$\underline{\overline{\mathbb{P}}}_{\mathcal{F}}\|\mathcal{H}_7(\mathrm{b}_7)$	$2.35 \cdot 10^{-6}$	$1.61 \cdot 10^{-7}$	1.88
$\underline{\overline{\mathbb{P}}}_{\mathcal{F}}\|\mathcal{H}_8(\mathrm{b}_8)$	$7.78 \cdot 10^{-6}$	$2.94 \cdot 10^{-7}$	1.71
$\underline{\overline{\mathbb{P}}}_{\mathcal{F}}\|\mathcal{H}_9(\mathrm{b}_9)$	$6.69 \cdot 10^{-6}$	$2.50 \cdot 10^{-7}$	1.32
$\underline{\overline{\mathbb{P}}}_{\mathcal{F}}\|\mathcal{H}_{10}(\mathrm{b}_{10})$	$3.40 \cdot 10^{-7}$	$5.72 \cdot 10^{-8}$	2.60
$\underline{\overline{\mathbb{P}}}_{\mathcal{F}}\|\mathcal{H}_{11}(\mathrm{b}_{11})$	$1.01 \cdot 10^{-5}$	$3.48 \cdot 10^{-7}$	1.21
$\underline{\overline{\mathbb{P}}}_{\mathcal{F}}\|\mathcal{H}_{12}(\mathrm{b}_{12})$	$1.20 \cdot 10^{-7}$	$3.27 \cdot 10^{-8}$	3.39
$\underline{\overline{\mathbb{P}}}_{\mathcal{F}}\|\mathcal{H}_{13}(\mathrm{b}_{13})$	-	-	-
$\underline{\overline{\mathbb{P}}}_{\mathcal{F}}\|\mathcal{H}_{14}(\mathrm{b}_{14})$	$1.02 \cdot 10^{-3}$	$3.26 \cdot 10^{-6}$	1.70
$\underline{\overline{\mathbb{P}}}_{\mathcal{F}}\|\mathcal{H}_{15}(\mathrm{b}_{15})$	$7.80 \cdot 10^{-7}$	$9.27 \cdot 10^{-8}$	1.38

Table 2.5: Verification of results in Table 2.3 using the values from Table 2.4.

Cases	$\mathsf{P}(\mathcal{H}_0)$	Max. $\overline{\underline{\mathbb{P}}}_{\mathcal{F}}(\mathbf{b})$	Std.
1	0.8500	$1.07 \cdot 10^{-5}$	$3.35 \cdot 10^{-8}$
2	0.9850	$1.07 \cdot 10^{-6}$	$3.35 \cdot 10^{-9}$
3	0.9985	$1.07 \cdot 10^{-7}$	$3.35 \cdot 10^{-10}$

2.4.2 Probability of positioning failure for varying vehicle and safety-region orientation

Although vehicles change their orientation as they move—for example, when making U-turns, exiting highways, or turning left or right—over a short time frame (e.g., a few minutes), we can assume that the receiver-satellite geometry depicted in Fig. 2.5 remains constant because GNSS satellites orbit Earth at altitudes around 20.000 km. This assumption allows us to focus our analysis on the vehicle's changing orientation. Therefore, we modify the safety region from (2.45) to incorporate dependence on the orientation angle ϕ, measured clockwise relative to the vertical axis,

$$\mathcal{B}_\phi = \{\theta \in \mathbb{R}^2 \mid ||\theta - \theta_{\text{true}}||^2_{Q_{\mathcal{B}_\phi}} \leq 1\}, \tag{2.49}$$

where $Q^{-1}_{\mathcal{B}_\phi}$ now depends on ϕ and $\phi \in [0^\circ,\ 180^\circ]$. The maximum $\overline{\underline{\mathbb{P}}}_{\mathcal{F}}(\mathbf{b})$ is computed as *a function* of ϕ from its components: $\overline{\underline{\mathbb{P}}}_{\mathcal{F}}|\mathcal{H}_0$ and $\max_{b_1,\ldots,b_k} \sum_{i=1}^{15} \overline{\underline{\mathbb{P}}}_{\mathcal{F}}|\mathcal{H}_i(b_i)$. Fig. 2.11(a) illustrates the variations of $\overline{\underline{\mathbb{P}}}_{\mathcal{F}}|\mathcal{H}_0$ as a function of ϕ. As ϕ approaches 60°, the components of $f_{\overline{\underline{\theta}}}(\theta|\mathcal{H}_0)$ that are less aligned with $\mathcal{B}_\phi$ contribute the most (e.g., see $f_{\overline{\underline{\theta}}|\text{FA}_6}(\theta|\text{FA}_6)$, $f_{\overline{\underline{\theta}}|\text{FA}_{14}}(\theta|\text{FA}_{14})$ from Fig. 2.7), reaching a global maximum of $5.87 \cdot 10^{-9}$ at $\phi = 60^\circ$. For $\phi > 60^\circ$, the values of $\overline{\underline{\mathbb{P}}}_{\mathcal{F}}|\mathcal{H}_0$ decrease until $\phi = 100^\circ$, after which they begin to rise again, reaching a local maximum of $3.37 \cdot 10^{-9}$ at $\phi = 120^\circ$ due to $f_{\overline{\underline{\theta}}|\text{FA}_5}(\theta|\text{FA}_5)$, $f_{\overline{\underline{\theta}}|\text{FA}_{10}}(\theta|\text{FA}_{10})$, and $f_{\overline{\underline{\theta}}|\text{FA}_{15}}(\theta|\text{FA}_{15})$ having most of their probability density outside $\mathcal{B}_\phi$. A similar reasoning can be applied to the behaviour of $\max_{b_1,\ldots,b_k} \sum_{i=1}^{15} \overline{\underline{\mathbb{P}}}_{\mathcal{F}}|\mathcal{H}_i(b_i)$ in Fig. 2.11(b).

The results from Fig. 2.11(a) and 2.11(b) are combined with the assumptions made on the a-priori probabilities $\mathsf{P}(\mathcal{H}_0)$ and $\mathsf{P}(\mathcal{H}_i)$ for $i > 0$, as discussed previously, to obtain the results from Fig. 2.11(c). In the most conservative case (Case 1), the maximum $\overline{\underline{\mathbb{P}}}_{\mathcal{F}}(\mathbf{b})$ at $\phi = 130^\circ$ is $2.04 \cdot 10^{-5}$ while for the most optimistic (Case 3) is $2.07 \cdot 10^{-7}$ (see Table 2.6). Considering this is a snapshot positioning scenario for an automated vehicle with decimeter-level accuracy and a horizontal positioning precision of approximately 0.5 meters (95% circular probability radius), while accounting for one-dimensional outliers in the observables, the result in Case 1 is relatively large.

This type of results helps determine whether the target requirements or guidelines for positioning safety are met at a particular time instant. This assessment is based on the assumed functional and stochastic models in (2.39), the receiver-satellite geometry in Fig. 2.5, the statistical hypothesis testing procedure in (2.40)-(2.42), and the safety-region $\mathcal{B}_\phi$ defined in (2.49).

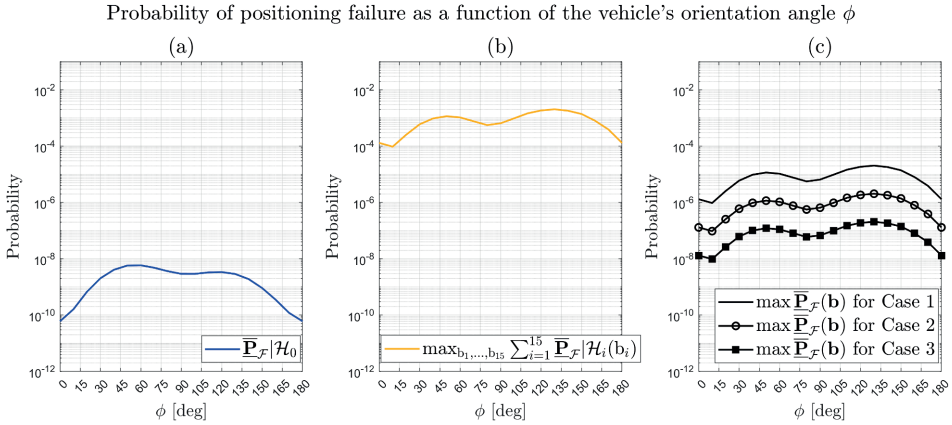

Figure 2.11: (a) Computed $\overline{\mathbb{P}}_{\mathcal{F}}|\mathcal{H}_0$ over the angles ϕ with $N_{\text{sim}} = 50$; (b) Computed $\max_{b_1,...,b_k} \sum_{i=1}^{k} \overline{\mathbb{P}}_{\mathcal{F}}|\mathcal{H}_i(b_i)$ over the angles ϕ with $N_{\text{sim}} = 50$; (c) Computed maximum total probability of positioning failure $\overline{\mathbb{P}}_{\mathcal{F}}(\mathbf{b})$ over the angles ϕ for the three cases: (i) Case 1 when the a-priori $\mathsf{P}(\mathcal{H}_0) = 0.8500$ and $\mathsf{P}(\mathcal{H}_i) = 10^{-2}$ for $i \in \{1, ..., 15\}$, (ii) Case 2 when the a-priori $\mathsf{P}(\mathcal{H}_0) = 0.9850$ and $\mathsf{P}(\mathcal{H}_i) = 10^{-3}$ for $i \in \{1, ..., 15\}$, and (iii) Case 3 when the a-priori $\mathsf{P}(\mathcal{H}_0) = 0.9985$ and $\mathsf{P}(\mathcal{H}_i) = 10^{-4}$ for $i \in \{1, ..., 15\}$.

Table 2.6: Maximum values of $\underline{\mathbb{P}}_{\mathcal{F}}(\mathbf{b})$ at the worst-orientation of the vehicle w.r.t. the satellite geometry from Fig. 2.5.

Cases	$\mathsf{P}(\mathcal{H}_0)$	Max. $\underline{\mathbb{P}}_{\mathcal{F}}(\mathbf{b})$ at $\phi = 130^\circ$	Std.
1	0.8500	$2.04 \cdot 10^{-5}$	$4.52 \cdot 10^{-7}$
2	0.9850	$2.04 \cdot 10^{-6}$	$4.52 \cdot 10^{-8}$
3	0.9985	$2.07 \cdot 10^{-7}$	$4.52 \cdot 10^{-9}$

If the requirements or guidelines are not met, adjustments may be needed in various aspects, such as the measurement setup (including functional and stochastic models), the definition of the safety region, or the combined approach for parameter estimation and statistical hypothesis testing. For example, recent theoretical advancements show how tailored statistical hypothesis testing can improve the performance of DIA-estimators [42].

2.4.3 Computational resources

To provide context regarding the computational resources used to carry-out the positioning safety analyses based on the proposed method, we detail the used hardware and software. The computations were performed on a laptop Dell Latitude 7440 equipped with a 13th Gen Intel Core i7 processor featuring 10 physical cores and 16 GB RAM. The operating system is Windows 10 Enterprise and the programming language is MATLAB 2024a with the Parallel Computing Toolbox. The analyses leveraged 8 physical cores of the processor through MATLAB's parallel computing capabilities.

For example, the computation time to generate the results from Table 2.1 (components

of $\overline{\mathbb{P}}_{\mathcal{F}}|\mathcal{H}_0$) with $\tilde{N}_i = 10^5$ (for $i \geq 0$) i.i.d. pseudo-random samples generated from the IS densities and $N_{\text{sim}} = 100$ for the simulation uncertainty quantification, was ≈ 5 minutes. To obtain the results from Fig. 2.9 (components of $\overline{\mathbb{P}}_{\mathcal{F}}|\mathcal{H}_{14}(\mathrm{b}_{14})$ evaluated at 10 values of b_{14}), with $\check{N}_i = 10^5$ (for $i \geq 0$) i.i.d. pseudo-random samples generate from the IS densities and $N_{\text{sim}} = 100$, was ≈ 50 minutes. For the other alternative hypotheses, the computations times ranged between ≈ 50 minutes and ≈ 150 minutes. Note that these computation times can be improved if more physical cores are available and by reducing the number of independent simulation repetitions N_{sim} (e.g., to 50 [54]). They also depend on the chosen programming language, code implementation and the configuration parameters of the CE method. To generate the results from Table **??** and Fig. 2.11 we have used computational resources from Delft High Performance Computing Centre (DHPC) [73].

2.4.4 Limitations and potential improvements of the proposed method

We now turn our attention to limitations of the proposed method, emphasizing those that, in our opinion, are particularly relevant to address in future work.

- Dimensionality of $\mathrm{b}_i \in \mathbb{R}^{q_i}$: The computation of a $\overline{\mathbb{P}}_{\mathcal{F}}|\mathcal{H}_i(\mathrm{b}_i)$, for $i > 0$, requires assumptions on the values of $\mathrm{b}_i \in \mathbb{R}^{q_i}$. Currently, the maximum $\overline{\mathbb{P}}_{\mathcal{F}}|\mathcal{H}_i(\mathrm{b}_i)$ is found by defining a range for $\mathrm{b}_i \in \mathbb{R}^{q_i}$, when $q_i = 1$, and then perform the computations (e.g., Fig. 2.9). This approach can be computationally too expensive, especially when $q_i > 1$, as it would require searches over q_i-dimensional grids. Therefore, a more efficient approach to find the maximum $\underline{\mathbb{P}}_{\mathcal{F}}|\mathcal{H}_i(\mathrm{b}_i)$ is sought.

- Integration regions $\mathcal{B}^c \cap \mathcal{P}_i$: The expected values in (2.17) are integrals over the regions resulting from $\mathcal{B}^c \cap \mathcal{P}_i$ for $i \in \{0, ..., k\}$. A characterization of these regions by determining, a priori, their number and potentially their relative 'distance' (w.r.t. some metric), could offer insights for better choices of families of PDFs for the IS densities. In this context, choosing the parametric family of Gaussian PDFs for the IS density may not always be appropriate, especially if the dimension of the misclosure vector $\underline{\mathrm{t}} \in \mathbb{R}^r$ becomes large (e.g., > 40). Once this type of characterization is done, several approaches can be tried with respect to the choice of the parametric family for IS densities [56–58].

- Initialization of the CE method: Currently, the distributional parameters of IS densities are found by solving (2.36) using the (multilevel) CE method, as described in [52] (page 73). In this approach, the initialization parameters of the CE method, such as (i) initial IS densities to start the CE method and (ii) number of i.i.d. pseudo-random samples to be used $\tilde{N}_{\text{CE}}$, are chosen empirically. To overcome some of these shortcomings, a Fully Adaptive Cross-Entropy (FACE) method is proposed in Chapter 5 of [52] .

It is also important to mention that improvements of the CE method, especially for high-dimensional problems, have been recently proposed in [74, 75]. Such studies and developments could also bring benefits in the context of our proposed method (i.e., solving (2.36)).

2.5 Summary and conclusions

The study of the event of positioning failure $\mathcal{F} = \underline{\mathbb{x}} \in \mathcal{B}^c$ [6], through computing its probability $\mathbb{P}_{\mathcal{F}}(\mathbf{b})$, is of importance for a wide range of safety-critical applications in automotive, aviation, rail, and maritime domains. In this contribution, we have proposed a method to compute the probability of positioning failure and its conditional components, while accounting for the dependence between parameter estimation and statistical hypothesis testing. In addition, our proposed method allows positioning safety when the dimension of the position vector is larger than one (i.e., $n > 1$). The method has been developed based on principles and techniques from rare event simulation, specifically Importance Sampling and the Cross-Entropy method [38, 39]. Three limitations of the proposed method, along with potential improvements, have also been discussed: (i) handling the increase in the computation time due to the dimensionality of the model misspecification $\mathrm{b}_i \in \mathbb{R}^{q_i}$ for $i > 0$, (ii) accounting for the characteristics of the integration regions $\mathcal{B}^c \cap \mathcal{P}_i$ in the choices of the family of PDFs for the IS densities (other than the Gaussian PDFs), and (iii) the initialization strategy of the CE method which currently is empirical. These limitations can be alleviated by recent advances in the CE method (e.g., [56–58, 74, 75]) and by adaptive versions of it [52]. These topics represent areas to explore in future work.

The computation and analysis of $\mathbb{P}_{\mathcal{F}}(\mathbf{b})$ is aimed at the design stage of positioning algorithms, where decisions are to be made about (i) measurement models, (ii) parameter estimation methods for the position vector, (iii) statistical hypothesis testing procedures to accommodate for model misspecifications (e.g., outliers or faults in measurements), and (iv) positioning scenarios for vehicles, among other factors. This approach aligns with the principles of scenario-based safety assessment framework which is used or proposed for studies of automated and autonomous vehicles [11–13]. As an example, we have applied the proposed method to perform a positioning safety analysis, at a single epoch, for an automated vehicle in the context of decimeter-level precision GNSS positioning. The method enabled an extensive analysis of a worst-case scenario with the objective of finding the maximum $\underline{\mathbb{P}}_{\mathcal{F}}(\mathbf{b})$. Such analyses can be used to decide whether positioning safety targets or requirements are met. Although the chosen positioning scenario was centered in the automotive domain, the method for computing the probability of positioning failure and its analysis are also applicable to other safety-critical fields such as civil aviation, shipping, and rail. Further improvements of the proposed method can be made based on the existing literature and recent advances in the CE method, extending the range of scenarios for positioning safety analyses and development of positioning algorithms. Moreover, since the dependence between parameter estimation and statistical hypothesis testing has been acknowledged across various disciplines such as mathematical statistics, biometrics, econometrics, and signal processing [22–27], the principles of the distributional theory for the DIA method and the proposed method of the present contribution may also be applicable there, particularly in the context of linear(ized) functional models.

BIBLIOGRAPHY

[1] P. J. G. Teunissen and O. Montenbruck, editors. *Handbook of Global Navigation Satellite Systems*. Springer, 2017.

[2] J. C. J. Koelemeij et al. A hybrid optical-wireless network for decimetre-level terrestrial positioning. *Nature*, 611(7936):473–478, November 2022.

[3] N. Nadarajah, P. J. G. Teunissen, and N. Raziq. Instantaneous GPS-Galileo Attitude Determination: Single-Frequency Performance in Satellite-Deprived Environments. *IEEE Transactions on Vehicular Technology*, 62(7):2963–2976, 2013.

[4] B. C. Vani et al. A Novel Approach to Improve GNSS Precise Point Positioning During Strong Ionospheric Scintillation: Theory and Demonstration. *IEEE Transactions on Vehicular Technology*, 68(5):4391–4403, 2021.

[5] V. G. Juan et al. Asynchronous Sensor Fusion of GPS, IMU and CAN-Based Odometry for Heavy-Duty Vehicles. *IEEE Transactions on Vehicular Technology*, 70(9):8617–8626, 2021.

[6] RTCA-Special Committee 159. Minimum Operational Performance Standards (MOPS) for Global Positioning System/Satellite-Based Augmentation System Airborne Equipment. Do-229f, Radio Technical Commission for Aeronautics, 2020.

[7] T. G. R. Reid et al. Localization Requirements for Autonomous Vehicles. *SAE International Journal of Connected and Automated Vehicles*, 2019.

[8] K. Jin et al. An approach to constructing effective training data for a classification model to evaluate the reliability of a passive safety system. *Reliability Engineering and System Safety*, 222:1–10, 2022.

[9] V. Chabridon et al. Evaluation of failure probability under parameter epistemic uncertainty: Application to aerospace system reliability assessment. *Aerospace Science and Technology*, 69:526–537, 2017.

[10] M. Shinozuka. Basic analysis of structural safety. *Journal of Structural Engineering*, 109(3):721–740, 1983.

[11] S. Riedmaier et al. Survey on Scenario-Based Safety Assessment of Automated Vehicles. *IEEE Access*, 8:87456–87477, 2020.

[12] U.N.E.C.E. New Assessment/Test Method for Automated Driving (NATM) Guidelines for Validating Automated Driving Systems (ADS). Report, United Nations Economic Commission for Europe - Inland Transport Committee, 2023.

[13] E. de Gelder et al. TNO Street Wise: Scenario-Based Safety Assessment of Automated Driving Systems. White paper, Netherlands Organisation for Applied Scientific Research (TNO), 2024.

[14] P. J. G. Teunissen. An integrity and quality control procedure for use in multi-sensor integration. In *ION GPS*, pages 513–522, 1990.

[15] I. Gillissen and I. A. Elema. Test results of DIA: A real-time adaptive integrity monitoring procedure, used in an integrated navigation system. *International Hydrographic Review*, 73(1):75–103, 1996.

[16] L. Yang, Y. Li, and C. Rizos. An enhanced MEMS-INS/GNSS integrated system with fault detection and exclusion capability for land vehicle navigation in urban areas. *GPS Solutions*, 18(4):593–603, 2013.

[17] J. Liu, G. Guo, and R. Zhang. Residual-Based Fault Detection and Exclusion With Enhanced Localization Integrity. *IEEE Transactions on Vehicular Technology*, 72(5):5798–5808, 2023.

[18] P. J. G. Teunissen. Distributional theory for the DIA method. *Journal of Geodesy*, 92(1):59–80, 2018.

[19] S. Zaminpardaz, P. J. G. Teunissen, and C. C. J. M. Tiberius. Risking to underestimate the integrity risk. *GPS Solutions*, 23(29):1–16, 2019.

[20] S. Zaminpardaz and P. J. G. Teunissen. On the computation of confidence regions and error ellipses: A critical appraisal. *Journal of Geodesy*, 96(10):1–18, 2022.

[21] S. Ciuban, P. J. G. Teunissen, and C. C. J. M. Tiberius. Dependence Between Parameter Estimation and Statistical Hypothesis Testing: Positioning Safety Analysis for Automated/Autonomous Vehicles. *IEEE Transactions on Intelligent Transportation Systems*, 26(4):5509–5521, 2025.

[22] T. A. Bancroft. On Biases in Estimation Due to the Use of Preliminary Tests of Significance. *Annals of Mathematical Statistics*, 15(2):190–204, 1944.

[23] S. Sarkadi. Estimation after selection. *Studia Scientiarum Mathematicarum Hungarica*, pages 341–350, 1967.

[24] N. L. Hjort and G. Claeskens. Frequentist Model Average Estimators. *Journal of the American Statistical Association*, 98(464):879–899, 2003.

[25] S. T. Buckland, K. P. Burnham, and N. H. Augustin. Model Selection: An Integral Part of Inference. *Biometrics*, 53(2):603–618, 1997.

[26] H. Leeb and B. M. Pötscher. The Finite-Sample Distribution of Post-Model-Selection Estimators and Uniform versus Nonuniform Approximations. *Econometric Theory*, 19(1):100–142, 2003.

[27] T. Routtenberg and L. Tong. Estimation After Parameter Selection: Performance Analysis and Estimation Methods. *IEEE Transactions on Signal Processing*, 64(20):5268–5281, 2016.

[28] J. Blanch et al. Baseline Advanced RAIM User Algorithm and Possible Improvements. *IEEE Transactions on Aerospace and Electronic Systems*, 51(1):713–732, 2015.

[29] Working Group C. Advanced RAIM Technical Subgroup Reference Airborne Algorithm Description Document. Technical report, 2019.

[30] P. Zhao et al. A New Method to Bound the Integrity Risk for Residual-Based ARAIM. *IEEE Transactions on Aerospace and Electronic Systems*, 57(2):1378–1385, 2020.

[31] G. Huang et al. Bayesian fault-tolerant protection level for multi-constellation navigation from integrity perspective. *Aerospace Science and Technology*, 130(107954), 2022.

[32] S. Wang et al. Bayesian upper bound on GNSS posterior integrity risk. *IEEE Transactions on Aerospace and Electronic Systems*, 60(6):7945–7961, December 2024.

[33] L. Li et al. GNSS integrity risk evaluation in the position domain based on the generalized Pareto distribution. *Measurement Science and Technology*, 34(8):1–11, 2023.

[34] N. Zhu et al. GNSS Position Integrity in Urban Environments: A Review of Literature. *IEEE Transactions on Intelligent Transportation Systems*, 19(9):2762–2778, 2018.

[35] G. Gottschalg et al. Integrity Concept for Sensor Fusion Algorithms used in a Prototype Vehicle for Automated Driving. In *European Navigation Conference*, pages 1–10, 2020.

[36] H. Jing et al. Integrity Monitoring of GNSS/INS Based Positioning Systems for Autonomous Vehicles: State-of-the-Art and Open Challenges. *IEEE Transactions on Intelligent Transportation Systems*, 23(9):14166–14187, 2022.

[37] D. P. Kroese, T. Taimre, and Z. I. Botev, editors. *Handbook of Monte Carlo Methods*. Wiley Series in Probability and Statistics. Wiley, 2011.

[38] H. Kahn and A. W. Marshall. Methods of Reducing Sample Size in Monte Carlo Computations. *Journal of the Operations Research Society of America*, 1(5):263–278, 1953.

[39] R. Y. Rubinstein. The Cross-Entropy Method for Combinatorial and Continuous Optimization. *Methodology and Computing in Applied Probability*, 1:127–190, 1999.

[40] P. J. G. Teunissen. Batch and Recursive Model Validation. In P. J. G. Teunissen and O. Montenbruck, editors, *Springer Handbook of Global Navigation Satellite Systems*, pages 687–720. Springer, 2017.

[41] S. Zaminpardaz and P. J. G. Teunissen. Detection-only versus detection and identification of model misspecifications. *Journal of Geodesy*, 97(55):1–19, 2023.

[42] P. J. G. Teunissen. On the Optimality of DIA-Estimators: Theory and Applications. *Journal of Geodesy*, 98(43):1–26, 2024.

[43] D. Odijk. Positioning Model. In P. J. G. Teunissen and O. Montenbruck, editors, *Springer Handbook of Global Navigation Satellite Systems*, pages 623–630. Springer, 2017.

[44] D. P. Kroese and R. Y. Rubinstein. The Transform Likelihood Ratio Method for Rare Event Simulation with Heavy Tails. *Queueing Systems*, 46(3/4):317–351, 2004.

[45] R. Y. Rubinstein and D. P. Kroese. *Simulation and the Monte Carlo Method*. Wiley Series in Probability and Statistics. Wiley, 2008.

[46] I. Papaioannou, C. Papadimitriou, and D. Straub. Sequential Importance Sampling for Structural Reliability Analysis. *Structural Safety*, 62:66–75, 2016.

[47] B. J. Garrick et al. Reliability Analysis of Nuclear Power Plant Protective Systems. Research and development report, Holmes and Narver Inc. Nuclear Division, 1967.

[48] M. Mitici and H. A. P. Blom. Mathematical Models for Air Traffic Conflict and Collision Probability Estimation. *IEEE Transactions on Intelligent Transportation Systems*, 20(3):1052–1068, 2019.

[49] G. Biondini. An Introduction to Rare Event Simulation and Importance Sampling, booktitle = Handbook of Statistics. pages 29–68. Elsevier B.V., 2015.

[50] R. Y. Rubinstein. Optimization of Computer Simulation Models with Rare Events. *European Journal of Operational Research*, 99(1):89–112, 1997.

[51] S. Kullback and R. A. Leibler. On Information and Sufficiency. *Annals of Mathematical Statistics*, 22(1):79–86, 1951.

[52] R. Y. Rubinstein and D. P. Kroese. *The Cross-Entropy Method: A Unified Approach to Combinatorial Optimization, Monte Carlo Simulation, and Machine Learning*. Springer Series in Information Science and Statistics. Springer, 2004.

[53] P. T. de Boer et al. A Tutorial on the Cross-Entropy Method. *Annals of Operations Research*, 134:19–67, 2005.

[54] J. Morio and M. Balesdent. *Estimation of Rare Event Probabilities in Complex Aerospace and Other Systems - A Practical Approach*. Elsevier B.V., 2016.

[55] M. El Masri, J. Morio, and F. Simatos. Improvement of the Cross-Entropy Method in High Dimension for Failure Probability Estimation through a One-Dimensional Projection Without Gradient Estimation. *Reliability Engineering and System Safety*, 216:1–10, 2021.

[56] S. Geyer, I. Papaioannou, and D. Straub. Cross-Entropy-Based Adaptive Importance Sampling Using Gaussian Densities Revisited. *Structural Safety*, 76:15–27, 2019.

[57] N. Kurtz and J. Song. Cross-Entropy-Based Adaptive Importance Sampling Using Gaussian Mixture. *Structural Safety*, 42:35–44, 2013.

[58] Z. Wang and J. Song. Cross-Entropy-Based Adaptive Importance Sampling Using von Mises-Fisher Mixture for High Dimensional Reliability Analysis. *Structural Safety*, 59:42–52, 2016.

[59] G. Weber et al. Networked Transport of RTCM via Internet Protocol (Ntrip) - IP - Streaming for Real-Time GNSS Applications. In *ION GNSS*, pages 2243–2247, 2005.

[60] A. Kealy and T. Moore. Land-Based Applications of GNSS. In P. J. G. Teunissen and O. Montenbruck, editors, *Springer Handbook of Global Navigation Satellite Systems*, pages 842–856. Springer, 2017.

[61] D. Odijk and L. Wanninger. Differential Positioning. In P. J. G. Teunissen and O. Montenbruck, editors, *Springer Handbook of Global Navigation Satellite Systems*, pages 687–720. Springer, 2017.

[62] D. Odijk. *Fast Precise GPS Positioning in the Presence of Ionospheric Delays*. PhD thesis, Delft University of Technology, 2002.

[63] H. J. Euler and C. C. Goad. On Optimal Filtering of GPS Dual Frequency Observations Without Using Orbit Information. *Bulletin Geodesique*, 65(2):130–143, 1991.

[64] A. Hauschild. Combination of Observations. In P. J. G. Teunissen and O. Montenbruck, editors, *Handbook of Global Navigation Satellite Systems*, pages 594–596. Springer, 2017.

[65] P. J. G. Teunissen. Nonlinear Least Squares. *Manuscripta Geodaetica*, 15(3):137–150, 1990.

[66] W. Baarda. A Testing Procedure for Use in Geodetic Networks. *Netherlands Geodetic Commission, Publications on Geodesy*, 2(5):1–97, 1968.

[67] J. J. Kok. On Data Snooping and Multiple Outlier Testing. Technical report, US Department of Commerce, National Oceanic and Atmospheric Administration, National Ocean Service, Charting and Geodetic Services, 1984.

[68] W. Baarda. Statistical Concepts in Geodesy. *Netherlands Geodetic Commission, Publications on Geodesy*, 2(4):1–74, 1967.

[69] Y. Feng, C. Wang, and C. Karl. Determination of Required Positioning Integrity Parameters for Design of Vehicle Safety Applications. In *ION GNSS*, pages 129–141, 2018.

[70] O. N. Kigotho and J. H. Rife. Comparison of Rectangular and Elliptical Alert Limits for Lane-Keeping Applications. In *ION GNSS*, pages 93–104, 2021.

[71] Ç. Tanil et al. Optimal INS/GNSS Coupling for Autonomous Car Positioning Integrity. In *ION GNSS*, pages 3123–3140, 2019.

[72] S. Ciuban, P. J. G. Teunissen, and C. C. J. M. Tiberius. GNSS Positioning Safety: Probability of Positioning Failure and its Components. In *Proc. 37th Int. Tech. Meeting Satellite Div. Inst. Navig. (ION GNSS+)*, pages 2228–2249, 2024.

[73] Delft High Performance Computing Centre. Delft supercomputer (phase 1). Technical report, 2022.

[74] I. Papaioannou, S. Geyer, and D. Straub. Improved Cross-Entropy-Based Importance Sampling with Flexible Mixture Model. *Reliability Engineering and System Safety*, 191:1–11, 2019.

[75] F. Uribe et al. Cross-Entropy-Based Importance Sampling with Failure-Informed Dimension Reduction for Rare Event Simulation. *Journal of Uncertainty Quantification*, 9(2):818–847, 2021.

3

Positioning Safety Analysis for Automated/Autonomous Vehicles

The analysis of positioning safety often employs a probability-based formulation. This approach quantifies the probability of positioning failure, which is the probability of the position estimator being outside a safety region, and compares it against an application specific requirement. The design of positioning algorithms for safety-critical applications, such as automated/autonomous vehicles, should consider the dependence between parameter or state estimation and statistical hypothesis testing for model misspecifications in the evaluation of positioning safety. If this dependence is not considered, as this article shows, the conclusions drawn from the positioning safety analysis might be overly-optimistic. Therefore, this article focuses on the aforementioned dependence through a vehicle positioning scenario based on an Extended Kalman Filter (EKF) and the Detection, Identification, and Adaptation (DIA) method for misspecifications in the motion and measurement models. Grounded in the distributional theory for the DIA method, our positioning safety analysis utilizes the conditional probability density functions (PDFs) of the combined EKF and DIA position error, which are generally nonnormal. We compute the probability of vehicle positioning failure in two cases: (i) when the dependence is considered and (ii) when it is not, to quantify the over-optimism introduced by ignoring this dependence. Finally, we present our conclusions and recommendations.

This chapter is based on the journal article *S. Ciuban, P.J.G. Teunissen, and C.C.J.M. Tiberius. "Dependence Between Parameter Estimation and Statistical Hypothesis Testing: Positioning Safety Analysis for Automated/Autonomous Vehicles", IEEE Transactions on Intelligent Transportation Systems, 26(4):5509 - 5521, 2025.*

3.1 Introduction

Parameter or state estimation and statistical hypothesis testing for model misspecifications are two central statistical inference tools in the design of positioning systems for safety-critical applications, such as automated/autonomous vehicles ([1–3]). Given a chosen parameter estimation and statistical hypothesis testing procedure, along with the obtained n-dimensional position estimation error $\underline{\epsilon} \in \mathbb{R}^n$ of a vehicle and an application-specific safety region $\mathcal{B} \subset \mathbb{R}^n$, the event of positioning failure can be formulated as $\mathcal{F} = \{\underline{\epsilon} \notin \mathcal{B}\}$ [4]. For positioning safety analyses the *probability of positioning failure* (denoted as $\mathbb{P}_{\mathcal{F}}$) can be used to verify whether requirements or guidelines are being met (e.g., the ones in [5]). The probability of positioning failure can be expressed as,

$$\mathbb{P}_{\mathcal{F}} = \int_{\mathcal{B}^c} f_{\underline{\epsilon}}(e)\, de, \tag{3.1}$$

where $f_{\underline{\epsilon}}(\epsilon)$ is the probability density function (PDF) of $\underline{\epsilon}$ and $\mathcal{B}^c \subset \mathbb{R}^n$ is the complement of the safety-region $\mathcal{B} \subset \mathbb{R}^n$. Such probability-based formulations, along with the computation or upperbounding of these probabilities, are widely used for safety analyses of failure events in nuclear power plants, aerospace systems, structural engineering, and Global Navigation Satellite System (GNSS) based positioning for civil aviation applications ([6–11]). The application of similar principles from GNSS-based positioning in civil aviation has also been discussed for automated/autonomous vehicles in ([3, 12, 13]).

Since both parameter estimation and statistical hypothesis testing are used in the algorithms of positioning systems, the dependence between them should be reflected in the PDF $f_{\underline{\epsilon}}(\epsilon)$ ([14–24]). To the best of the authors' knowledge, there is a lack of positioning safety analyses for automated/autonomous vehicles that specifically address the dependence between parameter estimation and statistical hypothesis testing when quantifying $\mathbb{P}_{\mathcal{F}}$. Therefore, we put forward the following question in the context of positioning safety analyses for automated/autonomous vehicles:

How do the results for $\mathbb{P}_{\mathcal{F}}$ differ when the dependence between parameter estimation and statistical hypothesis testing is accounted for, compared to when it is ignored?

In this article, we show through a positioning scenario of an automated vehicle, driving cooperatively with an adjacent vehicle, that ignoring the aforementioned dependence can result in its $\mathbb{P}_{\mathcal{F}}$ being one order of magnitude too optimistic. The consequence of this over-optimism is that it may lead to safety requirements or guidelines being declared satisfied when they are not.

For vehicle positioning, we use an Extended Kalman Filter (EKF) for parameter (or state) estimation ([25, 26]), along with the Detection, Identification, and Adaptation (DIA) procedure to perform statistical hypothesis testing to accommodate for multiple model misspecifications ([14, 27]). Examples of model misspecifications are unmodelled accelerations in the vehicle's motion model, outliers and anomalies which may incidentally corrupt sensor measurements (e.g., from a GNSS receiver), etc. To account for the dependence between parameter estimation and statistical hypothesis testing in the PDF $f_{\underline{\epsilon}}(\epsilon)$ of the estimation

error $\underline{\epsilon} \in \mathbb{R}^n$ we apply the principles of the theoretical framework introduced recently in [14]. Building on this setup, we proceed with the positioning safety analysis based on $\mathbb{P}_{\mathcal{F}}$ during design stage of the positioning systems (i.e., offline). At the design stage, decisions are made regarding (i) measurement models, (ii) parameter estimation methods, (iii) statistical hypothesis testing procedures to accommodate for model misspecifications (e.g., missmodeling of the vehicles' motion, outliers or faults in sensor measurements), and (iv) positioning scenarios for vehicles, among other factors. This approach aligns with the scenario-based safety assessment framework used for automated and autonomous vehicles [28–30].

This article is organized as follows: In Section 3.2 we present the combined Kalman Filter (KF) and DIA method, while discussing the principles of approaching statistical hypothesis testing through the partitioning of the vector space of KF-predicted residuals. These principles, though illustrated with the KF and DIA method, are equally applicable to the EKF and DIA method. In Section 3.3 we show the expression of the PDF $f_{\underline{\epsilon}}(\epsilon)$ which accounts for the dependence between the (E)KF and the DIA method. Section 3.3 further shows: (i) the formulation of the probability of positioning failure based on $f_{\underline{\epsilon}}(\epsilon)$ and its conditional components resulted from the application of the rule of total probability; (ii) the formulation of the probability of positioning failure when the aforementioned dependence is *ignored*. Section 3.4 presents, by means of an example, a quantitative positioning safety analysis for an automated vehicle driving cooperatively with an adjacent vehicle. First, we carry out an analysis based on the components of the PDF $f_{\underline{\epsilon}}(\epsilon)$ which is used to determine which of these components have the largest (or smallest) impact on the probability of positioning failure. Secondly, we compare the obtained results with the case when the aforementioned dependence is ignored and quantify the difference. Finally, we present our conclusions and recommendations in Section 3.5.

Throughout the paper we make use of the following notation: an underscore denotes a random quantity (e.g., the random vector $\underline{x} \in \mathbb{R}^n$), $f_{\underline{x}}(x)$ is the PDF of $\underline{x}$, $\mathsf{E}(\underline{x})$ is the expectation, $\mathsf{D}(\underline{x})$ is the dispersion or variance operator, and $\mathsf{C}\left(\underline{x},\underline{y}\right)$ is the covariance operator. The error-variance matrices are denoted with a capital italic P while the probability of an event $\mathcal{E}$ is denoted $\mathsf{P}_{\mathcal{E}} = \mathsf{P}(\mathcal{E})$. For the weighted squared norm of a vector we use the notation $\|.\|^2_{\mathrm{Q}} = (.)^T \mathrm{Q}^{-1}(.)$. We also provide a table below with the notation for key symbols:

Table 3.1: Key symbols and their description

Symbol	Description
$\underline{\nu}$	Vector of predicted residuals
$\mathrm{Q}_{\nu\nu}$	Variance-covariance matrix of $\underline{\nu}$
$f_{\underline{\nu}}(\nu)$	PDF of $\underline{\nu}$
$\mathcal{H}_i$	Hypothesis i
$f_{\underline{\nu}}(\nu\|\mathcal{H}_i)$	PDF of $\underline{\nu}$ under $\mathcal{H}_i$
C_i	Vector/matrix of model misspecification under a $\mathcal{H}_i$
$\mathcal{R}(\mathrm{C}_i)$	Range space of C_i

Symbol	Description
$\mathbf{\Pi}_{\mathrm{C}_i}$	Projection matrix onto the range space of C_i
$\mathcal{P}_i$	Partition i of the predicted residuals vector space
L_i	Term adapting the model under $\mathcal{H}_0$ to $\mathcal{H}_{i\neq 0}$
b_i	Size of the model misspecification
q_i	Dimension of $\mathrm{b}_i \in \mathbb{R}^{q_i}$
$\underline{\hat{\epsilon}}_i$	Filter error of the (E)KF using the models under $\mathcal{H}_i$
$\overline{\underline{\epsilon}}$	Filter error of the combined (E)KF and DIA method
$f_{\overline{\underline{\epsilon}}}(\epsilon\|\mathcal{H}_i)$	PDF of $\overline{\underline{\epsilon}}$ under $\mathcal{H}_i$
$f_{\overline{\underline{\epsilon}}\|\mathcal{E}}(\epsilon\|\mathcal{E})$	PDF of $\overline{\underline{\epsilon}}$ conditioned on the event $\mathcal{E}$
$\mathcal{B}$	Safety-region of the vehicle
$\mathbb{P}_{\mathcal{F}}$	Probability of positioning failure
$\mathbb{P}_{\mathcal{F}}\|\mathcal{H}_i$	$\mathbb{P}_{\mathcal{F}}$ under $\mathcal{H}_i$
$\mathbb{P}_{\mathcal{F}}\|\mathcal{E}$	$\mathbb{P}_{\mathcal{F}}$ conditioned on the event $\mathcal{E}$

3.2 Combined Kalman Filter and DIA method

The discrete-time evolution of the state vector $\underline{\mathrm{x}}_k \in \mathbb{R}^n$ (at epoch k) can be captured by the linear(ized) motion model

$$\underline{\mathrm{x}}_k = \Phi_{k,k-1}\underline{\mathrm{x}}_{k-1} + \underline{\mathrm{d}}_k, \tag{3.2}$$

where $\Phi_{k,k-1} \in \mathbb{R}^{n\times n}$ denotes the transition matrix, $\underline{\mathrm{d}}_k \in \mathbb{R}^n$ is the process noise which is assumed to have a normal distribution with $\mathsf{E}\left(\underline{\mathrm{d}}_k\right) = 0_{n\times 1}$, $\mathsf{C}\left(\underline{\mathrm{d}}_k, \underline{\mathrm{d}}_l\right) = \mathrm{Q}_{\mathrm{d}_k\mathrm{d}_k}\delta_{kl}$, and $\mathsf{C}\left(\underline{\mathrm{d}}_k, \underline{\mathrm{x}}_{\mathrm{init}}\right) = 0_{n\times n}$ with δ_{kl} being the Kronecker delta and $\underline{\mathrm{x}}_{\mathrm{init}}$ is the normally distributed initial state vector.

The following linear(ized) measurement model describes the relation between the random vector of observables $\underline{\mathrm{y}}_k \in \mathbb{R}^{m_k}$ and $\underline{\mathrm{x}}_k$,

$$\underline{\mathrm{y}}_k = \mathrm{A}_k\,\underline{\mathrm{x}}_k + \underline{\mathrm{e}}_k, \tag{3.3}$$

where $\mathrm{A}_k \in \mathbb{R}^{m_k\times n}$ is the design matrix and $\underline{\mathrm{e}}_k \in \mathbb{R}^{m_k}$ is the measurement noise which is assumed to have a normal distribution with $\mathsf{E}\left(\underline{\mathrm{e}}_k\right) = 0_{m_k\times 1}$, $\mathsf{C}\left(\underline{\mathrm{e}}_k, \underline{\mathrm{e}}_l\right) = R_k\delta_{kl}$, $\mathsf{C}\left(\underline{\mathrm{e}}_k, \underline{\mathrm{x}}_{\mathrm{init}}\right) = 0_{m_k\times n}$, and $\mathsf{C}\left(\underline{\mathrm{e}}_k, \underline{\mathrm{d}}_k\right) = 0_{m_k\times n}$.

Misspecifications could occur in the functional and stochastic models from (3.2) and (3.3). We consider the case of misspecifications only in the functional models as these are the most common occurring in practice [31]. In subsequent developments, we omit the k index for simplicity. Based on the vector of predicted residuals $\underline{\nu} \in \mathbb{R}^m$ (Figure 3.1), a DIA procedure can be designed ([27, 31–33]). The multiple statistical hypothesis testing problem is

$$\mathcal{H}_0 : \mathsf{E}(\underline{\nu}) = 0_{m\times 1} \quad \text{vs.} \quad \mathcal{H}_{i\neq 0} : \mathsf{E}(\underline{\nu}) \quad = \mathrm{C}_i\mathrm{b}_i, \tag{3.4}$$

for $i \in \{1, ..., n_{\mathcal{H}}\}$, where $\mathrm{C}_i \in \mathbb{R}^{m\times q_i}$ has $\mathrm{rank}(\mathrm{C}_i) = q_i$ for $i \neq 0$. The matrix C_i specifies the type of model misspecification (e.g., unmodelled accelerations, outliers in sensor measurements), $\mathrm{b}_i \in \mathbb{R}^{q_i}$ is the size of the model misspecification and $q_i \in \{1, ..., m\}$ is its dimension for $i \neq 0$.

It is possible to unambiguously link the testing decisions for the $\mathcal{H}_i$'s to partitions $\mathcal{P}_i$ of vector space $\mathbb{R}^m$ such that $\cup_{i=0}^{n_\mathcal{H}} \mathcal{P}_i = \mathbb{R}^m$ and $\mathcal{P}_i \cap \mathcal{P}_j = \emptyset$ for $i \neq j$. Therefore, if the predicted residual $\underline{\nu}$ lands in a $\mathcal{P}_i \subset \mathbb{R}^m$ (i.e., $\underline{\nu} \in \mathcal{P}_i$) then hypothesis $\mathcal{H}_i$ is selected as most likely. The equations of the KF together with the local Detection ($\mathcal{D}$) Identification ($\mathcal{I}$) and Adaptation ($\mathcal{A}$) procedure are shown in Figure 3.1. The initialization of the KF is done according to Lemma 7 in [34] yielding $\hat{\underline{x}}_{\text{init}}$ and its error-variance matrix P_{init}.

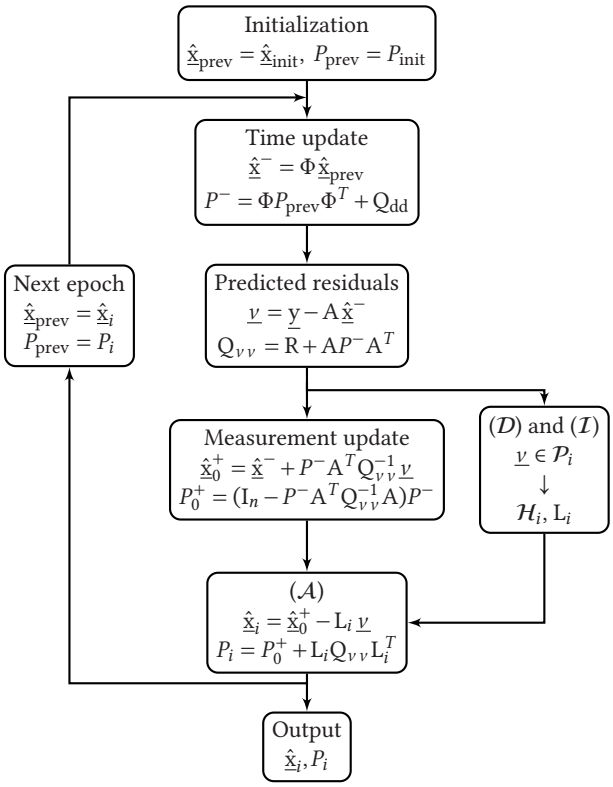

Figure 3.1: KF equations and DIA procedure. Time updated variables have the $[.]^-$ superscript and the measurement updated ones have $[.]^+$. The subscript $[.]_0$ indicates the vector or matrix using the models of $\mathcal{H}_0$. The $L_i \in \mathbb{R}^{n\times m}$ is given in equations (3.5), (3.6), and it drives the adaptation step under a $\mathcal{H}_{i\neq 0}$ while $L_i = 0_{n\times m}$ for $i = 0$.

The adaptation term $L_i \in \mathbb{R}^{n\times m}$ in Figure 3.1 for model misspecifications in the motion model and $i \neq 0$ is given by

$$L_i = (I_n - P^{-1}A^TQ_{\nu\nu}^{-1}A)\Phi C_i \underbrace{(-A\Phi C_i)^+}_{(C_i^*)^+} \text{ and } \left(C_i^*\right)^+ = \left(\left(C_i^*\right)^T Q_{\nu\nu}^{-1}\left(C_i^*\right)\right)^{-1}\left(C_i^*\right)^T Q_{\nu\nu}^{-1}\,. \tag{3.5}$$

Similarly, it follows that for model misspecifications in the measurement model we obtain

$$L_i = P^{-1}A^TQ_{\nu\nu}^{-1}C_iC_i^+ \text{ and } C_i^+ = \left(C_i^TQ_{\nu\nu}^{-1}C_i\right)^{-1}C_i^TQ_{\nu\nu}^{-1}\,. \tag{3.6}$$

where $\mathrm{C}_i\mathrm{C}_i^{+} = \mathbf{\Pi}_{\mathrm{C}_i}$ is the projection matrix onto $\mathcal{R}(\mathrm{C}_i)$.

The *combined* outcome of the KF and of the DIA procedure is expressed as

$$\underline{\overline{\mathrm{x}}} = \sum_{i=0}^{n_{\mathcal{H}}} \hat{\underline{\mathrm{x}}}_i \, p_i(\underline{\nu}), \tag{3.7}$$

where $p_i(\underline{\nu})$ is an indicator function which takes the value 1 if $\underline{\nu} \in \mathcal{P}_i$, and 0 otherwise. Note that the uncertainty of (3.7) is driven by $\hat{\underline{\mathrm{x}}}_i$ and by $p_i(\underline{\nu})$. The definitions of the partitions are (an example is shown in Figure 3.2)

$$\mathcal{P}_0 = \left\{ \nu \in \mathbb{R}^m \mid \|\nu\|^2_{\mathrm{Q}_{\nu\nu}} \leq \chi^2_\alpha(m,0) \right\}, \quad \mathcal{P}_{i\neq 0} = \left\{ \nu \in \mathbb{R}^m \mid \nu \notin \mathcal{P}_0, \check{\mathsf{T}}_i = \max_{j\in\{1,\ldots,n_{\mathcal{H}}\}} \mathsf{T}_j \right\}, \tag{3.8}$$

where $\|\underline{\nu}\|^2_{\mathrm{Q}_{\nu\nu}}$ is the overall model test statistic, $\chi^2_\alpha(m,0)$ is the Chi-squared critical value for a level of significance α, and $\underline{\mathsf{T}}_j$ is the result of the following transformation ([31, 35])

$$\underline{\mathsf{T}}_j = \mathrm{CDF}_{\chi^2(q_j,0)}\left(\|\mathbf{\Pi}_{\mathrm{C}_j}\underline{\nu}\|^2_{\mathrm{Q}_{\nu\nu}} \right), \tag{3.9}$$

where $\mathrm{CDF}_{\chi^2(q_j,0)}(.)$ is the cumulative distribution function (CDF) of $\chi^2(q_j,0)$, $\|\mathbf{\Pi}_{\mathrm{C}_j}\underline{\nu}\|^2_{\mathrm{Q}_{\nu\nu}} \overset{\mathcal{H}_0}{\sim} \chi^2(q_j,0)$, $\mathbf{\Pi}_{\mathrm{C}_j} = \mathrm{C}_j\left(\mathrm{C}_j^T\mathrm{Q}_{\nu\nu}^{-1}\mathrm{C}_j\right)^{-1}\mathrm{C}_j^T\mathrm{Q}_{\nu\nu}^{-1}$ is a projection matrix onto $\mathcal{R}\left(\mathrm{C}_j\right)$, and $\underline{\mathsf{T}}_l$ has a uniform distribution on the interval $[0,1]$ under $\mathcal{H}_0$. This transformation is applied such that all $\underline{\mathsf{T}}_j$ have the same PDF under $\mathcal{H}_0$ as the dimension of the model misspecification $\mathrm{b}_i \in \mathbb{R}^{q_i}$ would generally differ across $\mathcal{H}_{i\neq 0}$. Therefore, $\underline{\check{\mathsf{T}}}_i$ corresponds to the most likely $\mathcal{H}_{i\neq 0}$.

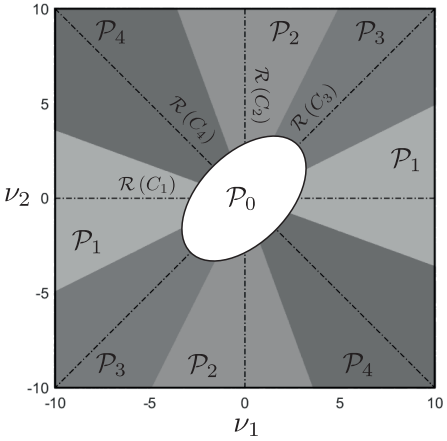

Figure 3.2: Example of partitioning predicted residual vector space $\mathbb{R}^{m=2}$ when $\underline{\nu} \sim \mathcal{N}(\mathsf{E}(\underline{\nu}), \mathrm{Q}_{\nu\nu})$, $\mathrm{Q}_{\nu\nu} = \begin{bmatrix} 2 & 1 \\ 1 & 2 \end{bmatrix}$, $\mathcal{H}_0 : \mathsf{E}(\underline{\nu}) = 0_{m\times 1}$, $\mathcal{H}_{i\neq 0} : \mathsf{E}(\underline{\nu}) = \mathrm{C}_i\mathrm{b}_i$, $i \in [1,4]$, and level of significance $\alpha = 10^{-1}$. The following types of 1D model misspecifications are considered: $\mathrm{C}_1 = \begin{bmatrix} 1 & 0 \end{bmatrix}^T$, $\mathrm{C}_2 = \begin{bmatrix} 0 & 1 \end{bmatrix}^T$, $\mathrm{C}_3 = \begin{bmatrix} 1 & 1 \end{bmatrix}^T$, and $\mathrm{C}_4 = \begin{bmatrix} 1 & -1 \end{bmatrix}^T$. The dotted lines are the vector spaces spanned by $\mathcal{R}(\mathrm{C}_i) \subset \mathbb{R}^{m=2}$.

Equation (3.7) together with (3.8) describe the following procedure

$$\begin{cases} \text{if } \underline{\nu} \in \mathcal{P}_0 \text{ (no Detection)} \rightarrow \text{ output } \hat{\underline{x}}_0, \\ \text{if } \underline{\nu} \notin \mathcal{P}_0 \text{ (Detection)} \rightarrow \ \underline{\nu} \in \mathcal{P}_{i\neq 0} \text{ (Identification)} \rightarrow \text{ output } \hat{\underline{x}}_i \text{ (Adaptation).} \end{cases} \tag{3.10}$$

3.3 Conditional PDFs and total probability of positioning failure

From (3.7) is clear that $p_i(\underline{\nu})$ defines a nonlinear mapping of $\underline{\nu}$ which causes the PDF of the filter error $\overline{\underline{\epsilon}} = \underline{x} - \overline{\underline{x}}$ *to not be normally distributed* despite that $\hat{\underline{\epsilon}}_i \sim \mathcal{N}(0_{n\times 1}, P_i)$. The PDF of $\overline{\underline{\epsilon}}$ follows from Theorem 1 in [14]

$$\begin{aligned} f_{\overline{\underline{\epsilon}}}(\epsilon) &= \sum_{i=0}^{n_{\mathcal{H}}} \int_{\mathcal{P}_i} f_{\hat{\underline{\epsilon}}_i, \underline{\nu}}(\epsilon, \upsilon) d\upsilon \\ &= \sum_{i=0}^{n_{\mathcal{H}}} \int_{\mathcal{P}_i} f_{\hat{\underline{\epsilon}}_0}(\epsilon + \mathrm{L}_i \upsilon) f_{\underline{\nu}}(\upsilon) d\upsilon, \end{aligned} \tag{3.11}$$

where use has been made of the independence between the normally distributed $\hat{\underline{\epsilon}}_0$ and $\underline{\nu}$ [34]. However, $\hat{\underline{\epsilon}}_i$ and $\underline{\nu}$ are *dependent* since the joint PDF $f_{\hat{\underline{\epsilon}}_i, \underline{\nu}}(\epsilon, \nu) \neq f_{\hat{\underline{\epsilon}}_i}(\epsilon) f_{\underline{\nu}}(\nu)$ for $i > 0$ [14]. One can decompose (3.11) via the rule of total probability to obtain the conditional PDFs which account for the testing decisions under $\mathcal{H}_0$, such as Correct Acceptance (CA) when $\mathcal{H}_0$ is accepted and False Alarm (FA_i) when $\mathcal{H}_0$ is rejected and $\mathcal{H}_i$ is accepted,

$$f_{\overline{\underline{\epsilon}}}(\epsilon|\mathcal{H}_0) = f_{\overline{\underline{\epsilon}}|\mathrm{CA}}(\epsilon|\mathrm{CA})\mathsf{P}_{\mathrm{CA}} + \sum_{i=1}^{n_{\mathcal{H}}} f_{\overline{\underline{\epsilon}}|\mathrm{FA}_i}(\epsilon|\mathrm{FA}_i)\mathsf{P}_{\mathrm{FA}_i}, \tag{3.12}$$

where $f_{\overline{\underline{\epsilon}}|\mathrm{CA}}(\epsilon|\mathrm{CA}) = f_{\hat{\underline{\epsilon}}_0}(\epsilon|\mathcal{H}_0) = \mathcal{N}(0_{n\times 1}, P_0)$ and

$$f_{\overline{\underline{\epsilon}}|\mathrm{FA}_i}(\epsilon|\mathrm{FA}_i) = \frac{\int_{\mathcal{P}_i} f_{\hat{\underline{\epsilon}}_0}(\epsilon + \mathrm{L}_i \upsilon|\mathcal{H}_0) f_{\underline{\nu}}(\upsilon|\mathcal{H}_0) d\upsilon}{\mathsf{P}_{\mathrm{FA}_i}} \tag{3.13}$$

for $i > 0$, $\mathsf{P}_{\mathrm{CA}} = \mathsf{P}(\underline{\nu} \in \mathcal{P}_0|\mathcal{H}_0)$, $\mathsf{P}_{\mathrm{FA}_i} = \mathsf{P}(\underline{\nu} \in \mathcal{P}_i|\mathcal{H}_0)$ are the probabilities of the events of CA and FA_i such that $\mathsf{P}_{\mathrm{FA}} = \sum_{i=1}^{n_{\mathcal{H}}} \mathsf{P}_{\mathrm{FA}_i}$ and $1 = \mathsf{P}_{\mathrm{CA}} + \mathsf{P}_{\mathrm{FA}}$. The summation term in (3.12) causes $f_{\overline{\underline{\epsilon}}}(\epsilon|\mathcal{H}_0)$ to be a nonnormal PDF. Similarly, under an alternative hypothesis $\mathcal{H}_a$ the decomposition of (3.11) gives the following result based on the testing decisions: Missed Detection (MD_a) when $\mathcal{H}_0$ is accepted, Correct Identification (CI_a) when $\mathcal{H}_0$ is rejected and $\mathcal{H}_a$ is accepted, and Wrong Identification (WI) when $\mathcal{H}_0$ is rejected and $\mathcal{H}_j$ is accepted for $j \notin \{0, a\}$,

$$f_{\overline{\underline{\epsilon}}}(\epsilon|\mathcal{H}_a) = f_{\overline{\underline{\epsilon}}|\mathrm{MD}_a}(\epsilon|\mathrm{MD}_a)\mathsf{P}_{\mathrm{MD}_a} + f_{\overline{\underline{\epsilon}}|\mathrm{CI}_a}(\epsilon|\mathrm{CI}_a)\mathsf{P}_{\mathrm{CI}_a} + \sum_{i\neq 0,a}^{n_{\mathcal{H}}} f_{\overline{\underline{\epsilon}}|\mathrm{WI}_i}(\epsilon|\mathrm{WI}_i)\mathsf{P}_{\mathrm{WI}_i}, \tag{3.14}$$

where $f_{\underline{\epsilon}|\mathrm{MD}_a}(\epsilon|\mathrm{MD}_a) = f_{\hat{\underline{\epsilon}}_0}(\epsilon|\mathcal{H}_a) = \mathcal{N}(\mathrm{L}_a\mathrm{C}_a\mathrm{b}_a, P_0)$,

$$
\begin{aligned}
f_{\underline{\epsilon}|\mathrm{CI}_a}(\epsilon|\mathrm{CI}_a) &= \frac{\int_{\mathcal{P}_a} f_{\hat{\underline{\epsilon}}_0}(\epsilon + \mathrm{L}_a v|\mathcal{H}_a)\, f_{\underline{\nu}}(v|\mathcal{H}_a) dv}{\mathsf{P}_{\mathrm{CI}_a}}, \\
f_{\underline{\epsilon}|\mathrm{WI}_i}(\epsilon|\mathrm{WI}_i) &= \frac{\int_{\mathcal{P}_i} f_{\hat{\underline{\epsilon}}_0}(\epsilon + \mathrm{L}_i v|\mathcal{H}_a)\, f_{\underline{\nu}}(v|\mathcal{H}_a) dv}{\mathsf{P}_{\mathrm{WI}_i}},
\end{aligned}
\tag{3.15}
$$

with $\mathsf{P}_{\mathrm{MD}_a} = \mathsf{P}(\underline{\nu} \in \mathcal{P}_0|\mathcal{H}_a)$, $\mathsf{P}_{\mathrm{CI}_a} = \mathsf{P}(\underline{\nu} \in \mathcal{P}_a|\mathcal{H}_a)$, and $\mathsf{P}_{\mathrm{WI}_i} = \mathsf{P}(\underline{\nu} \in \mathcal{P}_i|\mathcal{H}_a)$ for $i \notin \{0, a\}$ being the probabilities of the events of MD_a, CI_a, and WI_j such that $1 = \mathsf{P}_{\mathrm{MD}_a} + \mathsf{P}_{\mathrm{CI}_a} + \sum_{i\neq 0,a}^{n_{\mathcal{H}}} \mathsf{P}_{\mathrm{WI}_i}$. The second and third terms in (3.14) cause $f_{\underline{\epsilon}}(\epsilon|\mathcal{H}_a)$ to be a nonnormal PDF.

Next, we formulate the total probability of positioning failure based on (3.12), (3.14), a given safety-region $\mathcal{B} \subset \mathbb{R}^n$, and its complement $\mathcal{B}^c = \mathbb{R}^n / \mathcal{B}$

$$
\begin{aligned}
\mathbb{P}_{\mathcal{F}}(\mathbf{b}) &= \int_{\mathcal{B}^c} f_{\underline{\epsilon}}(e)\, de \\
&= \omega_0 \int_{\mathcal{B}^c} f_{\underline{\epsilon}}(e|\mathcal{H}_0)\, de + \sum_{i=1}^{n_{\mathcal{H}}} \omega_i \left(\int_{\mathcal{B}^c} f_{\underline{\epsilon}}(e|\mathcal{H}_i)\, de \right) \\
&= \omega_0\, \mathbb{P}_{\mathcal{F}}|\mathcal{H}_0 + \sum_{i=1}^{n_{\mathcal{H}}} \omega_i (\mathbb{P}_{\mathcal{F}}|\mathcal{H}_i(\mathrm{b}_i)),
\end{aligned}
\tag{3.16}
$$

where the dependence on the size of the model misspecifications $\mathbf{b} = \left\{ \mathrm{b}_1, \mathrm{b}_2, \ldots, \mathrm{b}_{n_{\mathcal{H}}} \right\}$ has been accounted for in the notation, and $\omega_i = \mathsf{P}(\mathcal{H}_i)$ are the a-priori probabilities of occurrence of the hypotheses $\mathcal{H}_i$ for $i \in \{0, \ldots, n_{\mathcal{H}}\}$. A further decomposition of (3.16) via the rule of total probability gives

$$
\begin{aligned}
\mathbb{P}_{\mathcal{F}}(\mathbf{b}) = \omega_0 (\mathsf{P}_{\mathrm{CA}} \mathbb{P}_{\mathcal{F}}|\mathrm{CA} + \sum_{i=1}^{n_{\mathcal{H}}} \mathsf{P}_{\mathrm{FA}_i} \mathbb{P}_{\mathcal{F}}|\mathrm{FA}_i) + \sum_{a=1}^{n_{\mathcal{H}}} \omega_a (\mathsf{P}_{\mathrm{MD}_a} \mathbb{P}_{\mathcal{F}}|\mathrm{MD}_a(\mathrm{b}_a) + \mathsf{P}_{\mathrm{CI}_a} \mathbb{P}_{\mathcal{F}}|\mathrm{CI}_a(\mathrm{b}_a) + \\
\sum_{i\neq 0,a}^{n_{\mathcal{H}}} \mathsf{P}_{\mathrm{WI}_i} \mathbb{P}_{\mathcal{F}}|\mathrm{WI}_i(\mathrm{b}_a)),
\end{aligned}
\tag{3.17}
$$

The decomposition of $\mathbb{P}_{\mathcal{F}}(\mathbf{b})$ is useful in the design stage of the positioning system. It helps identify which hypotheses, along with the associated testing decision outcomes, have the largest impact or are most influential to $\mathbb{P}_{\mathcal{F}}(\mathbf{b})$. The evaluation of (3.17) is mainly driven by three factors: (i) the structure of the nonnormal conditional PDFs, (ii) the range of the model misspecifications inside the set $\mathbf{b}$ to find the worst-case $\mathbb{P}_{\mathcal{F}}(\mathbf{b})$, and (iii) the shape and size of the safety-region $\mathcal{B}$.

If, in the safety-analysis, one would *ignore* the dependence between parameter estimation and statistical hypothesis testing and assume $\hat{\underline{\epsilon}}_i$ and $\underline{\nu}$ to be *independent* for all $i \in \{0, \ldots, n_{\mathcal{H}}\}$ then (3.11) would become

$$
f_{\underline{\epsilon}^o}(\epsilon) = \sum_{i=0}^{n_{\mathcal{H}}} f_{\hat{\underline{\epsilon}}_i}(\epsilon) \int_{\mathcal{P}_i} f_{\underline{\nu}}(v) dv,
\tag{3.18}
$$

where $f_{\underline{\hat{\epsilon}}_i,\underline{\nu}}(\epsilon,\nu) = f_{\underline{\hat{\epsilon}}_i}(\epsilon) f_{\underline{\nu}}(\nu)$ is expressed as a product of the marginal PDFs. Then the formulation of the probability of the positioning failure, when the aforementioned dependence is ignored, is based on

$$\mathbb{P}^o_{\mathcal{F}}(\mathbf{b}) = \int_{\mathcal{B}^c} f^o_{\underline{\tilde{\epsilon}}}(e)\, de, \tag{3.19}$$

and decompositions via the rule of total probability can similarly be done as in (3.16) and (3.17).

3.4 Quantitative Safety Analysis for Cooperative Vehicle Positioning

To illustrate the principles from the previous sections we consider, as an example, the case of two connected vehicles driving on a highway in a cooperative positioning setting. The two-vehicles are capable of exchanging positional coordinates as provided by their positioning systems (e.g., via Cooperative Awareness Messages) and conduct inter-vehicle distance measurements (e.g., via LiDAR, Radar) [36–38]. Each vehicle runs an EKF which makes use of the cooperative positioning information to improve its positioning performance. In the following sub-sections we present the chosen motion and measurement models, the simulation scenario, and the results of the positioning safety-analysis for single and multiple configurations of the vehicles.

3.4.1 Motion and measurement models

Curvilinear motion models are commonly used for vehicle tracking ([39–41]). Among them we choose the Constant Turn Rate and Velocity (CTRV) model given its suitability for highway driving conditions. The perturbed nonlinear equations of motion are

$$\underbrace{\begin{bmatrix} \dot{\underline{\mathsf{u}}} \\ \dot{\underline{\mathsf{v}}} \\ \dot{\underline{\mathsf{s}}} \\ \dot{\underline{\psi}} \\ \dot{\underline{\theta}} \end{bmatrix}}_{\dot{\underline{\mathrm{x}}}} = \underbrace{\begin{bmatrix} \mathsf{s}\cos(\psi) \\ \mathsf{s}\sin(\psi) \\ 0 \\ \theta \\ 0 \end{bmatrix}}_{\Phi(\mathrm{x})} + \underbrace{\begin{bmatrix} 0 & 0 \\ 0 & 0 \\ 1 & 0 \\ 0 & 0 \\ 0 & 1 \end{bmatrix}}_{\mathrm{G}} \underbrace{\begin{bmatrix} \underline{z}_{\dot{\mathsf{s}}} \\ \underline{z}_{\dot{\theta}} \end{bmatrix}}_{\underline{\mathrm{z}}}, \tag{3.20}$$

where $\Phi(\mathrm{x})$ is a nonlinear vector function, u and v are the coordinates in [m] of the vehicle in a uv-plane, s is the speed of the vehicle (sometimes referred to as 'polar velocity') in [m/s], ψ is the heading angle with respect to (w.r.t.) the u-axis in [rad], θ is the heading rate in [rad/s], $\underline{z}_{\dot{\mathsf{s}}}$ is the process noise modelling the longitudinal acceleration in [m/s^2], and $\underline{z}_{\dot{\theta}}$ is the process noise modelling the heading acceleration in [rad/s^2]. We assume that $\underline{\mathrm{z}} \in \mathbb{R}^2$ is a white-noise random process with spectral density matrix $\mathrm{S}_{zz} = \mathrm{diag}([q_{\dot{\mathsf{s}}} \;\; q_{\dot{\theta}}])$, where $q_{\dot{\mathsf{s}}}$ is the spectral density in [m^2/s^3] and $q_{\dot{\theta}}$ in [rad^2/s^3]. These assumptions are suitable for highway driving conditions [39]. The process-noise is $\underline{\mathrm{d}} = \int_{\Delta \mathrm{t}} e^{\mathrm{F}(\mathrm{t}-\tau)} \mathrm{G}\, \underline{\mathrm{z}}(\tau) d\tau$ and the process-noise variance-covariance matrix is given by [42]

$$\mathrm{Q}_{\mathrm{dd}} = \int_{\Delta \mathrm{t}} \left(e^{\mathrm{F}(\mathrm{t}-\tau)}\mathrm{G}\right) \mathrm{S}_{zz} \left(e^{\mathrm{F}(\mathrm{t}-\tau)}\mathrm{G}\right)^T d\tau, \tag{3.21}$$

where $\Delta t = t - t_0$ is the time update step in $[s]$, $e^{F(t-\tau)} = \sum_{j=0}^{\infty} \frac{F^j (t-\tau)^j}{j!}$, and $F = \partial_{x^T} \Phi\left(x^{(0)}\right)$ for an appropriately chosen linearization point $x^{(0)}$.

The following measurement model is considered

$$\begin{aligned} E(\underline{y}^{(co)}) &= \begin{bmatrix} u^{(1)} & v^{(1)} & u^{(2)} & v^{(2)} & l^{(12)} & l^{(21)} \end{bmatrix}^T, \\ R^{(co)} &= \text{blkdiag}([R_1 \;\; R_2 \;\; R_l]), \end{aligned} \tag{3.22}$$

3

where $(u^{(1)}, v^{(1)})$ is the position of vehicle 1 in [m], $(u^{(2)}, v^{(2)})$ of vehicle 2 in [m], $l^{(12)}$ and $l^{(21)}$ are the inter-vehicle distances in [m]. Then we have for $j \in \{1, 2\}$, the variance-covariance of the position measurements $R_j = \begin{bmatrix} \sigma_{u_j}^2 & \rho_j \sigma_{u_j} \sigma_{v_j} \\ \rho_j \sigma_{u_j} \sigma_{v_j} & \sigma_{v_j}^2 \end{bmatrix}$ [m^2] and that of the distance measurements $R_l = \text{diag}\left(\begin{bmatrix} \sigma_{l_{12}}^2 & \sigma_{l_{21}}^2 \end{bmatrix}\right)$ [m^2]. Sensor calibration is presumed to ensure that all measurements are referenced to a defined Center of Reference (CoR) situated at the geometric center of the vehicle's rooftop. Since these motion and measurement models are nonlinear, we implement an EKF. The framework presented in Section 3.2 holds as it is valid for both linear and linearized models with the appropriate changes (e.g., using the jacobian $J_\Phi \in \mathbb{R}^{n \times n}$ of the vector function $\Phi(.)$ and $J_A \in \mathbb{R}^{m \times n}$ of the vector function $A(.)$) [43]. From (3.22) it follows that $m = 6$.

3.4.2 Alternative hypotheses

Based on the previously discussed motion and measurement models, we formulate the following alternative hypotheses for the statistical testing procedure in which we account for:

- *Model misspecifications in motion models*
  $\mathcal{H}_1 : E(\underline{\nu}) = (-J_A J_\Phi) C_1 b_1$ and $\mathcal{H}_2 : E(\underline{\nu}) = (-J_A J_\Phi) C_2 b_2$, with $q_1 = q_2 = 1$, and $b_1, b_2 \in \mathbb{R}$ in $[m/s^2]$, account for longitudinal deceleration or acceleration of vehicles 1 and 2. These types of model misspecifications are expressed as

$$\begin{aligned} C_1 &= \begin{bmatrix} 0 & 0 & 1 & 0 & 0 & 0 & 0 & 0 & 0 & 0 \end{bmatrix}^T, \\ C_2 &= \begin{bmatrix} 0 & 0 & 0 & 0 & 0 & 0 & 0 & 1 & 0 & 0 \end{bmatrix}^T. \end{aligned} \tag{3.23}$$

- *Model misspecifications in position measurements*
  $\mathcal{H}_3 : E(\underline{\nu}) = C_3 b_3$ and $\mathcal{H}_4 : E(\underline{\nu}) = C_4 b_4$, with $q_3 = q_4 = 2$, and $b_3, b_4 \in \mathbb{R}^2$ in [m], account for 2D model misspecifications in the position measurements of vehicles 1 and 2 (outliers in positions). These types of model misspecifications are expressed as

$$\begin{aligned} C_3 &= \begin{bmatrix} 1 & 0 & 0 & 0 & 0 & 0 \\ 0 & 1 & 0 & 0 & 0 & 0 \end{bmatrix}^T, \\ C_4 &= \begin{bmatrix} 0 & 0 & 1 & 0 & 0 & 0 \\ 0 & 0 & 0 & 1 & 0 & 0 \end{bmatrix}^T. \end{aligned} \tag{3.24}$$

- *Model misspecifications in inter-vehicle distance measurements*
  $\mathcal{H}_5 : E(\underline{\nu}) = C_5 b_5$ and $\mathcal{H}_6 : E(\underline{\nu}) = C_6 b_6$, with $q_5 = q_6 = 1$, and $b_5, b_6 \in \mathbb{R}$ in [m],

account for 1D model misspecifications in the inter-vehicle distance measurements. These types of model misspecifications are expressed as

$$\begin{aligned} \mathrm{C}_5 &= \begin{bmatrix} 0 & 0 & 0 & 0 & 1 & 0 \end{bmatrix}^T, \\ \mathrm{C}_6 &= \begin{bmatrix} 0 & 0 & 0 & 0 & 0 & 1 \end{bmatrix}^T. \end{aligned} \tag{3.25}$$

With the alternative hypotheses defined, the formulation of the partitions $\mathcal{P}_i \subset \mathbb{R}^m$ can carried out according to the principles in (3.4) and (3.8). The combined outcome of the EKF and of the DIA procedure for the two-car cooperative (co) positioning setting is

$$\overline{\underline{\mathrm{x}}}^{(co)} = \begin{bmatrix} \overline{\underline{\mathrm{x}}}^{(1)} \\ \overline{\underline{\mathrm{x}}}^{(2)} \end{bmatrix}. \tag{3.26}$$

which results in the dimension $n = n_1 + n_2 = 10$. The filter error $\overline{\underline{\epsilon}}^{(co)} = \underline{\mathrm{x}}^{(co)} - \overline{\underline{\mathrm{x}}}^{(co)}$ and the process-noise variance-covariance matrix are expressed as

$$\overline{\underline{\epsilon}}^{(co)} = \begin{bmatrix} \overline{\underline{\epsilon}}^{(1)} \\ \overline{\underline{\epsilon}}^{(2)} \end{bmatrix}, \quad \mathrm{Q}_{\mathrm{dd}}^{(co)} = \mathrm{blkdiag}\left(\begin{bmatrix} \mathrm{Q}_{\mathrm{dd}}^{(1)} & \mathrm{Q}_{\mathrm{dd}}^{(2)} \end{bmatrix} \right). \tag{3.27}$$

3.4.3 Scenario with a single configuration of the vehicles

In this simulation scenario, two vehicles are driving on a highway, on the Center of Lanes (CoL), which are parallel, and have a width (l_{w}) of 3.5 [m] each [44]. Both vehicles are set to have a length of 4.5 [m] and a width of 1.8 [m] [45]. The geometry of the scenario and the details of the simulation parameters are given in Figure 3.3 and Table 3.2.

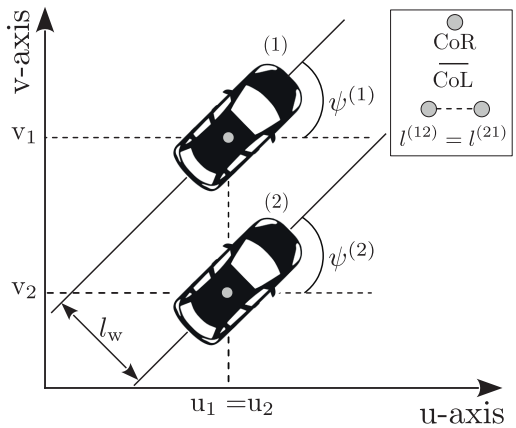

Figure 3.3: Schematic representation of the 2D geometry for the single configuration simulation scenario. Source: Adapted from [46].

The spectral densities are chosen to model realistic vehicle behavior on a highway, accounting for gentle acceleration or deceleration of 0.5 [m/s^2] in the longitudinal direction [47]. For smooth lateral maneuvers, such as lane changes, the spectral density corresponds to

variations of 0.03 [rad/s^2] (1.81 [deg/s^2]). The position measurements have a precision (standard deviation) of 0.100 [m], indicative of positioning via Differential GNSS (DGNSS) [48]. The precision of the inter-vehicle distance measurements (0.050 [m]) is assumed to rely on an automotive-grade LiDAR system.

Table 3.2: Simulation parameters and their values

Parameter(s)	Value	Details
$\mathrm{s}^{(j)}$	28 [m/s] (≈101 [km/h])	$j = \{1, 2\}$
$\psi^{(j)}$	45 [deg]	
$q_{\dot{\mathrm{s}}}^{(j)}$	0.250 [m^2/s^3]	
$q_{\dot{\theta}}^{(j)}$	0.001 [rad^2/s^3]	
σ_{u_j}, σ_{v_j}	0.100 [m]	
ρ_j	0.200	
$\sigma_{l_{12}}$, $\sigma_{l_{21}}$	0.050 [m]	-
$l^{(12)}$, $l^{(21)}$	4.950 [m]	$\sqrt{2}\, l_{\mathrm{w}}$
$\Delta\mathrm{t}$	1 [s]	time update step

Our analysis focuses on vehicle 1, though a similar approach is applicable to vehicle 2. Therefore we are interested only in the filter error of the 2D position of vehicle 1 (at a single-epoch), $\underline{\varepsilon} = \mathrm{H}^T \underline{\varepsilon}^{(co)}$, with $\mathrm{H}^T = [\mathrm{I}_2 \;\; 0_{2\times 8}]$ (we omit the index (1) for simplicity). The PDF of $\underline{\varepsilon}$ is

$$f_{\underline{\varepsilon}}(\varepsilon) = \sum_{i=0}^{n_{\mathcal{H}}} \int_{\mathcal{P}_i} f_{\underline{\hat{\varepsilon}}_0}\left(\varepsilon + \mathrm{H}^T \mathrm{L}_i v\right) f_{\underline{v}}(v) dv, \tag{3.28}$$

and the results from Section 3.3 follow similarly.

Established requirements for the shape and size of the safety-region $\mathcal{B}$ are not yet formalized for positioning of automated/autonomous vehicles. However, some research studies are available in which rectangular and elliptical shapes have been used ([5, 49, 50]). For our analysis we choose an ellipse to inscribe the shape of the vehicle. The safety region is defined as

$$\mathcal{B} = \left\{ \varepsilon \in \mathbb{R}^2 \middle| \, \|\varepsilon\|^2_{\mathrm{Q}_\mathcal{B}} \leq 1 \right\}, \tag{3.29}$$

where $\mathrm{Q}_\mathcal{B}^{-1} = \begin{bmatrix} 0.358 & -0.259 \\ -0.259 & 0.358 \end{bmatrix}$ [m^{-2}]. The major-axis of $\mathcal{B}$ has a length of 6.36 [m] with an orientation w.r.t. the horizontal axis of 45°, and the minor-axis has a length of 2.55 [m]. In the next subsections (C.1 and C.2) we present an analysis of the components of the PDFs of $\underline{\varepsilon}$ under $\mathcal{H}_0$ and $\mathcal{H}_{i\neq 0}$. In the last subsection (C.3), the resulting probability of positioning failure is discussed, comparing the cases where the dependence between parameter estimation and statistical hypothesis testing is accounted for and when it is ignored.

C.1 Components of $f_{\underline{\varepsilon}}(\varepsilon|\mathcal{H}_0)$

The components of $f_{\underline{\varepsilon}}(\varepsilon|\mathcal{H}_0)$ are shown in Figure 3.4. Since in $\mathbb{R}^m$ there is a symmetry of $f_{\underline{\nu}}(\nu|\mathcal{H}_0)$ about the origin and the partitions $\mathcal{P}_i$, it follows that $\mathsf{E}(\underline{\varepsilon}|\mathcal{H}_0) = 0_{n_1\times 1}$. Under the events of FA_i's, the orientation, shape, size, and multimodality are an outcome of the averaged shifted functions $f_{\underline{\hat{\varepsilon}}_0}\left(\varepsilon + \mathrm{H}^T\mathrm{L}_i\,\nu|\mathcal{H}_0\right)$ for $\underline{\nu} \in \mathcal{P}_i$ (the outcome of statistical testing).

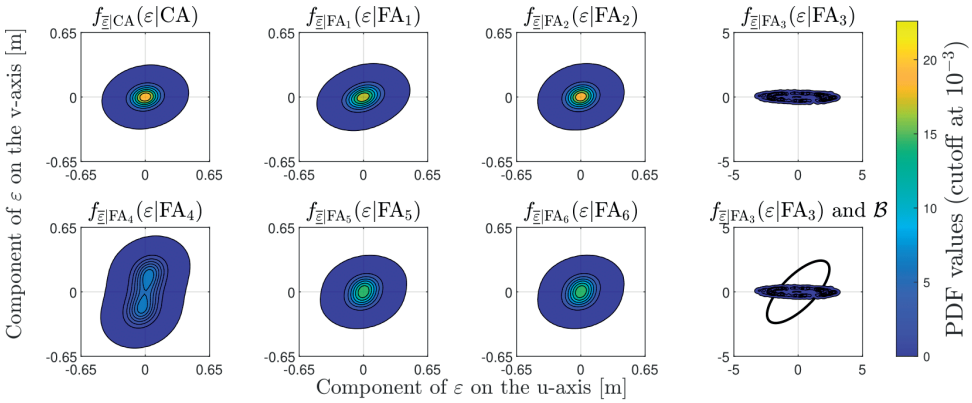

Figure 3.4: Components of $f_{\underline{\varepsilon}}(\varepsilon|\mathcal{H}_0)$ for $\alpha = 10^{-3}$ and $n_\nu = 10^6$ pseudo-random samples drawn from $f_{\underline{\nu}}(\nu|\mathcal{H}_0)$ (note the different scale of $f_{\underline{\varepsilon}|\mathrm{FA}_3}(\varepsilon|\mathrm{FA}_3)$). The last figure in the second row is $f_{\underline{\varepsilon}|\mathrm{FA}_3}(\varepsilon|\mathrm{FA}_3)$ in relation with the safety region $\mathcal{B}$.

The study of the variability of the shifting term $\mathrm{H}^T\mathrm{L}_i\,\underline{\nu}$ will give an indication of the amount of variability under $\mathcal{H}_{i\neq 0}$, while $\mathcal{H}_0$ is valid. Therefore we do an analysis of the ellipses spanned by $\zeta^T\mathrm{Q}_i^{-1}\zeta = 1$, with $\zeta \in \mathbb{R}^2$, $\mathrm{Q}_i^{-1} = \left[\left(\mathrm{H}^T\mathrm{L}_i\right)\mathrm{Q}_{\nu\nu}\left(\mathrm{L}_i^T\mathrm{H}\right)\right]^{-1}$ which can be factorized as $\mathrm{Q}_i^{-1} = \mathrm{U}_i\Lambda_i\mathrm{U}_i^T$ (based on the eigendecomposition). Table 3.3 shows the eigenvalues of each Q_i^{-1}, the length of the principal axis (p.a.), and the angle ($\measuredangle$) of the p.a.'s w.r.t. the u-axis (measured counterclockwise).

Table 3.3: Eigenvalues, length of p.a., and $\measuredangle$ of p.a. w.r.t. u-axis

Q_i^{-1}	Eigenvalues [m^{-2}]	Length of p.a. [m]	$\measuredangle$ [deg]
1	$(4.17\cdot 10^3,\ 0)$	$1.55\cdot 10^{-2}$	30.03
2	$(0,\ 2.06\cdot 10^4)$	$6.97\cdot 10^{-3}$	80.18
3	$(0.26\cdot 10^1,\ 1.81\cdot 10^2)$	$1.96\cdot 10^{-1}$	178.71
4	$(5.33\cdot 10^7,\ 2.21\cdot 10^2)$	$6.73\cdot 10^{-2}$	78.77
5	$(0,\ 3.72\cdot 10^3)$	$1.64\cdot 10^{-2}$	78.79
6	$(0,\ 3.72\cdot 10^3)$	$1.64\cdot 10^{-2}$	78.79

Since the hypotheses $\mathcal{H}_i$ model 1D model misspecifications for $i \in \{1,2,5,6\}$, it means that through the corresponding L_i terms, the obtained Q_i^{-1} matrices have only one nonzero eigenvalue. Although $\mathcal{H}_1$ models a model misspecification in the longitudinal speed of vehicle 1, the orientation of the p.a. of Q_1^{-1} is driven by the direction of motion of vehicle 1

and by the correlation between the position states of the two vehicles due to the distance measurements. The correlation depends on the relative position of vehicle 2 w.r.t. vehicle 1, and on the structure in (3.22). As the CoR of vehicle 2 has almost the same u-coordinates as of vehicle 1, the aforementioned (inter-vehicle) correlation will 'pull' the p.a. of Q_1^{-1} from an angle of 45 [deg] to one of 30.03 [deg]. The direction of the p.a. of Q_2^{-1} is tilted more towards the v-axis, the main contributor being the relative position of the vehicles (captured by the inter-vehicle correlation). The p.a.'s of Q_5^{-1} and Q_6^{-1} are also tilted more towards the v-axis due to the inter-vehicle correlation.

The parameters of the ellipses corresponding to Q_5^{-1} and Q_6^{-1} are the same since the corresponding entries in the design matrix and the precision of the distance measurements, for both ways, are the same. The conditional PDFs $f_{\underline{\varepsilon}|\mathrm{FA}_i}(\varepsilon|\mathrm{FA}_i)$ for $i \in \{1,2,5,6\}$ do not exhibit multimodality as the outcome of statistical testing reveals that $\mathrm{H}^T\mathrm{L}_i\,\underline{\nu}$ with $\underline{\nu} \in \mathcal{P}_i$ is closely distributed across the p.a. The impact of falsely accepting $\mathcal{H}_1$, $\mathcal{H}_2$, $\mathcal{H}_5$ or $\mathcal{H}_6$, while $\mathcal{H}_0$ is valid, on the positioning safety of vehicle 1 is not expected to be significant (see Figure 3.4).

As the hypotheses $\mathcal{H}_3$ and $\mathcal{H}_4$ model 2D model misspecifications in the position measurements of vehicle 1 and vehicle 2, the matrices Q_3^{-1} and Q_4^{-1} have two nonzero eigenvalues. The eigenvalues and the orientation of the p.a. of Q_3^{-1} indicate a larger variation along the u-axis than along the v-axis. The variation is smaller on the v-axis due contribution of the [cm]-level inter-vehicle distance measurements and due to the relative position of vehicle 2 w.r.t. vehicle 1. The large variation along the u-axis is captured by the length of the p.a. and its explanation can be given by investigating the components of

$$Q_3^{-1} = \left[\left(\mathrm{H}^T\mathrm{L}_3\right)\mathrm{R}\left(\mathrm{L}_3^T\mathrm{H}\right) + \left(\mathrm{H}^T\mathrm{L}_3\right)\mathrm{J}_\mathrm{A}P^{-}\mathrm{J}_\mathrm{A}^T\left(\mathrm{L}_3^T\mathrm{H}\right)\right]^{-1}. \tag{3.30}$$

The second term in (3.30) is dominant through the contribution of the process-noise variance-covariance matrix Q_{dd} (see also Table 2.1). Despite the [dm]-level position measurements and [cm]-level inter-vehicle distance measurements, the considered variations in longitudinal acceleration and in heading acceleration are the driving factors. At the bottom right of Figure 3.4 the component $f_{\underline{\varepsilon}|\mathrm{FA}_3}(\varepsilon|\mathrm{FA}_3)$ is displayed in relation with the safety region $\mathcal{B}$, which indicates that it has the largest probability density outside $\mathcal{B}$ among all components of $f_{\underline{\varepsilon}}(\varepsilon|\mathcal{H}_0)$. Although the term $\mathrm{H}^T\mathrm{L}_3\,\underline{\nu}$ with $\underline{\nu} \in \mathcal{P}_3$ is sparsely distributed, it manifests a 'smearing' effect by $f_{\underline{\varepsilon}_0}\left(\varepsilon + \mathrm{H}^T\mathrm{L}_3\,\nu|\mathcal{H}_0\right)$ instead of a multimodality. The 'smearing' is related to the elongation of Q_3^{-1} in the 2D space (a condition number of 2.638). In the case of Q_4^{-1}, the largest variation is along the v-axis as the direction of the p.a. is driven by the inter-vehicle correlation and their relative positions. Since the ellipse is highly elongated along the p.a. (a condition number of $4.91 \cdot 10^2$), which also has the second largest length, the sparsely distributed $\mathrm{H}^T\mathrm{L}_4\,\underline{\nu}$ with $\underline{\nu} \in \mathcal{P}_4$ is causing $f_{\underline{\varepsilon}|\mathrm{FA}_4}(\varepsilon|\mathrm{FA}_4)$ to be bimodal.

C.2 Components of $f_{\underline{\varepsilon}}(\varepsilon|\mathcal{H}_1)$

Since under any $\mathcal{H}_{i\neq 0}$ the PDF of $\underline{\varepsilon}$ depends on the b_i's (see (3.14)), one needs to choose or make assumptions on the size of the model misspecification. We show the analysis of the

components of $f_{\underline{\varepsilon}}(\varepsilon|\mathcal{H}_1)$, though similarly this can be done for the other hypotheses. Under $\mathcal{H}_1$ we assume a model misspecification of $b_1 = -3$ [m/s^2] (a longitudinal deceleration). This case corresponds to a braking event done by vehicle 1 (e.g., due to a congestion on the lane). In this case there is no symmetry of $f_{\underline{\nu}}(\nu|\mathcal{H}_1)$ about the origin and the partitions $\mathcal{P}_i$ (this is true for any $\mathcal{H}_{i\neq 0}$). The simulated probabilities of the decision events are shown in Figure 3.5.

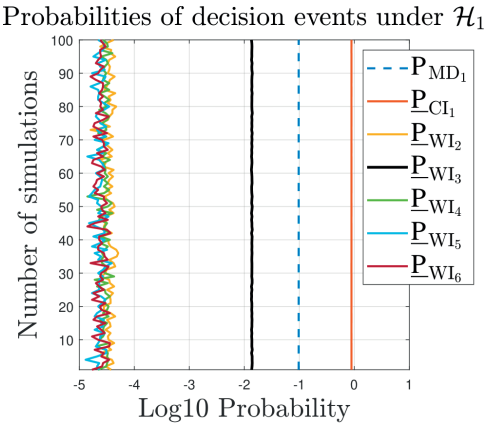

Figure 3.5: The probabilities of MD_1, CI_1, and WI_i (for $i \notin \{0,1\}$) over 100 simulations with $n_\nu = 10^6$, $\alpha = 10^{-3}$, and $b_1 = -3$ [m/s^2].

The variability of the probabilities across the simulations in Figure 3.5 is higher for the lower ones given the same number of used pseudo-random samples, in this case $n_\nu = 10^6$. An indicator for the separability between the probabilities of the events of MD_1, CI_1, and WI_i (for $i \notin \{0,1\}$) is represented by the angles between the subpaces of $\mathbb{R}^m$ spanned by $\mathcal{R}\left(C_1^*\right)$, $\mathcal{R}\left(C_2^*\right)$, and $\mathcal{R}(C_i)$, for $i \notin \{0,1,2\}$. The angles between a one-dimensional subspace and a higher-dimensional subspace in $\mathbb{R}^m$ can be computed in two steps: (i) project the one-dimensional subspace onto the higher-dimensional subspace, (ii) compute the angle between the one-dimensional subspace and the projection. When comparing subspaces in $\mathbb{R}^m$, each with a dimension larger than one, the concept of canonical (or principal angles) is used ([51–53]). The inner products involved in the computation of the angles are with respect to the metric defined by $Q_{\nu\nu}^{-1}$ (Algorithm 6.1 of [53]). The obtained angles are presented in Table 3.4.

Table 3.4: Angles between $\mathcal{R}\left(C_1^*\right)$ and $\mathcal{R}\left(C_2^*\right)$, $\mathcal{R}(C_i)$ for $i \notin \{0,1,2\}$

Subspace	$\mathcal{R}\left(C_2^*\right)$	$\mathcal{R}(C_3)$	$\mathcal{R}(C_4)$	$\mathcal{R}(C_5)$	$\mathcal{R}(C_6)$
$\mathcal{R}\left(C_1^*\right)$	85.98°	38.13°	84.22°	88.34°	88.34°

Table 3.4 shows that the angle $\measuredangle\left(\mathcal{R}\left(C_1^*\right), \mathcal{R}(C_3)\right) = 38.13°$ is by far the smallest which means that as $f_{\underline{\nu}}(\nu|\mathcal{H}_1)$ moves along $\mathcal{R}\left(C_1^*\right)$ in $\mathcal{P}_1$, the probability density outside $\mathcal{P}_1$ will be larger in $\mathcal{P}_3$ than in $\mathcal{P}_2$, $\mathcal{P}_4$, $\mathcal{P}_5$, or $\mathcal{P}_6$. This is confirmed by Figure 3.5 which shows that, among the wrong identifications, $\underline{P}_{WI_3}$ is largest with a mean value of $0.137 \cdot 10^{-1} \pm$

$1.177 \cdot 10^{-5}$ (over 100 simulations). In practice this means that in the case of a moderate to hard braking event by vehicle 1, the probability to wrongly identify $\mathcal{H}_3$, when $\mathcal{H}_1$ is valid, is significantly larger than any of the other probabilities of wrong identification. With respect to the components of $f_{\underline{\varepsilon}}(\varepsilon|\mathcal{H}_1)$ we observe that $f_{\underline{\varepsilon}|\mathrm{WI}_3}(\varepsilon|\mathrm{WI}_3)$ is the most shifted away from the origin (see Figure 3.6).

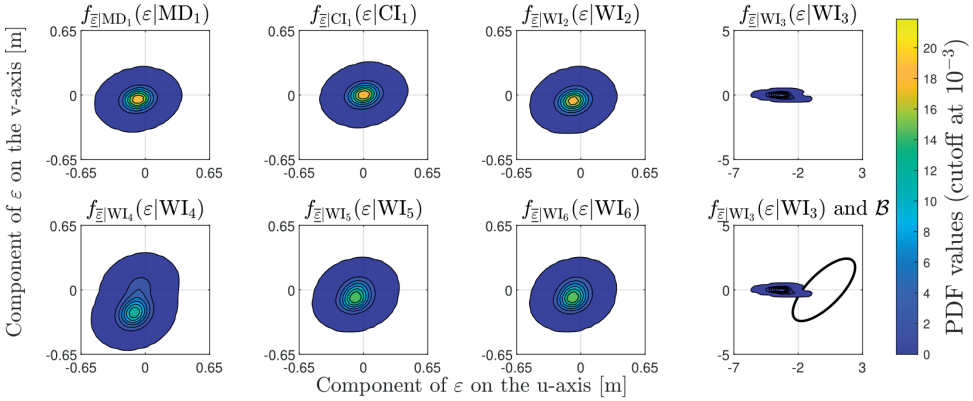

Figure 3.6: Components of $f_{\underline{\varepsilon}}(\varepsilon|\mathcal{H}_1)$ for $\alpha = 10^{-3}$, $\mathrm{b}_1 = -3$ [m/s^2], and $n_\nu = 10^6$ pseudo-random samples drawn from $f_{\underline{\nu}}(\nu|\mathcal{H}_1)$ (note the different scale of $f_{\underline{\varepsilon}|\mathrm{WI}_3}(\varepsilon|\mathrm{WI}_3)$). The last figure from the second-column is $f_{\underline{\varepsilon}|\mathrm{WI}_3}(\varepsilon|\mathrm{WI}_3)$ in relation with the safety region $\mathcal{B}$.

In the case of an alternative hypothesis such as $\mathcal{H}_1$, the shape of the conditional PDFs is also driven by the model misspecification. The term $\mathrm{H}^T\mathrm{L}_i\,\underline{\nu}$ with $\underline{\nu} \in \mathcal{P}_i$ and $\underline{\nu} \sim f_{\underline{\nu}}(\nu|\mathcal{H}_1)$ is distributed and shifted along the subspaces of $\mathbb{R}^2$ spanned by $\mathcal{R}\left(\mathrm{H}^T\mathrm{L}_i\mathrm{C}_1^*\right)$ for $i \in \{1,...,6\}$. This in turn impacts the modes of the conditional PDFs as a result of the averaging of the shifted functions $f_{\underline{\hat{\varepsilon}}_0}\left(\varepsilon + \mathrm{H}^T\mathrm{L}_i\,\nu|\mathcal{H}_1\right)$ according to (3.28). As Figure 3.6 shows, the impact of wrongly identifying $\mathcal{H}_3$, while $\mathcal{H}_1$ is valid, on the positioning safety of vehicle 1 will be largest. A similar analysis for the other $f_{\underline{\varepsilon}}(\varepsilon|\mathcal{H}_i)$ when $i \in \{2,4,5,6\}$ reveals that the positioning safety of vehicle 1 is also impacted most by the component corresponding to the wrong identification of $\mathcal{H}_3$. In the case of $f_{\underline{\varepsilon}}(\varepsilon|\mathcal{H}_3)$, the conditional component $f_{\underline{\varepsilon}|\mathrm{MD}_3}(\varepsilon|\mathrm{MD}_3)$ has the largest impact.

C.3 Total probability of positioning failure

The total probability of positioning failure $\mathbb{P}_{\mathcal{F}}(\mathbf{b})$ depends on $\mathbf{b} = \left\{\mathrm{b}_1,\ \mathrm{b}_2\ ,\ldots\ ,\mathrm{b}_{n_\mathcal{H}}\right\}$. By evaluating $\mathbb{P}_{\mathcal{F}}(\mathbf{b})$ over ranges of the model misspecifications one can obtain the worst-case scenario. First, we show the results of the computations for $\mathbb{P}_{\mathcal{F}}|\mathcal{H}_0$ and for the maximum $\mathbb{P}_{\mathcal{F}}|\mathcal{H}_i(\mathrm{b}_i)$ for $i \in \{1,...,n_\mathcal{H}\}$ in Table 3.5 over 100 simulations together with the determined Most Influential Component (MIC). We define the MIC to be the component which has the largest contribution, or is the most influential ($\mathrm{MIC}_\mathrm{E} = \mathsf{P}_\mathrm{E}\,\mathbb{P}_{\mathcal{F}}|\mathrm{E}$). The MICs are also useful to compare the safety-performance of different statistical hypothesis testing strategies (i.e., different choices of partitioning of $\mathbb{R}^m$).

In the case of $\underline{\mathbb{P}}_{\mathcal{F}}|\mathcal{H}_0$ the mean value of $1.3 \cdot 10^{-4} \pm 8.3 \cdot 10^{-7}$ is rather high considering [dm]-level positioning measurement and [cm]-level inter-vehicle distance measurements.

Table 3.5: Computed maximum probabilities of positioning failure over 100 simulations (μ_{sim} and σ_{sim}), worst-case biases per $\mathcal{H}_i$ for $i \in \{1, ..., n_{\mathcal{H}}\}$, and MICs.

Comp.	μ_{sim}	σ_{sim}	$\mathbf{b}$ [unit]	MIC
$\underline{\mathbb{P}}_{\mathcal{F}}\|\mathcal{H}_0$	$1.3 \cdot 10^{-4}$	$8.3 \cdot 10^{-7}$	-	MIC_{FA_3}
$\underline{\mathbb{P}}_{\mathcal{F}}\|\mathcal{H}_1(\text{b}_1)$	$1.9 \cdot 10^{-2}$	$1.1 \cdot 10^{-4}$	± 2.2 [m/s^2]	MIC_{WI_3}
$\underline{\mathbb{P}}_{\mathcal{F}}\|\mathcal{H}_2(\text{b}_2)$	$4.1 \cdot 10^{-4}$	$3.7 \cdot 10^{-6}$	± 1.5 [m/s^2]	MIC_{WI_3}
$\underline{\mathbb{P}}_{\mathcal{F}}\|\mathcal{H}_3(\text{b}_3)$	$8.3 \cdot 10^{-1}$	$3.4 \cdot 10^{-3}$	$\pm[2.1\ 0.0]^T$ [m]	MIC_{MD_3}
$\underline{\mathbb{P}}_{\mathcal{F}}\|\mathcal{H}_4(\text{b}_4)$	$4.8 \cdot 10^{-2}$	$1.5 \cdot 10^{-4}$	$\pm[0.3\ -0.9]^T$ [m]	MIC_{WI_3}
$\underline{\mathbb{P}}_{\mathcal{F}}\|\mathcal{H}_5(\text{b}_5)$	$4.9 \cdot 10^{-4}$	$4.5 \cdot 10^{-6}$	± 0.2 [m]	MIC_{WI_3}
$\underline{\mathbb{P}}_{\mathcal{F}}\|\mathcal{H}_6(\text{b}_6)$	$4.9 \cdot 10^{-4}$	$4.7 \cdot 10^{-6}$	± 0.2 [m]	MIC_{WI_3}

As an example, the MIC of $\underline{\mathbb{P}}_{\mathcal{F}}|\mathcal{H}_0$ is

$$\text{MIC}_{\text{FA}_3} = \mathsf{P}_{\text{FA}_3}\left(\int_{\mathcal{B}^c} f_{\underline{\varepsilon}|\text{FA}_3}(\varepsilon|\text{FA}_3)\, d\varepsilon\right) \tag{3.31}$$

with $f_{\underline{\varepsilon}|\text{FA}_3}(\varepsilon|\text{FA}_3) = \frac{\int_{p_3} f_{\underline{\varepsilon}_0}\left(\varepsilon + \text{H}^T \text{L}_3 \upsilon | \mathcal{H}_0\right) f_{\underline{\upsilon}}(\upsilon|\mathcal{H}_0) d\upsilon}{\mathsf{P}_{\text{FA}_3}}$ having the most probability density outside $\mathcal{B}$ across all of the components. This confirms the analysis done based on Figure 3.4 and of $\text{Q}_3^{-1} = \left[\left(\text{H}^T \text{L}_3\right) \text{Q}_{\upsilon\upsilon} \left(\text{L}_3^T \text{H}\right)\right]^{-1}$ from Table 3.3 and (3.30). Under $\mathcal{H}_3$, in the case of model misspecifications in the GNSS-based position measurements at [m]-level ($\pm[2.1\ 0.0]^T$ [m]) for vehicle 1, the maximum of the mean value of $\underline{\mathbb{P}}_{\mathcal{F}}|\mathcal{H}_3(\text{b}_3)$ is $8.3 \cdot 10^{-1} \pm 3.4 \cdot 10^{-3}$, which is also the largest across all components from Table 3.5. The result is expected since, among all alternative hypotheses $\mathcal{H}_{i \neq 0}$ considered, alternative hypothesis $\mathcal{H}_3$ specifically addresses model misspecifications in the position measurements of vehicle 1.

Once the maximum $\underline{\mathbb{P}}_{\mathcal{F}}|\mathcal{H}_i(\text{b}_i)$ for $i \in \{1, ..., n_{\mathcal{H}}\}$ are determined, the next step is to compute the worst-case total probability of positioning failure based on (3.17), in which the weights $\omega_i = \mathsf{P}(\mathcal{H}_i)$ have to be set. In line with the EKF update step of $\Delta t = 1$ [s], the a-priori $\mathsf{P}(\mathcal{H}_i)$ are chosen on a per second basis. The chosen values serve as examples based on several studies and existing standards: (i) $\mathsf{P}(\mathcal{H}_1) = \mathsf{P}(\mathcal{H}_2) = 10^{-6}$ which corresponds to harsh vehicle braking events while driving on highways [54], (ii) $\mathsf{P}(\mathcal{H}_3) = \mathsf{P}(\mathcal{H}_4) = 10^{-5}$ corresponds to a position error potentially due to a fault in the signal-in-space of a GNSS (e.g., GPS) satellite [55], (iii) $\mathsf{P}(\mathcal{H}_5) = \mathsf{P}(\mathcal{H}_6) = 10^{-5}$ represents an example of a probability of failure of the LiDAR according to a study in [56], and (iv) $\mathsf{P}(\mathcal{H}_0) = 1 - \sum_{i=1}^{n_{\mathcal{H}}} \mathsf{P}(\mathcal{H}_i) = 9.9996 \cdot 10^{-1}$. Using these assumptions and the results from Table 3.5, the worst-case scenario total probability of positioning failure is computed to be

$$\underline{\mathbb{P}}_{\mathcal{F}}(\mathbf{b}) = 1.4 \cdot 10^{-4} \pm 8.3 \cdot 10^{-7}. \tag{3.32}$$

In the case that safety requirements are established, (3.32) can be used to determine whether the requirements are met.

If, in the safety-analysis, one would *ignore* the dependence between parameter estimation and statistical hypothesis testing then the worst-case scenario total probability of

positioning failure would be based on (3.18) and (3.19), which gives

$$\underline{\mathbb{P}}^{o}_{\mathcal{F}}(\mathbf{b}) = 1.2 \cdot 10^{-5} \pm 4.5 \cdot 10^{-8}. \tag{3.33}$$

We notice that $\underline{\mathbb{P}}^{o}_{\mathcal{F}}(\mathsf{b})$ is lower than $\underline{\mathbb{P}}_{\mathcal{F}}(\mathsf{b})$ from (3.32) by approximately *an order of magnitude* (i.e., it provides a too optimistic assessment).

C.4 Verification of results

To verify the results from Table 3.5 we use a 'crude' Monte Carlo simulation to generate $n_\varepsilon = 10^5$ pseudo-random samples $\overline{\varepsilon}$ from $f_{\overline{\varepsilon}}(\varepsilon|\mathcal{H}_i)$ for $i \in \{0, ..., n_{\mathcal{H}}\}$. This approach corresponds to the simulation of the EKF and the DIA procedure a chosen number of times (in this case 100) for each hypothesis. Doing so, the probabilities of positioning failure can be computed for the worst-case scenario. The obtained results are shown in Table 3.6.

Table 3.6: Validation of results in Table 3.5 via standard Monte Carlo over 100 simulations (μ_{sim} and σ_{sim}).

Comp.	μ_{sim}	σ_{sim}	b [unit]
$\underline{\mathbb{P}}_{\mathcal{F}}\|\mathcal{H}_0$	$1.3 \cdot 10^{-4}$	$3.4 \cdot 10^{-6}$	-
$\underline{\mathbb{P}}_{\mathcal{F}}\|\mathcal{H}_1(\mathsf{b}_1)$	$1.9 \cdot 10^{-2}$	$4.1 \cdot 10^{-5}$	-2.2 [m/s^2]
$\underline{\mathbb{P}}_{\mathcal{F}}\|\mathcal{H}_2(\mathsf{b}_2)$	$4.2 \cdot 10^{-4}$	$6.9 \cdot 10^{-6}$	± 1.5 [m/s^2]
$\underline{\mathbb{P}}_{\mathcal{F}}\|\mathcal{H}_3(\mathsf{b}_3)$	$8.3 \cdot 10^{-1}$	$1.2 \cdot 10^{-4}$	$\pm$[-2.1 0.0]^T[m]
$\underline{\mathbb{P}}_{\mathcal{F}}\|\mathcal{H}_4(\mathsf{b}_4)$	$4.8 \cdot 10^{-2}$	$6.4 \cdot 10^{-5}$	$\pm$[0.3 -0.9]^T[m]
$\underline{\mathbb{P}}_{\mathcal{F}}\|\mathcal{H}_5(\mathsf{b}_5)$	$4.9 \cdot 10^{-4}$	$6.3 \cdot 10^{-6}$	± 0.2 [m]
$\underline{\mathbb{P}}_{\mathcal{F}}\|\mathcal{H}_6(\mathsf{b}_6)$	$4.9 \cdot 10^{-4}$	$6.9 \cdot 10^{-6}$	± 0.2 [m]

Next, the worst-case scenario total probability of failure is computed

$$\underline{\mathbb{P}}^{\text{MC}}_{\mathcal{F}}(\mathsf{b}) = 1.4 \cdot 10^{-4} \pm 3.4 \cdot 10^{-6}. \tag{3.34}$$

The results from Table 3.6 and (3.34) agree with those from Table 3.5 and (3.32) as the relative differences are below 3%.

3.4.4 Scenario with multiple configurations of the vehicles

In this simulation scenario, we study 14 distinct configurations of the two vehicles using the same simulation parameters from Table 2.1 and the previous a-priori probabilities of the hypotheses. Figure 3.7 provides a schematic representation of the configurations considered between vehicles 1 and 2. In these configurations, vehicle 2 is positioned at 14 equally spaced points along the center of its lane. For instance, in configuration 8, vehicle 2 is placed nearly parallel to vehicle 1.

Figure 3.8(a) presents the results of the worst-case probabilities of positioning failure, comparing the scenarios where the dependence between parameter estimation and statistical hypothesis testing is accounted for (blue) and where it is not (red). When vehicle 2 is positioned in its own lane, either behind or in front of vehicle 1, the worst-case $\underline{\mathbb{P}}_{\mathcal{F}}(\mathbf{b})$ is highest. This is because the conditional density $f_{\overline{\varepsilon}|\text{FA}_3}(\varepsilon|\text{FA}_3)$ becomes the main contributor. Figure 3.8(b) illustrates that for configurations 1, 10, and 14, the conditional density

$f_{\overline{\varepsilon}|\mathrm{FA}_3}(\varepsilon|\mathrm{FA}_3)$ has a large probability density outside the safety-region $\mathcal{B}$. In contrast for configuration 8, when the two vehicles are nearly parallel, most of the probability density lies within $\mathcal{B}$.

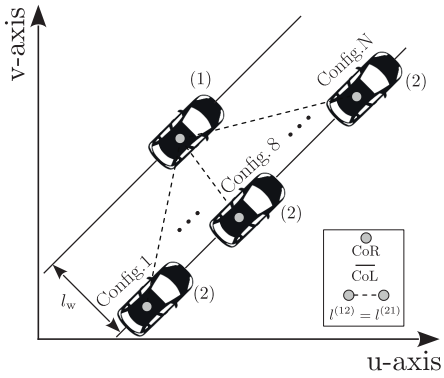

Figure 3.7: Schematic representation of the 2D geometry for the multiple configuration simulation scenario simulation scenario. Source: Adapted from [46].

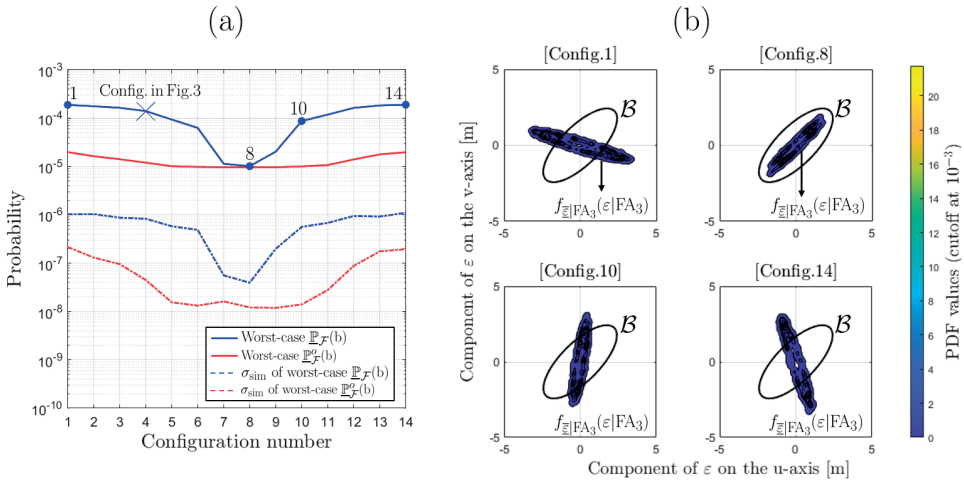

Figure 3.8: (a) Worst-case probabilities of positioning failure, and their simulation standard deviations, for the 14 configurations, showing the cases where the dependence between parameter estimations is considered (blue) and ignored (red); (b) Conditional PDF $f_{\overline{\varepsilon}|\mathrm{FA}_3}(\varepsilon|\mathrm{FA}_3)$ in relation to the safety region $\mathcal{B}$ of vehicle 1 for configurations 1, 8, 10 and 14.

The over-optimism resulting from ignoring the dependence between parameter estimation and statistical hypothesis testing is quantified in Figure 3.9 as the ratio of the worst-case results shown in blue and red in Figure 3.8(a). We observe that the ratio is large when vehicle 2 is positioned in its own lane, either behind or in front of vehicle 1. However, the ratio approaches 1 when the vehicles are nearly parallel.

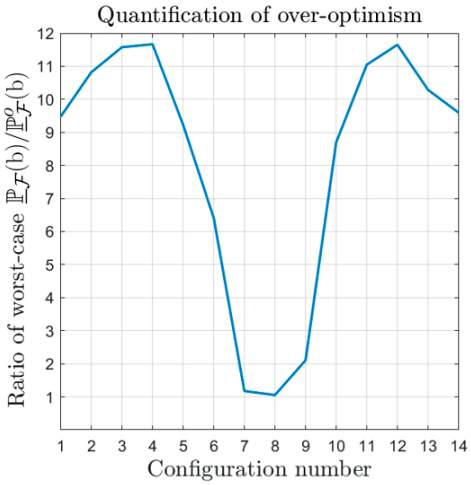

Figure 3.9: Ratio of the worst-case $\underline{\mathbb{P}}_{\mathcal{F}}(\mathbf{b})/\underline{\mathbb{P}}^{o}_{\mathcal{F}}(\mathbf{b})$ to quantify the over-optimism caused by ignoring the dependence between parameter estimation and statistical hypothesis testing.

Thus, ignoring the aforementioned dependence leads to an overly optimistic assessment, by an order of magnitude, of the worst-case total probability of positioning failure in most of the two-vehicle configurations shown in this scenario. This could result in wrongful positioning safety assessments, such as concluding that safety requirements or guidelines are met when they are not.

3.4.5 Computational resources

The computations were carried out on a Dell Latitude 7440 laptop, equipped with a 13th Gen Intel Core i7 processor with 10 physical cores and 16 GB of RAM. The system runs Windows 10 Enterprise, and the programming environment is MATLAB 2024a with the Parallel Computing Toolbox. The analyses utilized 10 physical cores of the processor, taking advantage of MATLAB's parallel computing capabilities. As an example, the computation time to obtain $\underline{\mathbb{P}}_{\mathcal{F}}|\mathcal{H}_0$ from Table 3.5 over 100 simulation repetitions for uncertainty quantification, was $\approx$ 5 minutes. Similarly, computing $\underline{\mathbb{P}}_{\mathcal{F}}|\mathcal{H}_i(\mathrm{b}_i)$ for a size of model missepecification was $\approx$ 5 to 7 minutes. These computation times could be reduced with access to more physical cores or by decreasing the number of independent simulation repetitions. They also depend on on the programming language and code implementation. The results shown in Figure 3.8(a) were generated using computational resources from the Delft High Performance Computing Centre (DHPC) [57].

3.5 Summary and Conclusions

This contribution addressed the dependence between parameter estimation and statistical hypothesis testing in automated/autonomous vehicle positioning safety analysis and quantified the consequences of neglecting this dependence. The positioning safety discussed in this article focuses on the design stage of positioning system (i.e., offline). At this stage, key

decisions are made regarding (i) measurement models, (ii) parameter estimation methods, (iii) statistical hypothesis testing procedures to account for model misspecifications (e.g., mismodeling of vehicle motion, outliers, or sensor measurement faults), and (iv) positioning scenarios for vehicles, among other factors. This approach aligns with the scenario-based safety assessment framework used for automated and autonomous vehicles [28–30]. Firstly, we have based the positioning safety analysis on the distributional theory for the DIA method which gave access to the PDFs conditioned on the statistical hypothesis testing decision outcomes [14]. Using these conditional PDFs, the probability of positioning failure was computed for a chosen safety region $\mathcal{B}$. The expression of the total probability of positioning failure considering a set of model misspecifications $\mathbf{b} = \left\{ \mathrm{b}_1, \mathrm{b}_2, \ldots, \mathrm{b}_{n_{\mathcal{H}}} \right\}$ is,

$$\mathbb{P}_{\mathcal{F}}(\mathbf{b}) = \sum_{a=0}^{n_{\mathcal{H}}} \omega_a \int_{\mathcal{B}^c} f_{\underline{\varepsilon}}(e|\mathcal{H}_a)\, de, \tag{3.35}$$

with

$$\begin{aligned} f_{\underline{\varepsilon}}(\varepsilon|\mathcal{H}_a) &= \sum_{i=0}^{n_{\mathcal{H}}} \int_{\mathcal{P}_i} f_{\underline{\hat{\varepsilon}}_i, \underline{v}}(\varepsilon, v|\mathcal{H}_a) dv \\ &= \sum_{i=0}^{n_{\mathcal{H}}} \int_{\mathcal{P}_i} f_{\underline{\hat{\varepsilon}}_0}\left(\varepsilon + \mathrm{H}^T \mathrm{L}_i v|\mathcal{H}_a\right) f_{\underline{v}}(v|\mathcal{H}_a) dv, \end{aligned} \tag{3.36}$$

where, in the case of $i = 0$, use has been made of the independence between the normally distributed $\underline{\hat{\epsilon}}_0$ and $\underline{v}$ [34]. It is important to note that $\underline{\hat{\epsilon}}_i$ and $\underline{v}$ are *dependent* since $f_{\underline{\hat{\epsilon}}_i, \underline{v}}(\epsilon, v) \neq f_{\underline{\hat{\epsilon}}_i}(\epsilon) f_{\underline{v}}(v)$ for $i \in \{1, \ldots, n_{\mathcal{H}}\}$ [14].

Using, as an example, a simulation scenario of two connected vehicles driving on a highway in a cooperative positioning setting, we have accounted in the motion model of the EKF (the CTRV model), for: (i) gentle acceleration or deceleration by setting the spectral density $q_{\ddot{\mathrm{s}}}^{(j)} = 0.250$ [m^2/s^3] corresponding to variations of 0.5 [m/s^2], and (ii) smooth lateral maneuvers (e.g., lane changes) by setting $q_{\ddot{\theta}}^{(j)} = 0.001$ [rad^2/s^3] corresponding to variations of 1.81 [deg/s^2], for both vehicles ($j \in \{1, 2\}$). In the measurement model of the EKF, the precision of the position measurements was set at 0.100 [m] (indicative of DGNSS) and for the inter-vehicle distance measurements at 0.050 [m] (indicative of an automotive-grade LiDAR system). Based on this setup, we have carried out a positioning safety analysis for vehicle 1 by computing the total probability of positioning failure for a worst case-scenario at a single-epoch. To achieve this we have computed first the conditional probabilities of positioning failure under each considered hypothesis where: (i) $\mathcal{H}_0$ is the null hypothesis, (ii) $\mathcal{H}_1$ and $\mathcal{H}_2$ account for 1D unmodelled longitudinal accelerations or decelerations of vehicle 1 and vehicle 2, (iii) $\mathcal{H}_3$ and $\mathcal{H}_4$ account for 2D model misspecifications in the position measurements of vehicles 1 and 2, and (iv) $\mathcal{H}_5$ and $\mathcal{H}_6$ account for 1D model misspecifications in the inter-vehicle distance measurements from both vehicles. The results were shown in Table 3.5, and their validation was presented in Table 3.6, the relative biases between them being below 3%. Next, assumptions were made on the a-priori probabilities of the hypotheses occurrence $\omega_i = \mathsf{P}(\mathcal{H}_i)$, for $i \in \{0, \ldots, 6\}$, to compute the worst-case total probability of positioning failure

$$\underline{\mathbb{P}}_{\mathcal{F}}(\mathbf{b}) = 1.4 \cdot 10^{-4} \pm 8.3 \cdot 10^{-7}. \tag{3.37}$$

This result shows that, in this scenario and the considered models and assumptions, even in a setup of [dm]-level vehicle positioning via a combined EKF and DIA method, the probability is rather large compared to what is considered to be desirable for automotive applications (e.g., [5]).

Secondly, we have considered the case when the dependence between parameter estimation and statistical hypothesis testing is *ignored*. In this situation, the evaluation of (3.35) is based on the following PDFs

$$f_{\underline{\hat{\epsilon}}^o}(\varepsilon|\mathcal{H}_a) = \sum_{a=0}^{n_{\mathcal{H}}} f_{\underline{\hat{\epsilon}}_i}(\varepsilon|\mathcal{H}_a) \int_{\mathcal{P}_i} f_{\underline{v}}(v|\mathcal{H}_a) dv. \tag{3.38}$$

where $f_{\underline{\hat{\epsilon}}_i,\underline{v}}(\epsilon, v) = f_{\underline{\hat{\epsilon}}_i}(\epsilon) f_{\underline{v}}(v)$ for $i \in \{0, ..., n_{\mathcal{H}}\}$. The resulting worst-case total probability of positioning failure is

$$\underline{\mathbb{P}}^o_{\mathcal{F}}(\mathbf{b}) = 1.2 \cdot 10^{-5} \pm 4.5 \cdot 10^{-8}, \tag{3.39}$$

which is approximately one order of magnitude *lower* than $\underline{\mathbb{P}}_{\mathcal{F}}(\mathbf{b})$ in (3.37). Furthermore, we have extended the positioning safety-analyses by considering multiple configurations between the two vehicles. For most of the configurations the worst-case scenario $\underline{\mathbb{P}}^o_{\mathcal{F}}(\mathbf{b})$ is overly-optimistic. Therefore, ignoring the dependence between parameter estimation and statistical hypothesis testing can result in wrongful positioning safety assessments, such as concluding that safety requirements or guidelines are met when they are not. The conclusion about the consequence of ignoring the aforementioned dependence is consistent with existing research from various other disciplines such as, mathematical statistics, econometrics, and signal processing ([17–24]). We also note that addressing more complex vehicle scenarios—planned as future work—will increase the dimensionality of vector spaces (e.g., the predicted residual space $\mathbb{R}^m$ if additional sensors are used in the vehicle's positioning system), and therefore an increase in the computation times to determine the probability of positioning failure. While these computations are expected to remain feasible offline within a scenario-based safety framework, future work includes also studying computation times for more complex scenarios.

Below we provide several remarks and recommendations regarding positioning safety analyses:

- Any procedure which uses parameter or state estimation and statistical hypothesis testing should consider the dependence between them either through a rigorous theoretical framework or through conservative assumptions which ensure that the conditional PDFs are overbounded with simpler PDFs (e.g., normal distributions).
- We recommend the *distributional theory for the DIA method*, a theoretical framework that rigorously addresses the aforementioned dependence and which gives access to the PDFs conditioned on the statistical hypothesis testing outcome [14].
- The probability of positioning failure should be formulated based on the conditional PDFs. Doing so, a component-wise positioning safety analysis starting from (3.17) is made possible.

- If a quantity requires numerical simulation (e.g., via Monte Carlo methods) such as the probabilities in (3.13)-(3.15) or the probabilities of positioning failure in (3.35), the simulation uncertainty (e.g., simulation standard deviation) should be quantified and reported.

BIBLIOGRAPHY

[1] P. J. G. Teunissen and O. Montenbruck, editors. *Springer Handbook of Global Navigation Satellite Systems*. Springer, 2017.

[2] Y. T. J. Morton et al., editors. *Position, Navigation, and Timing Technologies in the 21st Century: Integrated Satellite Navigation, Sensor Systems, and Civil Applications*. Wiley, IEEE Press, 2020.

[3] H. Jing, Y. Gao, S. Shahbeigi, and M. Dianati. Integrity Monitoring for GNSS/INS Based Positioning Systems for Autonomous Vehicles: State-of-the-Art and Open Challenges. *IEEE Transactions on Intelligent Transportation Systems*, 23(9):14166–14187, 2022.

[4] RTCA-Special Committee 159. Minimum Operational Performance Standards (MOPS) for Global Positioning System/Satellite-Based Augmentation System Airborne Equipment. Do-229f, Radio Technical Commission for Aeronautics, 2020.

[5] T. G. R. Reid, S. Houts, R. Cammarata, et al. Localization Requirements for Autonomous Vehicles. *SAE International Journal of Connected and Automated Vehicles*, 2019.

[6] K. Jin, H. Kim, S. Ryu, S. Kim, and J. Park. An Approach to Constructing Effective Training Data for a Classification Model to Evaluate the Reliability of a Passive Safety System. *Reliability Engineering and System Safety*, 222:108446, 2022.

[7] V. Chabridon, M. Balesdent, J.-M. Bourinet, J. Morio, and N. Gayton. Evaluation of Failure Probability Under Parameter Epistemic Uncertainty: Application to Aerospace System Reliability Assessment. *Aerospace Science and Technology*, 69:526–537, 2017.

[8] M. Shinozuka. Basic Analysis of Structural Safety. *Journal of Structural Engineering*, 109(3):721–740, 1983.

[9] J. Blanch et al. Baseline Advanced RAIM User Algorithm and Possible Improvements. *IEEE Transactions on Aerospace and Electronic Systems*, 51(1):713–732, 2015.

[10] Working Group C. Advanced RAIM Technical Subgroup Reference Airborne Algorithm Description Document. Technical report, 2019.

[11] P. Zhao et al. A New Method to Bound the Integrity Risk for Residual-Based ARAIM. *IEEE Transactions on Aerospace and Electronic Systems*, 57(2):1378–1385, 2020.

[12] N. Zhu et al. GNSS Position Integrity in Urban Environments: A Review of Literature. *IEEE Transactions on Intelligent Transportation Systems*, 19(9):2762–2778, 2018.

[13] G. Gottschalg et al. Integrity Concept for Sensor Fusion Algorithms Used in a Prototype Vehicle for Automated Driving. In *European Navigation Conference*, pages 1–10, 2020.

[14] P. J. G. Teunissen. Distributional Theory for the DIA Method. *Journal of Geodesy*, 92(1):59–80, 2018.

[15] S. Zaminpardaz, P. J. G. Teunissen, and C. C. J. M. Tiberius. Risking to Underestimate the Integrity Risk. *GPS Solutions*, 23(29):1–16, 2019.

[16] S. Zaminpardaz and P. J. G. Teunissen. On the Computation of Confidence Regions and Error Ellipses: A Critical Appraisal. *Journal of Geodesy*, 96(10):1–18, 2022.

[17] T. A. Bancroft. On Biases in Estimation Due to the Use of Preliminary Tests of Significance. *Annals of Mathematical Statistics*, 15(2):190–204, 1944.

[18] S. Sarkadi. Estimation After Selection. *Studia Scientiarum Mathematicarum Hungarica*, pages 341–350, 1967.

[19] N. L. Hjort and G. Claeskens. Frequentist Model Average Estimators. *Journal of the American Statistical Association*, 98(464):879–899, 2003.

[20] S. T. Buckland, K. P. Burnham, and N. H. Augustin. Model Selection: An Integral Part of Inference. *Biometrics*, 53(2):603–618, 1997.

[21] H. Leeb and B. M. Pötscher. The Finite-Sample Distribution of Post-Model-Selection Estimators and Uniform Versus Nonuniform Approximations. *Econometric Theory*, 19(1):100–142, 2003.

[22] H. Leeb and B. M. Pötscher. Model Selection and Inference: Facts and Fiction. *Econometric Theory*, 21(1):21–59, 2005.

[23] D. Danilov and J. R. Magnus. On the Harm That Ignoring Pretesting Can Cause. *Journal of Econometrics*, 122(1):27–46, 2004.

[24] T. Routtenberg and L. Tong. Estimation After Parameter Selection: Performance Analysis and Estimation Methods. *IEEE Transactions on Signal Processing*, 64(20):5268–5281, 2016.

[25] C. Rose, J. Britt, and D. Bevly. An Integrated Vehicle Navigation System Utilizing Lane-Detection and Lateral Position Estimation Systems in Difficult Environments for GPS. *IEEE Transactions on Intelligent Transportation Systems*, 15(6):2615–2629, 2014.

[26] P. J. G. Teunissen. Least-Squares Estimation and Kalman Filtering. In P. J. G. Teunissen and O. Montenbruck, editors, *Springer Handbook of Global Navigation Satellite Systems*, chapter 22, pages 639–660. Springer, 2017.

[27] I. Gillissen and I. A. Elema. Test Results of DIA: A Real-Time Adaptive Integrity Monitoring Procedure, Used in an Integrated Navigation System. *International Hydrographic Review*, 73(1):75–103, 1996.

[28] S. Riedmaier et al. Survey on Scenario-Based Safety Assessment of Automated Vehicles. *IEEE Access*, 8:87456–87477, 2020.

[29] U.N.E.C.E. New Assessment/Test Method for Automated Driving (NATM) Guidelines for Validating Automated Driving Systems (ADS). Technical report, United Nations Economic Commission for Europe - Inland Transport Committee, 2023.

[30] E. de Gelder et al. TNO Street Wise: Scenario-Based Safety Assessment of Automated Driving Systems. White paper, Netherlands Organisation for Applied Scientific Research (TNO), 2024.

[31] P. J. G. Teunissen. Batch and Recursive Model Validation. In P. J. G. Teunissen and O. Montenbruck, editors, *Springer Handbook of Global Navigation Satellite Systems*, chapter 24, pages 687–720. Springer, 2017.

[32] W. Baarda. A Testing Procedure for Use in Geodetic Networks. *Publications on Geodesy of Netherlands Geodetic Commission*, 9(5):1–97, 1968.

[33] M. A. Salzmann. *Least Squares Filtering and Testing for Geodetic Navigation Applications*, volume 37 of *Publications on Geodesy of Netherlands Geodetic Commission*. 1993.

[34] P. J. G. Teunissen and A. Khodabandeh. BLUE, BLUP and the Kalman Filter: Some New Results. *Journal of Geodesy*, 87(5):461–473, 2013.

[35] S. Zaminpardaz and P. J. G. Teunissen. Detection-only versus Detection and Identification of Model Misspecifications. *Journal of Geodesy*, 97(55):1–19, 2023.

[36] T. L. Willke, P. Tientrakool, and N. F. Maxemchuk. A Survey of Inter-Vehicle Communication Protocols and Their Applications. *IEEE Communications Surveys and Tutorials*, 11(2):3–20, 2009.

[37] M. Boban and P. M. d'Orey. Exploring the Practical Limits of Cooperative Awareness in Vehicular Communications. *IEEE Transactions on Vehicular Technology*, 65(6):3904–3916, 2016.

[38] S. Sivaraman and M. M. Trivedi. Looking at Vehicles on the Road: A Survey of Vision-Based Vehicle Detection, Tracking, and Behavior Analysis. *IEEE Transactions on Intelligent Transportation Systems*, 14(4):1773–1795, 2013.

[39] X. Rong Li and V. P. Jilkov. Survey of Maneuvering Target Tracking. Part I: Dynamic Models. *IEEE Transactions on Aerospace and Electronic Systems*, 39(4):1333–1364, 2003.

[40] M. Tsogas, A. Polychronopoulos, and A. Amditis. Unscented Kalman Filter Design for Curvilinear Motion Models Suitable for Automotive Safety Applications. In *Proceedings of the 7th IEEE International Conference on Information Fusion*, 2005.

[41] R. Schubert, E. Richter, and G. Wanielik. Comparison and Evaluation of Advanced Motion Models for Vehicle Tracking. In *Proceedings of the 11th IEEE International Conference on Information Fusion*, 2008.

[42] P. J. G. Teunissen. *Dynamic Data Processing: Recursive Least-Squares*. Mathematical Geodesy and Positioning. Delft University Press, 2001.

[43] S. Verhagen and P. J. G. Teunissen. Least-Squares Estimation and Kalman Filtering. In P. J. G. Teunissen and O. Montenbruck, editors, *Springer Handbook of Global Navigation Satellite Systems*, chapter 22, pages 639–660. Springer, 2017.

[44] European Commission. European Road Safety Report: Motorways. Technical report, 2018. Available online: https://road-safety.transport.ec.europa.eu/system/files/2021-07/ersosynthesis2018-motorways.pdf.

[45] The International Council on Clean Transportation. European Vehicle Market Statistics: Pocketbook 2022-23. Technical report, 2023.

[46] Wikimedia Commons. Citroen C3, top. Available at https://commons.wikimedia.org/wiki/File:C3top.png#file.

[47] G. Genta. Motor Vehicle Dynamics: Modelling and Simulation. In *Series of Advances in Mathematics for Applied Sciences*, volume 43, chapter 4, pages 171–178. 1997.

[48] A. Kealy and T. Moore. Land-Based Applications of GNSS. In P. J. G. Teunissen and O. Montenbruck, editors, *Springer Handbook of Global Navigation Satellite Systems*, chapter 29.1, pages 841–856. Springer, 2017.

[49] Y. Feng, C. Wang, and C. Karl. Determination of Required Positioning Integrity Parameters for Design of Vehicle Safety Applications. In *Proceedings of the 2018 International Technical Meeting of the Institute of Navigation*, pages 129–141, 2018.

[50] O. N. Kigotho and J. H. Rife. Comparison of Rectangular and Elliptical Alert Limits for Lane-Keeping Applications. In *Proceedings of the 34th International Technical Meeting of the Satellite Division of the Institute of Navigation GNSS+*, pages 93–104, 2021.

[51] S. N. Afriat. Orthogonal and Oblique Projectors and the Characterization of Pairs of Vector Spaces. *Mathematical Proceedings of the Cambridge Philosophical Society*, 53(4):800–816, 1957.

[52] Å. Björck and G. H. Golub. Numerical Methods for Computing Angles Between Linear Subspaces. *Mathematics of Computation*, 27(123):579–594, 1973.

[53] A. V. Knyazev and M. E. Argentati. Principal Angles Between Subspaces in an A-Based Scalar Product: Algorithms and Perturbation Estimates. *SIAM Journal on Scientific Computing*, 23(6):2008–2040, 2002.

[54] J. Martins et al. Defining a Braking Probability to Estimate Extreme Braking Forces on Road Bridges. In *12th International Conference on Applications of Statistics and Probability in Civil Engineering (ICASP12)*, 2015.

[55] U.S. Department of Defense. GPS Standard Positioning Service Performance Standard. Technical report, 2020.

[56] A. Richter et al. Components and Their Failure Rates in Autonomous Driving. In *Proceedings of the 33rd European Safety and Reliability Conference (ESREL)*, 2023.

[57] Delft High Performance Computing Centre. Delft supercomputer (phase 1). Technical report, 2022.

4

Probability of Positioning Failure for UAVs in Multiple Authorized European Airspace Regions

Unmanned Aerial Vehicles (UAVs) support, or are planned to support, a wide range of operations, including emergency response, environmental research, urban air mobility, and (commercial) air transportation, where positioning safety is paramount. This contribution presents an approach for assessing positioning safety of UAVs by computing the probability of positioning failure while accounting for time-varying positioning models. The probability of positioning failure is defined as the probability that the UAV position estimator falls outside a designated safety-region. For the computation of this probability, we use a recently published method, developed in earlier work based on principles from rare event simulation, specifically Importance Sampling and the Cross-Entropy method. Our analysis focuses on the design stage of the positioning algorithms, as this facilitates key decisions about measurement models, position or state estimation algorithms, and statistical hypothesis testing procedures. In this contribution, we apply these principles to evaluate the positioning safety of UAVs in authorized European airspace regions across eight countries, using real GPS satellite orbit data. The UAVs' GPS receivers are set to achieve positioning performance comparable to Technical Standard Order (TSO)-certified GPS receivers. The probability of positioning failure is calculated every 5 minutes over a 24-hour period and aggregated into 1-hour intervals for analysis. The resulting values are then compared to the requirements for Specific Assurance and Integrity Levels (SAIL) 3 and 4 for en-route operations over a 1-hour period. This analysis framework supports use cases such as verifying positioning algorithm compliance, developing positioning safety requirements, and for vertiport operations and design.

This chapter is based on the journal article *S. Ciuban, C. Yin, P.J.G. Teunissen, and C.C.J.M. Tiberius. "Probability of Positioning Failure for UAVs in Multiple Authorized European Airspace Regions", IEEE Transactions on Vehicular Technologies, Submitted.*

4.1 Introduction

Unmanned Aerial Vehicles (UAVs) support, or are planned to support, a wide range of operations, including emergency response, search and rescue, forest fire monitoring, flood mapping, environmental research, urban air mobility, and (commercial) transportation [1–3]. Given the essential role of the positioning (or localization) function of the UAVs in performing these diverse operations effectively and safely, recent research has focused on enhancing their positioning performance [4–8]. The position coordinates of the UAVs can be estimated based on technologies such as Global Navigation Satellite Systems (GNSS), Terrestrial Networked Positioning Systems (TNPS), along with other sensors such as inertial measurement units, cameras, LiDAR [9–11]. Once a position estimator $\underline{\hat{x}} \in \mathbb{R}^n$ is formulated based on measurements from the positioning technology and/or sensors, and its probability density function (PDF) $f_{\underline{\hat{x}}}(x)$ is obtained, the UAV's positioning safety can be assessed through the *probability of positioning failure*

$$\mathbb{P}_{\mathcal{F}} = \mathsf{P}(\underline{\hat{x}} \in \mathcal{B}^c) = \int_{\mathcal{B}^c} f_{\underline{\hat{x}}}(x)\, dx, \tag{4.1}$$

where $\mathcal{F} = \{\underline{\hat{x}} \in \mathcal{B}^c\}$ is the event of positioning failure [12], $\mathcal{B}^c \subset \mathbb{R}^n$ is the complement of a chosen safety-region $\mathcal{B} \subset \mathbb{R}^n$ around the UAV. The obtained probability of positioning failure can be compared against the target requirement or guideline to determine whether it is met. For example, recent efforts have aimed to propose positioning safety requirements for GNSS/GPS receivers used by UAVs [13, 14].

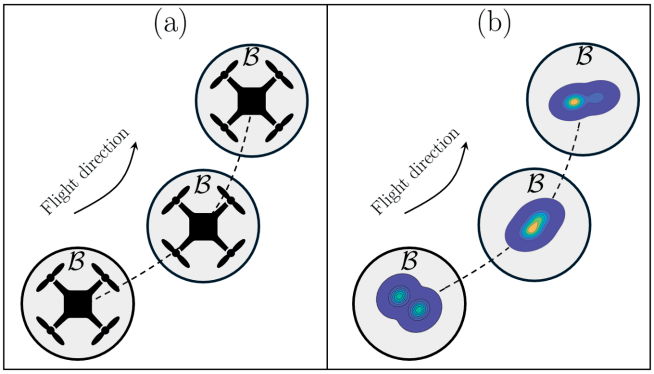

Figure 4.1: Illustration of a UAV flight and the contours of the PDF $f_{\underline{\hat{x}}}(x)$ of the UAV's position estimator $\underline{\hat{x}} \in \mathbb{R}^{n=2}$. (a) UAV flying along its trajectory at successive time steps, enclosed in the safety region $\mathcal{B} \subset \mathbb{R}^{n=2}$; (b) Contours of the corresponding (multimodal) PDF of the position estimator. The contour plots use a blue-to-yellow color scale, where blue indicates low and yellow indicates high probability density.

As illustrated in Fig.4.1, the PDF $f_{\underline{\hat{x}}}(x)$ of the UAV's position estimator evolves over time. Hence, capturing the time-varying functional and stochastic models in the computation of positioning failure probability is essential for safety assessments of positioning systems and algorithms. However, the computation of (4.1) is a challenging task, primarily due to: (i) the PDF $f_{\underline{\hat{x}}}(x)$ generally being *multimodal*, as the position estimator $\underline{\hat{x}} \in \mathbb{R}^n$ often results from a combined parameter (or state) estimation and statistical hypothesis testing

procedure to accommodate for model misspecifications (e.g., due to outliers in measurements) [1, 9, 15]—the dependence captured in the theoretical framework introduced in [16]; in recent work, we have shown that neglecting this dependence between parameter estimation and statistical hypothesis testing can lead to overly optimistic values of $\mathbb{P}_{\mathcal{F}}$, up to one order of magnitude lower across several scenarios for automated and autonomous vehicles [17]; (ii) the requirement for the positioning failure event $\mathcal{F} = \{\underline{\mathrm{x}} \in \mathcal{B}^c\}$ to be rare to meet stringent positioning safety requirements (e.g., $\mathbb{P}_{\mathcal{F}} < 10^{-5}$ [12–14]). We have addressed these challenges in recently published work by developing a method based on rare event simulation principles [18]. Specifically, the method (i) exploits the structure of the position estimator's PDF $f_{\underline{\mathrm{x}}}(x)$ through its conditional components; (ii) applies Importance Sampling and the Cross-Entropy method to estimate rare-event probabilities [19, 20]; and (iii) quantifies the associated uncertainties. Designed for use at the design stage of positioning algorithms, the approach supports decisions regarding (i) measurement models based on positioning technologies and sensors of choice, (ii) parameter estimation methods for the position vector, (iii) statistical hypothesis testing procedures to accommodate for model misspecifications, and (iv) positioning scenarios for vehicles, among other factors. This approach aligns with the scenario-based safety assessment framework commonly applied to automated and autonomous vehicles [21–23] and is also suitable for UAVs [24].

Compared to earlier work, where the method was introduced and demonstrated at a single time snapshot for a scenario involving an automated and autonomous vehicle with different orientations [18], the present study takes a step further and considers more complex scenarios that incorporate the time variation of both the positioning functional and the stochastic model in computing the probability of positioning failure. To this end, we demonstrate its applicability to simulation-based positioning-safety analysis for UAVs across multiple authorized European airspace regions: 1-Portugal, 2-Ireland, 3-Netherlands, 4-Norway, 5-Finland, 6-Romania, 7-Austria, and 8-Italy. The information about the locations of the authorized airspace regions within the chosen countries is provided by the European Union Aviation Safety Agency (EASA) [25]. In these airspace regions, which have open-sky conditions, we carry out positioning-safety analyses based on the UAVs' GPS receiver, set to achieve positioning performance similar to GPS receivers that have received Technical Standard Order (TSO) certification for GPS-based UAV positioning [13, 26]. We use real GPS precise satellite orbits from the International GNSS Service (IGS) over a 24-hour period to account for changes in satellites overpasses throughout the day [27]. We then compute the instantaneous probability of positioning failure, $\mathbb{P}_{\mathcal{F}}$, every 5 minutes, with this interval chosen due to the slow variations in the geometry between the UAVs' GPS receiver and GPS satellites at their altitude of approximately 20.000 km. Consequently, the results are representative of the satellite–receiver geometry across the selected regions. Next, we compare the obtained results with the preliminary requirements for Specific Assurance and Integrity Levels (SAIL) 3 and 4 for en-route operations, as specified in [14], and determine the percentage of UAVs' start flight times for which the requirements are met over the following hour. This type of positioning-safety analysis can be useful in various cases, such as: (i) verifying whether positioning algorithms for UAVs are meeting safety requirements, (ii) developing positioning safety requirements for various UAV applications such as the ones mentioned in the introduction, (iii) helping vertiport operators and designers deter-

mine the expected probabilities of positioning failures of the UAVs at the desired locations, and times of operations. Although the current positioning-safety analysis is based on the UAVs' GPS receiver, the proposed approach for formulating and computing the probability of positioning failure is also applicable to UAV multisensor positioning, which represents a topic for future work.

This contribution is organized as follows: In Section 3.2 we briefly review the main principles of the combined parameter estimation and statistical hypothesis testing to obtain the UAVs' position estimator $\underline{\hat{x}} \in \mathbb{R}^n$ and PDF $f_{\underline{\hat{x}}}(x)$. In Section 3.3 we present the formulation of the probability of positioning failure, its conditional components, and the main principles of the method for their computation. Section 3.4 presents the positioning-safety analysis by applying the computation method in [18] for UAVs operating in multiple authorized European airspace regions, and interpreting and discussing the results. Section 3.5 contains summary and conclusions of this contributions while suggesting several directions for future work.

Throughout the paper we make use of the following notation: an underscore denotes a random quantity (e.g., the random vector $\underline{y} \in \mathbb{R}^m$), $f_{\underline{y}}(y)$ is the PDF of $\underline{y} \in \mathbb{R}^m$, and $\mathsf{E}_{f_{\underline{y}}}(\underline{y}) = \int_{\mathbb{R}^m} y f_{\underline{y}}(y) dy$ is the expected value of $\underline{y} \in \mathbb{R}^m$. The joint PDF of two random vectors $\underline{x} \in \mathbb{R}^n$ and $\underline{y} \in \mathbb{R}^m$ is denoted $f_{\underline{x},\underline{y}}(x, y)$. A projection matrix is denoted as $\mathbf{\Pi}_{\mathrm{A}}$ and it projects orthogonally (w.r.t. some metric) onto the range space of the matrix $\mathrm{A} \in \mathbb{R}^{m \times n}$ ($\mathcal{R}(\mathrm{A})$). For the weighted squared norm of a vector we use the notation $\|\underline{y}\|^2_{\mathrm{Q}_{yy}} = \underline{y}^T \mathrm{Q}_{yy}^{-1} \underline{y}$. If the squared norm is w.r.t. the identity matrix then it is denoted $\|.\|^2$. A normal PDF is denoted as $\mathcal{N}(.,.)$, a chi-squared PDF as $\chi^2(.,.)$, and a uniform PDF as $\mathcal{U}(.,.)$.

4.2 Review of Combined Estimation and Hypothesis Testing Principles in Positioning

In this section we briefly review the principles of *combined* parameter estimation and statistical hypothesis testing as introduced in [16]. Assuming a linear(ized) observation model for positioning (e.g., using GNSS-based observations for UAV positioning) with normally distributed observables, $\underline{y} \in \mathbb{R}^m \sim \mathcal{N}\left(\mathsf{E}_{f_{\underline{y}}}(\underline{y}), \mathrm{Q}_{yy}\right)$ [28, 29], we formulate the following multiple hypothesis testing problem

$$\mathcal{H}_0 : \mathsf{E}_{f_{\underline{y}}}(\underline{y}) = \mathrm{A}x \quad \text{vs.} \quad \mathcal{H}_{i\neq 0} : \mathsf{E}_{f_{\underline{y}}}(\underline{y}) = \mathrm{A}x + \mathrm{C}_i b_i, \tag{4.2}$$

where $\mathrm{A} \in \mathbb{R}^{m \times n}$ is the design matrix with $\mathrm{rank}(\mathrm{A}) = n$, $x \in \mathbb{R}^n$ is the vector of unknown parameters, and $\mathrm{Q}_{yy} \in \mathbb{R}^{m \times m}$ is the symmetric positive definite variance-covariance (vc)-matrix of $\underline{y} \in \mathbb{R}^m$. We consider k alternative hypotheses with index $i \in \{1, ..., k\}$, $\mathrm{C}_i \in \mathbb{R}^{m \times q_i}$ models the type of model misspecification which is anticipated to occur (e.g., outliers in observables, GNSS satellite failure), $\mathrm{rank}([\mathrm{A}, \mathrm{C}_i]) = n + q_i$, $b_i \in \mathbb{R}^{q_i}$ is the size of the model misspecification which is unknown, and $1 \leq q_i \leq r$ for $i > 0$ (to allow for parameter estimation under $\mathcal{H}_{i\neq 0}$) with $r = m - n$ being the redundancy of $\mathcal{H}_0$. We use the misclosure vector $\underline{t} \in \mathbb{R}^r$ to build test statistics for the decision problem in (4.2), as it provides a measure of inconsistency between the model under $\mathcal{H}_0$ and the observables. The expressions of

$\underline{t} \in \mathbb{R}^r$ and of its vc-matrix $Q_{tt} \in \mathbb{R}^{r\times r}$ are [30]

$$\underline{t} = B^T \underline{y}, \quad Q_{tt} = B^T Q_{yy} B, \tag{4.3}$$

where $B \in \mathbb{R}^{m\times r}$ is a basis matrix of $\mathcal{R}(A)^\perp$ (i.e., $B^T A = 0_{r\times n}$). It is possible to link the Best Linear Unbiased Estimators (BLUEs) of $x \in \mathbb{R}^n$ under the alternative hypotheses $\mathcal{H}_{i\neq 0}$'s and under the null hypothesis $\mathcal{H}_0$ using the misclosure vector $\underline{t} \in \mathbb{R}^r$ as follows [16]

$$\begin{bmatrix} \underline{\hat{x}}_i \\ \underline{t} \end{bmatrix} = \underbrace{\begin{bmatrix} I_n & -L_i \\ 0_{r\times n} & I_r \end{bmatrix}}_{V_i} \begin{bmatrix} \underline{\hat{x}}_0 \\ \underline{t} \end{bmatrix}, \text{ with } L_i = \begin{cases} 0_{n\times r} & , i = 0 \\ A^+ C_i C_{t_i}^+ & , i > 0 \end{cases} \tag{4.4}$$

where $\underline{\hat{x}}_0 = A^+ \underline{y}$, $A^+ = Q_{\hat{x}_0\hat{x}_0} A^T Q_{yy}^{-1}$ is the BLUE-inverse of $A \in \mathbb{R}^{m\times n}$, and $Q_{\hat{x}_0\hat{x}_0} = (A^T Q_{yy}^{-1} A)^{-1}$ is the variance-covariance of $\underline{\hat{x}}_0$. The BLUE-inverse of $C_{t_i} = B^T C_i$ is $C_{t_i}^+ = (C_{t_i}^T Q_{tt}^{-1} C_{t_i})^{-1} C_{t_i}^T Q_{tt}^{-1}$. The transformation in (4.4) is in block-triangular form and its inverse is $V_i^{-1} = \begin{bmatrix} I_n & L_i \\ 0_{r\times n} & I_r \end{bmatrix}$. The joint PDF of $\left[\underline{\hat{x}}_i^T \ \underline{t}^T\right]^T$, under a hypothesis $\mathcal{H}_a$, is

$$\mathcal{H}_a : \begin{bmatrix} \underline{\hat{x}}_i \\ \underline{t} \end{bmatrix} \sim \mathcal{N}\left(\begin{bmatrix} x + A^+ R_i C_a b_a \\ B^T C_a b_a \end{bmatrix}, \begin{bmatrix} Q_{\hat{x}_0\hat{x}_0} + L_i Q_{tt} L_i^T & -L_i Q_{tt} \\ -Q_{tt} L_i^T & Q_{tt} \end{bmatrix} \right), \tag{4.5}$$

where $R_i = I_m - C_i \left(B^T C_i\right)^+ B^T$ and $\left(B^T C_i\right)^+ = C_{t_i}^+$. The matrix R_i projects along $\mathcal{R}(C_i)$ and onto $\mathcal{R}(A, Q_{yy} B (B^T C_i)^\perp)$ with $(B^T C_i)^\perp$ being a basis matrix of the null space of $C_i^T B$. The hypothesis testing problem in (4.2) can be captured in the misclosure vector space $\mathbb{R}^r$ by applying partitioning principles. A partition of $\mathbb{R}^r$ can be formulated based on the subsets $\mathcal{P}_i \subset \mathbb{R}^r$, for $i \in \{0, ..., k\}$, such that $\cup_{i=0}^k \mathcal{P}_i = \mathbb{R}^r$, and $\mathcal{P}_i \cap \mathcal{P}_j = \{0\}$ for $i \neq j$. The $k+1$ partitions can be defined as follows,

$$\begin{aligned} \mathcal{P}_0 &= \left\{ t \in \mathbb{R}^r \mid \|t\|_{Q_{tt}}^2 \leq \chi_\alpha^2(r,0) \right\}, \\ \mathcal{P}_{i\neq 0} &= \left\{ t \in \mathbb{R}^r \mid t \notin \mathcal{P}_0, \ \check{T}_i = \max_{l\in\{1,...,k\}} T_l \right\}, \end{aligned} \tag{4.6}$$

where $\|\underline{t}\|_{Q_{tt}}^2$ is the overall model test statistic, $\chi_\alpha^2(r,0)$ is the Chi-squared critical value for a level of significance α, and $\underline{T}_l$ is the result of the following transformation [31–33]

$$\underline{T}_l = \mathrm{CDF}_{\chi^2(q_l,0)}\left(\|\Pi_{C_{t_l}} \underline{t}\|_{Q_{tt}}^2 \right), \tag{4.7}$$

where $\mathrm{CDF}_{\chi^2(q_l,0)}(.)$ is the cumulative distribution function (CDF) of $\chi^2(q_l,0)$, $\|\Pi_{C_{t_l}} \underline{t}\|_{Q_{tt}}^2 \overset{\mathcal{H}_0}{\sim} \chi^2(q_l,0)$, $\Pi_{C_{t_l}} = C_{t_l} C_{t_l}^+$ projects onto $\mathcal{R}(C_{t_l})$, and $C_{t_l} = B^T C_l$ while $C_{t_l}^+ = (C_{t_l}^T Q_{tt}^{-1} C_{t_l})^{-1} C_{t_l}^T Q_{tt}^{-1}$, and $\underline{T}_l \overset{\mathcal{H}_0}{\sim} \mathcal{U}(0,1)$. If the dimension of $b_l \in \mathbb{R}^{q_l}$ is the same across the alternative hypotheses (i.e., $q_l = q_j$ for $l \neq j$), then the transformation step in (4.7) is unnecessary and the maximum across $\|\Pi_{C_{t_l}} \underline{t}\|_{Q_{tt}}^2$ can be directly used. The role of the partitions is such that a hypothesis $\mathcal{H}_i$, for $i \in \{0, ..., k\}$, is selected as the most likely one if and only if $\underline{t} \in \mathcal{P}_i$. Note that an undecided

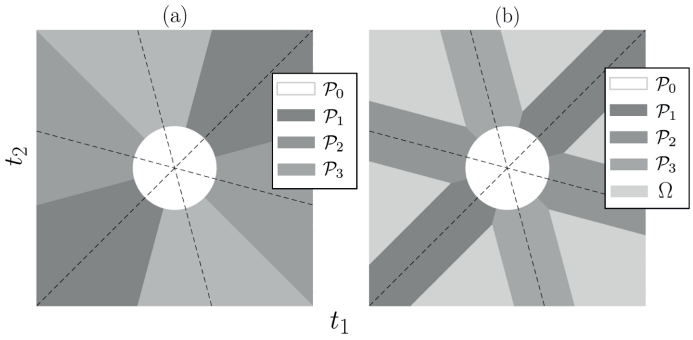

Figure 4.2: Partition of $\mathbb{R}^{r=2}$ when $\mathrm{A} = [1\ 1\ 1]^T$, $\mathrm{x} \in \mathbb{R}$, $\mathrm{Q_{yy}} = \mathrm{I}_3$, and $\mathrm{C}_i = \mathrm{c}_i$'s are the canonical unit vectors for $i = \{1, 2, 3\}$. The dashed lines are the spans of the vectors $\mathrm{B}^T \mathrm{c}_i$; (a) without undecided region $\Omega \subset \mathbb{R}^{r=2}$ included (b) with undecided region $\Omega \subset \mathbb{R}^{r=2}$ included.

4

region $\Omega \subset \mathbb{R}^r$ could also be included to accommodate for situations when it would be difficult to discriminate between hypotheses. An illustrative example of a partitioned misclosure vector space, with and without an undecided region $\Omega \subset \mathbb{R}^r$, is shown in Fig. 4.2.

In this contribution, we consider the partition of $\mathbb{R}^r$ as presented in (4.6) (i.e., no undecided region $\Omega \subset \mathbb{R}^r$ is included). Nevertheless, the presented approach is also applicable to partitions that include an undecided region, as well as to new partitioning strategies, as introduced in [34]. The Detection (D) Identification (I) and Adaptation (A) statistical testing procedure is then

$$\begin{cases} \text{if } \underline{\mathrm{t}} \in \mathcal{P}_0 \text{ (no Detection)} \rightarrow \text{ output } \underline{\hat{\mathrm{x}}}_0, \\ \text{if } \underline{\mathrm{t}} \notin \mathcal{P}_0 \text{ (Detection)} \rightarrow \underline{\mathrm{t}} \in \mathcal{P}_{i \neq 0} \text{ (Identification)} \rightarrow \text{ output } \underline{\hat{\mathrm{x}}}_i \text{ (Adaptation)}, \end{cases} \tag{4.8}$$

where $\underline{\hat{\mathrm{x}}}_0 \in \mathbb{R}^n$ and $\underline{\hat{\mathrm{x}}}_i \in \mathbb{R}^n$ are the Best Linear Unbiased Estimators (BLUEs) of $\mathrm{x} \in \mathbb{R}^n$ under $\mathcal{H}_0$ and $\mathcal{H}_{i \neq 0}$. The estimator that captures the procedure in (4.8), or any procedure of similar form, is the DIA-estimator [16]

$$\underline{\bar{\mathrm{x}}} = \sum_{i=0}^{k} \underline{\hat{\mathrm{x}}}_i \, p_i(\underline{\mathrm{t}}) = \underline{\hat{\mathrm{x}}}_0 - \sum_{i=1}^{k} \mathrm{L}_i \, \underline{\mathrm{t}} \, p_i(\underline{\mathrm{t}}), \tag{4.9}$$

where $\underline{\hat{\mathrm{x}}}_i = \underline{\hat{\mathrm{x}}}_0 - \mathrm{L}_i \, \underline{\mathrm{t}}$, $\underline{\hat{\mathrm{x}}}_0 = \mathrm{A}^+ \underline{\mathrm{y}}$, $\mathrm{A}^+ = \mathrm{Q}_{\hat{\mathrm{x}}_0 \hat{\mathrm{x}}_0} \mathrm{A}^T \mathrm{Q}_{\mathrm{yy}}^{-1}$ is the BLUE-inverse of $\mathrm{A} \in \mathbb{R}^{m \times n}$, $\mathrm{Q}_{\hat{\mathrm{x}}_0 \hat{\mathrm{x}}_0} = (\mathrm{A}^T \mathrm{Q}_{\mathrm{yy}}^{-1} \mathrm{A})^{-1}$ is the vc-matrix of $\underline{\hat{\mathrm{x}}}_0$, $\mathrm{L}_i = \mathrm{A}^+ \mathrm{C}_i \mathrm{C}_{\mathrm{t}_i}^+$ for $i > 0$, and $\mathrm{L}_0 = 0_{n \times r}$. The indicator function $p_i(\underline{\mathrm{t}}) = 1$ if $\underline{\mathrm{t}} \in \mathcal{P}_i$ and $p_i(\underline{\mathrm{t}}) = 0$ otherwise. The PDF of $\underline{\bar{\mathrm{x}}} \in \mathbb{R}^n$ follows from Theorem 1 in [16]

$$f_{\underline{\bar{\mathrm{x}}}}(x) = \sum_{i=0}^{k} \int_{\mathcal{P}_i} f_{\underline{\hat{\mathrm{x}}}_i, \underline{\mathrm{t}}}(x, t) \, dt, \tag{4.10}$$

where $f_{\underline{\hat{\mathrm{x}}}_i, \underline{\mathrm{t}}}(x, t)$ is the joint PDF of $\underline{\hat{\mathrm{x}}}_i$ and $\underline{\mathrm{t}}$ for $i \in \{0, ..., k\}$. It is important to emphasize that $\underline{\hat{\mathrm{x}}}_i$ and $\underline{\mathrm{t}}$ are *dependent* for $i \neq 0$ (i.e., $f_{\underline{\hat{\mathrm{x}}}_i, \underline{\mathrm{t}}}(x, t) \neq f_{\underline{\hat{\mathrm{x}}}_i}(x) f_{\underline{\mathrm{t}}}(t)$) while only $\underline{\hat{\mathrm{x}}}_0$ and $\underline{\mathrm{t}}$ are independent (see an illustrative example in [35]). It is the DIA-estimator's PDF in (4.10)

that is used in the formulation of the probability of positioning failure. We note that one may only be interested in specific components of the parameter vector $\mathrm{x} \in \mathbb{R}^n$, such as the 1D, 2D, or 3D position. The desired position components can be obtained through the transformation $\mathrm{h} = \mathrm{H}^T\mathrm{x}$ with an appropriately chosen $\mathrm{H} \in \mathbb{R}^{n\times p}$ where $p < n$. Further developments are done in terms of $\mathrm{x} \in \mathbb{R}^n$, however a similar route would apply also for $\mathrm{h} \in \mathbb{R}^p$.

4.3 Review of the method to compute the Probability of positioning failure and its components

This section briefly presents the main ideas of the recently published method for computing the probability of positioning failure and its components [18]. The starting point is the event of positioning failure which can be defined as $\mathcal{F} = \underline{\mathrm{x}} \in \mathcal{B}^c$ (based on page 15 of [12]), where $\mathcal{B} \subset \mathbb{R}^n$ is a safety-region and $\mathcal{B}^c = \mathbb{R}^n/\mathcal{B}$ is its complement (failure-region). Next, we formulate the probability of positioning failure [35]

$$\mathbb{P}_{\mathcal{F}}(\mathbf{b}) = \int_{\mathcal{B}^c} f_{\underline{\mathrm{x}}}(x)dx, \tag{4.11}$$

where $\mathbf{b} = \{\mathrm{b}_1, ..., \mathrm{b}_k\}$ accounts for the sizes of the model misspecification under the alternative hypotheses. By decomposing (4.11) via the rule of total probability we obtain

$$\mathbb{P}_{\mathcal{F}}(\mathbf{b}) = \mathsf{P}(\mathcal{H}_0) \underbrace{\int_{\mathcal{B}^c} f_{\underline{\mathrm{x}}}(x|\mathcal{H}_0)dx}_{\mathbb{P}_{\mathcal{F}}|\mathcal{H}_0} + \sum_{i=1}^{k} \mathsf{P}(\mathcal{H}_i) \underbrace{\int_{\mathcal{B}^c} f_{\underline{\mathrm{x}}}(x|\mathcal{H}_i)dx}_{\mathbb{P}_{\mathcal{F}}|\mathcal{H}_i(\mathrm{b}_i)}, \tag{4.12}$$

where $\mathsf{P}(\mathcal{H}_0)$ and $\mathsf{P}(\mathcal{H}_i)$ are the apriori probability of occurrence of the hypotheses. A further expansion of (4.12), based on (4.10), gives

$$\begin{aligned}\mathbb{P}_{\mathcal{F}}(\mathbf{b}) = \mathsf{P}(\mathcal{H}_0)\left(\sum_{j=0}^{k}\int_{\mathcal{B}^c}\int_{\mathcal{P}_j} f_{\hat{\underline{\mathrm{x}}}_j,\underline{\mathrm{t}}}(x,t|\mathcal{H}_0)\,dt\,dx\right) + \\ \sum_{i=1}^{k}\mathsf{P}(\mathcal{H}_i)\left(\sum_{j=0}^{k}\int_{\mathcal{B}^c}\int_{\mathcal{P}_j} f_{\hat{\underline{\mathrm{x}}}_j,\underline{\mathrm{t}}}(x,t|\mathcal{H}_i)\,dt\,dx\right),\end{aligned} \tag{4.13}$$

which can then be expressed in terms of expected values w.r.t. the joint PDFs $f_{\hat{\underline{\mathrm{x}}}_j,\underline{\mathrm{t}}}(x,t)$

$$\mathbb{P}_{\mathcal{F}}(\mathbf{b}) = \mathsf{P}(\mathcal{H}_0)\left(\sum_{j=0}^{k}\mathsf{E}_{f_{\hat{\underline{\mathrm{x}}}_j,\underline{\mathrm{t}}}}\left(\mathbb{1}_j(\underline{\mathrm{x}},\underline{\mathrm{t}})|\mathcal{H}_0\right)\right) + \sum_{i=1}^{k}\mathsf{P}(\mathcal{H}_i)\left(\sum_{j=0}^{k}\mathsf{E}_{f_{\hat{\underline{\mathrm{x}}}_j,\underline{\mathrm{t}}}}\left(\mathbb{1}_j(\underline{\mathrm{x}},\underline{\mathrm{t}})|\mathcal{H}_i\right)\right), \tag{4.14}$$

where the joint indicator function $\mathbb{1}_j(\underline{\mathrm{x}},\underline{\mathrm{t}}) = 1$ if $[\underline{\mathrm{x}}^T\ \underline{\mathrm{t}}^T]^T \in \left(\mathcal{B}^c \cap \mathcal{P}_j\right)$, and 0 otherwise. The developed method to compute (4.14) is based on principles from rare event simulation, specifically Importance Sampling and the Cross-Entropy Method [19, 20]. For safety-critical applications, such rare-event simulation techniques are needed since the probability of positioning failure must satisfy stringent requirements (e.g., below 10^{-5}), and

they enable both the computation of such low probabilities and the determination of the contributions of individual components. This, in turn, allows designers of the positioning algorithms, or systems, to identify the most influential factors already at the design stage and to guide the developments. We briefly describe the three main steps of the method below:

1. Transformation of $\underline{s}_j = [\underline{\hat{x}}_j^T \ \underline{t}^T]^T \in \mathbb{R}^{(n+r)}$, for $j \in \{1, ..., k\}$, via an invertible linear transformation defined by a $U_j : \mathbb{R}^{(n+r)} \to \mathbb{R}^{(n+r)}$ such that the resulting vector has an identity variance-covariance matrix

$$\underline{z}_j = U_j \underline{s}_j, \quad Q_{z_j z_j} = I_{(n+r)}, \tag{4.15}$$

where U_j can be constructed from the L_j term in (4.4) and from a one-time Cholesky decomposition of the variance–covariance matrices $Q_{\hat{x}_0 \hat{x}_0}$ and Q_{tt}. This transformation is needed to handle joint PDFs whose distributional parameters scale *linearly* with the dimension $(n+r)$, rather than quadratically as is the case in (4.14). Based on this transformation, we re-express the expected values in (4.14) using the change of variables rule

$$P_{\mathcal{F}}(\mathbf{b}) = P(\mathcal{H}_0)\left(\sum_{j=0}^{k} E_{f_{\underline{z}_j}}\left(\mathbb{1}_j\left(U_j^{-1}\underline{z}\right)|\mathcal{H}_0\right)\right) + \sum_{i=1}^{k} P(\mathcal{H}_i)\left(\sum_{j=0}^{k} E_{f_{\underline{z}_j}}\left(\mathbb{1}_j\left(U_j^{-1}\underline{z}\right)|\mathcal{H}_i\right)\right). \tag{4.16}$$

2. Re-express the expected values from Step 1) w.r.t. proposal PDFs, following the Importance Sampling principle. These proposal PDFs can be selected to have higher probability density over the regions $\left(\mathcal{B}^c \cap \mathcal{P}_j\right) \subset \mathbb{R}^{(n+r)}$ for $j \in \{0, ..., k\}$. An illustration of this idea is provided in Fig. 4.3.

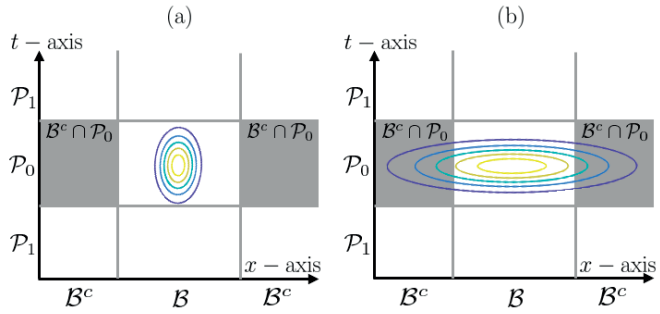

Figure 4.3: Example illustrating the region $(\mathcal{B}^c \cap \mathcal{P}_0) \subset \mathbb{R}^2$ (shaded in grey) for a simple hypothesis testing setup with $A = [1 \ 1]^T$, $x \in \mathbb{R}$, $Q_{yy} = \sigma_y^2 I_2$, and $c_1 = [1 \ 0]^T$. (a) The original PDF $f_{\underline{\hat{x}}_0, \underline{t}}(x, t|\mathcal{H}_0) = f_{\underline{z}_0}(z|\mathcal{H}_0)$ which has low probability density over the region; (b) A proposal PDF $\tilde{f}_0(z|\mathcal{H}_0)$, which places higher probability density over the same region.

The corresponding mathematical formulation of Importance Sampling is as follows

$$\mathbb{P}_{\mathcal{F}}(\mathbf{b}) = \mathsf{P}(\mathcal{H}_0)\left(\sum_{j=0}^{k} \mathsf{E}_{\check{f}_j}\left(\mathbb{1}_j\left(\mathrm{U}_j^{-1}\underline{\mathrm{z}}\right)\check{\mathcal{L}}_j(\underline{\mathrm{z}})|\mathcal{H}_0\right)\right) + \sum_{i=1}^{k}\mathsf{P}(\mathcal{H}_i)\left(\sum_{j=0}^{k} \mathsf{E}_{\tilde{f}_j}\left(\mathbb{1}_j\left(\mathrm{U}_j^{-1}\underline{\mathrm{z}}\right)\tilde{\mathcal{L}}_j(\underline{\mathrm{z}})|\mathcal{H}_i\right)\right), \tag{4.17}$$

where the ratios within the re-expressed expected values are

$$\check{\mathcal{L}}_j(\underline{\mathrm{z}}) = \frac{f_{\underline{\mathrm{z}}_j}(\underline{\mathrm{z}}|\mathcal{H}_0)}{\check{f}_j(\underline{\mathrm{z}})}, \quad \tilde{\mathcal{L}}_j(\underline{\mathrm{z}}) = \frac{f_{\underline{\mathrm{z}}_j}(\underline{\mathrm{z}}|\mathcal{H}_i)}{\tilde{f}_j(\underline{\mathrm{z}})}, \tag{4.18}$$

with $\check{f}_j(.)$ and $\tilde{f}_j(.)$ being the proposal PDFs. These proposal PDFs are determined via the Cross-Entropy Method, which minimizes the Kullback–Leibler divergence between the theoretical optimal proposal PDFs (i.e., those that achieve minimum simulation variance) and a parametric family of candidate PDFs (e.g., the exponential family).

3. Compute the components of $\mathbb{P}_{\mathcal{F}}(\mathbf{b})$ from the expected values from Step 2) by generating independent and identically distributed pseudo-random samples from the determined proposal PDFs ($\check{f}_j(.)$ and $\tilde{f}_j(.)$), and quantify the simulation uncertainty of the results by independent repetitions of the simulations a chosen number of times (e.g., 50 times [36]).

4.4 Positioning Safety Analysis for UAVs over Authorized European Airspace Regions

Building on previous work [18], the present contribution takes a step further and considers more complex scenarios that capture time-varying positioning functional and stochastic models when computing (4.14) and the corresponding components. Therefore, we apply the discussed principles—the combined parameter estimation and hypothesis testing, and the computation of the probability of positioning failure—to conduct positioning safety analyses in a scenario using real GPS satellite orbits from the International GNSS Service (IGS) over a 24-hour period on May 24, 2024 [27]. In this scenario, we select eight authorized airspace regions across different countries within E.U. and compute the instantaneous minimum and maximum of $\mathbb{P}_{\mathcal{F}}(\mathbf{b})$ at 5 minute intervals over 24 hours. Due to the high altitude of GPS satellites, approximately 20.000 km, their geometry relative to a UAV GPS receiver remains nearly constant over relatively short periods, such as a 5 minute window. The information about the locations of the authorized airspace regions is provided by the EASA [25], and the chosen geographic coordinates within these airspaces are illustrated in Fig. 4.4. The selected airspaces have open-sky conditions and they cover relatively small areas (e.g., a circular region with a radius of approximately 3 km in the selected airspace region from Portugal). Within each airspace region, a UAV is assumed to operate at a constant altitude of 45 meters above ground level, at the geographic coordinates listed in

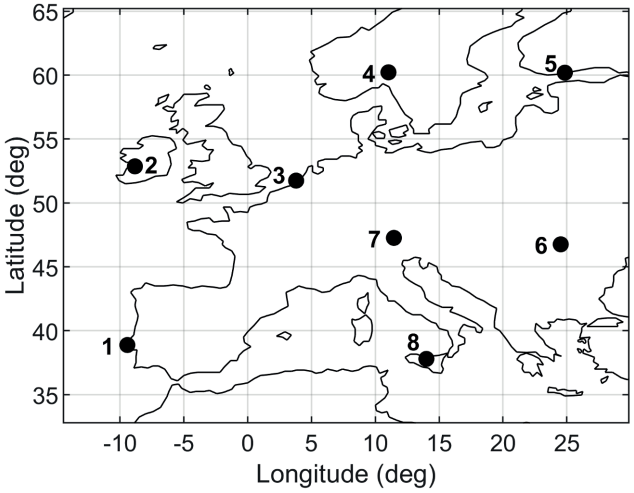

Figure 4.4: Geographic locations within the authorized airspaces for UAV operations in: 1-Portugal, 2-Ireland, 3-Netherlands, 4-Norway, 5-Finland, 6-Romania, 7-Austria, and 8-Italy. Coordinates are given in Table 4.1.

Table 4.1: Geographic coordinates of the eight locations expressed as Longitude, Latitude, and Altitude

Nb.	Country	Long.[deg], Lat.[deg], Alt.[m]
1	Portugal (PT)	−9.42869, 38.88371, 111.9
2	Ireland (IE)	−8.83542, 52.86114, 31.6
3	Netherlands (NL)	3.79322, 51.74368, 0.0
4	Norway (NO)	11.02785, 60.21601, 187.0
5	Finland (FI)	24.84807, 60.18738, 0.0
6	Romania (RO)	24.52379, 46.75973, 463.4
7	Austria (AT)	11.45355, 47.26376, 590.4
8	Italy (IT)	13.99929, 37.79651, 778.1

Table 4.1, ensuring compliance with height regulations in these airspaces. The choice of the positioning model for UAVs under nominal conditions (i.e., under $\mathcal{H}_0$) is based on (i) the TSO certification for GPS-based UAV positioning [13, 26] and (ii) preliminary requirements for rotary-wing drones at SAIL 3 and 4 for en-route operations, as specified in [14]. Hence, the linearized positioning model for the UAVs is based on GPS pseudoranges on single-frequency (L1 at 1575.42 MHz) resulting in

$$\mathcal{H}_0 : \mathsf{E}_{f_{\underline{y}}}\left(\underline{y}\right) = \underbrace{\begin{bmatrix} G & \mathbf{u}_m \end{bmatrix}}_{A} \underbrace{\begin{bmatrix} \Delta p \\ c\Delta t \end{bmatrix}}_{\Delta x}, \quad Q_{yy} = \sigma_y^2 W^{-1}, \tag{4.19}$$

with $\underline{y} \sim \mathcal{N}\left(A\Delta x, Q_{yy}\right)$, where the design matrix $A \in \mathbb{R}^{m\times 4}$ is of $\text{rank}(A) = 4$ with $G \in \mathbb{R}^{m\times 3}$ the matrix which rows contain the unit direction vectors (with the minus sign included)

between the unknown position of the UAVs' GPS receiver and the observed GPS satellites, in a local East-North-Up (ENU) coordinate system, and $\mathbf{u}_m \in \mathbb{R}^m$ is a vector of ones [37]. The parameter vector of unknowns $\Delta \mathrm{x} \in \mathbb{R}^4$ contains the UAV's GPS receiver ENU coordinates increments $\Delta \mathrm{p} \in \mathbb{R}^3$ and the receiver clock bias $\Delta \mathrm{t} \in \mathbb{R}$ while $\mathtt{c}$ is the speed of light in a vacuum. The redundancy under $\mathcal{H}_0$ is $r = m - 4$. The estimate $\hat{\mathrm{x}}$ (which includes the 3D full position vector and receiver clock bias) is obtained from a Gauss-Newton iteration scheme once the stop criterion is met for $\Delta\hat{\mathrm{x}}$ [38]. The variance-covariance matrix $\mathrm{Q}_{\mathrm{yy}} \in \mathbb{R}^{m\times m}$ is diagonal where $\mathrm{W} = \mathrm{diag}[\omega_1, ..., \omega_m] \in \mathbb{R}^{m\times m}$ is the weight matrix which components are the elevation-dependent weighting functions formulated based on the principles in [39]. We set the pseudorange precision to $\sigma_{\mathrm{y}} = 0.7$ [m] resulting in an average horizontal positioning precision of 3-4 meters (95% circular probability radius), and an average vertical positioning precision of approximately 6 meters (95% interval length), considering variations in satellite geometry over a 24 hour period. These positioning precisions are representative of certified GPS receivers used in UAVs (e.g., [40]). An elevation cut-off angle of 10° is applied, which excludes GPS satellites observed below this threshold from the positioning model.

Given the open-sky conditions over the selected airspaces, we account for individual outliers in the observations $\underline{\mathrm{y}} \in \mathbb{R}^m$ (e.g., due to GPS satellite failures), assuming that only one outlier occurs at a time. This is the case for datasnooping which results in as many alternative hypotheses as observables (i.e., $k = m$) and gives the following partitions of the misclosure vector space $\mathbb{R}^r$

$$\mathcal{P}_0 = \left\{ t \in \mathbb{R}^r \mid ||t||^2_{\mathrm{Q_{tt}}} \leq \chi^2_\alpha(r, 0) \right\}, \tag{4.20}$$

$$\mathcal{P}_{i\neq 0} = \left\{ t \in \mathbb{R}^r \mid t \notin \mathcal{P}_0,\ |w_i| = \max_{l\in\{1,...,k\}} |w_l| \right\}, \tag{4.21}$$

where $|\underline{w}_l| = ||\mathbf{\Pi}_{\mathrm{c_{t_l}}} \underline{\mathrm{t}}||_{\mathrm{Q_{tt}}}$ is the w-test statistic [30, 41], $\mathrm{c_{t_l}} = \mathrm{B}^T \mathrm{c}_l$, and c_l is the canonical unit vector for $l \in \{1, ..., k\}$ as C_l from (4.2) reduces to a vector. The level of significance is set to $\alpha = 3.33 \cdot 10^{-7}$ [12, 42, 43]. The corresponding `DIA`-estimators for the horizontal and vertical components of the UAVs' position are

$$\overline{\underline{\mathrm{h}}} = \mathrm{H}^T \underline{\overline{\mathrm{x}}} \ \text{ and } \ \underline{\overline{\mathrm{v}}} = \mathrm{V}^T \underline{\overline{\mathrm{x}}}, \tag{4.22}$$

where $\underline{\overline{\mathrm{x}}} = \sum_{i=0}^{k} \hat{\underline{\mathrm{x}}}_i\, p_i(\underline{\mathrm{t}})$ cf. (4.9), $\mathrm{H}^T = \begin{bmatrix} \mathrm{I}_2 & 0_{2\times 2} \end{bmatrix}$ and $\mathrm{V}^T = \begin{bmatrix} 0 & 0 & 1 & 0 \end{bmatrix}$. The horizontal and vertical safety-regions $\mathcal{B}_{\mathrm{h}} \subset \mathbb{R}^2$ and $\mathcal{B}_{\mathrm{v}} \subset \mathbb{R}$, around the true position, are defined as follows

$$\begin{aligned} \mathcal{B}_{\mathrm{h}} &= \{h \in \mathbb{R}^2 \mid ||h - \mathrm{h_{true}}|| \leq \mathrm{HAL}\}, \\ \mathcal{B}_{\mathrm{v}} &= \{v \in \mathbb{R} \mid |v - \mathrm{v_{true}}| \leq \mathrm{VAL}\}, \end{aligned} \tag{4.23}$$

where the Horizontal Alert Limit (HAL) is set to 11 m, and the Vertical Alert Limit (VAL) is set to 14 m, in line with SAIL 3 and SAIL 4 for en-route operations [14]. The probabilities of the UAVs horizontal and vertical positioning failure are

$$\mathbb{P}_{\mathcal{F}_{\mathrm{h}}}(\mathbf{b}) = \int_{\mathcal{B}^c_{\mathrm{h}}} f_{\underline{\overline{\mathrm{h}}}}(h)dh \ , \ \mathbb{P}_{\mathcal{F}_{\mathrm{v}}}(\mathbf{b}) = \int_{\mathcal{B}^c_{\mathrm{v}}} f_{\underline{\overline{\mathrm{v}}}}(v)dv, \tag{4.24}$$

and their decomposition follow the same approach as in (4.12)-(4.14). This decomposition we require the apriori probabilities of the hypotheses $\mathtt{P}(\mathcal{H}_0)$ and $\mathtt{P}(\mathcal{H}_i)$ for $i \in \{1, ..., k\}$.

We set $\mathsf{P}(\mathcal{H}_i) = 10^{-5}$ to account for the probability of an outlier in the observables due to a GPS satellite failure which is consistent with [12]. Consequently, this results in $\mathsf{P}(\mathcal{H}_0) = 1 - \sum_{i=1}^{k} \mathsf{P}(\mathcal{H}_i)$. The following results of the UAV positioning safety analysis focus on the horizontal position component (based on $\mathbb{P}_{\mathcal{F}_\mathrm{h}}(\mathbf{b})$), while the ones for the vertical component (based on $\mathbb{P}_{\mathcal{F}_\mathrm{v}}(\mathbf{b})$) can be conducted in a similar way.

Firstly, we show in Fig. 4.5(a) the number of observed GPS satellites (in black), using a 10° elevation mask, and the weighted Horizontal Dillution of Precision (wHDOP) in brown, which is computed as $\text{wHDOP} = \sqrt{\text{trace}\left(\mathrm{H}^T \left(\mathrm{A}^T \mathrm{Q}_{\mathrm{yy}}^{-1} \mathrm{A}\right)^{-1} \mathrm{H}\right)}$ based on [44]. The wHDOP is useful in giving an indication of the variation of the horizontal positioning precision as a function of the change in GPS satellite geometry while also taking into account the elevation-dependent weighting of the observables. For example, one can notice how wHDOP increases when the number of observed GPS satellites decreases, and vice-versa. The smallest variation in wHDOP occurs over the 8-Italy airspace, due to its proximity to the Equator—among all considered locations—where GPS satellite geometry is most favorable.

Secondly, Fig. 4.5(b) presents the results of the computed instantaneous minimum (blue) and maximum (orange) of $\mathbb{P}_{\mathcal{F}_\mathrm{h}}(\mathbf{b})$, which can be expressed as

$$\begin{aligned} \min_{\mathbf{b}} \mathbb{P}_{\mathcal{F}_\mathrm{h}}(\mathbf{b}) &= \mathsf{P}(\mathcal{H}_0)\mathbb{P}_{\mathcal{F}_\mathrm{h}}|\mathcal{H}_0 + \min_{\mathbf{b}} \sum_{i=1}^{k} \mathsf{P}(\mathcal{H}_i)\mathbb{P}_{\mathcal{F}_\mathrm{h}}|\mathcal{H}_i(\mathrm{b}_i), \\ \max_{\mathbf{b}} \mathbb{P}_{\mathcal{F}_\mathrm{h}}(\mathbf{b}) &= \mathsf{P}(\mathcal{H}_0)\mathbb{P}_{\mathcal{F}_\mathrm{h}}|\mathcal{H}_0 + \max_{\mathbf{b}} \sum_{i=1}^{k} \mathsf{P}(\mathcal{H}_i)\mathbb{P}_{\mathcal{F}_\mathrm{h}}|\mathcal{H}_i(\mathrm{b}_i), \end{aligned} \tag{4.25}$$

where $\mathbf{b} = \{\mathrm{b}_1, ..., \mathrm{b}_k\}$. Several remarks can be made: (i) the variations in the minimum and maximum of the computed $\underline{\mathbb{P}}_{\mathcal{F}_\mathrm{h}}(\mathbf{b})$ are following the behaviour of the wHDOP; (ii) in time windows where wHDOP shows large variations (e.g., between hours 3 and 6), the difference $\left(\max_{\mathbf{b}} \underline{\mathbb{P}}_{\mathcal{F}_\mathrm{h}}(\mathbf{b}) - \min_{\mathbf{b}} \underline{\mathbb{P}}_{\mathcal{F}_\mathrm{h}}(\mathbf{b})\right) \to 0$ as wHDOP increases, since the term $\mathsf{P}(\mathcal{H}_0)\underline{\mathbb{P}}_{\mathcal{F}_\mathrm{h}}|\mathcal{H}_0$ becomes increasingly dominant due to the poorer precision under $\mathcal{H}_0$; (iii) when wHDOP is low, the difference between the minimum and maximum of $\underline{\mathbb{P}}_{\mathcal{F}_\mathrm{h}}(\mathbf{b})$ spans from ≈1 order of magnitude up to ≈4 orders of magnitude (e.g., between hours 7 and 9).

Thirdly, we aim to relate the instantaneous minimum and maximum of the computed $\underline{\mathbb{P}}_{\mathcal{F}_\mathrm{h}}(\mathbf{b})$ with the preliminary positioning safety requirements for SAIL 3 and SAIL 4 which are 10^{-4}/hour (continuous red line in Fig. 4.5(c)) and 10^{-5}/hour (dotted red line in Fig. 4.5(c)) respectively from Table 3 in [14]. As an example, we compute a one-hour (1 hr) moving average based on (4.25) and a given flight start time denoted κ_0 as follows

$$\begin{aligned} \mathcal{MA}_{\min}(\kappa_0) &= \frac{1}{1\,\mathrm{hr}} \int_{\kappa_0}^{\kappa_0+1\,\mathrm{hr}} \min_{\mathbf{b}} \mathbb{P}_{\mathcal{F}_\mathrm{h}}(\mathbf{b}, \tau)\, d\tau, \\ \mathcal{MA}_{\max}(\kappa_0) &= \frac{1}{1\,\mathrm{hr}} \int_{\kappa_0}^{\kappa_0+1\,\mathrm{hr}} \max_{\mathbf{b}} \mathbb{P}_{\mathcal{F}_\mathrm{h}}(\mathbf{b}, \tau)\, d\tau. \end{aligned} \tag{4.26}$$

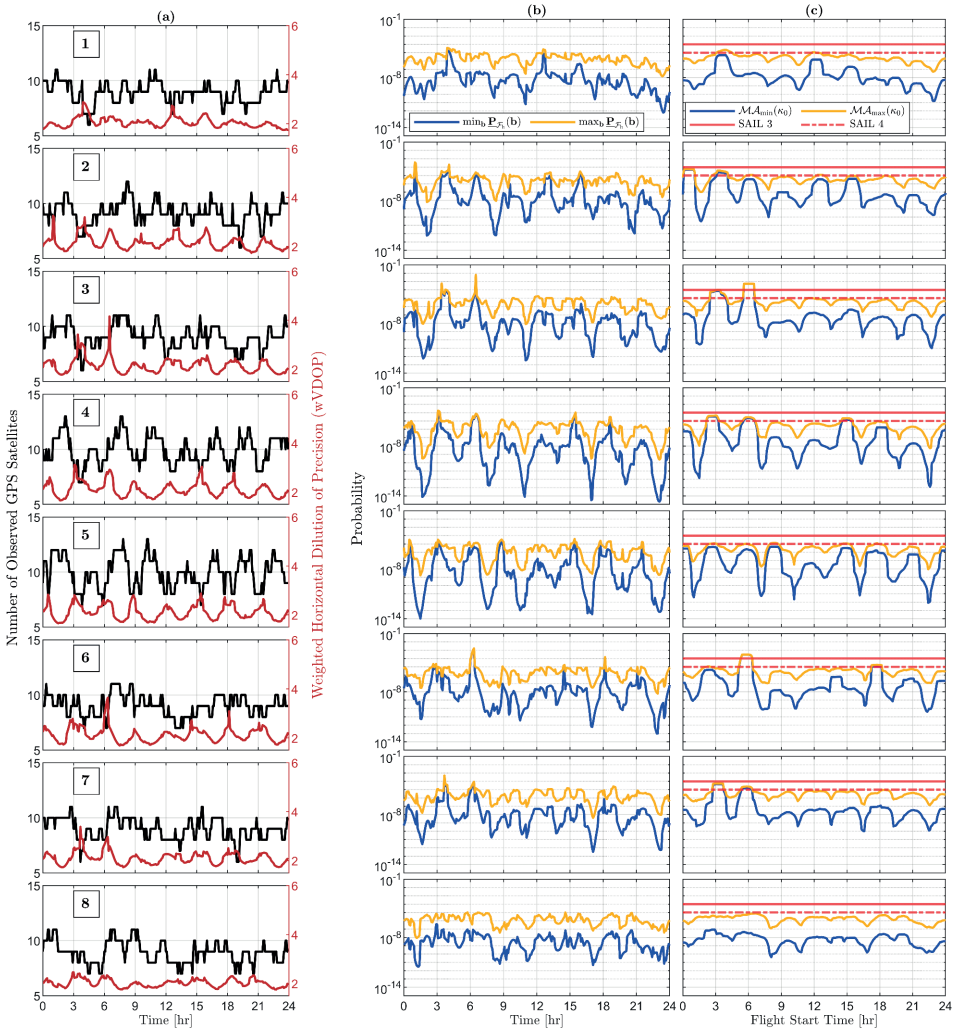

Figure 4.5: Positioning-safety results for the **horizontal** position: (a) Number of observed GPS satellites (black) after the application a 10° elevation mask and the wHDOP (brown); (b) Instantaneous minimum (blue) and maximum (orange) of $\underline{\mathbb{P}}_{\mathcal{F}_{\mathrm{h}}}(\mathbf{b})$ computed every 5 minutes for 24 hours; (c) One-hour moving average of the instantaneous minimum (blue) and maximum (orange) of $\underline{\mathbb{P}}_{\mathcal{F}_{\mathrm{h}}}(\mathbf{b})$. The positioning safety requirement for SAIL 3 is indicated by the solid red line at 10^{-4}, and for SAIL 4 by the dotted red line at 10^{-5}.

which are displayed in blue and orange respectively in Fig. 4.5(c). We use the results of the one-hour moving average to address the following question:

"For what percentage of flight start times (κ_0) does the average probability of positioning failure over the following 1 hour meet the horizontal positioning safety requirements for SAIL 3 and SAIL 4?".

Therefore, the following cases are considered for the computation of the percentage of flight start times at which

- $\mathcal{MA}_{\min}(\kappa_0) \leq 10^{-4}$ (Case 1) and $\mathcal{MA}_{\max}(\kappa_0) \leq 10^{-4}$ (Case 2) for SAIL 3,
- $\mathcal{MA}_{\min}(\kappa_0) \leq 10^{-5}$ (Case 3) and $\mathcal{MA}_{\max}(\kappa_0) \leq 10^{-5}$ (Case 4) for SAIL 4.

Table 4.2: Percentage of flight start time when $\mathcal{MA}_{\min}(\kappa_0)$ and $\mathcal{MA}_{\max}(\kappa_0)$ are meeting the **horizontal** positioning safety requirement of SAIL 3 and 4 for en-route UAV operations. The results for apriori probabilities set to $\mathsf{P}(\mathcal{H}_i) = 10^{-5}$ are shown in black, while those for $\mathsf{P}(\mathcal{H}_i) = 10^{-4}$ are displayed in olive, where $i \in \{1,\dots,k\}$.

Country	SAIL 3 (Horiz.)		SAIL 4 (Horiz.)	
	Case 1[%]	Case 2[%]	Case 3[%]	Case 4[%]
1-PT	100 | 100	100 | 95.53	100 | 100	92.97 | 24.92
2-IE	100 | 100	100 | 91.37	88.18 | 88.18	81.47 | 17.25
3-NL	96.17 | 96.17	96.17 | 89.14	90.73 | 90.73	88.18 | 21.08
4-NO	100 | 100	100 | 96.80	88.50 | 88.50	86.90 | 31.31
5-FI	100 | 100	100 | 99.36	100 | 100	88.82 | 30.67
6-RO	95.85 | 95.85	95.85 | 95.52	91.37 | 91.37	89.78 | 26.20
7-AT	100 | 100	100 | 94.89	92.65 | 92.65	91.69 | 23.64
8-IT	100 | 100	100 | 100	100 | 100	100 | 33.23

Table 4.2 presents the results, with values shown in black for apriori probabilities set to $\mathsf{P}(\mathcal{H}_i) = 10^{-5}$. For SAIL 3, the horizontal positioning safety requirements are not met for 100% of flight start times only in the selected airspaces over the Netherlands and Romania. In the case of SAIL 4, only in the selected airspace over Italy the horizontal positioning safety requirement is met 100% of flight start times for both SAIL 3 and SAIL 4. In Ireland, the percentages are lowest for both Case 3 and 4, at SAIL 4, among all chosen locations. When the apriori probabilities are changed to $\mathsf{P}(\mathcal{H}_i) = 10^{-4}$ for $i \in \{1,\dots,k\}$, the results, shown in olive, account for outliers in the observables caused by an event with higher probability (e.g., signal reflections from nearby infrastructure). For SAIL 3-Case 1 shown in black (i.e., $\mathcal{MA}_{\min}(\kappa_0) \leq 10^{-4}$) there are no differences w.r.t. the results in olive as the component $\mathsf{P}(\mathcal{H}_0)\underline{\mathbb{P}}_{\mathcal{F}_h}|\mathcal{H}_0$ is the dominant one and the apriori probability $\mathsf{P}(\mathcal{H}_0) = 1 - \sum_{i=1}^{k} \mathsf{P}(\mathcal{H}_i)$ is not significantly different when $\mathsf{P}(\mathcal{H}_i) = 10^{-5}$ or $\mathsf{P}(\mathcal{H}_i) = 10^{-4}$ for $i \in \{1,\dots,k\}$. However, the most significant decreases in the percentages of flight start times (greater than 50%) occur

for SAIL 4-Case 4 (i.e., $\mathcal{MA}_{\max}(\kappa_0) \leq 10^{-5}$) where the term $\max_{\mathbf{b}} \sum_{i=1}^{k} \mathsf{P}(\mathcal{H}_i)\underline{\mathbb{P}}_{\mathcal{F}_h}|\mathcal{H}_i(\mathrm{b}_i)$ is dominant and the assumptions on the apriori probabilities $\mathsf{P}(\mathcal{H}_i)$, for $i \in \{1,\ldots,k\}$, have an increased effect.

Similarly, the sensitivity of the results to the level of significance α can be studied in Table 4.3, which shows the results for $\mathsf{P}(\mathcal{H}_i) = 10^{-5}$ for all $i \in \{1,\ldots,k\}$. The table presents results for two significance levels: $\alpha = 3.33 \cdot 10^{-7}$ (in black) and $\alpha = 10^{-3}$ (in gray).

Table 4.3: Percentage of flight start time when $\mathcal{MA}_{\min}(\kappa_0)$ and $\mathcal{MA}_{\max}(\kappa_0)$ are meeting the **horizontal** positioning safety requirement of SAIL 3 and 4 for en-route UAV operations when $\mathsf{P}(\mathcal{H}_i) = 10^{-5}$ for $i \in \{1,\ldots,k\}$. The results for the level of significance set to $\alpha = 3.33 \cdot 10^{-7}$ are shown in black, while those for $\alpha = 10^{-3}$ are displayed in gray.

Country	SAIL 3 (Horiz.)		SAIL 4 (Horiz.)	
	Case 1[%]	Case 2[%]	Case 3[%]	Case 4[%]
1-PT	100 | 99.04	100 | 98.40	100 | 71.57	92.97 | 69.32
2-IE	100 | 98.40	100 | 98.40	88.18 | 53.03	81.47 | 49.84
3-NL	96.17 | 91.37	96.17 | 91.05	90.73 | 53.35	88.18 | 49.52
4-NO	100 | 99.68	100 | 99.36	88.50 | 70.29	86.90 | 66.45
5-FI	100 | 100	100 | 100	100 | 58.15	88.82 | 53.99
6-RO	95.85 | 95.85	95.85 | 95.85	91.37 | 64.54	89.78 | 61.66
7-AT	100 | 96.49	100 | 96.17	92.65 | 56.87	91.69 | 53.99
8-IT	100 | 100	100 | 100	100 | 92.01	100 | 87.54

For SAIL 3, the differences range from 0% (e.g., FI) to 5.12% (NL) in Cases 1 and 2. These differences are more pronounced in Cases 3 and 4, ranging from 7.99% (IT) to 41.85% (FI). In these situations, increasing the level of significance $\alpha = 3.33 \cdot 10^{-7}$ to $\alpha = 10^{-3}$, it increases the contribution of the conditional component of $\underline{\mathbb{P}}_{\mathcal{F}_h}|\mathcal{H}_0$ on the events of false alarms (i.e., accepting a $\mathcal{H}_{i\neq 0}$ when $\mathcal{H}_0$ is valid) over the conditional components on the event of correct acceptance (i.e., accepting $\mathcal{H}_0$ when $\mathcal{H}_0$ is valid).

Therefore, the results can be highly sensitive to the assumed aprior probabilities of the hypotheses and the chosen level of significance. These aspects should be carefully considered during the design stage of UAV positioning algorithms. To increase the percentages from Tables 4.2 and 4.3 for SAIL 3 and SAIL 4 en-route UAV operations, several options, or combinations thereof, could be considered: (i) certification of additional GNSS constellations, such as the European Galileo, to be used alongside GPS for UAV operations, (ii) usage of GPS receivers with better precision of the observables, (iii) application of principles from the new theoretical framework introduced in [34] to design parameter estimation and statistical hypothesis testing procedures with the objective to minimize the probability of positioning failure.

Next, as an example, we are examining the components of the probability of positioning failure in (4.25) for the selected authorized airspace in the Netherlands. A similar examination can be done for other countries. The following analysis is considering the first setting of the apriori probabilities of the alternative hypotheses of $\mathsf{P}(\mathcal{H}_i) = 10^{-5}$ for $i \in \{1, \ldots, k\}$, corresponding to the results in Figure 4.5.

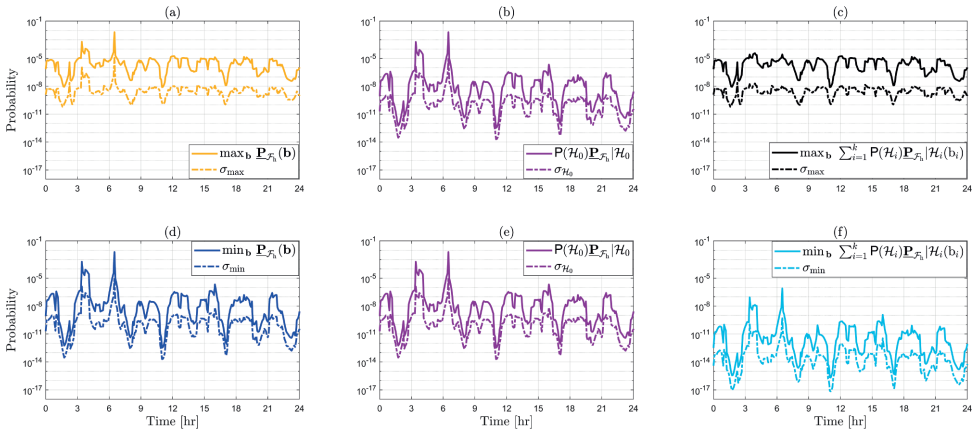

Figure 4.6: Over selected airspace in the Netherlands: (a) Instantaneous $\max_{\mathbf{b}} \underline{\mathbb{P}}_{\mathcal{F}_h}(\mathbf{b})$ and its simulation standard deviation ($\sigma_{\max}$); (b) Component $\mathsf{P}(\mathcal{H}_0)\underline{\mathbb{P}}_{\mathcal{F}_h}|\mathcal{H}_0$ and its $\sigma_{\mathcal{H}_0}$; (c) Component $\max_{\mathbf{b}} \sum_{i=1}^{k} \mathsf{P}(\mathcal{H}_i)\underline{\mathbb{P}}_{\mathcal{F}_h}|\mathcal{H}_i(\mathrm{b}_i)$ and its $\sigma_{\max}$; (d) Instantaneous $\min_{\mathbf{b}} \underline{\mathbb{P}}_{\mathcal{F}_h}(\mathbf{b})$ and its simulation standard deviation ($\sigma_{\min}$) ; (e) Component $\mathsf{P}(\mathcal{H}_0)\underline{\mathbb{P}}_{\mathcal{F}_h}|\mathcal{H}_0$ and its $\sigma_{\mathcal{H}_0}$; (f) Component $\min_{\mathbf{b}} \sum_{i=1}^{k} \mathsf{P}(\mathcal{H}_i)\underline{\mathbb{P}}_{\mathcal{F}_h}|\mathcal{H}_i(\mathrm{b}_i)$ and its $\sigma_{\min}$.

Figure 4.6(a) shows the computed instantaneous $\max_{\mathbf{b}} \underline{\mathbb{P}}_{\mathcal{F}_h}(\mathbf{b})$ over 24 hours, while Figures 4.6(b)-(c) show the computed components $\mathsf{P}(\mathcal{H}_0)\underline{\mathbb{P}}_{\mathcal{F}_h}|\mathcal{H}_0$ and $\max_{\mathbf{b}} \sum_{i=1}^{k} \mathsf{P}(\mathcal{H}_i)\underline{\mathbb{P}}_{\mathcal{F}_h}|\mathcal{H}_i(\mathrm{b}_i)$, respectively. Figures 4.6(a)-(c) show that between 10^{-8} and 10^{-5} the behaviour of $\max_{\mathbf{b}} \underline{\mathbb{P}}_{\mathcal{F}_h}(\mathbf{b})$ is driven by the component in Figure 4.6(c), while the 'spikes' that are larger than 10^{-5} are those from the component of Figure 4.6(b) due to the large wHDOP (see Figure 4.5(a)). The largest 'spike' in $\max_{\mathbf{b}} \underline{\mathbb{P}}_{\mathcal{F}_h}(\mathbf{b})$ occurs at 6.5 hours and has a value of $6.43 \cdot 10^{-3} \pm 0.0110 \cdot 10^{-3}$, when the wHDOP reaches 4.15, indicating an unfavorable GPS satellite geometry.

We further examine the conditional components of the computed probability of positioning failure under $\mathcal{H}_0$ from Fig. 4.6(b). Specifically, we consider the components of $\underline{\mathbb{P}}_{\mathcal{F}_h}|\mathcal{H}_0$, conditioned on the hypothesis testing decisions: Correct Acceptance (CA) when the positioning model under $\mathcal{H}_0$ (see (4.19)) is chosen while it is also valid, and False Alarms (FA_j), when the positioning model under an alternative hypothesis $\mathcal{H}_{j\neq 0}$ is chosen while the one under $\mathcal{H}_0$ is valid. Therefore, we re-express $\underline{\mathbb{P}}_{\mathcal{F}_h}|\mathcal{H}_0$ as follows

$$\underline{\mathbb{P}}_{\mathcal{F}_h}|\mathcal{H}_0 = \mathsf{P}_{\mathrm{CA}}\underline{\mathbb{P}}_{\mathcal{F}_h}|\mathrm{CA} + \sum_{j=1}^{k} \underline{\mathsf{P}}_{\mathrm{FA}_j}\underline{\mathbb{P}}_{\mathcal{F}_h}|\mathrm{FA}_j \,, \tag{4.27}$$

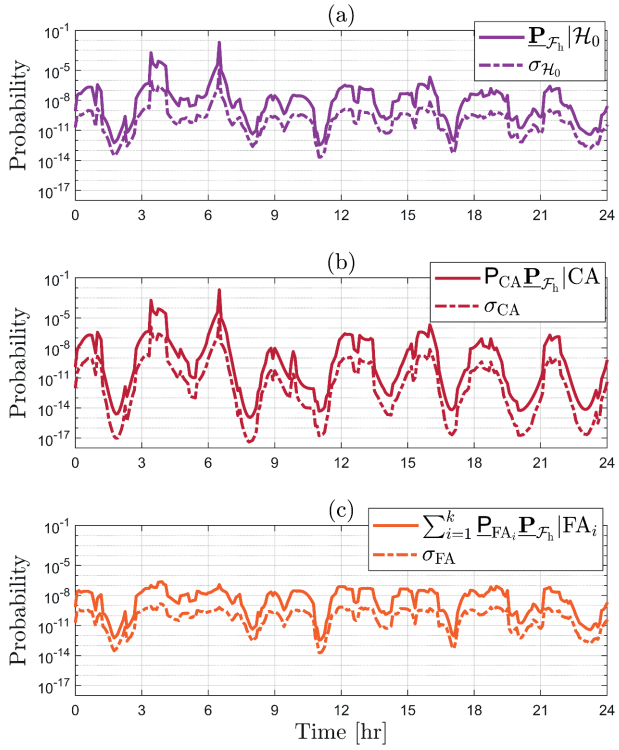

Figure 4.7: Over selected airspace in the Netherlands, the computed instantaneous: (a) $\underline{\mathbb{P}}_{\mathcal{F}_h}|\mathcal{H}_0$ and its simulation standard deviation ($\sigma_{\mathcal{H}_0}$); (b) $\mathsf{P}_{CA}\underline{\mathbb{P}}_{\mathcal{F}_h}|CA$ and its simulation standard deviation (σ_{CA}); (c) $\sum_{j=1}^{k}\underline{\mathsf{P}}_{FA_j}\underline{\mathbb{P}}_{\mathcal{F}_h}|FA_j$ and its simulation standard deviation (σ_{FA}). The chosen level of significance is $\alpha = 3.33\cdot 10^{-7}$.

where $\mathsf{P}_{CA} = \mathsf{P}(\underline{t} \in \mathcal{P}_0|\mathcal{H}_0)$, $\underline{\mathbb{P}}_{\mathcal{F}_h}|CA$ is the probability of positioning failure conditioned on the CA decision, and the product $\mathsf{P}_{CA}\underline{\mathbb{P}}_{\mathcal{F}_h}|CA$ corresponds to the case when $j = 0$ in the summation term under $\mathcal{H}_0$ (first term) of (4.17). Similarly, $\mathsf{P}_{FA_j} = \mathsf{P}(\underline{t} \in \mathcal{P}_{j\neq 0}|\mathcal{H}_0)$, $\underline{\mathbb{P}}_{\mathcal{F}_h}|FA_j$ is the probability of positioning failure conditioned on the FA_j decision, and the summation term in (4.27) corresponds to the one under $\mathcal{H}_0$ (first term) of (4.17) for $j \neq 0$. Note that, for this example the level of significance of the statistical hypothesis testing procedure is $\alpha = \sum_{j=1}^{k}\mathsf{P}_{FA_j} = 3.33\cdot 10^{-7}$ (see (4.20) and (4.21)) while $\mathsf{P}_{CA} = 1-\alpha$. Fig. 4.7 illustrates that $\mathsf{P}_{CA}\underline{\mathbb{P}}_{\mathcal{F}_h}|CA$ gives the higher values ('peaks') of $\underline{\mathbb{P}}_{\mathcal{F}_h}|\mathcal{H}_0$, while the component $\sum_{j=1}^{k}\underline{\mathsf{P}}_{FA_j}\underline{\mathbb{P}}_{\mathcal{F}_h}|FA_j$ drives its lower values ('valleys'). Choosing a larger level of significance, for example $\alpha = 10^{-3}$, increases the contribution of the component $\sum_{j=1}^{k}\underline{\mathsf{P}}_{FA_j}\underline{\mathbb{P}}_{\mathcal{F}_h}|FA_j$ to $\underline{\mathbb{P}}_{\mathcal{F}_h}|\mathcal{H}_0$ (see Fig. 4.10 of Appendix 4.6). Accordingly, the necessary trade-offs should be considered at the design stage of the positioning estimation and hypothesis testing procedure: a smaller α reduces detection sensitivity to outlier sizes but lowers the contribution of $\sum_{j=1}^{k}\underline{\mathsf{P}}_{FA_j}\underline{\mathbb{P}}_{\mathcal{F}_h}|FA_j$, whereas a larger α increases detection sensitivity but also increases this contribution.

The aforementioned unfavorable GPS satellite geometry at 6.5 hours is illustrated in the skyplot of Fig. 4.8(a), which shows the positions of the GPS satellites as observed by the UAV GPS receiver at 6.5 hours. These positions are expressed in terms of their azimuth (relative to the North direction) and elevation angles (relative to the horizontal plane), both measured in degrees. Fig. 4.8(a) shows that most of the GPS satellites are distributed across the East-West direction leading to high uncertainties of the estimated 2D position coordinates along the South-North direction. Conversely, in the case of the smallest 'spike' in $\max_{\mathbf{b}} \underline{\mathsf{P}}_{\mathcal{F}_\mathrm{h}}(\mathbf{b})$ occurs at 11 hours, with a value of $8.01 \cdot 10^{-8} \pm 0.1155 \cdot 10^{-8}$. At this time, the wHDOP is 1.82 which indicates a favorable GPS satellite geometry as illustrated in Figure 4.8(b).

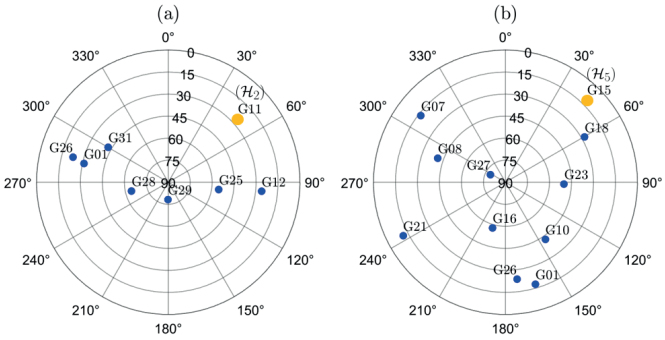

Figure 4.8: Over selected airspace in the Netherlands: (a) Skyplot of 8 GPS satellites at 6.5 hours with a wHDOP value of 4.15; (b) Skyplot of 11 GPS satellites at 11 hours with a wHDOP value of 1.82.

For the GPS satellite geometries in Fig. 4.8, we analyze the conditional components of the positioning failure probability under the alternative hypothesis $\mathcal{H}_2$ (outliers in G11 from Fig. 4.8(a)), and $\mathcal{H}_5$ (outliers in G15 from Fig. 4.8(b)). It should be noted that the two alternative hypotheses correspond to different time steps; the time index is omitted for notational simplicity. For an alternative hypothesis $\mathcal{H}_i$, one can decompose $\underline{\mathsf{P}}_{\mathcal{F}_\mathrm{h}}|\mathcal{H}_i(\mathrm{b}_i)$ as follows

$$\underline{\mathsf{P}}_{\mathcal{F}_\mathrm{h}}|\mathcal{H}_i(\mathrm{b}_i) = \mathsf{P}_{\mathrm{MD}_i}\underline{\mathsf{P}}_{\mathcal{F}_\mathrm{h}}|\mathrm{MD}_i + \underline{\mathsf{P}}_{\mathrm{CI}_i}\underline{\mathsf{P}}_{\mathcal{F}_\mathrm{h}}|\mathrm{CI}_i + \sum_{j\neq 0,i}^{k} \underline{\mathsf{P}}_{\mathrm{WI}_j}\underline{\mathsf{P}}_{\mathcal{F}_\mathrm{h}}|\mathrm{WI}_j \,, \tag{4.28}$$

where the testing decision events are Missed Detection (MD_i) with its probability $\mathsf{P}_{\mathrm{MD}_i} = \mathsf{P}(\underline{\mathrm{t}} \in \mathcal{P}_0|\mathcal{H}_i)$, Correct Indentification (CI_i) with $\mathsf{P}_{\mathrm{CI}_i} = \mathsf{P}(\underline{\mathrm{t}} \in \mathcal{P}_i|\mathcal{H}_i)$, and Wrong Identification (WI_j) with $\mathsf{P}_{\mathrm{WI}_j} = \mathsf{P}(\underline{\mathrm{t}} \in \mathcal{P}_j|\mathcal{H}_i)$ where $j \notin \{0, i\}$. The corresponding conditional probabilities of positioning failure are denoted $\underline{\mathsf{P}}_{\mathcal{F}_\mathrm{h}}|\mathcal{E}$, with $\mathcal{E} \in \{\mathrm{MD}_i,\ \mathrm{CI}_i,\ \mathrm{WI}_j\}$.

Fig. 4.9(a) shows that $\underline{\mathsf{P}}_{\mathcal{F}_\mathrm{h}}|\mathcal{H}_2(\mathrm{b}_2)$ is dominated by $\mathsf{P}_{\mathrm{MD}_2}\underline{\mathsf{P}}_{\mathcal{F}_\mathrm{h}}|\mathrm{MD}_2$ (with a maximum at $8.4302 \cdot 10^{-1}$ for $\mathrm{b}_2 = 16.68$ [m]) for outlier sizes b_2 up to 32 [m], after which $\underline{\mathsf{P}}_{\mathrm{CI}_2}\underline{\mathsf{P}}_{\mathcal{F}_\mathrm{h}}|\mathrm{CI}_2$ becomes dominant. This can be explained by mainly two aspects: (i) as outlier size b_2 increases, $\mathsf{P}_{\mathrm{MD}_2}$ decreases towards 0, reducing the contribution of $\underline{\mathsf{P}}_{\mathcal{F}_\mathrm{h}}|\mathrm{MD}_2$, while $\underline{\mathsf{P}}_{\mathrm{CI}_2}$ increases towards 1, thus increasing the contribution of $\underline{\mathsf{P}}_{\mathcal{F}_\mathrm{h}}|\mathrm{CI}_2$; (ii) when the outlier in G11 is correctly identified and excluded in the Adaptation step of the DIA procedure, the

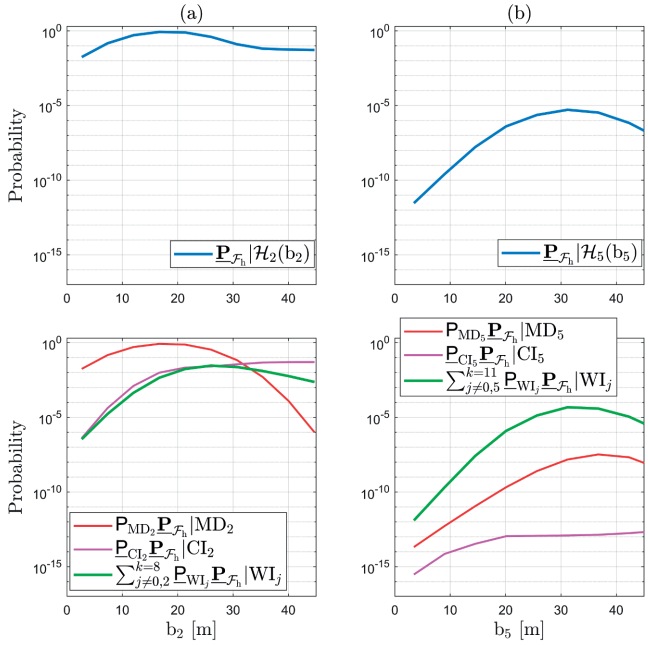

Figure 4.9: Over selected airspace in the Netherlands, the computed instantaneous: (a) $\underline{\mathbb{P}}_{\mathcal{F}_h}|\mathcal{H}_2(b_2)$ and its conditional components as function of outlier size b_2, at 6.5 hours; (b) $\underline{\mathbb{P}}_{\mathcal{F}_h}|\mathcal{H}_5(b_5)$ and its conditional components as function of outlier size b_5, at 11 hours.

remaining GPS geometry becomes highly unfavorable, as the satellites are nearly colinear along the East-West direction (see Fig. 4.8(a)), which increases $\underline{\mathbb{P}}_{\mathcal{F}_h}|\mathrm{CI}_2$. Another notable aspect of the geometry in Fig. 4.8(a) is that $\underline{\mathsf{P}}_{\mathrm{CI}_2}\underline{\mathbb{P}}_{\mathcal{F}_h}|\mathrm{CI}_i$ *exceeds* $\sum_{j\neq 0,2}^{k}\underline{\mathsf{P}}_{\mathrm{WI}_j}\underline{\mathbb{P}}_{\mathcal{F}_h}|\mathrm{WI}_j$ over almost the entire range of outlier sizes b_2 (except near 26 m). This indicates that the *total wrongful exclusions* does not necessarily yield higher probabilities of positioning failure under $\mathcal{H}_2$. In contrast, the case of a more favorable GPS satellite goemetry as shown in Fig. 4.9(b), considering outlier of varying sizes in satellite G15 ($\mathcal{H}_5$), shows that $\underline{\mathbb{P}}_{\mathcal{F}_h}|\mathcal{H}_5(b_5)$ is *completely* dominated by the term $\sum_{j\neq 0,5}^{k}\underline{\mathsf{P}}_{\mathrm{WI}_j}\underline{\mathbb{P}}_{\mathcal{F}_h}|\mathrm{WI}_j$ (with a maximum at $5.1597\cdot 10^{-6}$ for $b_5 = 31.19$ [m]), while $\underline{\mathsf{P}}_{\mathrm{CI}_5}\underline{\mathbb{P}}_{\mathcal{F}_h}|\mathrm{CI}_5$ has the lowest values across all outlier sizes b_5.

These results highlight the importance of a component-wise analysis of the probability of positioning failure. This approach reveals how specific testing decision outcomes and GPS satellite geometries drive the maximum (worst-case) or minimum (best-case) failure probabilities across different UAV positioning models. Such insight enables a deeper analysis of the chosen parameter estimation and hypothesis testing approaches, supports informed design trade-offs, and ultimately strengthens the safety assessment of positioning algorithms and systems. This level of detailed positioning safety analysis has been made possible by the computation method developed in [18].

4.5 Summary and Conclusions

In this contribution, we presented an approach for carrying out positioning safety analyses for UAVs in eight authorized European airspace regions. This approach is based mainly on the following: (i) the event of positioning failure [12] and its probability, (ii) accounting for the combined uncertainty of parameter estimation and statistical hypothesis testing in the PDF of the UAV position estimator according to the principles [16], and (iii) the recently developed method for computing the probability of positioning failure using principles from rare event simulation [18]. The application of this approach aligns with the scenario-based safety assessment framework applied to automated and autonomous vehicles [21–23] and is also suitable for UAVs [24].

We carried out positioning safety analyses using real GPS precise satellite orbits from the International GNSS Service (IGS) for a 24-hour period over the chosen eight European airspace regions: 1-Portugal, 2-Ireland, 3-Netherlands, 4-Norway, 5-Finland, 6-Romania, 7-Austria, and 8-Italy. The choice of the positioning model for UAVs under nominal conditions was based on the TSO certification for GPS-based UAV positioning [13, 26]. The results showed that the computed instantaneous maximum and minimum of $\mathbb{P}_{\mathcal{F}_\mathrm{h}}(\mathbf{b})$ vary significantly with the change in GPS satellite geometry over 24 hours (e.g., variations of approximately 9 orders of magnitude within 2 hours in the case of 5-Finland for the minimum of $\mathbb{P}_{\mathcal{F}_\mathrm{h}}(\mathbf{b})$). We also computed one-hour moving averages using the instantaneous $\mathbb{P}_{\mathcal{F}_\mathrm{h}}(\mathbf{b})$, at different UAV start flight times, to relate the results with the preliminary requirements at SAIL 3 (10^{-4}/hr) and 4 (10^{-5}/hr) [14]. For SAIL 3, only in the selected airspaces over the Netherlands and Romania are the horizontal positioning safety requirements not met for 100% of flight start times. In the case of SAIL 4, only in the selected airspace over Italy the horizontal positioning safety requirement is met 100% of flight start times for both SAIL 3 and SAIL 4. In Ireland the percentages are lowest for both Case 3 and 4, at SAIL 4, among all chosen locations. The sensitivity to the assumptions about the apriori probabilities of the hypotheses and the choice of the level of significance was also analyzed, revealing that the positioning safety requirements may not be met in more than 50% of the flight starting times. To increase the percentages from Tables 4.2 and 4.3 for SAIL 3 and SAIL 4 en-route UAV operations, several options, or combinations thereof, could be considered: (i) certification of additional GNSS constellations, such as the European Galileo, to be used alongside GPS for UAV operations, (ii) usage of GPS receivers with better precision of the observables, (iii) application of principles from the new theoretical framework introduced in [34] to design parameter estimation and statistical hypothesis testing procedures with the objective to minimize the probability of positioning failure. Additionally, as a concrete example, the results over the Netherlands demonstrated how the developed method [18] enables a component-wise analysis of the probability of positioning failure. The decomposition into components conditioned on hypothesis testing decisions (i.e., correct acceptance, false alarm, missed detection, correct identification, wrong identification) revealed how an unfavorable satellite geometry (e.g., nearly colinear satellite constellation) and different decision outcomes drive the highest and lowest values of the probability of positioning failure under a given alternative hypothesis, and how the choice of significance level α drives the relative contributions of the components conditioned on correct acceptance and false alarm decisions. We also showed that a situation arises where the wrongful exclusion

of satellites does not necessarily yield the highest contributions of the corresponding conditional components to the probability of positioning failure under the given alternative hypothesis. This case study illustrates the advantages of the method in providing detailed insight into the mechanisms underlying positioning safety, thereby supporting informed design trade-offs and improving safety assessments of UAV positioning algorithms and systems.

This type of positioning-safety analysis can be useful in various other cases, such as further development and verification of UAV positioning safety requirements, helping vertiport operators and designers determine the expected probabilities of positioning failures of the UAVs at the desired locations. Although the presented positioning-safety analysis was based on the positioning performance of a representative TSO-certified GPS receiver, the proposed method for formulating and computing the probability of positioning failure is also applicable to UAV multisensor positioning, which represents a topic for future work. Moreover, the developed computation method of the probability of positioning failure can be incorporated into positioning-safety simulators, enabling integrated studies together with other key functionalities of automated navigation systems, such as planning, control, and perception [23].

4.6 Appendix: Components of $\underline{\mathbb{P}}_{\mathcal{F}_h}|\mathcal{H}_0$ over Netherlands when $\alpha = 10^{-3}$

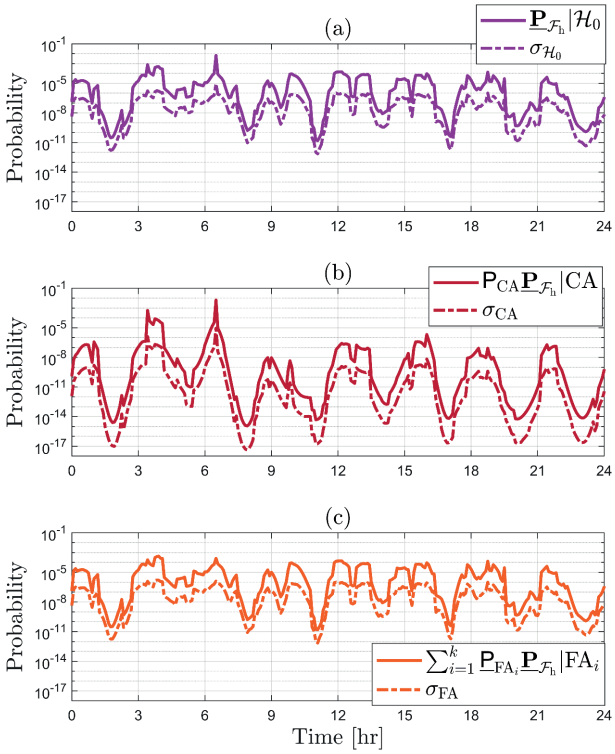

Figure 4.10: Over selected airspace in the Netherlands, the computed instantaneous: (a) $\underline{\mathbb{P}}_{\mathcal{F}_h}|\mathcal{H}_0$ and its simulation standard deviation ($\sigma_{\mathcal{H}_0}$); (b) $\mathsf{P}_{\mathrm{CA}}\underline{\mathbb{P}}_{\mathcal{F}_h}|\mathrm{CA}$ and its simulation standard deviation (σ_{CA}); (c) $\sum_{j=1}^{k}\underline{\mathsf{P}}_{\mathrm{FA}_j}\underline{\mathbb{P}}_{\mathcal{F}_h}|\mathrm{FA}_j$ and its simulation standard deviation (σ_{FA}). The chosen level of significance is $\alpha = 10^{-3}$.

Bibliography

[1] Y. T. J. Morton et al., editors. *Position, Navigation, and Timing Technologies in the 21st Century: Integrated Satellite Navigation, Sensor Systems, and Civil Applications.* Wiley, IEEE Press, 2020.

[2] J. C. Hodgson et al. Precision Wildlife Monitoring Using Unmanned Aerial Vehicles. *Nature Scientific Reports*, 6(22574):1–7, 2016.

[3] O. G. Crespillo et al. Vertiport Navigation Requirements and Multisensor Architecture Considerations for Urban Air Mobility. *CEAS Aeronautical Journal*, 2024.

[4] C. Luo et al. UAV Position Estimation and Collision Avoidance Using the Extended Kalman Filter. *IEEE Transactions on Vehicular Technology*, 62(6):2749–2762, 2013.

[5] Z. Wang et al. Feasibility Study of UAV-Assisted Anti-Jamming Positioning. *IEEE Transactions on Vehicular Technology*, 70(8):7718–7733, 2021.

[6] W. Zhang and W. Zhang. An Efficient UAV Localization Technique Based on Particle Swarm Optimization. *IEEE Transactions on Vehicular Technology*, 71(9):9544–9557, 2022.

[7] F. Zhou, J. Tang, and W. Chen. Placement and Concise MSE Lower-Bound for UAV-Enabled Localization via RSS. *IEEE Transactions on Vehicular Technology*, 71(2):2209–2213, 2022.

[8] S. Bayat and R. Amiri. Advances in UAV-Assisted Localization: Joint Source and UAV Parameter Estimation. *IEEE Transactions on Vehicular Technology*, 72(11):14268–14278, 2023.

[9] P. J. G. Teunissen and O. Montenbruck, editors. *Handbook of Global Navigation Satellite Systems.* Springer, 2017.

[10] J. C. J. Koelemeij et al. A Hybrid Optical-Wireless Network for Decimetre-Level Terrestrial Positioning. *Nature*, 611(7936):473–478, November 2022.

[11] J. Peng et al. UAV Positioning Based on Multi-Sensor Fusion. *IEEE Access*, 8:34455–34467, 2020.

[12] RTCA-Special Committee 159. Minimum Operational Performance Standards (MOPS) for Global Positioning System/Satellite-Based Augmentation System Airborne Equipment. Do-229f, Radio Technical Commission for Aeronautics, 2020.

[13] Federal Aviation Administration. Technical Standard Order C-145e: Airborne Navigation Sensors Using the Global Positioning System Augmented by the Satellite Based Augmentation System (SBAS). Technical report, 2017.

[14] European Union Agency for the Space Programme. Report on Aviation and Drones: User Needs and Requirements. Technical report, 2023.

[15] Q. Cheng, R. Sun, and J. Wang. A New Historical Data Based GNSS Fault Detection and Exclusion Algorithm for UAV Positioning. In *IEEE International Conference on Civil Aviation Safety and Information Technology*, 2020.

[16] P. J. G. Teunissen. Distributional Theory for the DIA Method. *Journal of Geodesy*, 92(1):59–80, 2018.

[17] S. Ciuban, P. J. G. Teunissen, and C. C. J. M. Tiberius. Dependence Between Parameter Estimation and Statistical Hypothesis Testing: Positioning Safety Analysis for Automated/Autonomous Vehicles. *IEEE Transactions on Intelligent Transportation Systems*, 26(4):5509–5521, 2025.

[18] S. Ciuban, P. J. G. Teunissen, and C. C. J. M. Tiberius. A Method to Compute the Probability of Positioning Failure for Vehicles in the Context of Dependence Between Parameter Estimation and Statistical Hypothesis Testing. *IEEE Transactions on Vehicular Technology*, 74(10):15238–15253, 2025.

[19] H. Kahn and A. W. Marshall. Methods of Reducing Sample Size in Monte Carlo Computations. *Journal of the Operations Research Society of America*, 1(5):263–278, 1953.

[20] R. Y. Rubinstein. The Cross-Entropy Method for Combinatorial and Continuous Optimization. *Methodology and Computing in Applied Probability*, 1:127–190, 1999.

[21] S. Riedmaier et al. Survey on Scenario-Based Safety Assessment of Automated Vehicles. *IEEE Access*, 8:87456–87477, 2020.

[22] U.N.E.C.E. New Assessment/Test Method for Automated Driving (NATM) Guidelines for Validating Automated Driving Systems (ADS). Technical report, United Nations Economic Commission for Europe - Inland Transport Committee, 2023.

[23] E. de Gelder et al. TNO Street Wise: Scenario-Based Safety Assessment of Automated Driving Systems. White paper, Netherlands Organisation for Applied Scientific Research (TNO), 2024.

[24] S. Khatiri et al. Simulation-Based Test Case Generation for Unmanned Aerial Vehicles in the Neighborhood of Real Flights. In *IEEE Conference on Software Testing, Verification, and Validation*, 2023.

[25] European Union Aviation Safety Agency. National Aviation Authority Drone Website Reference. Available at `https://www.easa.europa.eu/en/domains/civil-drones/naa`.

[26] T. Cozzens. uAvionix receives FAA order for certified drone GPS receiver, 2021. GPS World, August, 2021. [Online].

[27] G. Johnston, A. Riddell, and G. Hausler. The International GNSS Service. In P. J. G. Teunissen and O. Montenbruck, editors, *Springer Handbook of Global Navigation Satellite Systems*, pages 967–982. Springer, 2017.

[28] D. Odijk. Positioning Model. In P. J. G. Teunissen and O. Montenbruck, editors, *Springer Handbook of Global Navigation Satellite Systems*, page 617. Springer, 2017.

[29] M. Maaref, J. Khalife, and Z. M. Kassas. Aerial Vehicle Protection Level Reduction by Fusing GNSS and Terrestrial Signals of Opportunity. *IEEE Transactions on Intelligent Transportation Systems*, 22(9):5976–5993, 2021.

[30] P. J. G. Teunissen. *Testing Theory: An Introduction.* Mathematical Geodesy and Positioning. Delft University Press, 2nd edition, 2006.

[31] C. P. Robert and G. Casella. *Monte Carlo Statistical Methods.* Springer, 1999.

[32] P. J. G. Teunissen. Batch and Recursive Model Validation. In P. J. G. Teunissen and O. Montenbruck, editors, *Springer Handbook of Global Navigation Satellite Systems*, pages 687–720. Springer, 2017.

[33] S. Zaminpardaz and P. J. G. Teunissen. Detection-only Versus Detection and Identification of Model Misspecifications. *Journal of Geodesy*, 97(55):1–19, 2023.

[34] P. J. G. Teunissen. On the Optimality of DIA-Estimators: Theory and Applications. *Journal of Geodesy*, 98(43):1–26, 2024.

[35] S. Ciuban, P. J. G. Teunissen, and C. C. J. M. Tiberius. GNSS Positioning Safety: Probability of Positioning Failure and Its Components. In *Proceedings of the 37th International Technical Meeting of the Satellite Division of the Institute of Navigation (ION GNSS+)*, pages 2228–2249, 2024.

[36] J. Morio and M. Balesdent. *Estimation of Rare Event Probabilities in Complex Aerospace and Other Systems: A Practical Approach.* Elsevier B.V, 2016.

[37] D. Odijk. Positioning Model. In P. J. G. Teunissen and O. Montenbruck, editors, *Springer Handbook of Global Navigation Satellite Systems*, pages 612–618. Springer, 2017.

[38] P. J. G. Teunissen. Nonlinear Least Squares. *Manuscripta Geodaetica*, 15(3):137–150, 1990.

[39] H. J. Euler and C. C. Goad. On Optimal Filtering of GPS Dual Frequency Observations Without Using Orbit Information. *Bulletin Geodesique*, 65(2):130–143, 1991.

[40] uAvionix. truFYX TSO GPS Receiver for Unmanned Aerial Systems: Product Details and Specifications. Available at `https://uavionix.store/unmanned-navigation/trufyx-tso`.

[41] W. Baarda. Statistical Concepts in Geodesy. *Netherlands Geodetic Commission, Publications on Geodesy*, 2(4):1–74, 1967.

[42] S. Wang et al. Enhancing Navigation Integrity for Urban Air Mobility with Redundant Inertial Sensors. *Aerospace Science and Technology*, 126(107631):1–13, 2022.

[43] J. She et al. Implementation of the Reference Advanced RAIM User Algorithm. In *Proceedings of the 36th International Technical Meeting of the Satellite Division of the Institute of Navigation (ION GNSS+)*, pages 1099–1127, 2023.

[44] D. H. Won et al. Weighted DOP With Consideration on Elevation-Dependent Range Errors of GNSS Satellites. *IEEE Transactions on Instrumentation and Measurement*, 61(12):3241–3250, 2012.

5

DIA-estimator and multidimensional model misspecifications

The Detection, Identification, and Adaptation (DIA)-estimator integrates parameter estimation and hypothesis testing for model misspecifications. This contribution presents a positioning safety analysis approach grounded in the DIA-estimator framework, with a particular emphasis on multidimensional model misspecifications, such as simultaneous outliers in the observations. While recent work has focused on the performance of the detection and identification of multidimensional model misspecifications, we turn our attention to how they affect the probability density function (PDF) of the DIA-estimator and, consequently, the probability of positioning failure—an indicator relevant for safety-of-life applications (e.g., automotive, aviation, rail, maritime). This work formulates and quantifies the probability of positioning failure and its conditional components. A representative simulation-based study is presented for a UAV equipped with a GPS receiver configured to achieve performance comparable to Technical Standard Order (TSO)-certified receivers. The analysis is carried out for two scenarios: a fixed GPS satellite geometry at a single time snapshot, and for a varying GPS satellite geometry over a 24-hour period over an authorized UAV airspace region in the Netherlands using real satellite ephemeris data. Together, these scenarios provide insights into the structure of the DIA-estimator's PDF, such as multimodality and orientation with respect to the chosen positioning safety region, and support comprehensive evaluation of positioning safety. Although the current focus is on GPS-based positioning, the presented approach is general and can be extended to include multisensor configurations, additional GNSS constellations, and applied to other safety-critical applications, which are subjects of future work.

This chapter is based on the journal article *S. Ciuban, P.J.G. Teunissen, and C.C.J.M. Tiberius. "DIA-Estimator and Multidimensional Model Misspecifications: GNSS-based Positioning Safety Analysis for UAVs", GPS Solutions, Submitted.*

5.1 Introduction

The Detection, Identification, and Adaptation (DIA)-estimator $\underline{\hat{x}} \in \mathbb{R}^n$, introduced by Teunissen, is part of a unifying framework that captures the interplay between parameter estimation and hypothesis testing in the context of the DIA method [1]. Parameter estimation is performed to obtain estimates of the parameters of interest, while hypothesis testing is used to validate these results and adapt the underlying models in the case of misspecifications. The DIA method has found applications across a wide range of domains, such as in GNSS-based positioning [2–4], quality control in geodetic networks [5], deformation monitoring [6], quality control in navigation system [7], and, more recently, in positioning safety analyses for automated and autonomous driving [8], among others.

Accounting for the occurrence of multidimensional misspecifications (e.g., multiple outliers) when deciding on the alternative models (hypotheses) for the DIA method is of particular interest, as it more accurately reflects real-world conditions. Recent studies have investigated the performance of the testing procedure with respect to its ability to detect and identify multiple outliers [9–11]. However, these studies have primarily focused on the detection and identification aspects, without considering how such multidimensional misspecifications affect the probability density function (PDF) $f_{\underline{\hat{x}}}(x)$ of the DIA-estimator. This consideration is particularly important for positioning safety analyses in safety-of-life applications (e.g., automotive, aviation, rail, maritime), where the probability of positioning failure is of interest [4, 8, 12]

$$\mathbb{P}_{\mathcal{F}} = \mathsf{P}(\underline{\hat{x}} \in \mathcal{B}^c) = \int_{\mathcal{B}^c} f_{\underline{\hat{x}}}(x)\, dx, \tag{5.1}$$

with $\mathcal{F} = \{\underline{\hat{x}} \in \mathcal{B}^c\}$ being the event of positioning failure [13] and $\mathcal{B}^c \subset \mathbb{R}^n$ is the complement of an application specific safety-region $\mathcal{B} \subset \mathbb{R}^n$. In this contribution, we present an approach for performing positioning safety analyses aimed at quantifying (5.1) and its conditional components, while accounting for multidimensional model misspecifications caused by outliers in the observations.

With respect to our previous research [4, 8, 12], the main contributions are as follows: (i) analysis of the impact of multidimensional outliers on the shape of the conditional components of the DIA-estimator's $f_{\underline{\hat{x}}}(x)$; (ii) consideration of time-varying positioning functional and stochastic models (e.g., due to the evolution of GPS satellite geometry over 24 hours) into the computation of the probability of positioning failure; (iii) application of the DIA estimator's framework to Unmanned Aerial Vehicle (UAV) cases, demonstrating its relevance in this domain.

To illustrate the approach for positioning safety analysis, we present a representative case study for an Unmanned Aerial Vehicle (UAV) assumed to be equipped with a GPS receiver configured to achieve positioning performance comparable to that of receivers certified under the Technical Standard Order (TSO) for GPS-based UAV operations [14, 15]. The analysis is carried out for two scenarios. The first scenario considers a GPS satellite geometry as observed by the UAV's GPS receiver at a snapshot of time, enabling detailed analysis of the conditional components of the DIA-estimator's PDF relative to the shape of

the safety region $\mathcal{B} \subset \mathbb{R}^n$, as well as the computed components of the probability of positioning failure. In the second scenario we consider a 24-hours (on May 24, 2024) evolution of GPS satellites moving over an airspace region in The Netherlands for which authorization can be obtained for UAV operations [16]. Together, these scenarios provide insights into the behavior of the DIA-estimator's PDF and, consequently, into the components of the probability of positioning failure—supporting a comprehensive evaluation of positioning safety. The presented positioning safety analysis is consistent with scenario-based safety assessment frameworks, which are widely used in domains such as automated and autonomous vehicles [17–19] and UAVs [20], among others.

This contribution is organized as follows: In Section 5.2 we briefly review the main principles of the DIA-estimator $\underline{\hat{x}} \in \mathbb{R}^n$ and of its PDF $f_{\underline{\hat{x}}}(x)$. In Section 5.3 we present the formulation of the probability of positioning failure and its components. Section 5.4 presents the positioning-safety analysis for a UAV at a single snapshot of time and over a period of 24 hours. Section 5.5 gives several details about the used computational resources and Section 5.6 contains the summary and the concluding remarks of this contribution.

Throughout the paper we make use of the following notation: an underscore denotes a random quantity (e.g., the random vector $\underline{y} \in \mathbb{R}^m$), $f_{\underline{y}}(y)$ is the PDF of $\underline{y} \in \mathbb{R}^m$, and $\mathsf{E}_{f_{\underline{y}}}(\underline{y}) = \int_{\mathbb{R}^m} y f_{\underline{y}}(y) dy$ is the expected value of $\underline{y} \in \mathbb{R}^m$. The joint PDF of two random vectors $\underline{x} \in \mathbb{R}^n$ and $\underline{y} \in \mathbb{R}^m$ is denoted $f_{\underline{x},\underline{y}}(x, y)$. A projection matrix is denoted as $\mathbf{\Pi}_A$ and it projects orthogonally onto the range space of the matrix $A \in \mathbb{R}^{m \times n}$ ($\mathcal{R}(A)$). For the weighted squared norm of a vector we use the notation $\|\underline{y}\|^2_{Q_{yy}} = \underline{y}^T Q_{yy}^{-1} \underline{y}$. If the squared norm is with respect to (w.r.t.) the identity matrix then it is denoted $\|.\|^2$. A normal PDF is denoted as $\mathcal{N}(.,.)$, a chi-squared PDF as $\chi^2(.,.)$, and a uniform PDF as $\mathcal{U}(.,.)$.

5.2 Review of DIA-Estimator

This section provides a concise review of the principles of *combined* parameter estimation and statistical hypothesis testing, as established in the theoretical framework of the DIA-estimator [1]. We start by considering a linear(ized) observation model with normally (Gaussian) distributed observables [21–23],

$$\underline{y} \in \mathbb{R}^m \sim \mathcal{N}\left(\mathsf{E}_{f_{\underline{y}}}(\underline{y}), Q_{yy}\right), \tag{5.2}$$

where misspecifications could occur in the mean $\mathsf{E}_{f_{\underline{y}}}(\underline{y}) \in \mathbb{R}^m$, vc-matrix $Q_{yy} \in \mathbb{R}^{m \times m}$, and/or in the assumed type of the probability distribution $f_{\underline{y}}(y)$, meaning the Gaussian assumption may not hold. In this contribution, we focus on the case of misspecifications in the mean, as these are the most common in practice (e.g., caused by outliers) [24]. To account for such misspecifications of the observation model, the following multiple hypothesis testing problem is formulated

$$\mathcal{H}_0 : \mathsf{E}_{f_{\underline{y}}}(\underline{y}) = Ax \quad \text{vs.} \quad \mathcal{H}_{i \neq 0} : \mathsf{E}_{f_{\underline{y}}}(\underline{y}) = Ax + C_i b_i, \tag{5.3}$$

where $A \in \mathbb{R}^{m \times n}$ is the design matrix with $\text{rank}(A) = n$, $x \in \mathbb{R}^n$ is the vector of unknown parameters, and k-alternative hypotheses with index $i \in \{1, ..., k\}$. The outliers in the obser-

vation model are specified by the matrix $C_i \in \mathbb{R}^{m\times q_i}$, and $\text{rank}([A, C_i]) = n + q_i$ with $b_i \in \mathbb{R}^{q_i}$ being the (unknown) vector containing the sizes of the outliers. The misclosure vector $\underline{t} \in \mathbb{R}^r$, which has the dimension of the redundancy $r = m - n$, can be used to build test statistics for the decision problem in (5.3), since it provides a measure of inconsistency between the model under $\mathcal{H}_0$ and the observables. The expressions of $\underline{t} \in \mathbb{R}^r$ and its vc-matrix $Q_{tt} \in \mathbb{R}^{r\times r}$ are [25]

$$\underline{t} = B^T \underline{y}, \quad Q_{tt} = B^T Q_{yy} B, \tag{5.4}$$

where $B \in \mathbb{R}^{m\times r}$ is a basis matrix of $\mathcal{R}(A)^\perp$ (i.e., $B^T A = 0_{r\times n}$). The misclosure vector $\underline{t} \in \mathbb{R}^r$ can be used to connect the Best Linear Unbiased Estimators (BLUEs) of $x \in \mathbb{R}^n$ under the alternative hypotheses $\mathcal{H}_{i\neq 0}$'s, to the corresponding estimator under $\mathcal{H}_0$, as follows [1]

$$\begin{bmatrix} \underline{\hat{x}}_i \\ \underline{t} \end{bmatrix} = \begin{bmatrix} I_n & -L_i \\ 0_{r\times n} & I_r \end{bmatrix} \begin{bmatrix} \underline{\hat{x}}_0 \\ \underline{t} \end{bmatrix}, \text{ with } L_i = \begin{cases} 0_{n\times r} & , i = 0 \\ A^+ C_i C_{t_i}^+ & , i \neq 0 \end{cases} \tag{5.5}$$

where $\underline{\hat{x}}_0 = A^+ \underline{y}$ and $A^+ = Q_{\hat{x}_0\hat{x}_0} A^T Q_{yy}^{-1}$ is the BLUE-inverse of $A \in \mathbb{R}^{m\times n}$. The BLUE-inverse of $C_{t_i} = B^T C_i$ is $C_{t_i}^+ = (C_{t_i}^T Q_{tt}^{-1} C_{t_i})^{-1} C_{t_i}^T Q_{tt}^{-1}$. The PDF of $\left[\underline{\hat{x}}_i^T \ \underline{t}^T\right]^T$, under hypothesis $\mathcal{H}_a$ with $a \in \{0, ..., k\}$, is

$$\mathcal{H}_a : \begin{bmatrix} \underline{\hat{x}}_i \\ \underline{t} \end{bmatrix} \sim \mathcal{N}\left(\begin{bmatrix} x + A^+ R_i C_a b_a \\ B^T C_a b_a \end{bmatrix}, \begin{bmatrix} Q_{\hat{x}_0\hat{x}_0} + L_i Q_{tt} L_i^T & -L_i Q_{tt} \\ -Q_{tt} L_i^T & Q_{tt} \end{bmatrix} \right), \tag{5.6}$$

where $R_i = I_m - C_i \left(B^T C_i\right)^+ B^T$, in which $\left(B^T C_i\right)^+ = \left(C_i^T B Q_{tt}^{-1} B^T C_i\right)^{-1} C_i^T B Q_{tt}^{-1}$. The matrix R_i projects along $\mathcal{R}(C_i)$ and onto $\mathcal{R}(A, Q_{yy}B(B^T C_i)^\perp)$ with $(B^T C_i)^\perp$ being a basis matrix of the null space of $C_i^T B$. The variance-covariance $Q_{\hat{x}_0\hat{x}_0} = (A^T Q_{yy}^{-1} A)^{-1}$ is the one of $\underline{\hat{x}}_0$. Note that for a given $\mathcal{H}_a$, the following two-cases hold for the joint PDF of $\left[\underline{\hat{x}}_i^T \ \underline{t}^T\right]^T$,

$$f_{\underline{\hat{x}}_i, \underline{t}}(x, t) \begin{cases} = f_{\underline{\hat{x}}_0}(x) f_{\underline{t}}(t) & , \text{ if } i = 0 \\ \neq f_{\underline{\hat{x}}_i}(x) f_{\underline{t}}(t) & , \text{ if } i \neq 0, \end{cases} \tag{5.7}$$

which shows that, for $i \neq 0$, the BLUEs $\underline{\hat{x}}_i$ and the misclosure vector $\underline{t}$ are dependent (see an illustrative example in Section IV.1 of [4]). By applying partitioning principles, the hypothesis testing problem in (5.3) can be represented in the misclosure vector space $\mathbb{R}^r$. Partitions in $\mathbb{R}^r$ can be formulated based on the subsets $\mathcal{P}_i \subset \mathbb{R}^r$, for $i \in \{0, ..., k\}$, such that $\cup_{i=0}^k \mathcal{P}_i = \mathbb{R}^r$, and $\mathcal{P}_i \cap \mathcal{P}_j = \{0\}$ for $i \neq j$. The $k+1$ partitions can be defined as follows,

$$\begin{aligned} \mathcal{P}_0 &= \left\{ t \in \mathbb{R}^r \mid \|t\|_{Q_{tt}}^2 \leq \chi_\alpha^2(r, 0) \right\}, \\ \mathcal{P}_{i\neq 0} &= \left\{ t \in \mathbb{R}^r \mid t \notin \mathcal{P}_0, \ \check{T}_i = \max_{l\in\{1,...,k\}} T_l \right\}, \end{aligned} \tag{5.8}$$

where $\|\underline{t}\|_{Q_{tt}}^2$ is the overall model test statistic, $\chi_\alpha^2(r, 0)$ is the Chi-squared critical value for a level of significance α, and $\underline{T}_l$ is the result of the following transformation [9, 24]

$$\underline{T}_l = \text{CDF}_{\chi^2(q_l, 0)} \left(\|\Pi_{C_{t_l}} \underline{t}\|_{Q_{tt}}^2 \right), \tag{5.9}$$

where $\text{CDF}_{\chi^2(q_l,0)}(.)$ is the cumulative distribution function (CDF) of $\chi^2(q_l,0)$, $\|\boldsymbol{\Pi}_{\text{C}_{\text{t}_l}}\underline{\text{t}}\|^2_{\text{Q}_{\text{tt}}} \overset{\mathcal{H}_0}{\sim} \chi^2(q_l,0)$, $\boldsymbol{\Pi}_{\text{C}_{\text{t}_l}} = \text{C}_{\text{t}_l}\text{C}^+_{\text{t}_l}$ projects onto $\mathcal{R}(\text{C}_{\text{t}_l})$, and $\text{C}_{\text{t}_l} = \text{B}^T\text{C}_l$ while $\text{C}^+_{\text{t}_l} = (\text{C}^T_{\text{t}_l}\text{Q}^{-1}_{\text{tt}}\text{C}_{\text{t}_l})^{-1}\text{C}^T_{\text{t}_l}\text{Q}^{-1}_{\text{tt}}$, and $\underline{\text{T}}_l \overset{\mathcal{H}_0}{\sim} \mathcal{U}(0,1)$. Note that the evaluation of $\text{CDF}_{\chi^2(q_l,0)}(.)$ must be done k-times, which can be computationally expensive for a larger number of alternative hypothesis. To mitigate this, one can: (i) group the alternative hypotheses by their common dimension q_l, and denote the number of resulting groups as g; for a simple example with $m = 4$, $n = 1$, $r = 3$, and $k = 10$, we have four one-dimensional outliers, one per observation $q_{l\in\{1,...,4\}} = 1$ and six two-dimensional ones $q_{l\in\{5,...,10\}} = 2$, and thus $g = 2$; (ii) within each group $\mathcal{G}$, compute $\max_{l\in\mathcal{G}} \|\boldsymbol{\Pi}_{\text{C}_{\text{t}_l}}\underline{\text{t}}\|^2_{\text{Q}_{\text{tt}}}$; (iii) evaluate the corresponding CDF at each of these maximum values; (iv) select the maximum among these g transformed CDF values. This procedure reduces the evaluation of the CDF from k-times to g-times.

The role of the partitions in (5.8) is such that a hypothesis $\mathcal{H}_i$, for $i \in \{0,...,k\}$, is selected as the most likely one if and only if $\underline{\text{t}} \in \mathcal{P}_i$. Figure 5.1 shows the partitions (volumes) obtained when considering one and two-dimensional model outliers for a simple example.

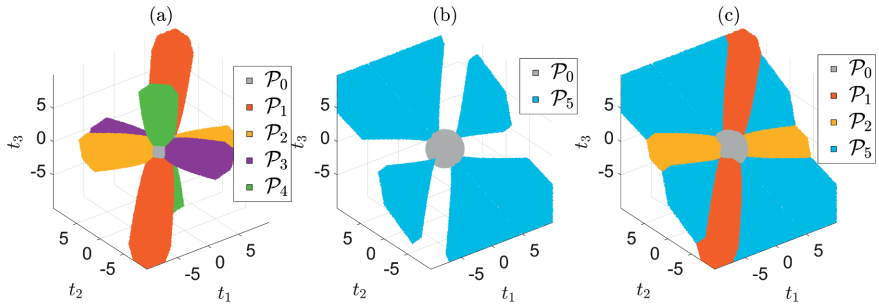

Figure 5.1: Partition of $\mathbb{R}^{r=3}$ when $\text{A} = [1\ 1\ 1\ 1]^T \in \mathbb{R}^{4\times 1}$, $\text{x} \in \mathbb{R}$, $\text{Q}_{\text{yy}} = \text{I}_4$, $\text{c}_i \in \mathbb{R}^{4\times(q_i=1)}$ models one-dimensional outliers for $i = \{1,..,4\}$ (e.g., $\text{c}_1 = \begin{bmatrix}1 & 0 & 0 & 0\end{bmatrix}^T$, and $\text{C}_i \in \mathbb{R}^{4\times(q_i=2)}$ model two dimensional outliers for $i = \{5,...,10\}$ (e.g., $\text{C}_5 = \begin{bmatrix}1 & 0 & 0 & 0\\ 0 & 1 & 0 & 0\end{bmatrix}^T = \begin{bmatrix}\text{c}_1^T\\ \text{c}_2^T\end{bmatrix}^T$). Partioning is done according to (5.8) for all $k+1$ hypotheses, with $k = 10$. As examples: (a) shows partitions $\mathcal{P}_0$ and $\mathcal{P}_{i\neq 0}$ for $i \in \{1,...,4\}$ in colors, while the white space represents $\mathbb{R}^{r=3}\backslash(\cup_{i=0}^4 \mathcal{P}_i)$; (b) shows partitions $\mathcal{P}_0$ and $\mathcal{P}_5$ while the white space represents $\mathbb{R}^{r=3}\backslash(\cup_{i\in\{0,5\}}\mathcal{P}_i)$; (c) partitions $\mathcal{P}_0$ and $\mathcal{P}_{i\neq 0}$ for $i \in \{1,2,5\}$ while the white space represents $\mathbb{R}^{r=3}\backslash(\cup_{i\in\{0,1,2,5\}}\mathcal{P}_i)$.

Note that an undecided region $\Omega \subset \mathbb{R}^r$ can be included to accommodate situations when it would be difficult to discriminate between hypotheses or when not all possible outliers can be anticipated. In this contribution, we consider that always an estimator is selected (i.e., no $\Omega \subset \mathbb{R}^r$ is included). The decision outcome in statistical hypothesis testing is determined by where the misclosure vector $\underline{\text{t}}$ lands in $\mathbb{R}^r$ with partitions $\mathcal{P}_i \subset \mathbb{R}^r$, for $i \in \{0,..,k\}$, cf. (5.8). Under $\mathcal{H}_0$, the decision results are: (i) Correct Acceptance (CA) of $\mathcal{H}_0$ when $\underline{\text{t}} \in \mathcal{P}_0$, and (ii) False Alarm (FA) when $\underline{\text{t}} \notin \mathcal{P}_0$, or specifically the FA per alternative hypothesis (i.e., FA_i) when $\underline{\text{t}} \in \mathcal{P}_i$ for $i > 0$. The probabilities of these decisions are given by

$$\text{P}_{\text{CA}} = \text{P}(\underline{\text{t}} \in \mathcal{P}_0|\mathcal{H}_0), \quad \text{P}_{\text{FA}} = \sum_{i=1}^{k} \underbrace{\text{P}(\underline{\text{t}} \in \mathcal{P}_i|\mathcal{H}_0)}_{\text{P}_{\text{FA}_i}}, \tag{5.10}$$

where $\mathsf{P}_{\text{FA}} = \alpha$ is the level of significance and $\mathsf{P}_{\text{CA}} + \mathsf{P}_{\text{FA}} = 1$. Similarly, under $\mathcal{H}_i$, for $i > 0$, the outcomes of the decisions are: (i) missed detection (MD) when $\underline{\mathrm{t}} \in \mathcal{P}_0$, (ii) Correct Identification (CI) when $\underline{\mathrm{t}} \in \mathcal{P}_i$, and (iii) Wrong Identification (WI) $\underline{\mathrm{t}} \in \mathcal{P}_j$ for $j \notin \{0, i\}$. Their probabilities are

$$\mathsf{P}_{\text{MD}_i} = \mathsf{P}\left(\underline{\mathrm{t}} \in \mathcal{P}_0 | \mathcal{H}_i\right), \;\; \mathsf{P}_{\text{CI}_i} = \mathsf{P}\left(\underline{\mathrm{t}} \in \mathcal{P}_i | \mathcal{H}_i\right), \;\; \mathsf{P}_{\text{WI}} = \sum_{j \neq 0, i}^{k} \underbrace{\mathsf{P}\left(\underline{\mathrm{t}} \in \mathcal{P}_j | \mathcal{H}_i\right)}_{\mathsf{P}_{\text{WI}_j}}, \tag{5.11}$$

where the decision outcome of Correct Detection (CD) is given by $\mathsf{P}_{\text{CD}_i} = \mathsf{P}_{\text{CI}_i} + \mathsf{P}_{\text{WI}}$ satisfying $\mathsf{P}_{\text{MD}_i} + \mathsf{P}_{\text{CD}_i} = 1$. The probabilities in (5.11) depend on the unknown model misspecification vector $\mathrm{b}_i \in \mathbb{R}^{q_i}$ since $f_{\underline{\mathrm{t}}}(t|\mathcal{H}_i) = \mathcal{N}\left(\mathrm{B}^T \mathrm{C}_i \mathrm{b}_i, \mathrm{Q}_{\mathrm{tt}}\right)$.

The Detection (D) Identification (I) and Adaptation (A) statistical testing procedure is then

$$\begin{cases} \text{if } \underline{\mathrm{t}} \in \mathcal{P}_0 \text{ (no D)} \rightarrow \text{ output } \hat{\underline{\mathrm{x}}}_0, \\ \text{if } \underline{\mathrm{t}} \notin \mathcal{P}_0 \text{ (D)} \rightarrow \; \underline{\mathrm{t}} \in \mathcal{P}_{i \neq 0} \text{ (I)} \rightarrow \text{ output } \hat{\underline{\mathrm{x}}}_i \text{ (A)}, \end{cases} \tag{5.12}$$

where $\hat{\underline{\mathrm{x}}}_0 \in \mathbb{R}^n$ and $\hat{\underline{\mathrm{x}}}_i \in \mathbb{R}^n$ are the Best Linear Unbiased Estimators (BLUEs) of $\mathrm{x} \in \mathbb{R}^n$ under $\mathcal{H}_0$ and $\mathcal{H}_{i \neq 0}$. The estimator that captures the procedure in (5.12) is the DIA-estimator [1]

$$\overline{\underline{\mathrm{x}}} = \sum_{i=0}^{k} \hat{\underline{\mathrm{x}}}_i \, p_i(\underline{\mathrm{t}}) = \hat{\underline{\mathrm{x}}}_0 - \sum_{i=1}^{k} \mathrm{L}_i \, \underline{\mathrm{t}} \, p_i(\underline{\mathrm{t}}), \tag{5.13}$$

where the indicator function $p_i(\underline{\mathrm{t}}) = 1$ if $\underline{\mathrm{t}} \in \mathcal{P}_i$ and $p_i(\underline{\mathrm{t}}) = 0$ otherwise. The uncertainty of parameter estimation is carried by the BLUEs $\hat{\underline{\mathrm{x}}}_i$ and uncertainty of statistical testing is carried by $p_i(\underline{\mathrm{t}})$. Note that $p_i(\underline{\mathrm{t}})$ is a nonlinear function of $\underline{\mathrm{t}}$, which causes the PDF of the DIA-estimator $\overline{\underline{\mathrm{x}}}$ to be *multimodal*, even though the individual PDFs of the BLUEs $\hat{\underline{\mathrm{x}}}_i$ are Gaussian. The PDF of $\overline{\underline{\mathrm{x}}} \in \mathbb{R}^n$ follows from Theorem 1 in [1]

$$f_{\overline{\underline{\mathrm{x}}}}(x) = \sum_{i=0}^{k} \int_{\mathcal{P}_i} f_{\hat{\underline{\mathrm{x}}}_i, \underline{\mathrm{t}}}(x, t) \, dt \, . \tag{5.14}$$

The conditional components of $f_{\overline{\underline{\mathrm{x}}}}(x)$ on the testing decisions under $\mathcal{H}_0$ (i.e., CA and FA_i) can be obtained from $f_{\overline{\underline{\mathrm{x}}}}(x|\mathcal{H}_0)$. Those corresponding to the testing decisions under $\mathcal{H}_i$ (i.e., MD_i, CI_i, WI_j) from $f_{\overline{\underline{\mathrm{x}}}}(x|\mathcal{H}_i)$ for $i \neq 0$. It is the DIA-estimator's PDF in (5.14) that is used in the formulation of the probability of positioning failure. We note that one may only be interested in specific components of the parameter vector $\mathrm{x} \in \mathbb{R}^n$, such as the 1D, 2D, or 3D position. The desired position components can be obtained through the linear transformation $\mathrm{h} = \mathrm{H}^T \mathrm{x}$ with an appropriately chosen $\mathrm{H} \in \mathbb{R}^{n \times p}$ where $p < n$. Further developments in this paper are done in terms of $\mathrm{x} \in \mathbb{R}^n$, however a similar approach would apply also for $\mathrm{h} \in \mathbb{R}^p$.

5.3 Probability of Positioning Failure and its Components

The *positioning failure* event is defined as $\mathcal{F} = \overline{\underline{\mathrm{x}}} \in \mathcal{B}^c$, according to page 15 of [13], where $\mathcal{B} \subset \mathbb{R}^n$ denotes the safety region, and its complement $\mathcal{B}^c = \mathbb{R}^n \setminus \mathcal{B}$ represents the failure

region. We now proceed to formulate the probability of positioning failure

$$\mathbb{P}_{\mathcal{F}}(\mathbf{b}) = \int_{\mathcal{B}^c} f_{\underline{\mathrm{x}}}(x)dx, \tag{5.15}$$

where $\mathbf{b} = \{\mathrm{b}_1 \in \mathbb{R}^{q_1}, \mathrm{b}_2 \in \mathbb{R}^{q_2}, ..., \mathrm{b}_k \in \mathbb{R}^{q_k}\}$ represents the vectors of the outliers in the observation model under the k-alternative hypotheses. In general, the dimensions of the model outliers may differ, i.e., $q_i \neq q_j$ for $i \neq j$. The next step is to decompose (5.15) via the rule of total probability

$$\mathbb{P}_{\mathcal{F}}(\mathbf{b}) = \mathsf{P}(\mathcal{H}_0) \underbrace{\int_{\mathcal{B}^c} f_{\underline{\mathrm{x}}}(x|\mathcal{H}_0)dx}_{\mathbb{P}_{\mathcal{F}}|\mathcal{H}_0} + \sum_{i=1}^{k} \mathsf{P}(\mathcal{H}_i) \underbrace{\int_{\mathcal{B}^c} f_{\underline{\mathrm{x}}}(x|\mathcal{H}_i)dx}_{\mathbb{P}_{\mathcal{F}}|\mathcal{H}_i(\mathrm{b}_i)}, \tag{5.16}$$

where $\mathsf{P}(\mathcal{H}_0)$ and $\mathsf{P}(\mathcal{H}_i)$ are the apriori probability of occurrence of the hypotheses. A further expansion of (5.16), based on (5.14), gives

$$\begin{aligned} \mathbb{P}_{\mathcal{F}}(\mathbf{b}) = \mathsf{P}(\mathcal{H}_0) \left(\sum_{j=0}^{k} \int_{\mathcal{B}^c} \int_{\mathcal{P}_j} f_{\hat{\underline{\mathrm{x}}}_j, \underline{\mathrm{t}}}(x, t|\mathcal{H}_0)\, dt\, dx \right) + \\ \sum_{i=1}^{k} \mathsf{P}(\mathcal{H}_i) \left(\sum_{j=0}^{k} \int_{\mathcal{B}^c} \int_{\mathcal{P}_j} f_{\hat{\underline{\mathrm{x}}}_j, \underline{\mathrm{t}}}(x, t|\mathcal{H}_i)\, dt\, dx \right), \end{aligned} \tag{5.17}$$

which can then be expressed in terms of expected values w.r.t. the joint PDFs $f_{\hat{\underline{\mathrm{x}}}_j, \underline{\mathrm{t}}}(x, t)$

$$\mathbb{P}_{\mathcal{F}}(\mathbf{b}) = \mathsf{P}(\mathcal{H}_0) \left(\sum_{j=0}^{k} \mathsf{E}_{f_{\hat{\underline{\mathrm{x}}}_j, \underline{\mathrm{t}}}} \left(\mathbb{1}_j(\underline{\mathrm{x}}, \underline{\mathrm{t}}) | \mathcal{H}_0 \right) \right) + \sum_{i=1}^{k} \mathsf{P}(\mathcal{H}_i) \left(\sum_{j=0}^{k} \mathsf{E}_{f_{\hat{\underline{\mathrm{x}}}_j, \underline{\mathrm{t}}}} \left(\mathbb{1}_j(\underline{\mathrm{x}}, \underline{\mathrm{t}}) | \mathcal{H}_i \right) \right), \tag{5.18}$$

with the joint indicator function $\mathbb{1}_j(\underline{\mathrm{x}}, \underline{\mathrm{t}}) = 1$ if $[\underline{\mathrm{x}}^T\ \underline{\mathrm{t}}^T]^T \in \left(\mathcal{B}^c \cap \mathcal{P}_j\right)$, and 0 otherwise. The two summations of joint probabilities in parentheses in (5.18) are rewritten below, explicitly incorporating the statistical testing decisions from (5.10)-(5.11) into the notation,

$$\begin{aligned} \sum_{j=0}^{k} \mathsf{E}_{f_{\hat{\underline{\mathrm{x}}}_j, \underline{\mathrm{t}}}} \left(\mathbb{1}_j(\underline{\mathrm{x}}, \underline{\mathrm{t}}) | \mathcal{H}_0 \right) &= \mathbb{P}_{\mathcal{F}}|\mathrm{CA}\, \mathsf{P}_{\mathrm{CA}} + \sum_{j=1}^{k} \mathbb{P}_{\mathcal{F}}|\mathrm{FA}_j\, \mathsf{P}_{\mathrm{FA}_j}, \\ \sum_{j=0}^{k} \mathsf{E}_{f_{\hat{\underline{\mathrm{x}}}_j, \underline{\mathrm{t}}}} \left(\mathbb{1}_j(\underline{\mathrm{x}}, \underline{\mathrm{t}}) | \mathcal{H}_i \right) &= \mathbb{P}_{\mathcal{F}}|\mathrm{MD}_i\, \mathsf{P}_{\mathrm{MD}_i} + \mathbb{P}_{\mathcal{F}}|\mathrm{CI}_i\, \mathsf{P}_{\mathrm{CI}_i} + \sum_{j \neq 0,i}^{k} \mathbb{P}_{\mathcal{F}}|\mathrm{WI}_j\, \mathsf{P}_{\mathrm{WI}_j}\ . \end{aligned} \tag{5.19}$$

where $\mathbb{P}_{\mathcal{F}}|\mathcal{E}$ is the probability of positioning failure conditioned on the testing decision $\mathcal{E} \in \{\mathrm{CA}, \mathrm{FA}_j, \mathrm{MD}_i, \mathrm{CI}_i, \mathrm{WI}_j\}$. These decompositions are schematically illustrated as a 'failure-tree' in Fig. 5.2, where Level 1 corresponds to (5.19) and Level 2 corresponds to (5.16). To obtain the Level 1 and Level 2 components depicted in Fig. 5.2, one can resort to Monte Carlo simulation to approximate the expected values in (5.18). However, if these components are on the order of 10^{-4} or less, the variance of the results of the standard Monte Carlo simulation may be too high or the probability may not be even computable [26].

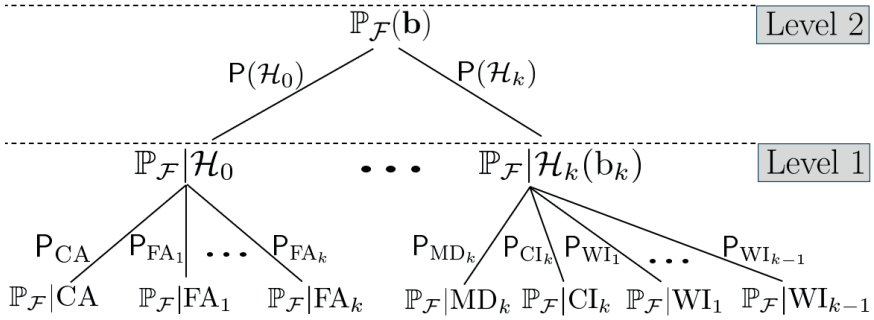

Figure 5.2: Representation of $\mathbb{P}_{\mathcal{F}}(\mathbf{b})$ as a 'failure-tree'. Level 1 corresponds to (5.19) and Level 2 to (5.16).

We have addressed these challenges in recent work [12], where we developed a method that enables the construction of the 'failure-tree' in Fig. 5.2 by leveraging principles from rare event simulation—an approach also applied in this contribution. We give the three main steps of the proposed method below:

1. Transform the joint vector $[\underline{\hat{x}}_j^T \ \underline{t}^T]^T$ to have an identity covariance matrix, and apply this change of variables to re-express the expectations in (5.18).

2. Reformulate these expectations using proposal PDFs based on the Importance Sampling principle [27], selecting PDFs with higher density over $\mathcal{B}^c \cap \mathcal{P}_j$, as determined via the Cross-Entropy Method [28].

3. Compute the Level 1 and Level 2 components of $\mathbb{P}_{\mathcal{F}}(\mathbf{b})$ by drawing i.i.d. samples from the proposal PDFs, and assess simulation uncertainty through multiple independent runs (e.g., 50 repetitions [29]).

After completing the computations, the maximum of (5.15) can be evaluated and compared against an application-specific requirement to determine whether the requirement is satisfied (e.g., [4, 8, 12])

$$\max_{\mathbf{b}} \mathbb{P}_{\mathcal{F}}(\mathbf{b}) = \mathsf{P}(\mathcal{H}_0)\mathbb{P}_{\mathcal{F}}|\mathcal{H}_0 + \max_{\mathrm{b}_1,\ldots,\mathrm{b}_k} \sum_{i=1}^{k} \mathsf{P}(\mathcal{H}_i)\mathbb{P}_{\mathcal{F}}|\mathcal{H}_i(\mathrm{b}_i). \tag{5.20}$$

5.4 Positioning Safety Analysis for a UAV under 2D Simultaneous Measurement Outliers

As an example, we present a positioning safety analysis for a UAV under multiple simultaneous outliers in the observations. The analysis is carried out for two scenarios using the principles from Sections 5.2 and 5.3. The first scenario considers a GPS satellite geometry as observed by a receiver at a snapshot of time, enabling detailed analysis of the conditional components of the DIA-estimator's PDF relative to the safety region shape, as well as the computed components of the probability of positioning failure. In the second scenario we consider a 24-hours (on May 24, 2024) evolution of GPS satellites moving over an airspace

region in The Netherlands for which authorization can be obtained for UAV operations (Latitude: 51.74368 [deg], Longitude 3.79322 [deg], Altitude: 0.0 [m], based on [16]), while the components of the probability of positioning failure are computed at 5 minute intervals. The selected airspace region has open-sky conditions while within it, the UAV is assumed to operate at a constant altitude of 45 meters above ground level ensuring compliance with height regulations. In both scenarios we are using real GPS satellite orbits provided by the International GNSS Service (IGS) [30]. The positioning model for the UAV under nominal conditions (i.e., under $\mathcal{H}_0$) is selected based on (i) the TSO certification standards for GPS-based UAV positioning [14, 15], and (ii) preliminary requirements for rotary-wing drones operating at SAIL level 4, as outlined in [31]. Therefore, the linearized positioning model is based on GPS pseudoranges on single-frequency (L1 at 1575.42 MHz) resulting in

$$\mathcal{H}_0 : \mathsf{E}_{f_{\underline{y}}}\left(\underline{y}\right) = \underbrace{\begin{bmatrix}\mathrm{G} & \mathbf{u}_m\end{bmatrix}}_{\mathrm{A}} \underbrace{\begin{bmatrix}\Delta \mathsf{p} \\ \mathsf{c}\Delta \mathsf{t}\end{bmatrix}}_{\Delta \mathrm{x}}, \quad \mathrm{Q}_{\mathrm{yy}} = \sigma_{\mathrm{y}}^2 \mathrm{W}^{-1}, \tag{5.21}$$

with $\underline{y} \sim \mathcal{N}\left(\mathrm{A}\Delta \mathrm{x}, \mathrm{Q}_{\mathrm{yy}}\right)$, where the design matrix $\mathrm{A} \in \mathbb{R}^{m\times 4}$ is of rank(A) = 4 (full rank) with $\mathrm{G} \in \mathbb{R}^{m\times 3}$ the matrix which rows contain the unit direction vectors (with the minus sign included) between the unknown position of the UAV's GPS receiver and the observed GPS satellites, in a local East-North-Up (ENU) coordinate system, and $\mathbf{u}_m \in \mathbb{R}^m$ is a vector of ones [21]. The parameter vector of unknowns $\Delta \mathrm{x} \in \mathbb{R}^4$ contains the UAV's GPS receiver ENU coordinates increments $\Delta \mathrm{p} \in \mathbb{R}^3$ and the receiver clock bias $\Delta \mathrm{t} \in \mathbb{R}$ while c is the speed of light in a vacuum. The redundancy under $\mathcal{H}_0$ is $r = m - 4$. The estimate $\hat{\mathrm{x}}$ (which includes the 3D full position vector and receiver clock bias) is obtained from a Gauss-Newton iteration scheme once the stop criterion is met for $\Delta\hat{\mathrm{x}}$ [32]. The variance-covariance matrix $\mathrm{Q}_{\mathrm{yy}} \in \mathbb{R}^{m\times m}$ is diagonal where $\mathrm{W} = \mathrm{diag}[\omega_1, ..., \omega_m] \in \mathbb{R}^{m\times m}$ is the weight matrix whose components are the elevation-dependent weighting functions based on [33]: $\omega_s = 1/(a_0 + a_1 \exp(-\mathrm{Elev}_s/E_0)^2)$ for $s \in \{1, ..., m\}$ with a_0, a_1, E_0 being the model coefficients and Elev_s being the elevation of satellite s in degrees. For both scenarios, we set $a_0 = 1.4$, $a_1 = 8$, $E_0 = 20$, as in [33], and $\sigma_{\mathrm{y}} = 0.7$ [m], which results in an average horizontal positioning precision of 3-4 meters (95% circular probability radius), and an average vertical positioning precision of approximately 6 meters (95% interval length), considering variations in satellite geometry over a 24 hour period. These positioning precisions are representative of certified GPS receivers used in UAVs (e.g., [34]). An elevation cut-off angle of 10° is applied, which excludes GPS satellites observed below this threshold from the positioning model.

5.4.1 GPS satellite geometry at a snapshot of time

The skyplot in Figure 5.3 shows the positions of eight (8) GPS satellites, at a snapshot of time, as observed by the UAV's GPS receiver. The corresponding dimensions of the vectors in the positioning model in (5.21) are: $m = 8$, $n = 4$, and $r = 4$.

Next, we motivate the consideration of one- and two-dimensional simultaneous outliers in the pseudorange observations, and provide the resulting number of alternative hypotheses for the testing procedure. Let us begin by determining the total number of possible one-dimensional and multi-dimensional pseudorange outliers among the m-observations (i.e.,

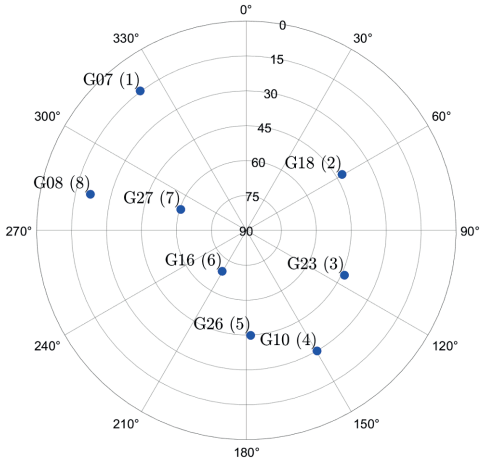

Figure 5.3: Skyplot view of the UAV GPS receiver-satellite geometry at an example location, with open-sky conditions, in Delft, The Netherlands (Latitude: 52 [deg], Longitude: 4 [deg], Altitude 0.0 [m]). GPS satellites IDs are renumbered clock-wise starting from G07 (1) and ending with G08 (8).

5

alternative hypotheses), based on the positioning model in (5.21) and the GPS satellite geometry shown in Figure 5.3. This number can be computed as follows [35–37]

$$k' = \sum_{q_i=1}^{m=8} \binom{m}{q_i} = 255, \tag{5.22}$$

where the binomial coefficient $\binom{m}{q_i}$ gives the number of possible combinations of q_i outliers in m-observations. While not all of these alternative hypotheses can really be included in the testing procedure due to redundancy and separability limitations, the total count illustrates the full set of potential simultaneous outliers that could occur in practice (e.g., up to eight simultaneous outliers in the event of a constellation failure). The number resulting for each $q_i \in \{1, ..., 8\}$ is shown in Figure 5.4(a). In the next step, we model the probability of occurrence of an alternative hypothesis $\mathsf{P}(\mathcal{H}_i)$ corresponding to a q_i-dimensional outlier. Under open-sky conditions for the GPS receiver, it is reasonable to model $\mathsf{P}(\mathcal{H}_i)$ as a decreasing function of q_i. Denoting π as the probability of the occurrence of one-dimensional outlier, and assuming that outlier occurrences are independent, then $\mathsf{P}(\mathcal{H}_i)$ can be modelled as follows [38–40]

$$\mathsf{P}(\mathcal{H}_i) = \prod_{\substack{a=1 \\ \mathbb{1}_{\mathcal{H}_i}(a)=1}}^{m} \pi \prod_{\substack{a=1 \\ \mathbb{1}_{\mathcal{H}_i}(a)=0}}^{m} (1-\pi) = \prod_{a=1}^{m} \pi^{\mathbb{1}_{\mathcal{H}_i}(a)} (1-\pi)^{\left[1-\mathbb{1}_{\mathcal{H}_i}(a)\right]}, \tag{5.23}$$

where $\mathbb{1}_{\mathcal{H}_i}(a) = 1$ if the a^{th} observation contains an outlier under hypothesis $\mathcal{H}_i$, and 0 otherwise. Note that $\sum_{a=1}^{m} \mathbb{1}_{\mathcal{H}_i}(a) = q_i$ equals the number of outliers under $\mathcal{H}_i$ and also that (5.23) yields the probability of the null hypothesis, $\mathsf{P}(\mathcal{H}_0) = (1-\pi)^m$, corresponding to $q_0 = 0$. The probabilities satisfy the condition $\sum_{i=0}^{k'} \mathsf{P}(\mathcal{H}_i) = 1$. Furthermore, (5.23) can be

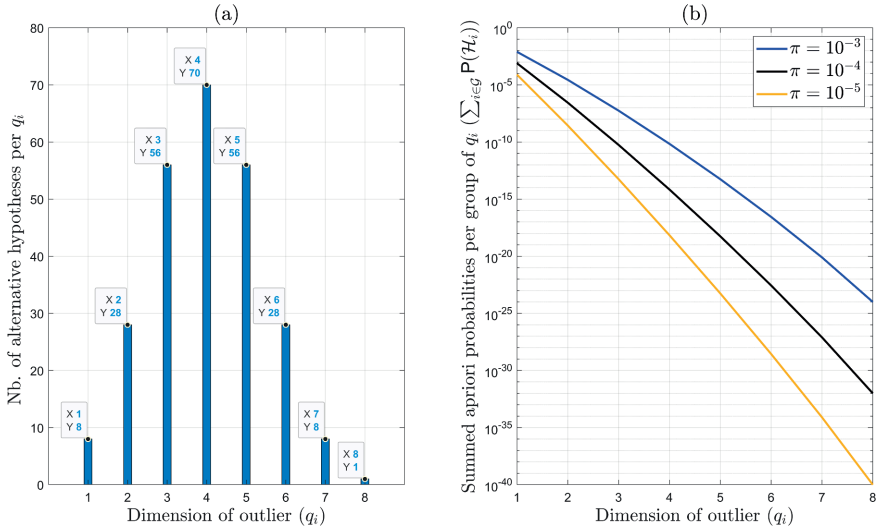

Figure 5.4: (a) Total number of alternative hypotheses corresponding to each value of q_i in (5.22); (b) Summed apriori probabilities of alternative hypotheses $\mathcal{H}_i$ per group $\mathcal{G}$ of q_i based on (5.23). For example, when the probability of one-dimensional outlier is $\pi = 10^{-3}$ (blue curve): $q_i = 1$ and $\sum_{i=1}^{8} \mathsf{P}(\mathcal{H}_i) = 794.41677 \cdot 10^{-5}$, $q_i = 2$ and $\sum_{i=9}^{36} \mathsf{P}(\mathcal{H}_i) = 2.78324 \cdot 10^{-5}$. Other curves correspond to the cases when $\pi = 10^{-4}$ and $\pi = 10^{-5}$.

re-expressed in a simpler form

$$\mathsf{P}(\mathcal{H}_i) = \pi^{q_i}(1-\pi)^{m-q_i}. \tag{5.24}$$

The model from (5.24), along with the specified positioning safety requirements (e.g., SAIL 4), can be used to determine the maximum dimension q_i, which also depends on the redundancy, to be included in the DIA procedure (see (5.12)). For example, let us consider the situation when the redundancy $r = 4$ and $\pi = 10^{-3}$. In this case, we obtain (see also Figure 5.4(b))

$$\begin{aligned} 1 - \mathsf{P}(\mathcal{H}_0) &= \underbrace{\sum_{i=1}^{8} \mathsf{P}(\mathcal{H}_i)}_{q_i=1} + \underbrace{\sum_{i=9}^{36} \mathsf{P}(\mathcal{H}_i)}_{q_i=2} + \underbrace{\sum_{i=37}^{255} \mathsf{P}(\mathcal{H}_i)}_{q_i\in\{3,\ldots,8\}} \\ &= 794.41677 \cdot 10^{-5} + 2.78324 \cdot 10^{-5} + 0.00557 \cdot 10^{-5}, \end{aligned} \tag{5.25}$$

which indicates that, given the SAIL 4 requirement for $\mathbb{P}_F(\mathbf{b})$ to be on the order of 10^{-5}, alternative hypotheses with dimensions $q_i > 2$ can be excluded from the testing procedure, as their contribution to the overall probability $\mathbb{P}_F(\mathbf{b})$ is negligible and also the redundancy does not allow for the identification of outliers with dimensions $q_i > 2$. Therefore, the misclosure space $\mathbb{R}^{r=4}$ is partitioned, according to (5.8), while accounting for one- and two-dimensional $q_i \in \{1, 2\}$ resulting in 36 alternative hypotheses ($k = 36$). For the positioning safety analysis, we focus on the horizontal component (a similar approach can be applied to the vertical component). The corresponding DIA estimator for the horizontal position

of the UAV is

$$\overline{\underline{\mathrm{h}}} = \mathrm{H}^T \overline{\underline{\mathrm{x}}}, \tag{5.26}$$

where $\overline{\underline{\mathrm{x}}} = \sum_{i=0}^{k=36} \hat{\underline{\mathrm{x}}}_i \, p_i(\underline{\mathrm{t}})$ cf. (5.13), $\mathrm{H}^T = \begin{bmatrix} \mathrm{I}_2 & 0_{2\times 2} \end{bmatrix}$. The horizontal safety-region $\mathcal{B}_\mathrm{h} \subset \mathbb{R}^2$, around the true position, is defined as follows

$$\mathcal{B}_\mathrm{h} = \{h \in \mathbb{R}^2 \mid \|h - \mathrm{h}_\mathrm{true}\| \leq \mathrm{HAL}\}, \tag{5.27}$$

where the Horizontal Alert Limit (HAL) is set to 11 m, in line with SAIL 4 for en-route operations [31]. The probability of the UAVs horizontal positioning failure is upperbounded (accounting for (5.25) and for the SAIL 4 requirement), as follows

$$\mathbb{P}_{\mathcal{F}_\mathrm{h}}(\mathbf{b}) \leq \underbrace{\left(\mathsf{P}(\mathcal{H}_0) \underbrace{\int_{\mathcal{B}_\mathrm{h}^c} f_{\overline{\underline{\mathrm{h}}}}(h|\mathcal{H}_0)dh}_{\mathbb{P}_{\mathcal{F}_\mathrm{h}}|\mathcal{H}_0} + \sum_{i=1}^{k=36} \mathsf{P}(\mathcal{H}_i) \underbrace{\int_{\mathcal{B}_\mathrm{h}^c} f_{\overline{\underline{\mathrm{h}}}}(h|\mathcal{H}_i)dh}_{\mathbb{P}_{\mathcal{F}_\mathrm{h}}|\mathcal{H}_i(\mathrm{b}_i)} + \sum_{i=37}^{k'=255} \mathsf{P}(\mathcal{H}_i) \right)}_{\check{\mathbb{P}}_{\mathcal{F}_\mathrm{h}}(\check{\mathbf{b}})}, \tag{5.28}$$

where the term $\sum_{i=37}^{k'=255} \mathsf{P}(\mathcal{H}_i)$ accounts for the hypotheses which were 'excluded' from the testing procedure (see (5.25)) and $\check{\mathbf{b}} = \{\mathrm{b}_1, ..., \mathrm{b}_{36}\} \subset \mathbf{b}$. The objective is to base the positioning safety analysis in the following subsections on the results obtained from computing $\check{\mathbb{P}}_{\mathcal{F}_\mathrm{h}}(\check{\mathbf{b}})$.

Results under $\mathcal{H}_0$

First, we analyze the components of the PDF of $\overline{\underline{\mathrm{h}}} \in \mathbb{R}^2$ under $\mathcal{H}_0$

$$f_{\overline{\underline{\mathrm{h}}}}(h|\mathcal{H}_0) = \mathsf{P}_\mathrm{CA} \, f_{\overline{\underline{\mathrm{h}}}|\mathrm{CA}}(h|\mathrm{CA}) + \sum_{i=1}^{k=36} \mathsf{P}_{\mathrm{FA}_i} \, f_{\overline{\underline{\mathrm{h}}}|\mathrm{FA}_i}(h|\mathrm{FA}_i), \tag{5.29}$$

to highlight the factors influencing the shapes of the conditional PDFs. The significance level was set to $\alpha = \mathsf{P}_\mathrm{FA} = 10^{-3}$ to limit false alarms that would lead to satellite exclusion and degraded satellite geometry, while not making the Detection step (of the DIA method) too insensitive to smaller outliers. Similar values have been used in related studies [41, 42]. Under the event of a CA testing decision, the PDF $f_{\overline{\underline{\mathrm{h}}}|\mathrm{CA}}(h|\mathrm{CA}) = f_{\hat{\underline{\mathrm{h}}}_0}(h|\mathcal{H}_0)$, with $\mathsf{E}\left(\hat{\underline{\mathrm{h}}}_0|\mathcal{H}_0\right) = \mathrm{h}$ where $\mathrm{h} \in \mathbb{R}^2$ is the true horizontal position vector and $\mathrm{Q}_{\hat{\mathrm{h}}_0\hat{\mathrm{h}}_0} = \mathrm{H}^T \mathrm{Q}_{\hat{\mathrm{x}}_0\hat{\mathrm{x}}_0} \mathrm{H}$. For simplicity, in the simulations we set $\mathrm{h} = 0_{2\times 1}$. Hence, the design-matrix A and vc-matrix Q_{yy} are driving the shape of $f_{\overline{\underline{\mathrm{h}}}|\mathrm{CA}}(h|\mathrm{CA})$. The precision of the horizontal position components $\sigma_{\hat{\mathrm{h}}_0,\mathrm{east}} = 1.32$ [m], $\sigma_{\hat{\mathrm{h}}_0,\mathrm{north}} = 1.53$ [m], and the correlation coefficient is $\rho_{\hat{\mathrm{h}}_0} = 0.25$. The contours of $f_{\overline{\underline{\mathrm{h}}}|\mathrm{CA}}(h|\mathrm{CA})$ 'weighted' by P_CA, along with the safety region $\mathcal{B}_\mathrm{h}$ are shown in Figure 5.5 (first plot from the top row). Since the product $\mathsf{P}_\mathrm{CA} \, f_{\overline{\underline{\mathrm{h}}}|\mathrm{CA}}(h|\mathrm{CA})$ is predominantly concentrated within the safety region $\mathcal{B}_\mathrm{h}$, its integral outside this region (i.e., $\mathcal{B}_\mathrm{h}^c$)—and thus its contribution to $\mathbb{P}_{\mathcal{F}_\mathrm{h}}|\mathcal{H}_0$—is small.

Regarding the components of $f_{\overline{\underline{\mathrm{h}}}}(h|\mathcal{H}_0)$ associated with the FA_i testing decisions, we select as examples the terms $\mathsf{P}_{\mathrm{FA}_i} \, f_{\overline{\underline{\mathrm{h}}}|\mathrm{FA}_i}(h|\mathrm{FA}_i)$ for: (i) one-dimensional outliers affecting, one

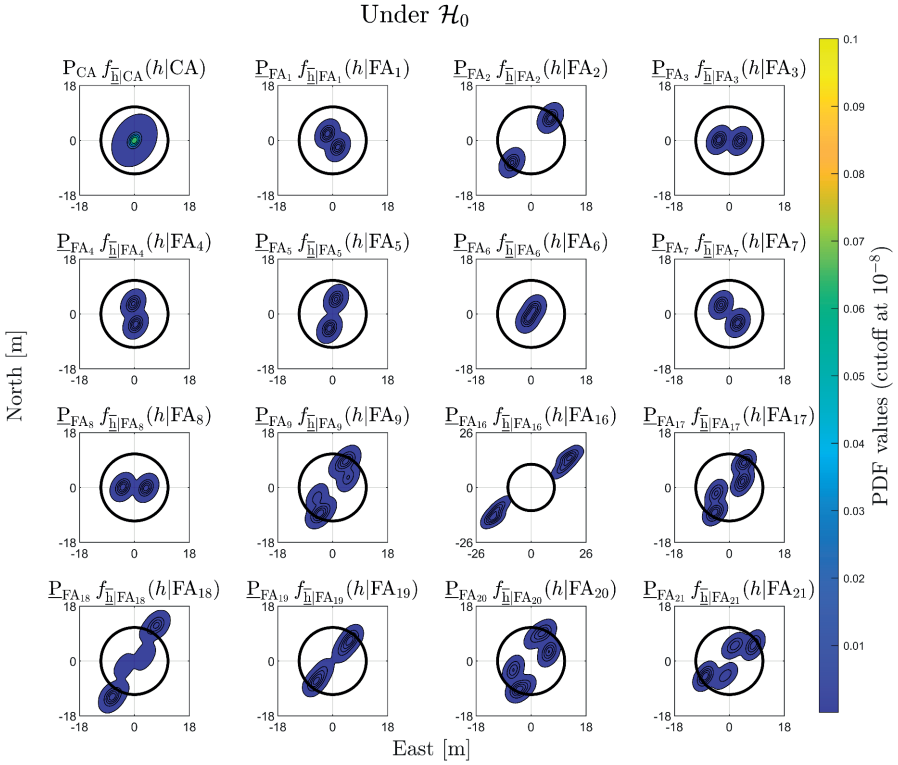

Figure 5.5: Components of $f_{\underline{\mathrm{h}}}(h|\mathcal{H}_0)$ for $\mathsf{P}_{\mathrm{CA}} = 1 - \mathsf{P}_{\mathrm{FA}}$ and $\alpha = \mathsf{P}_{\mathrm{FA}} = 10^{-3}$, in relation with the safety region $\mathcal{B}_{\mathrm{h}} \subset \mathbb{R}^2$ defined in (5.27). Examples of $\underline{\mathsf{P}}_{\mathrm{FA}_i}\, f_{\underline{\mathrm{h}}|\mathrm{FA}_i}(h|\mathrm{FA}_i)$ were selected for one-dimensional outliers affecting the pseudoranges from each individual GPS satellite ($q_i = 1$, for $i \in \{1,\ldots,8\}$), and for two-dimensional outliers involving all combinations that include GPS satellite 2 ($q_i = 2$, for $i \in \{9,16,\ldots,21\}$).

at-a-time, the pseudorange from each individual GPS satellite with $q_i = 1$, for $i \in \{1,\ldots,8\}$, and (ii) two-dimensional outliers involving all combinations that include GPS satellite 2 (2-1, 2-3, ..., 2-8.), with $q_i = 2$, for $i \in \{9,16,\ldots,21\}$. These selections allow us to highlight the differences between the components $\mathsf{P}_{\mathrm{FA}_i}\, f_{\underline{\mathrm{h}}|\mathrm{FA}_i}(h|\mathrm{FA}_i)$ associated with one- and two-dimensional outlier hypotheses. Combinations of two-dimensional outliers involving GPS satellite 2 were chosen specifically because it is the only satellite located in the azimuth range $0^\circ - 90^\circ$ in the skyplot shown in Figure 5.3, which makes it a particularly interesting case to illustrate. We now turn our attention to the properties of the conditional PDF $f_{\underline{\mathrm{h}}|\mathrm{FA}_i}(h|\mathrm{FA}_i)$—such as orientation and multimodality—which can be studied from its expression [1]

$$f_{\underline{\mathrm{h}}|\mathrm{FA}_i}(h|\mathrm{FA}_i) = \frac{\mathsf{E}_{f_{\underline{\mathrm{t}}}}\left[f_{\underline{\hat{\mathrm{h}}}_0}(h + \mathrm{G}_i \mathrm{C}_{\mathrm{t}_i}^{+}\underline{\mathrm{t}}|\mathcal{H}_0)p_i(\underline{\mathrm{t}})\right]}{\mathsf{P}_{\mathrm{FA}_i}}, \tag{5.30}$$

where $\mathrm{G}_i \in \mathbb{R}^{2\times q_i}$ and $\mathrm{G}_i = \mathrm{H}^T\mathrm{A}^{+}\mathrm{C}_i$. For every $h \in \mathbb{R}^2$ in the horizontal position domain, the numerator in the above equation captures two main aspects: (i) how the misclosure vector $\underline{\mathrm{t}} \in \mathbb{R}^r$ is first transformed in the domain of $\mathbb{R}^{q_i}$ via the BLUE-inverse $\mathrm{C}_{\mathrm{t}_i}^{+} \in \mathbb{R}^{q_i \times r}$,

and afterwards to the horizontal position domain via $G_i \in \mathbb{R}^{2\times q_i}$; (ii) the values of the PDF $f_{\underline{\hat{h}}_0}(.)$ evaluated at $h + G_i C_{t_i}^{+} \underline{t}$ are averaged for all the misclosure vectors (via $E_{\underline{f}_t}[.]$) that are in the partition $\mathcal{P}_{i\neq 0}$ (i.e., for which the indicator function $p_i(\underline{t}) = 1$). The term $G_i \in \mathbb{R}^{2\times q_i}$ specifies which parts (or regions) of the PDF $f_{\underline{\hat{h}}_0}(.)$ $(= f_{\underline{\hat{h}}|\mathrm{CA}}(.))$ are evaluated through the linear combination of its columns with the coefficients given by $\left(C_{t_i}^{+} \underline{t}\right) \in \mathbb{R}^{q_i}$. Therefore, the structure of $f_{\underline{\hat{h}}|\mathrm{FA}_i}(h|\mathrm{FA}_i)$ is determined by the averaged shifted PDF $f_{\underline{\hat{h}}_0}\left(h + G_i C_{t_i}^{+} \underline{t} | \mathcal{H}_0\right)$ while accounting for testing decisions through the indicator function $p_i(\underline{t})$. For example, in the case of $q_i = 1$ with $i \in \{1, ..., 8\}$, the orientation of $f_{\underline{\hat{h}}|\mathrm{FA}_i}(h|\mathrm{FA}_i)$ is driven by the direction of the vector $G_i \in \mathbb{R}^{2\times(q_i=1)}$ and how $\left(C_{t_i}^{+} \underline{t}\right)$ varies along its span for $\underline{t} \in \mathcal{P}_i$. Consider the conditional PDF $f_{\underline{\hat{h}}|\mathrm{FA}_2}(h|\mathrm{FA}_2)$ (conditioned on the exclusion of the GPS satellite 2 observation while $\mathcal{H}_0$ is valid), which is aligned with the span of G_2 (see Figure 5.5 and Figure 5.6(a)). This shows that excluding GPS satellite 2, while $\mathcal{H}_0$ is valid, increases horizontal positioning uncertainty in its direction. The two modes of $f_{\underline{\hat{h}}|\mathrm{FA}_2}(h|\mathrm{FA}_2)$ depend on how $\left(C_{t_2}^{+} \underline{t}\right)$ varies across the span of G_2 for $\underline{t} \in \mathcal{P}_2$.

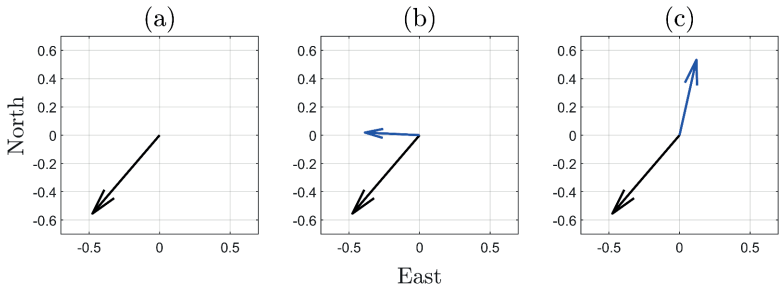

Figure 5.6: Visual representation of the columns of matrix $G_i \in \mathbb{R}^{2\times q_i}$, for $i \in \{2, 16, 18\}$, which maps $\left(C_{t_i}^{+} \underline{t}\right) \in \mathbb{R}^{q_i}$ onto the horizontal position domain; (a) Column vector $G_2 \in \mathbb{R}^{2\times(q_2=1)}$; (b) Columns of $G_{16} = [G_2 \;\; G_3] \in \mathbb{R}^{2\times(q_{16}=2)}$; (c) Columns of $G_{18} = [G_2 \;\; G_5] \in \mathbb{R}^{2\times(q_{18}=2)}$.

For the case where $q_i = 2$—for example, when $i \in \{16, 18\}$, which corresponds to the exclusion of GPS satellites 2–3 ($\mathcal{H}_{16}$) and 2–5 ($\mathcal{H}_{18}$)—the respective columns of $G_{16} \in \mathbb{R}^{2\times 2}$ and $G_{18} \in \mathbb{R}^{2\times 2}$ are shown in Figures 5.6(b) and 5.6(c). The orientation of the conditional PDFs $f_{\underline{\hat{h}}|\mathrm{FA}_i}(h|\mathrm{FA}_i)$, for $i \in \{16, 18\}$, is primarily determined by the direction of the columns of G_{16} and G_{18} associated with GPS satellite 2. Their multimodal structure is determined by the linear combinations of the columns of G_{16} and G_{18}, where the coefficients in the vector result from $\left(C_{t_i}^{+} \underline{t}\right)$ for $\underline{t} \in \mathcal{P}_i$. Accounting for the computed $\underline{P}_{\mathrm{FA}_i}$, Figure 5.5 shows that $\underline{P}_{\mathrm{FA}_{16}} f_{\underline{\hat{h}}|\mathrm{FA}_{16}}(h|\mathrm{FA}_{16})$ and $\underline{P}_{\mathrm{FA}_{18}} f_{\underline{\hat{h}}|\mathrm{FA}_{18}}(h|\mathrm{FA}_{18})$ have the most probability density outside the safety-region $\mathcal{B}_{\mathrm{h}}$ *among all* components of $f_{\underline{\hat{h}}}(h|\mathcal{H}_0)$.

Secondly, we compute the Level 1 components corresponding to $\mathcal{H}_0$ (see Figure 5.2)

$$\underline{\mathbb{P}}_{\mathcal{F}_{\mathrm{h}}}|\mathcal{H}_0 = \mathsf{P}_{\mathrm{CA}} \underline{\mathbb{P}}_{\mathcal{F}_{\mathrm{h}}}|\mathrm{CA} + \sum_{i=1}^{k=36} \underline{P}_{\mathrm{FA}_i} \underline{\mathbb{P}}_{\mathcal{F}_{\mathrm{h}}}|\mathrm{FA}_i. \tag{5.31}$$

Figure 5.7 presents the results obtained from 50 independent simulation runs ($N_{\mathrm{sim}} = 50$), which were used to empirically quantify the uncertainty in the computations [29].

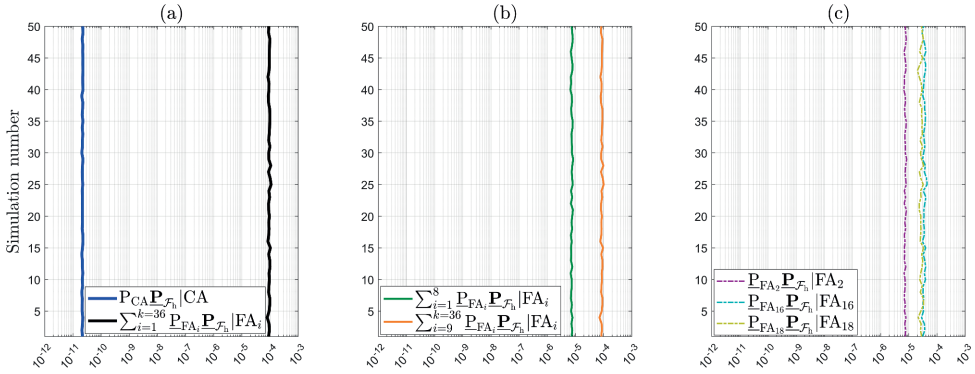

Figure 5.7: Components of $\underline{\mathbb{P}}_{\mathcal{F}_\mathrm{h}}|\mathcal{H}_0$: (a) $\mathrm{P}_{\mathrm{CA}}\underline{\mathbf{P}}_{\mathcal{F}_\mathrm{h}}|\mathrm{CA}$ and $\sum_{i=1}^{k=36}\underline{\mathrm{P}}_{\mathrm{FA}_i}\underline{\mathbf{P}}_{\mathcal{F}_\mathrm{h}}|\mathrm{FA}_i$; (b) $\sum_{i=1}^{8}\underline{\mathrm{P}}_{\mathrm{FA}_i}\underline{\mathbf{P}}_{\mathcal{F}_\mathrm{h}}|\mathrm{FA}_i$ corresponds to outlier dimension $q_i = 1$ and $\sum_{i=9}^{k=36}\underline{\mathrm{P}}_{\mathrm{FA}_i}\underline{\mathbf{P}}_{\mathcal{F}_\mathrm{h}}|\mathrm{FA}_i$ to outlier dimension $q_i = 2$; (c) $\underline{\mathrm{P}}_{\mathrm{FA}_i}\underline{\mathbf{P}}_{\mathcal{F}_\mathrm{h}}|\mathrm{FA}_i$ for $i \in \{2, 16, 18\}$ correspond to the conditioning of falsely accepting hypotheses $\mathcal{H}_2$ ($q_2 = 1$ one-dimensional outlier in GPS Satellite 2), $\mathcal{H}_{16}$ ($q_{16} = 2$ two-dimensional outlier in GPS satellites 2 and 3), $\mathcal{H}_{18}$ ($q_{18} = 2$ two-dimensional outlier in GPS satellites 2 and 5).

5

The uncertainty in the computation of the expected values in (5.18) is due to the use of simulations. Figure 5.7(a) shows that the component corresponding to the CA testing decision (accepting $\mathcal{H}_0$ while $\mathcal{H}_0$ is valid) has a mean value μ_{sim} of $2.1872 \cdot 10^{-11}$ across the 50 simulations. In contrast, the sum component related to *all* of the FA_i testing decisions (accepting $\mathcal{H}_{i\neq 0}$ while $\mathcal{H}_0$ is valid) has a mean value μ_{sim} of $9.3056 \cdot 10^{-5}$, which not only represents the dominant contribution to $\underline{\mathbb{P}}_{\mathcal{F}_\mathrm{h}}|\mathcal{H}_0$, but is also approximately *seven* orders of magnitude larger than than the component corresponding to the CA testing decision. If the summation in (5.31) is split into two parts—one corresponding to alternative hypotheses involving one-dimensional outliers ($q_i = 1$ for $i \in \{1, .., 8\}$) and the other to those involving all the two-dimensional outliers ($q_i = 2$ for $i \in \{9, ..., 36\}$) —then the latter is shown in Figure 5.7(b) to contribute most significantly to $\underline{\mathbb{P}}_{\mathcal{F}_\mathrm{h}}|\mathcal{H}_0$. This is expected since the components $\underline{\mathrm{P}}_{\mathrm{FA}_i} f_{\underline{\mathrm{h}}|\mathrm{FA}_i}(h|\mathrm{FA}_i)$, for $q_i = 2$, tend to exhibit 'quad'-modal behavior with a greater portion of their density lying outside the safety region—already accounted for by the 'weighting' with $\underline{\mathrm{P}}_{\mathrm{FA}_i}$. The contribution of $\sum_{i=9}^{k=36}\underline{\mathrm{P}}_{\mathrm{FA}_i}\underline{\mathbb{P}}_{\mathcal{F}_\mathrm{h}}|\mathrm{FA}_i$ to $\underline{\mathbb{P}}_{\mathcal{F}_\mathrm{h}}|\mathcal{H}_0$ is approximately one order of magnitude larger than the one of $\sum_{i=1}^{8}\underline{\mathrm{P}}_{\mathrm{FA}_i}\underline{\mathbb{P}}_{\mathcal{F}_\mathrm{h}}|\mathrm{FA}_i$. Taking a closer look at the two summation term $\sum_{i=1}^{8}\underline{\mathrm{P}}_{\mathrm{FA}_i}\underline{\mathbb{P}}_{\mathcal{F}_\mathrm{h}}|\mathrm{FA}_i$, Figure 5.7(c) shows that the component $\underline{\mathrm{P}}_{\mathrm{FA}_2}\underline{\mathbb{P}}_{\mathcal{F}_\mathrm{h}}|\mathrm{FA}_2$ is the largest among the group with $q_i = 1$, which is consistent with the fact that GPS satellite 2 is the only one located in the azimuth range $0^\circ - 90^\circ$ (see Figure 5.3). In the case of $\sum_{i=9}^{k=36}\underline{\mathrm{P}}_{\mathrm{FA}_i}\underline{\mathbb{P}}_{\mathcal{F}_\mathrm{h}}|\mathrm{FA}_i$, with $q_i = 2$, the components $\underline{\mathrm{P}}_{\mathrm{FA}_{16}}\underline{\mathbb{P}}_{\mathcal{F}_\mathrm{h}}|\mathrm{FA}_{16}$ and $\underline{\mathrm{P}}_{\mathrm{FA}_{18}}\underline{\mathbb{P}}_{\mathcal{F}_\mathrm{h}}|\mathrm{FA}_{18}$ are most dominant - not only within that group, but also among all components with $i \in \{1, ..., 36\}$. Therefore, falsely excluding GPS satellite 2—or the satellite pairs 2–3 and 2–5—degrades the receiver-satellite geometry, causing the corresponding components $\underline{\mathrm{P}}_{\mathrm{FA}_i}\underline{\mathbb{P}}_{\mathcal{F}_\mathrm{h}}|\mathrm{FA}_i$ to contribute the most to $\underline{\mathbb{P}}_{\mathcal{F}_\mathrm{h}}|\mathcal{H}_0$. This numerical analysis aligns with the visual interpretation discussed at Figure 5.5 and the results are summarized in Table 5.1.

Table 5.1: Components of $\underline{\mathbb{P}}_{\mathcal{F}}|\mathcal{H}_0$. Results are obtained over $N_{\text{sim}} = 50$, from which the mean values (μ_{sim}) and their standard deviation (σ_{sim}) were computed.

Component	Dim. outlier (q_i)	μ_{sim}	σ_{sim} of μ_{sim}
$\mathsf{P}_{\text{CA}}\underline{\mathbb{P}}_{\mathcal{F}_\text{h}}\|\text{CA}$	-	$2.1872 \cdot 10^{-11}$	$0.0084 \cdot 10^{-11}$
$\sum_{i=1}^{8} \underline{\mathsf{P}}_{\text{FA}_i}\underline{\mathbb{P}}_{\mathcal{F}_\text{h}}\|\text{FA}_i$	1	$0.7391 \cdot 10^{-5}$	$0.0057 \cdot 10^{-5}$
$\sum_{i=9}^{k=36} \underline{\mathsf{P}}_{\text{FA}_i}\underline{\mathbb{P}}_{\mathcal{F}_\text{h}}\|\text{FA}_i$	2	$8.5665 \cdot 10^{-5}$	$0.0682 \cdot 10^{-5}$
$\underline{\mathbb{P}}_{\mathcal{F}_\text{h}}\|\mathcal{H}_0$	1 and 2	$9.3056 \cdot 10^{-5}$	$0.0684 \cdot 10^{-5}$

The probabilities of the testing decisions from Table 5.1 are shown in Table 5.2. As expected, the sum of the probabilities of false alarms for hypotheses with two-dimensional outliers is larger than that for hypotheses with one-dimensional outliers.

Table 5.2: Probabilities of several testing decisions under $\mathcal{H}_0$. Results are obtained over $N_{\text{sim}} = 50$, from which the mean values (μ_{sim}) and their standard deviation (σ_{sim}) were computed.

Component	Dim. outlier (q_i)	μ_{sim}	σ_{sim} of μ_{sim}
P_{CA}	-	0.9990	-
$\sum_{i=1}^{8} \underline{\mathsf{P}}_{\text{FA}_i}$	1	$2.9500 \cdot 10^{-4}$	$0.4536 \cdot 10^{-4}$
$\sum_{i=9}^{k=36} \underline{\mathsf{P}}_{\text{FA}_i}$	2	$7.2140 \cdot 10^{-4}$	$0.8372 \cdot 10^{-4}$
Total	1 and 2	1.0000	$0.9522 \cdot 10^{-4}$

Results under $\mathcal{H}_{i\neq 0}$

Under the alternative hypotheses, the probability $\underline{\mathbb{P}}_{\mathcal{F}_\text{h}}|\mathcal{H}_i(\text{b}_i)$ for $i \neq 0$ depends on the vector containing the sizes of the outliers $\text{b}_i \in \mathbb{R}^{q_i}$. The objective is to find its maximum (worst-case scenario). As a first example, we express the computed Level 1 components corresponding to $\mathcal{H}_7$ (with $q_7 = 1$, a one-dimensional outlier in GPS Satellite 7) as follows

$$\underline{\mathbb{P}}_{\mathcal{F}_\text{h}}|\mathcal{H}_7(\text{b}_7) = \mathsf{P}_{\text{MD}_7}\underline{\mathbb{P}}_{\mathcal{F}_\text{h}}|\text{MD}_7 + \underline{\mathsf{P}}_{\text{CI}_7}\underline{\mathbb{P}}_{\mathcal{F}_\text{h}}|\text{CI}_7 + \sum_{j\neq 0,7}^{k=36} \underline{\mathsf{P}}_{\text{WI}_j}\underline{\mathbb{P}}_{\mathcal{F}_\text{h}}|\text{WI}_j, \tag{5.32}$$

where $\mathsf{P}_{\text{MD}_7} = \mathsf{P}(\underline{\text{t}} \in \mathcal{P}_0|\mathcal{H}_7)$ can be computed exactly for any value of b_7. Figure 5.8 shows the terms in (5.32), averaged over $N_{\text{sim}} = 50$ independent simulation runs to obtain the empirical simulation uncertainty in the results. In Figure 5.8(a), the behavior of the function $\underline{\mathbb{P}}_{\mathcal{F}_\text{h}}|\mathcal{H}_7(\text{b}_7)$ displays a local maximum of $1.2927 \cdot 10^{-2}$ (with $\sigma_{\text{sim}} = 0.0047 \cdot 10^{-2}$) at $\text{b}_7 = 8.45$ [m], while the global maximum is $2.1132 \cdot 10^{-2}$ (with $\sigma_{\text{sim}} = 0.0048 \cdot 10^{-2}$) for $\text{b}_7 = 21.00$ [m]. To gain insights into the components that contribute to the local and global maxima, the individual terms in (5.32) are presented in Figure 5.8(b). The figure shows that $\underline{\mathbb{P}}_{\mathcal{F}_\text{h}}|\mathcal{H}_7(\text{b}_7)$ is *completely* driven by the term $\sum_{j\neq 0,7}^{k=36} \underline{\mathsf{P}}_{\text{WI}_j}\underline{\mathbb{P}}_{\mathcal{F}_\text{h}}|\text{WI}_j$, which accounts for all the wrong identification testing decisions. The other two terms, $\mathsf{P}_{\text{MD}_7}\underline{\mathbb{P}}_{\mathcal{F}_\text{h}}|\text{MD}_7$ and $\underline{\mathsf{P}}_{\text{CI}_7}\underline{\mathbb{P}}_{\mathcal{F}_\text{h}}|\text{CI}_7$, are in the range of $10^{-11} - 10^{-6}$, while $\sum_{j\neq 0,7}^{k=36} \underline{\mathsf{P}}_{\text{WI}_j}\underline{\mathbb{P}}_{\mathcal{F}_\text{h}}|\text{WI}_j$ is in the range of $10^{-4} - 10^{-2}$. In the case of $\mathsf{P}_{\text{MD}_7}\underline{\mathbb{P}}_{\mathcal{F}_\text{h}}|\text{MD}_7$, as the outlier b_7 increases, the probability density of $f_{\underline{\text{h}}|\text{MD}_7}(h|\text{MD}_7)$ increases outside $\mathcal{B}_\text{h}$, while P_{MD_7} decreases (i.e., the probability density

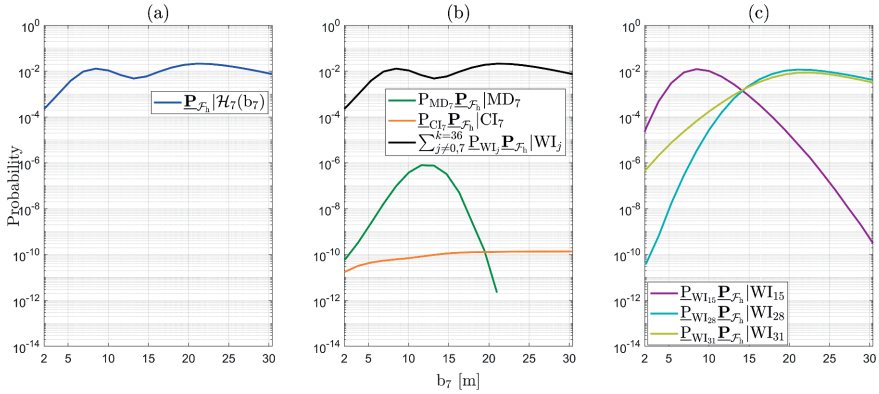

Figure 5.8: (a) Computed $\underline{\mathrm{P}}_{\mathcal{F}_\mathrm{h}}|\mathcal{H}_7(\mathrm{b}_7)$ as a function of outlier size b_7 [m]; (b) Components of $\underline{\mathrm{P}}_{\mathcal{F}_\mathrm{h}}|\mathcal{H}_7(\mathrm{b}_7)$ as a function of b_7 [m]: $\mathrm{P}_{\mathrm{MD}_7}\underline{\mathrm{P}}_{\mathcal{F}_\mathrm{h}}|\mathrm{MD}_7$, $\underline{\mathrm{P}}_{\mathrm{CI}_7}\underline{\mathrm{P}}_{\mathcal{F}_\mathrm{h}}|\mathrm{CI}_7$, and $\sum_{j\neq 0,7}^{k=36}\underline{\mathrm{P}}_{\mathrm{WI}_j}\underline{\mathrm{P}}_{\mathcal{F}_\mathrm{h}}|\mathrm{WI}_j$; (c) $\underline{\mathrm{P}}_{\mathrm{WI}_j}\underline{\mathrm{P}}_{\mathcal{F}_\mathrm{h}}|\mathrm{WI}_j$ for $j \in \{15, 28, 31\}$ correspond to the conditioning of wrongly accepting hypotheses $\mathcal{H}_{15}$ ($q_{15} = 2$ two-dimensional outlier in GPS satellites 1 and 8), $\mathcal{H}_{28}$ ($q_{28} = 2$ two-dimensional outlier in GPS satellites 4 and 6), $\mathcal{H}_{31}$ ($q_{31} = 2$ two-dimensional outlier in GPS satellites 5 and 6).

5

of $f_{\underline{\mathrm{t}}}(t|\mathcal{H}_7)$ decreases in the acceptance region $\mathcal{P}_0 \subset \mathbb{R}^{r=4}$). After $\mathrm{P}_{\mathrm{MD}_7}\underline{\mathrm{P}}_{\mathcal{F}_\mathrm{h}}|\mathrm{MD}_7$ reaches its maximum at $7.9663 \cdot 10^{-7}$ (with $\sigma_{\mathrm{sim}} = 0.1025 \cdot 10^{-7}$) for $\mathrm{b}_7 = 11.58$ [m], its decrease is driven by $\mathrm{P}_{\mathrm{MD}_7}$ as its values are significantly lower than those of $\underline{\mathrm{P}}_{\mathcal{F}_\mathrm{h}}|\mathrm{MD}_7$. The behavior of $\mathrm{P}_{\mathrm{MD}_7}$ is also shown in Figure 5.9(a).

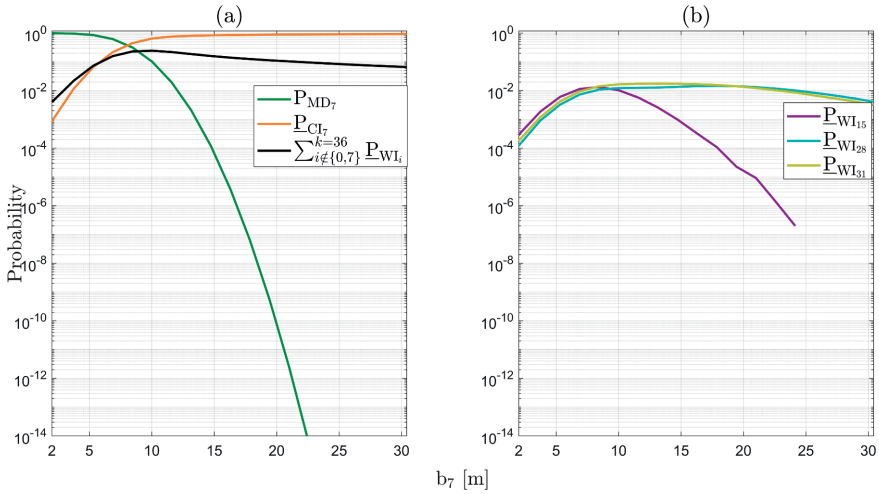

Figure 5.9: (a) Computed probabilities of testing decisions under $\mathcal{H}_7$: $\mathrm{P}_{\mathrm{MD}_7}$, $\underline{\mathrm{P}}_{\mathrm{CI}_7}$, $\sum_{j\neq 0,7}^{k=36}\underline{\mathrm{P}}_{\mathrm{WI}_j}$ as a function of outlier size b_7 [m]; (b) Terms of $\sum_{j\neq 0,7}^{k=36}\underline{\mathrm{P}}_{\mathrm{WI}_j}$ as a function of b_7 [m]: $\underline{\mathrm{P}}_{\mathrm{WI}_j}$ for $j \in \{15, 28, 31\}$.

Figure 5.8(c) shows the terms of $\sum_{j\neq 0,7}^{k=36}\underline{\mathrm{P}}_{\mathrm{WI}_j}\underline{\mathrm{P}}_{\mathcal{F}_\mathrm{h}}|\mathrm{WI}_j$ that contribute most to it. These terms are $\underline{\mathrm{P}}_{\mathrm{WI}_{15}}\underline{\mathrm{P}}_{\mathcal{F}_\mathrm{h}}|\mathrm{WI}_{15}$, $\underline{\mathrm{P}}_{\mathrm{WI}_{28}}\underline{\mathrm{P}}_{\mathcal{F}_\mathrm{h}}|\mathrm{WI}_{28}$, and $\underline{\mathrm{P}}_{\mathrm{WI}_{31}}\underline{\mathrm{P}}_{\mathcal{F}_\mathrm{h}}|\mathrm{WI}_{31}$, which correspond to the wrongful

identification of $\mathcal{H}_{15}$, $\mathcal{H}_{28}$, and $\mathcal{H}_{31}$, while $\mathcal{H}_7$ is valid. The corresponding probabilities of wrong identifications (related only to the testing decisions) are shown in Figure 5.9(b). Each of these alternative hypotheses accounts for two-dimensional outliers ($q_{15} = q_{28} = q_{31} = 2$) affecting the pseudoranges of the following pairs of GPS satellites: 1-8 ($\mathcal{H}_{15}$), 4-6 ($\mathcal{H}_{28}$), 5-6 ($\mathcal{H}_{31}$).

Table 5.3: Angles between $\mathcal{R}\left(\mathrm{c}_{\mathrm{t}_7}\right)$ and $\mathcal{R}\left(\mathrm{C}_{\mathrm{t}_j}\right)$ for $j \in \{15, 28, 31\}$

Subspace	$\mathcal{R}\left(\mathrm{C}_{\mathrm{t}_{15}}\right)$	$\mathcal{R}\left(\mathrm{C}_{\mathrm{t}_{28}}\right)$	$\mathcal{R}\left(\mathrm{C}_{\mathrm{t}_{31}}\right)$
$\mathcal{R}\left(\mathrm{c}_{\mathrm{t}_7}\right)$	31.06°	12.32°	13.80°

One contributing factor to the dominant behavior of the three components in Figure 5.8(c) is the angles between the subspaces spanned by $\mathcal{R}\left(\mathrm{C}_{\mathrm{t}_j}\right)$, for $j \in \{15, 28, 31\}$, and the subspace spanned by $\mathcal{R}\left(\mathrm{c}_{\mathrm{t}_7}\right)$ in the misclosure space $\mathbb{R}^{r=4}$. The smaller these angles are, the closer the corresponding subspaces are, and hence the larger the probabilities of wrong identifications. As $f_{\underline{\mathrm{t}}}(t|\mathcal{H}_7)$ moves along $\mathcal{R}\left(\mathrm{c}_{\mathrm{t}_7}\right)$ in $\mathcal{P}_7$ (as b_7 increases), the probability density outside $\mathcal{P}_7$ is also increasing in $\mathcal{P}_{15}$, $\mathcal{P}_{28}$, $\mathcal{P}_{31}$ up until b_7 reaches approximately 8.4 [m] (see the corresponding $\underline{\mathsf{P}}_{\mathrm{WI}_j}$ in Figure 5.9(b)). After b_7 reaches approximately 8.4 [m], the faster decreasing behavior of the density in $\mathcal{P}_{15}$ (i.e., $\underline{\mathsf{P}}_{\mathrm{WI}_{15}}$) is due to the larger angle $\measuredangle\left(\mathcal{R}\left(\mathrm{c}_{\mathrm{t}_7}\right), \mathcal{R}\left(\mathrm{C}_{\mathrm{t}_{15}}\right)\right)$ compared with $\measuredangle\left(\mathcal{R}\left(\mathrm{c}_{\mathrm{t}_7}\right), \mathcal{R}\left(\mathrm{C}_{\mathrm{t}_{28}}\right)\right)$ and $\measuredangle\left(\mathcal{R}\left(\mathrm{c}_{\mathrm{t}_7}\right), \mathcal{R}\left(\mathrm{C}_{\mathrm{t}_{31}}\right)\right)$. The second contributing factor is how the probability density of conditional PDFs $f_{\underline{\mathrm{h}}|\mathrm{WI}_j}\left(h|\mathrm{WI}_j\right)$ for $j \in \{15, 28, 31\}$ varies in relation to the safety region as a function of b_7. For example, if the satellite pair 1-8 ($\mathcal{H}_{15}$) is wrongfully excluded while the outlier is in satellite 7, leads to $f_{\underline{\mathrm{h}}|\mathrm{WI}_7}(h|\mathrm{WI}_7)$ having a high density outside $\mathcal{B}_{\mathrm{h}}$ in the horizontal direction corresponding to the skyplot azimuth range $270^\circ - 0^\circ$ (see Figure 5.3). Hence, the dominant behavior of $\underline{\mathsf{P}}_{\mathrm{WI}_{15}}\underline{\mathbb{P}}_{\mathcal{F}_{\mathrm{h}}}|\mathrm{WI}_{15}$ is initially driven by $\underline{\mathbb{P}}_{\mathcal{F}_{\mathrm{h}}}|\mathrm{WI}_{15}$ up to its peak around $\mathrm{b}_7 = 8.4$ [m]. Beyond that point, the behavior is governed by $\underline{\mathsf{P}}_{\mathrm{WI}_{15}}$ which decreases more rapidly than the other components in the plot as the angle $\measuredangle\left(\mathcal{R}\left(\mathrm{c}_{\mathrm{t}_7}\right), \mathcal{R}\left(\mathrm{C}_{\mathrm{t}_{15}}\right)\right) = 31.06^\circ$ is larger than $\measuredangle\left(\mathcal{R}\left(\mathrm{c}_{\mathrm{t}_7}\right), \mathcal{R}\left(\mathrm{C}_{\mathrm{t}_{28}}\right)\right) = 12.32^\circ$ and $\measuredangle\left(\mathcal{R}\left(\mathrm{c}_{\mathrm{t}_7}\right), \mathcal{R}\left(\mathrm{C}_{\mathrm{t}_{31}}\right)\right) = 13.80^\circ$ (see Table 5.3). A similar reasoning can be extended to the remaining components. Therefore, wrongfully excluding these groups of satellites—while the actual outlier is present in GPS satellite 7—leads the corresponding terms $\underline{\mathsf{P}}_{\mathrm{WI}_j}\underline{\mathbb{P}}_{\mathcal{F}_{\mathrm{h}}}|\mathrm{WI}_j$, for $j \in \{15, 28, 31\}$, to dominate $\underline{\mathbb{P}}_{\mathcal{F}_{\mathrm{h}}}|\mathcal{H}_7(\mathrm{b}_7)$ for outlier b_7 values around 8 and 21 [m]. An interesting point to note is that the global maximum of $\underline{\mathbb{P}}_{\mathcal{F}_{\mathrm{h}}}|\mathcal{H}_7(\mathrm{b}_7)$ arises from the combined contribution of $\underline{\mathsf{P}}_{\mathrm{WI}_{28}}\underline{\mathbb{P}}_{\mathcal{F}_{\mathrm{h}}}|\mathrm{WI}_{28}$ and $\underline{\mathsf{P}}_{\mathrm{WI}_{31}}\underline{\mathbb{P}}_{\mathcal{F}_{\mathrm{h}}}|\mathrm{WI}_{31}$.

As a second example, we analyze the probabilities of positioning failure under several hypotheses where $q_i = 2$, such as $\mathcal{H}_9$ (outliers in GPS Satellites 1 and 2), $\mathcal{H}_{16}$ (outliers in GPS Satellites 2 and 3), and $\mathcal{H}_{17}$ (outliers in GPS Satellites 2 and 4). The corresponding probabilities $\underline{\mathbb{P}}_{\mathcal{F}_{\mathrm{h}}}|\mathcal{H}_i(\mathrm{b}_i)$, for $i \in \{9, 16, 17\}$, are displayed on two-dimensional grids in Figure 5.10. These grids were obtained based on the following parametrization [25]

$$\mathrm{b}_i = \sqrt{\frac{\lambda_0^2}{||\Pi_{\mathrm{A}}^{\perp}\mathrm{C}_i\,\mathrm{d}||^2_{\mathrm{Q_{yy}}}}}\,\mathrm{d} = \sqrt{\frac{\lambda_0^2}{||\mathrm{C}_{\mathrm{t}_i}\,\mathrm{d}||^2_{\mathrm{Q_{tt}}}}}\,\mathrm{d}, \tag{5.33}$$

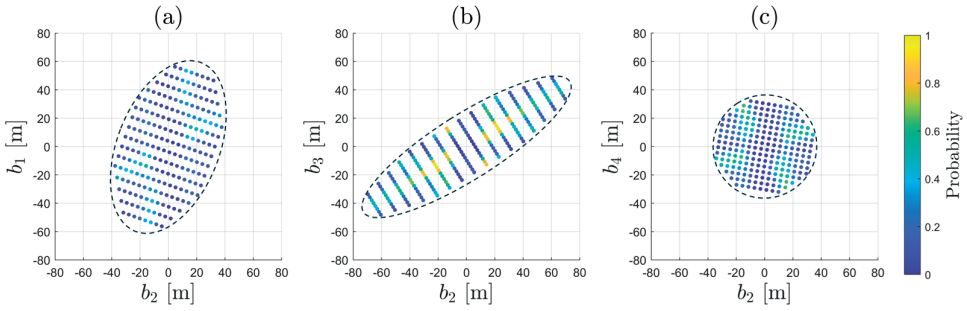

Figure 5.10: Ellipses shown with dashed lines are defined by (5.33), the interiors of which are then discretized; (a) $\underline{\mathbb{P}}_{\mathcal{F}_h}|\mathcal{H}_9(\mathrm{b}_9)$ over a grid $\mathrm{b}_9 = [\mathrm{b}_2\ \mathrm{b}_1]^T \in \mathbb{R}^{q_9=2}$ [m]; (b) $\underline{\mathbb{P}}_{\mathcal{F}_h}|\mathcal{H}_{16}(\mathrm{b}_{16})$ over a grid $\mathrm{b}_{16} = [\mathrm{b}_2\ \mathrm{b}_3]^T \in \mathbb{R}^{q_{16}=2}$ [m]; (c) $\underline{\mathbb{P}}_{\mathcal{F}_h}|\mathcal{H}_{17}(\mathrm{b}_{17})$ over a grid $\mathrm{b}_{17} = [\mathrm{b}_2\ \mathrm{b}_4]^T \in \mathbb{R}^{q_{17}=2}$ [m].

where λ_0^2 is the non-centrality parameter of $\|\underline{\mathrm{t}}\|^2_{\mathrm{Q_{tt}}} \overset{\mathcal{H}_i}{\sim} \chi^2(r, \lambda_0^2)$ and $\mathrm{d} \in \mathbb{R}^{q_i=2}$ is a unit vector which scans the unit circle in $\mathbb{R}^{q_i=2}$. As a result, b_i scans an ellipse in $\mathbb{R}^{q_i=2}$ as described by $\lambda_0^2 = \|\Pi_{\mathrm{A}}^{\perp}\mathrm{C}_i\,\mathrm{b}_i\|^2_{\mathrm{Q_{yy}}}$ (see [25] at page 105 and Figure 5.10). The non-centrality parameter λ_0^2 is selected such that the corresponding probability of correct detection is high (i.e., close to 1), ensuring that the ellipse encompasses a representative set of vectors b_i. The area within these ellipses is then discretized to form 2D grids of b_i, over which the probabilities are computed. In all three plots in Figure 5.10, the probabilities are highest (dot colors ranging from light blue to yellow) in situations where there is an approximately one-to-one relationship between the components of b_i's, for $i \in \{9, 16, 17\}$. In contrast, the probabilities are lowest (dot colors in dark blue) when b_2 lies approximately in the range of -10 to 10 [m], while b_1, b_3, and b_4 vary across their entire respective ranges. Figure 5.10(a) illustrates the shape and orientation of the grid for $\mathrm{b}_9 = [\mathrm{b}_2\ \mathrm{b}_1]^T \in \mathbb{R}^2$, corresponding to the exclusion of GPS satellites 2 and 1 from the positioning model in (5.21). Figure 5.10(b) shows that the grid of $\mathrm{b}_{16} = [\mathrm{b}_2\ \mathrm{b}_3]^T \in \mathbb{R}^2$ has the largest elongation in the North-East direction as GPS satellite 2 and 3 are the only ones in the azimuth range of 0°-120° (see Figure 5.3). In the case of Figure 5.10(c), the grid of $\mathrm{b}_{17} = [\mathrm{b}_2\ \mathrm{b}_4]^T \in \mathbb{R}^2$ is closer to a circular shape, as the elongation caused by the exclusion from the positioning model of satellites 2 and 4 is less pronounced. The maximum value for $\underline{\mathbb{P}}_{\mathcal{F}_h}|\mathcal{H}_9(\mathrm{b}_9)$ is attained at $4.8613 \cdot 10^{-1}$ (with $\sigma_{\mathrm{sim}} = 0.0047 \cdot 10^{-1}$) for $\pm\mathrm{b}_9 = [15.79\ 13.70]^T$ [m]. In the case of $\underline{\mathbb{P}}_{\mathcal{F}_h}|\mathcal{H}_{16}(\mathrm{b}_{16})$ (Figure 5.10(b)) the maximum is $9.1177 \cdot 10^{-1}$ (with $\sigma_{\mathrm{sim}} = 0.0053 \cdot 10^{-1}$) for $\pm\mathrm{b}_{16} = [21.04\ 14.68]^T$ [m], and that of $\underline{\mathbb{P}}_{\mathcal{F}_h}|\mathcal{H}_{17}(\mathrm{b}_{17})$ (Figure 5.10(c)) the maximum is $5.9342 \cdot 10^{-1}$ (with $\sigma_{\mathrm{sim}} = 0.0050 \cdot 10^{-1}$) for $\pm\mathrm{b}_{17} = [15.35\ -24.90]^T$ [m]. The maximum is determined in a similar manner for the other cases of $\underline{\mathbb{P}}_{\mathcal{F}_h}|\mathcal{H}_i(\mathrm{b}_i)$, for $i \notin \{0, 9, 16, 17\}$. The maximum values of $\underline{\mathbb{P}}_{\mathcal{F}_h}|\mathcal{H}_i(\mathrm{b}_i)$ for all $i \in \{1, ..., 36\}$ are shown in Figure 5.11.

Figure 5.11 shows that the maximum values of $\underline{\mathbb{P}}_{\mathcal{F}_h}|\mathcal{H}_i(\mathrm{b}_i)$ among the components corresponding to $q_i = 1$ (i.e., $i \in \{1, ..., 8\}$) are highest for $\underline{\mathbb{P}}_{\mathcal{F}_h}|\mathcal{H}_2(\mathrm{b}_2)$ and $\underline{\mathbb{P}}_{\mathcal{F}_h}|\mathcal{H}_3(\mathrm{b}_3)$. This is expected, as one-dimensional outliers at a time in GPS satellites 2 and 3—the only ones located in the azimuth range $0^\circ - 120^\circ$ of the skyplot—have a greater impact on horizontal positioning performance. Since GPS satellites 2 and 3 are the only ones in the aforemen-

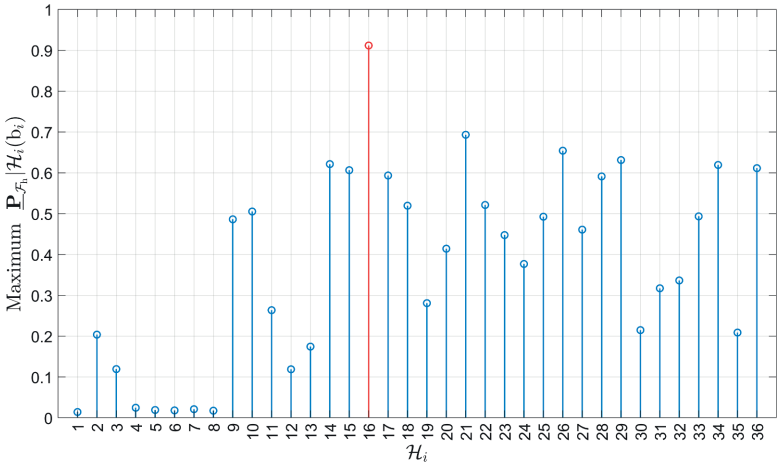

Figure 5.11: Maximum values of $\underline{\mathbb{P}}_{\mathcal{F}_h}|\mathcal{H}_i(b_i)$ for all $i \in \{1,...,36\}$. The red stem represents $\underline{\mathbb{P}}_{\mathcal{F}_h}|\mathcal{H}_{16}(b_{16})$, which corresponds to two-dimensional outliers in the pseudoranges from GPS Satellites 2 and 3.

-tioned azimuth range, outliers in their measurements have a stronger influence on the horizontal solution due to the receiver–satellite geometry. Furthermore, the maximum values of $\underline{\mathbb{P}}_{\mathcal{F}_h}|\mathcal{H}_i(b_i)$ for $q_i = 2$ (i.e., $i \in \{9,...,36\}$) are several times larger than those for $q_i = 1$ (i.e., $i \in \{1,..,8\}$). The largest value among all alternative hypotheses corresponds to $\underline{\mathbb{P}}_{\mathcal{F}_h}|\mathcal{H}_{16}(b_{16})$, which is associated with the simultaneous two-dimensional outliers in the pseudoranges from GPS satellites 2 and 3 (see Figure 5.3).

Worst-case scenario with respect to $b_i \in \mathbb{R}^{q_i}$

By using the a priori probabilities of the alternative hypotheses from Figure 5.4, the computed value of $\underline{\mathbb{P}}_{\mathcal{F}_h}|\mathcal{H}_0$ from Table 5.1, and the maximum values of $\underline{\mathbb{P}}_{\mathcal{F}_h}|\mathcal{H}_i(b_i)$ from Figure 5.11, one can evaluate the upper bound in the worst-case scenario, w.r.t. to $b_i \in \mathbb{R}^{q_i}$, from (5.28) as follows:

$$\max_{\check{\mathbf{b}}} \underline{\check{\mathbb{P}}}_{\mathcal{F}_h}(\check{\mathbf{b}}) = \mathsf{P}(\mathcal{H}_0)\underline{\mathbb{P}}_{\mathcal{F}_h}|\mathcal{H}_0 + \left(\max_{b_1,...,b_k} \sum_{i=1}^{k=36} \mathsf{P}(\mathcal{H}_i)\underline{\mathbb{P}}_{\mathcal{F}_h}|\mathcal{H}_i(b_i) \right) + \sum_{i=37}^{k'=255} \mathsf{P}(\mathcal{H}_i). \tag{5.34}$$

The numerical results are presented in Table 5.4 (for $\alpha = 10^{-3}$), covering a range from more conservative cases (Case 1 with $\pi = 10^{-3}$) to more optimistic ones (Case 3 with $\pi = 10^{-5}$) cf. Fig. 5.4(b). None of the cases, when $\alpha = 10^{-3}$, approaches the level of 10^{-5} for the maximum $\underline{\check{\mathbb{P}}}_{\mathcal{F}_h}(\check{\mathbf{b}})$, which would be needed for SAIL 4 en-route operations. If we set the level of significance to a much lower value, for example $\alpha = 10^{-5}$, the results indicate that only Case 3 (the most optimistic) would be appropriate for SAIL 4. This is because the contribution of false alarm components to $\underline{\mathbb{P}}_{\mathcal{F}_h}|\mathcal{H}_0$ is lower when $\alpha = 10^{-5}$, and also because the a priori probability $\mathsf{P}(\mathcal{H}_0)$ is high for $\pi = 10^{-5}$, resulting in a greater contribution to (5.34). However, caution should be exercised when relying too heavily on the $\mathcal{H}_0$ component, particularly in safety-of-life applications.

Table 5.4: Maximum values of $\underline{\check{\mathrm{P}}}_{\mathcal{F}_\mathrm{h}}(\check{\mathbf{b}})$ and their standard deviations (σ_{sim}) for the three cases and for $\alpha = 10^{-3}$ and $\alpha = 10^{-5}$.

			$\alpha = 10^{-3}$		$\alpha = 10^{-5}$	
Cases	π	$\mathsf{P}(\mathcal{H}_0)$	Max. $\underline{\check{\mathrm{P}}}_{\mathcal{F}_\mathrm{h}}(\check{\mathbf{b}})$	σ_{sim}	Max. $\underline{\check{\mathrm{P}}}_{\mathcal{F}_\mathrm{h}}(\check{\mathbf{b}})$	σ_{sim}
1	10^{-3}	0.99203	$5.1816 \cdot 10^{-4}$	$0.0059 \cdot 10^{-4}$	$5.7009 \cdot 10^{-4}$	$0.0033 \cdot 10^{-4}$
2	10^{-4}	0.99920	$1.3446 \cdot 10^{-4}$	$0.0050 \cdot 10^{-4}$	$0.5757 \cdot 10^{-4}$	$0.0019 \cdot 10^{-4}$
3	10^{-5}	0.99992	$0.9700 \cdot 10^{-4}$	$0.0049 \cdot 10^{-4}$	$0.0720 \cdot 10^{-4}$	$0.0019 \cdot 10^{-4}$

Since these results correspond to a receiver–GPS satellite geometry at a single instant of time (see Figure 5.3), the next step is to investigate the results obtained over a 24-hour period, accounting for the evolution of GPS satellite positions in their orbits.

5.4.2 GPS satellite geometry over 24 hours period

In Figure 5.12(a) we show the number of observed GPS satellites (in black), using a 10° elevation mask, and the weighted Horizontal Dilution of Precision (wHDOP) in orange, which is computed as wHDOP $= \sqrt{\mathrm{trace}\left(\mathrm{H}^T \left(\mathrm{A}^T \mathrm{Q}_{\mathrm{yy}}^{-1} \mathrm{A}\right)^{-1} \mathrm{H}\right)}$ [m] based on [43]. The wHDOP is useful for giving an indication of the variation of the horizontal positioning precision as a function of the change in GPS satellite geometry while also taking into account the elevation-dependent weighting of the observables. Figure 5.12(b) shows the total number of alternative hypotheses $\mathcal{H}_{i\neq 0}$, including both one-dimensional ($q_i = 1$) and two-dimensional ($q_i = 2$) outliers. It can be seen that the total number of hypotheses (k) varies between 21 and 66. The components of $\underline{\mathrm{P}}_{\mathcal{F}_\mathrm{h}}|\mathcal{H}_0$ are shown in Figure 5.12(c), where the dominant component is $\sum_{i=1}^{k} \underline{\mathrm{P}}_{\mathrm{FA}_i} \underline{\mathrm{P}}_{\mathcal{F}_\mathrm{h}}|\mathrm{FA}_i$ except at 3 h and 25 min ($\approx$ 3.4 hours) and at 6 h and 30 min (6.5 hours), when $\mathsf{P}_{\mathrm{CA}} \underline{\mathrm{P}}_{\mathcal{F}_\mathrm{h}}|\mathrm{CA}$ domaintes due to poor wHDOP. The values obtained for $\underline{\mathrm{P}}_{\mathcal{F}_\mathrm{h}}|\mathcal{H}_0$ are shown in Figure 5.12(d). When $\alpha = 10^{-3}$, even under $\mathcal{H}_0$, the values of $\underline{\mathrm{P}}_{\mathcal{F}_\mathrm{h}}|\mathcal{H}_0$ are *above* 10^{-5} for approximately 78.27% of the time. Redoing the computations for $\alpha = 10^{-5}$, the values of $\underline{\mathrm{P}}_{\mathcal{F}_\mathrm{h}}|\mathcal{H}_0$ exceed 10^{-5} only 4.15% of the time (due to the lower value of the component $\sum_{i=1}^{k} \underline{\mathrm{P}}_{\mathrm{FA}_i} \underline{\mathrm{P}}_{\mathcal{F}_\mathrm{h}}|\mathrm{FA}_i$).

We select seven points that are below 10^{-5} (highlighted in Figure 5.12(d) by dots) and compute the remaining components of $\max_{\check{\mathbf{b}}} \underline{\check{\mathrm{P}}}_{\mathcal{F}_\mathrm{h}}(\check{\mathbf{b}})$, as done in (5.34), to verify whether the requirement is still met for the same cases from Table 5.4, which are restated as follows as a function of the apriori probabilities of the null hypothesis $\mathcal{H}_0$: (i) Case 1 with $\mathsf{P}(\mathcal{H}_0) = 0.99203$; (ii) Case 2 with $\mathsf{P}(\mathcal{H}_0) = 0.99920$; (iii) Case 3 with $\mathcal{H}_0 = 0.99992$. When $\alpha = 10^{-3}$, Figure 5.13(a) shows that, for Case 1, the requirement is not met at any of the selected points. In Case 2, the requirement is not satisfied only once—at point index 6. For Case 3, the requirement is satisfied at all points, although the value at index 6 is just below the threshold. Notably, at point 6, the value of $\underline{\mathrm{P}}_{\mathcal{F}_\mathrm{h}}|\mathcal{H}_0$ is already close to 10^{-5}. Figure 5.13(b) shows the results for $\alpha = 10^{-5}$. In Case 1, only at index 3 does the maximum value fall slightly below the requirement. For Case 2, as before, the requirement is not met only once—at point index 6. For Case 3, the requirement is satisfied at all points. The results

for Case 3 are more sensitive to changes in α, which is consistent with the explanation provided for the results in Table 5.4.

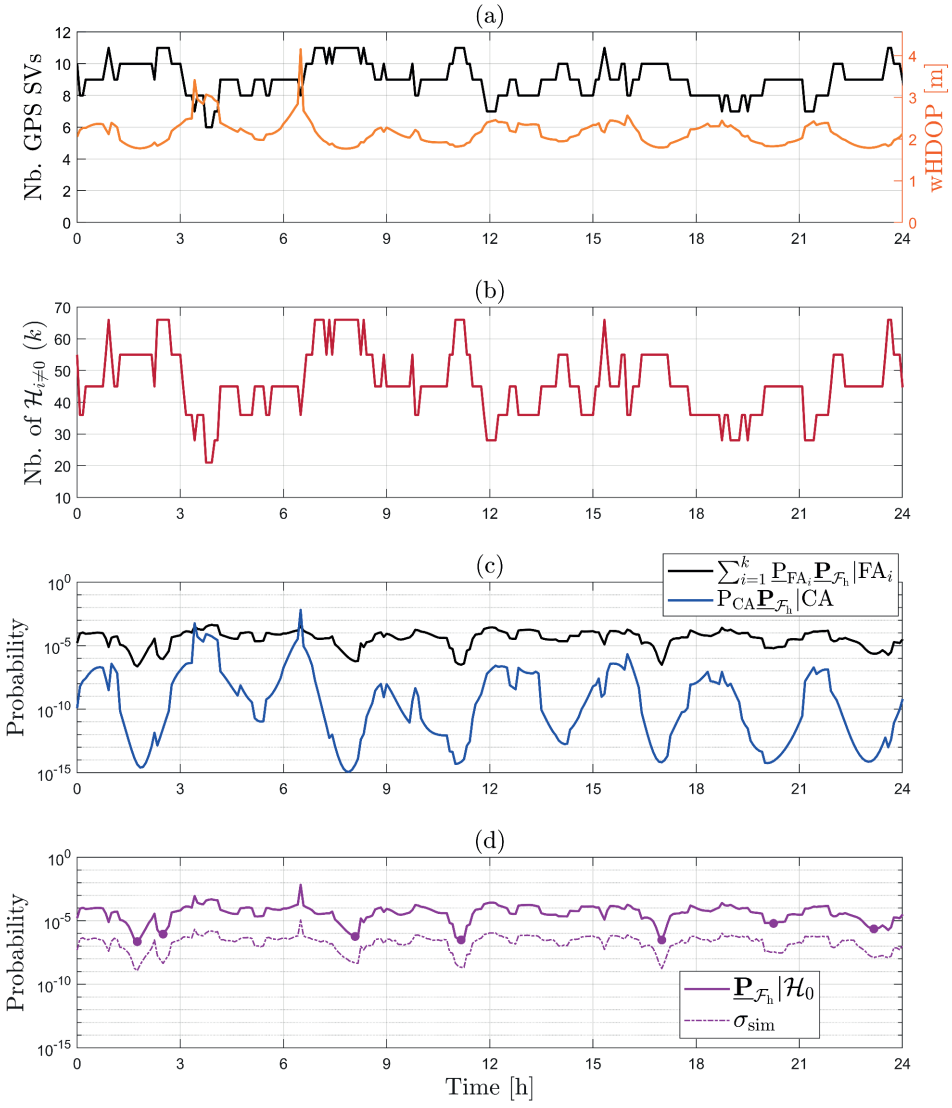

Figure 5.12: Results over time (with $\alpha = 10^{-3}$): (a) Nb. of GPS Satellites and wHDOP; (b) Nb. of alternative hypotheses $\mathcal{H}_{i\neq 0}$ (k); (c) Components $\mathrm{P}_{\mathrm{CA}} \underline{\mathbb{P}}_{\mathcal{F}_\mathrm{h}} | \mathrm{CA}$ and $\sum_{i=1}^{k} \underline{\mathrm{P}}_{\mathrm{FA}_i} \underline{\mathbb{P}}_{\mathcal{F}_\mathrm{h}} | \mathrm{FA}_i$; (d) $\underline{\mathbb{P}}_{\mathcal{F}_\mathrm{h}} | \mathcal{H}_0$, its σ_{sim}.

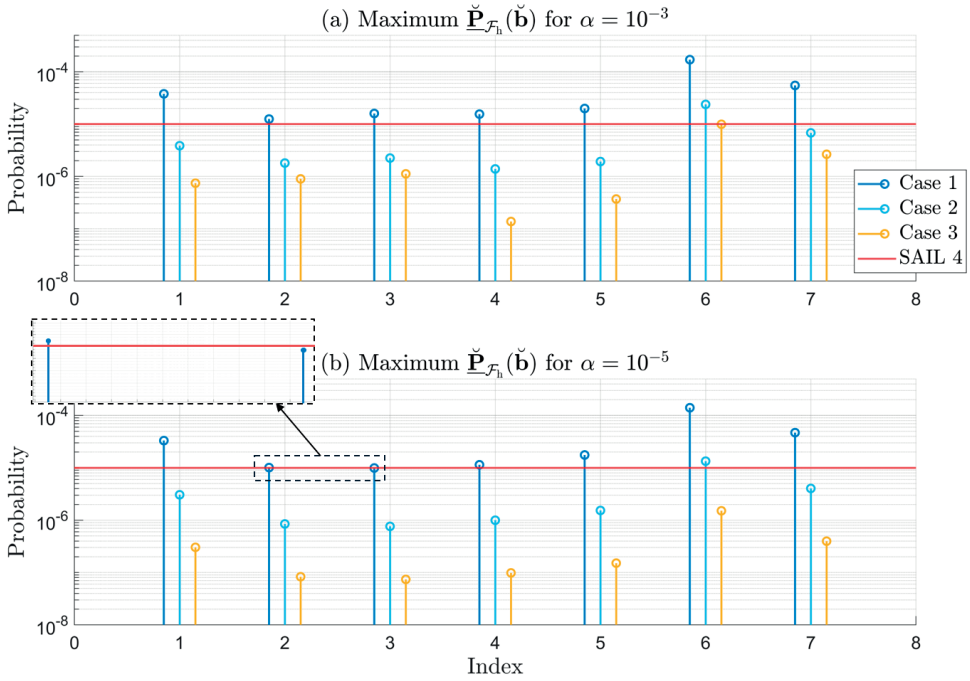

Figure 5.13: Maximum values of $\underline{\breve{\mathbb{P}}}_{\mathcal{F}_h}(\breve{\mathbf{b}})$ for the highlighted seven points in Figure 5.12. In the current plot these points are indexed from 1 to 7, left to right; (a) for $\alpha = 10^{-3}$; (b) for $\alpha = 10^{-5}$.

If the requirements and guidelines are not satisfied, then appropriate changes to the measurement setup (functional and stochastic models), safety-region, or the combined parameter estimation and statistical hypothesis testing procedure, may be necessary. For instance, the new theoretical framework introduced in [44] shows how fit-for-purpose statistical hypothesis testing can improve the performance of DIA-estimators in terms of positioning safety.

5.5 Computational resources

The computations in this work were performed using MATLAB R2023b with the Parallel Computing Toolbox on the Snellius Supercomputer, provided by the Dutch National e-Infrastructure. As an illustration of the computational load, evaluating the components (5.32) to obtain the results in Figures 5.8 required computation times on the order of several minutes. These times should be seen as indicative, since they depend on the implementation details, available hardware, and programming language.

5.6 Summary and concluding remarks

In this contribution, we presented a general approach for performing safety analyses—such as positioning safety—based on the DIA-estimator, while accounting for multidimensional model misspecifications. Specifically, the study focused on misspecifications in the mean

of the observation model—such as those caused by outliers in the observations. The approach includes: (i) use of the DIA-estimator and of its PDF to account for the combined uncertainty of estimation and hypothesis testing [1]; (ii) formulation of the probability of positioning failure and of its components for an application dependent safety-region [4, 8]; (iii) computation of the probability of positioning failure and of its conditional components via a recently developed method [12]. This approach is consistent with the scenario-based safety assessment framework, which is commonly used in domains such as automated and autonomous vehicles [17–19] and UAVs [20], among others.

As an illustrative case, we conducted a positioning safety analysis for a UAV, considering two scenarios involving one- and two-dimensional outlier misspecifications in the pseudorange measurements. The choice of the positioning model for the UAV, under nominal conditions, was based on the TSO certification for GPS-based UAV positioning [14, 15]. In the first scenario, we considered a fixed receiver-satellite geometry at a single snapshot of time (see Figure 5.3) to study the shape of the DIA-estimator PDF and to gain insights into the components that contribute the most to the probability of positioning failure under $\mathcal{H}_0$. For example, the conditional components related to the False Alarm (FA_i) testing decisions of the DIA-estimator's PDF (see Figure 5.5) exhibited bimodal and quadrimodal structures (e.g., $f_{\underline{\hat{h}}|\mathrm{FA}_2}(h|\mathrm{FA}_2)$, $f_{\underline{\hat{h}}|\mathrm{FA}_{20}}(h|\mathrm{FA}_{20})$). The number of modes of a component $f_{\underline{\hat{h}}|\mathrm{FA}_i}(h|\mathrm{FA}_i) = \mathsf{E}_{\underline{t}}\left[f_{\underline{\hat{h}}_0}(h + \mathrm{G}_i\mathrm{C}_{t_i}^{+}\underline{t}|\mathcal{H}_0)p_i(\underline{t})\right]/\mathsf{P}_{\mathrm{FA}_i}$ depends on: (i) the number of columns of the matrix $\mathrm{G}_i \in \mathbb{R}^{2\times q_i}$, and hence the dimension of the model misspecification q_i, and (ii) on the linear combinations of the columns of $\mathrm{G}_i \in \mathbb{R}^{2\times q_i}$, weighted by the coefficients $\left(\mathrm{C}_{t_i}^{+}\underline{t}\right)$, for $\underline{t} \in \mathcal{P}_i$ (see Figure 5.6). Notably, point (ii) depends on the hypothesis testing procedure, specifically on the partitions $\mathcal{P}_i \subset \mathbb{R}^r$ of the misclosure vector $\underline{t} \in \mathbb{R}^r$, meaning that different partitions (e.g., [44]) can lead to different number of modes and shapes for $f_{\underline{\hat{h}}|\mathrm{FA}_i}(h|\mathrm{FA}_i)$.

The positioning safety analysis under $\mathcal{H}_7$ (one-dimensional outlier in GPS satellite 7) revealed that the probability $\underline{\mathsf{P}}_{\mathcal{F}_\mathrm{h}}|\mathcal{H}_7(\mathrm{b}_7)$ has a local and global maximum (see Figure 5.8). These maxima were caused by the components conditioned on the Wrongful Identification (WI) testing decision $\underline{\mathsf{P}}_{\mathrm{WI}_{15}}\underline{\mathsf{P}}_{\mathcal{F}_\mathrm{h}}|\mathrm{WI}_{15}$ (pair 1-8), $\underline{\mathsf{P}}_{\mathrm{WI}_{28}}\underline{\mathsf{P}}_{\mathcal{F}_\mathrm{h}}|\mathrm{WI}_{28}$ (pair 4-6), and $\underline{\mathsf{P}}_{\mathrm{WI}_{31}}\underline{\mathsf{P}}_{\mathcal{F}_\mathrm{h}}|\mathrm{WI}_{31}$ (pair 5-6). The primary reason these components contributed the most is the strong correlation between the corresponding test statistics, combined with the degraded satellite geometry caused by the wrongful exclusion of these satellite pairs while $\mathcal{H}_7$ was valid. In general, the probability $\underline{\mathsf{P}}_{\mathcal{F}_\mathrm{h}}|\mathcal{H}_i(\mathrm{b}_i)$ can exhibit multiple local maxima as a function of $\mathrm{b}_i \in \mathbb{R}^{q_i}$. These components can be revealed through a component-wise analysis, as carried out in this contribution and in [4, 8, 12].

In the second scenario we have considered a 24-hours (on May 24, 2024) evolution of GPS satellites moving over an airspace region in The Netherlands for which authorization can be obtained for UAV operations (see Figure 5.12). The total number of alternative hypotheses (k) that account for both one- and two-dimensional outliers varied between 21 and 66. Under $\mathcal{H}_0$, the computed $\underline{\mathsf{P}}_{\mathcal{F}_\mathrm{h}}|\mathcal{H}_0$ was mainly driven by the component that accounts for all false alarm testing decisions $\sum_{i=1}^{k}\underline{\mathsf{P}}_{\mathrm{FA}_i}\underline{\mathsf{P}}_{\mathcal{F}_\mathrm{h}}|\mathrm{FA}_i$. There were two cases in

which $\underline{\mathsf{P}}_{\mathrm{CA}}\underline{\mathbb{P}}_{\mathcal{F}_\mathrm{h}}|\mathrm{CA} > \sum_{i=1}^{k}\underline{\mathsf{P}}_{\mathrm{FA}_i}\underline{\mathbb{P}}_{\mathcal{F}_\mathrm{h}}|\mathrm{FA}_i$ (see Figure 5.12(c)), both corresponding to the weakest satellite geometries over the 24 hours, characterized by wHDOP values of 3.4 and 4.1. The results of the worst-case scenarios (w.r.t $\mathrm{b}_i \in \mathbb{R}^{q_i}$) for the selected points (see Figure 5.12(d)) showed that Case 3 (when $\pi = 10^{-5}$ in Table 5.4) is consistently below 10^{-5} (order of SAIL 4 requirement en-route operations). However, caution should be exercised when relying too heavily on the $\mathcal{H}_0$ component of the maximum $\underline{\breve{\mathbb{P}}}_{\mathcal{F}_\mathrm{h}}(\breve{\mathbf{b}})$, particularly in safety-of-life applications.

This type of positioning-safety analysis is broadly applicable across a range of safety-critical applications (e.g., automotive, civil aviation, rail, maritime). For example, it can support the development of positioning algorithms and their verification with respect to safety and performance requirements, as well as help in studies aimed at defining or refining such requirements. Although the positioning safety analysis was illustrated using a representative TSO-certified GPS receiver in a UAV context, the example can be extended to incorporate multisensor fusion and additional GNSS constellations (e.g., Galileo), which will be the subject of future work.

BIBLIOGRAPHY

[1] P. J. G. Teunissen. Distributional theory for the DIA method. *J. Geod.*, 92(1):59–80, 2018.

[2] Peter F. de Bakker and Christian C. J. M. Tiberius. Real-time multi-GNSS single-frequency precise point positioning. *GPS Solut.*, 21:1791–1803, 2017.

[3] S. Zaminpardaz, P. J. G. Teunissen, and C. C. J. M. Tiberius. Risking to underestimate the integrity risk. *GPS Solut.*, 23(29):1–16, 2019.

[4] S. Ciuban, P. J. G. Teunissen, and C. C. J. M. Tiberius. GNSS Positioning Safety: Probability of Positioning Failure and its Components. In *Proc. 37th Int. Tech. Meeting Satellite Div. Inst. Navigation (ION GNSS+)*, pages 2228–2249, 2024.

[5] Delft Geodetic Computing Centre. The Delft Approach for the Design and Computation of Geodetic Networks. In *Forty Years of Thought: Anniversary Edition on the Occasion of the 65th Birthday of Professor W. Baarda*, volume 1, pages 202–274. 1984.

[6] S. Zaminpardaz, P. J. G. Teunissen, and C. C. J. M. Tiberius. A risk evaluation method for deformation monitoring systems. *J. Geod.*, 94(28):1–15, 2020.

[7] P. J. G. Teunissen. Quality control in integrated navigation systems. *IEEE Aerosp. Electron. Syst. Mag.*, 5(7):35–41, 1990.

[8] S. Ciuban, P. J. G. Teunissen, and C. C. J. M. Tiberius. Dependence Between Parameter Estimation and Statistical Hypothesis Testing: Positioning Safety Analysis for Automated/Autonomous Vehicles. *IEEE Transactions on Intelligent Transportation Systems*, 26(4):5509–5521, 2025.

[9] S. Zaminpardaz and P. J. G. Teunissen. Detection-only versus detection and identification of model misspecifications. *J. Geod.*, 97(55):1–19, 2023.

[10] Yangkang Yu, Ling Yang, Yunzhong Shen, and Nan Sun. A DIA method based on maximum a posteriori estimate for multiple outliers. *GPS Solut.*, 27(199):1–14, 2023.

[11] Yangkang Yu, Ling Yang, and Yunzhong Shen. An extended w-test for outlier diagnostics in linear models. *J. Geod.*, 98(58):1–21, 2024.

[12] S. Ciuban, P. J. G. Teunissen, and C. C. J. M. Tiberius. A Method to Compute the Probability of Positioning Failure for Vehicles in the Context of Dependence Between Parameter Estimation and Statistical Hypothesis Testing. *IEEE Transactions on Vehicular Technologies*, 74(10):15238–15253, 2025.

[13] R.T.C.A. Special Committee 159. *Minimum Operational Performance Standards (MOPS) for Global Positioning System/Satellite-Based Augmentation System Airborne Equipment.* DO-229F. Radio Technical Commission for Aeronautics, Washington, D.C., 2020.

[14] Federal Aviation Administration (FAA). Technical Standard Order C-145e: Airborne Navigation Sensors Using the Global Positioning System Augmented by the Satellite Based Augmentation System (SBAS). Technical report, 2017.

[15] T. Cozzens. uAvionix receives FAA order for certified drone GPS receiver, 2021. GPS World, August, 2021. [Online].

[16] European Union Aviation Safety Agency (EASA). National aviation authority drone website reference. `https://www.easa.europa.eu/en/domains/civil-drones/naa`. [Online].

[17] S. Riedmaier et al. Survey on Scenario-Based Safety Assessment of Automated Vehicles. *IEEE Access*, 8:87456–87477, 2020.

[18] United Nations Economic Commission for Europe. New Assessment/Test Method for Automated Driving (NATM) Guidelines for Validating Automated Driving Systems (ADS). Report, 2023.

[19] E. de Gelder et al. TNO Street Wise: Scenario-Based Safety Assessment of Automated Driving Systems. Technical report, Netherlands Organisation for Applied Scientific Research (TNO), 2024.

[20] S. Khatiri et al. Simulation-based Test Case Generation for Unmanned Aerial Vehicles in the Neighborhood of Real Flights. In *Proc. IEEE Conf. Softw. Test. Verif. Valid.*, 2023.

[21] D. Odijk. Positioning Model. In P. J. G. Teunissen and O. Montenbruck, editors, *Springer Handbook of Global Navigation Satellite Systems*, chapter 21, page 617. Springer, Cham, 2017.

[22] M. Maaref, J. Khalife, and Z. M. Kassas. Aerial Vehicle Protection Level Reduction by Fusing GNSS and Terrestrial Signals of Opportunity. *IEEE Trans. Intell. Transp. Syst.*, 22(9):5976–5993, 2021.

[23] Shuchen Liu, Kaizheng Wang, and Dirk Abel. Robust state and protection-level estimation within tightly coupled GNSS/INS navigation system. *GPS Solutions*, 27(111), 2023.

[24] P. J. G. Teunissen. Batch and Recursive Model Validation. In P. J. G. Teunissen and O. Montenbruck, editors, *Springer Handbook of Global Navigation Satellite Systems*, chapter 24, pages 687–720. Springer, Cham, 2017.

[25] P. J. G. Teunissen. *Testing Theory: An Introduction.* Mathematical Geodesy and Positioning. Delft University Press, Delft, 2nd edition, 2006.

[26] R. Y. Rubinstein and D. P. Kroese. *Simulation and the Monte Carlo Method.* Wiley Series in Probability and Statistics. Wiley, Hoboken, NJ, 2nd edition, 2008.

[27] H. Kahn and A. W. Marshall. Methods of Reducing Sample Size in Monte Carlo Computations. *J. Oper. Res. Soc. Am.*, 1(5):263–278, 1953.

[28] R. Y. Rubinstein. The cross-entropy method for combinatorial and continuous optimization. *Methodol. Comput. Appl. Prob.*, 1:127–190, 1999.

[29] J. Morio and M. Balesdent. *Estimation of Rare Event Probabilities in Complex Aerospace and Other Systems - A Practical Approach.* Elsevier B.V., Amsterdam, 2016.

[30] G. Johnston, A. Riddell, and G. Hausler. The International GNSS Service. In P. J. G. Teunissen and O. Montenbruck, editors, *Springer Handbook of Global Navigation Satellite Systems*, pages 967–982. Springer, Cham, 2017.

[31] European Union Agency for the Space Programme (EUSPA). Report on aviation and drones: User needs and requirements. Technical report, 2023.

[32] P. J. G. Teunissen. Nonlinear least squares. *Manuscr. Geod.*, 15(3):137–150, 1990.

[33] H. J. Euler and C. C. Goad. On optimal filtering of GPS dual frequency observations without using orbit information. *Bull. Geod.*, 65(2):130–143, 1991.

[34] uAvionix. trufyx tso gps receiver for unmanned aerial systems: Product details and specifications. `https://uavionix.store/unmanned-navigation/trufyx-tso`. [Online].

[35] Rüdiger Lehmann and Michael Lösler. Multiple Outlier Detection: Hypothesis Tests versus Model Selection by Information Criteria. *J. Surv. Eng.*, 142(4), November 2016.

[36] Karl-Rudolf Koch. Expectation Maximization algorithm and its minimal detectable outliers. *Stud. Geophys. Geod.*, 61(1):1–18, 2017.

[37] Davide Imparato. *GNSS-based Receiver Autonomous Integrity Monitoring for Aircraft Navigation.* Ph.D. Thesis, Delft University of Technology, 2016.

[38] J. Blanch et al. Baseline Advanced RAIM User Algorithm and Possible Improvements. *IEEE Aerosp. Electr. Syst.*, 51(1):713–732, 2015.

[39] Working Group C. ARAIM Technical Subgroup Milestone 3. Technical report, EU-US Cooperation on Satellite Navigation, Working Group C, 2016.

[40] Baoyu Liu, Yang Gao, Yuting Gao, and Shizhuang Wang. HPL calculation improvement for Chi-squared residual-based ARAIM. *GPS Solutions*, 26(45), 2022.

[41] P. F. De Bakker, H. Van der Marel, and P. J. G. Teunissen. The Minimal Detectable Bias for Gnss Observations with a Single Receiver Setup and a Geometry-Free Model. In *Proceedings of the European Navigation Conference GNSS (ENC-GNSS)*, Naples, Italy, 2009.

[42] W. Wen, Q. Meng, and L.-T. Hsu. Integrity Monitoring for GNSS Positioning via Factor Graph Optimization in Urban Canyons. In *Proceedings of the 34th International Technical Meeting of the Satellite Division of The Institute of Navigation (ION GNSS+)*, pages 1508–1515, September 2021.

[43] D. H. Won et al. Weighted DOP With Consideration on Elevation-Dependent Range Errors of GNSS Satellites. *IEEE Trans. Instrum. Meas.*, 61(12):3241–3250, 2012.

[44] P. J. G. Teunissen. On the optimality of DIA-estimators: theory and applications. *J. Geod.*, 98(43):1–26, 2024.

6

Conclusions and recommendations

This chapter presents the main conclusions of the research conducted in this thesis. It summarizes the key contributions of Chapters 2 to 5. In addition, several recommendations are provided for future research.

6.1 Conclusions

The main conclusions, per chapter, are given below.

- **Chapter 2: Method to compute the probability of positioning failure and its conditional components**
  The study of the event of positioning failure $\mathcal{F} = \underline{\overline{x}} \notin \mathcal{B}$ [1], through computing its probability $\mathbb{P}_{\mathcal{F}}$, is of importance for a wide range of safety-critical applications in automotive, aviation, rail, and maritime domains. In this chapter, a method was proposed to compute the probability of positioning failure and its conditional components, *in line with the first research objective from Section 1.2.* This method accounts for the dependence between parameter estimation and statistical hypothesis testing in the formulation of $\mathbb{P}_{\mathcal{F}}$. The method has been developed in the context of the distributional theory of the Detection Identification and Adaptation (DIA) method [2, 3], and is based on principles and techniques from rare event simulation, specifically Importance Sampling and the Cross-Entropy method [4, 5]. The computation and analysis of $\mathbb{P}_{\mathcal{F}}$ is aimed at the design stage (offline) of positioning algorithms, where decisions are to be made about (i) measurement models, (ii) parameter estimation methods for the position vector, (iii) statistical hypothesis testing procedures to accommodate for model misspecifications (e.g., outliers or faults in measurements), and (iv) positioning scenarios for vehicles, among other factors. This approach aligns with the principles of scenario-based safety assessment framework which is used or proposed for studies of automated and autonomous vehicles [6–8]. Such analyses can be used to develop safe positioning algorithms by verifying whether positioning safety targets or requirements are met.

- **Chapter 3: Positioning safety analysis for automated/autonomous vehicles**
  This chapter addressed the dependence between parameter estimation and statistical hypothesis testing in automated/autonomous vehicle positioning safety analysis, and quantified the consequences of neglecting this dependence, *in line with the second research objective from Section 1.2.* Using, as an example, a simulation scenario of two connected vehicles (vehicle 1 and 2) driving on a highway in a cooperative positioning setting, the motion model of the Extended Kalman Filter (EKF) accounted for: (i) gentle acceleration or deceleration, and (ii) smooth lateral maneuvers (e.g., lane changes) for both vehicles. In the measurement model of the EKF, the precision of the position measurements was set at 0.100 [m] (indicative of DGNSS) and for the inter-vehicle distance measurements at 0.050 [m] (indicative of an automotive-grade LiDAR system). The considered hypotheses for the motion and measurement models were: (i) $\mathcal{H}_0$ is the null hypothesis, (ii) $\mathcal{H}_1$ and $\mathcal{H}_2$ account for 1D unmodelled longitudinal accelerations or decelerations of vehicle 1 and vehicle 2, (iii) $\mathcal{H}_3$ and $\mathcal{H}_4$ account for 2D model misspecifications in the position measurements of vehicles 1 and 2, and (iv) $\mathcal{H}_5$ and $\mathcal{H}_6$ account for 1D model misspecifications in the inter-vehicle distance measurements from both vehicles. Based on this setup, a positioning safety analysis was carried out for vehicle 1 by computing the probability of positioning failure. It was shown that ignoring the dependence between parameter estimation and statistical hypothesis testing can result in probabilities of positioning failure which are *one order of magnitude lower* (i.e., more optimistic). Thus, ignoring the aforementioned dependence can result in a wrongful positioning safety assessments, specifically concluding that safety requirements or guidelines are met when they are not. The conclusion about the consequence of ignoring the aforementioned dependence is consistent with existing research from various other disciplines such as, mathematical statistics, econometrics, and signal processing ([9–16]).

- **Chapter 4: Probability of positioning failure for UAVs in multiple authorized European airspace regions**
  In this chapter, a positioning safety analysis for Unmanned Aerial Vehicles (UAVs) was conducted across eight authorized European airspace regions over a 24-hour time window, which is *in line with the third research objective from Section 1.2.* In the positioning safety analyses real GPS precise satellite orbits were used from the International GNSS Service (IGS) for a 24-hour period over the chosen eight European airspace regions: 1-Portugal, 2-Ireland, 3-Netherlands, 4-Norway, 5-Finland, 6-Romania, 7-Austria, and 8-Italy. The choice of the positioning model for UAVs under nominal conditions was based on the Technical Standard Order (TSO) certification for GPS-based UAV positioning [17, 18]. The results showed that the computed maximum and minimum of the instantaneous probability of positioning failure vary significantly with the change in GPS satellite geometry over 24 hours (e.g., variations of approximately 9 orders of magnitude within 2 hours in the case of 5-Finland for the minimum of the probability of positioning failure). One-hour moving averages were computed of the probabilities of positioning failure, at different UAV start flight times, to relate the results with the preliminary requirements at SAIL 3 (10^{-4}/hr) and 4 (10^{-5}/hr) [19]. For SAIL 3, only in the selected airspaces over the Netherlands and Romania are the horizontal positioning safety requirements not met for 100%

of flight start times. In the case of SAIL 4, only in the selected airspace over Italy the horizontal positioning safety requirement is met 100% of flight start times for both Case 3 (minimum of the averaged probability of positioning failure) and Case 4 (maximum of the averaged probability of positioning failure). The sensitivity to the assumptions over the apriori probabilities of the hypotheses and the choice of the level of significance was also analyzed, revealing that the positioning safety requirements may not be met in more than 50% of the flight starting times (e.g., when the level of significance $\alpha = 10^{-3}$). To increase these percentages for SAIL 3 and SAIL 4 en-route UAV operations, several options, or combinations thereof, could be considered: (i) certification of additional GNSS constellations, such as the European Galileo system, to be used alongside GPS for UAV operations, (ii) usage of GPS receivers with better precision of the observables, (iii) application of principles from the new theoretical framework introduced in [3] to design parameter estimation and statistical hypothesis testing procedures explicitly with the objective to minimize the probability of positioning failure.

- **Chapter 5: DIA-estimator and multidimensional model misspecifications**
  This chapter presented a general approach for performing safety analyses—such as positioning safety—based on the DIA-estimator, while accounting for multidimensional model misspecifications and describing a transparent approach for determining the maximum dimension of model misspecification to be considered in the testing procedure. Specifically, the study focused on misspecifications in the mean of the observation model—such as those caused by outliers in the observations, which is *in line with the fourth research objective from Section 1.2.* As an illustrative case, a positioning safety analysis for a UAV was conducted, considering two scenarios involving one- and two-dimensional outlier misspecifications in the pseudorange measurements. The choice of the positioning model for the UAV, under nominal conditions, was based on the TSO certification for GPS-based UAV positioning [17, 18]. In the first scenario, a fixed receiver-satellite geometry at a single snapshot of time was considered to study the shape of the DIA-estimator PDF and to gain insights into the components that contribute the most to the probability of positioning failure under $\mathcal{H}_0$. For example, the conditional components related to the False Alarm (FA_i) testing decisions of the DIA-estimator's PDF exhibited bimodal and quadrimodal structures. The positioning safety analysis under $\mathcal{H}_7$ (one-dimensional outlier in GPS satellite 7) revealed that the probability of positioning failure has a local and global maximum. These maxima were caused by the components conditioned on the Wrongful Identification (WI) testing decision related to hypotheses $\mathcal{H}_{15}$ (pair 1-8), $\mathcal{H}_{28}$ (pair 4-6), and $\mathcal{H}_{31}$ (pair 5-6). The primary reason these components contributed the most is the strong correlation between the corresponding test statistics, combined with the degraded satellite geometry caused by the wrongful exclusion of these satellite pairs while $\mathcal{H}_7$ was valid. In general, the probability of positioning failure under any alternative hypothesis $\mathcal{H}_{i\neq 0}$ can exhibit multiple local maxima as a function of the model misspecification vector $\mathrm{b}_i \in \mathbb{R}^{q_i}$. These components can be revealed through a component-wise analysis, as carried out in this chapter. In the second scenario we have considered a 24-hours (on May 24, 2024) evolution of GPS satellites moving over an airspace region in The Netherlands for UAV operations.

Under $\mathcal{H}_0$, the computed probability of positioning failure was mainly driven by the component that accounts for all false alarm testing decisions. The results of the worst-case scenarios (w.r.t. $b_i \in \mathbb{R}^{q_i}$) showed that for one of the cases (Case 3: $\mathsf{P}(\mathcal{H}_0) = 0.99992$ and $\sum_{i=1}^{k} \mathsf{P}(\mathcal{H}_i) = 1 - \mathsf{P}(\mathcal{H}_0) = 8.0000 \cdot 10^{-5}$) is consistently below 10^{-5} (order of the SAIL 4 requirement for en-route operations).

The method proposed in this paper for computing the probability of positioning failure relies on numerical simulations, which may require considerable computational effort depending on the positioning scenario of interest. However, the computation times associated with the proposed method in this thesis could be further reduced by implementing it in a different programming language than MATLAB, such as Python or C/C++, and potentially by leveraging Graphics Processing Units (GPUs) as well. It is important to mention that although part of the research work in this thesis utilized computational resources (only Central Processing Units — CPUs) from the High Performance Computing (HPC) facilities provided by the Delft HPC Centre and Snellius (Dutch National Supercomputer), it is also possible to perform these computations on off-the-shelf computers, which cost several thousand euros. Taken together, these considerations render the proposed method computationally feasible and affordable for scenario-based safety assessments.

As a general closing remark, the method proposed in this thesis can be regarded as the first member of a broader 'family' or class of methods for computing the probability of positioning failure and its conditional components, in the context of rare event simulation. The development of other methods within this family should be possible, potentially leading to novel approaches for computing the positioning failure. The following subsection (6.2 Recommendations) provides several recommendations for further research that may support the development of a broader range of methods for rigorous positioning safety analyses in safety-critical applications.

6.2 Recommendations

The following recommendations are made for future work:

- Further improvements in terms of simulation variance reduction and/or computation times to the proposed method in this thesis may be achieved by selecting different families of proposal densities — other than Gaussian probability density functions (PDFs) — when re-expressing the conditional probabilities of positioning failure based on importance sampling principles. A starting point is provided by recent advances in the rare event simulation literature, where multimodal families of proposal densities have been investigated [20–24], which, in principle, should be suitable given that the integration regions related to the conditional probabilities of positioning failure are disconnected. Therefore, research on the potential benefits and drawbacks of these multimodal families of proposal densities would be of interest.

- Since not all conditional components of the probability of positioning failure (see Figure 2.2 in Chapter 2) contribute significantly, the proposed method could be enhanced — for example, by applying principles from dynamic programming — to compute only those Level 2 components that contribute most. This would improve

the efficiency of the method in finding the maximum (or minimum) of the probability of positioning failure.

- Positioning safety analyses aiming at the quantification of the probability of positioning-failure over a time-horizon T (e.g., seconds, minutes, hours) should be addressed. The objective would be to capture time-dependent effects, such as: (i) time-correlated measurement noise, (ii) time-dependent model misspecifications, (iii) variation of the satellite geometry, etc. This is particularly relevant for safety-critical applications, as vehicle operations often span extended time windows (e.g., aircraft landing or car lane changes). The probability of positioning failure over a time horizon T that also accounts for time-dependent safety-region $\mathcal{B}_\tau \subset \mathbb{R}^n$ (and its complement $\mathcal{B}_\tau^c \subset \mathbb{R}^n$) and time-dependent PDF $f_{\underline{\hat{x}}}(x,\tau)$ can be expressed as,

$$\mathbb{P}_{\mathcal{F}}(T) = \int_T \int_{\mathbb{R}^n} f_{\underline{\hat{x}}}(x,\tau)\, \mathbb{1}_{\mathcal{B}_\tau^c}(x,\tau)\, dx\, d\tau. \tag{6.1}$$

- Positioning safety analyses should be extended to include the velocity vector of the vehicle of interest. While position estimates are important for determining whether a vehicle is within a safety-region at a given time, velocity represents the evolution of the position over time and thus affects the system's ability to remain within safety bounds. For example, even if a vehicle is currently within a safety-region, a high or misestimated velocity (e.g., due to mismodelling) may lead to a future violation of safety margins before corrective action can be taken. Incorporating velocity would be useful for predictive positioning safety assessments.

- Research on the impact or consequence (C) of positioning failures ($\mathcal{F} = \{\underline{\hat{x}} \notin \mathcal{B}\}$) on other functions of automated and autonomous navigation systems (e.g., planning, control) is recommended. A small probability of positioning failure ($\mathbb{P}_{\mathcal{F}}$) does not necessarily guarantee that the output of the positioning system leads to a safe action by the overall system (e.g., a safe lane change by an autonomous vehicle). By quantifying the consequences of positioning failure, more realistic safety assessments become possible. Therefore, it is proposed that an additional safety indicator be considered, one that accounts for *both* the probability and the consequence of positioning failure, and which could be termed: **positioning risk**.

Bibliography

[1] RTCA-Special Committee 159. Minimum Operational Performance Standards (MOPS) for Global Positioning System/Satellite-Based Augmentation System Airborne Equipment. Do-229f, Radio Technical Commission for Aeronautics, 2020.

[2] P. J. G. Teunissen. Distributional theory for the DIA method. *Journal of Geodesy*, 92(1):59–80, 2018.

[3] P. J. G. Teunissen. On the Optimality of DIA-Estimators: Theory and Applications. *Journal of Geodesy*, 98(43):1–26, 2024.

[4] H. Kahn and A. W. Marshall. Methods of Reducing Sample Size in Monte Carlo Computations. *Journal of the Operations Research Society of America*, 1(5):263–278, 1953.

[5] R. Y. Rubinstein. The Cross-Entropy Method for Combinatorial and Continuous Optimization. *Methodology and Computing in Applied Probability*, 1:127–190, 1999.

[6] S. Riedmaier et al. Survey on Scenario-Based Safety Assessment of Automated Vehicles. *IEEE Access*, 8:87456–87477, 2020.

[7] U.N.E.C.E. New Assessment/Test Method for Automated Driving (NATM) Guidelines for Validating Automated Driving Systems (ADS). Report, United Nations Economic Commission for Europe - Inland Transport Committee, 2023.

[8] E. de Gelder et al. TNO Street Wise: Scenario-Based Safety Assessment of Automated Driving Systems. White paper, Netherlands Organisation for Applied Scientific Research (TNO), 2024.

[9] T. A. Bancroft. On Biases in Estimation Due to the Use of Preliminary Tests of Significance. *Annals of Mathematical Statistics*, 15(2):190–204, 1944.

[10] S. Sarkadi. Estimation After Selection. *Studia Scientiarum Mathematicarum Hungarica*, pages 341–350, 1967.

[11] N. L. Hjort and G. Claeskens. Frequentist Model Average Estimators. *Journal of the American Statistical Association*, 98(464):879–899, 2003.

[12] S. T. Buckland, K. P. Burnham, and N. H. Augustin. Model Selection: An Integral Part of Inference. *Biometrics*, 53(2):603–618, 1997.

[13] H. Leeb and B. M. Pötscher. The Finite-Sample Distribution of Post-Model-Selection Estimators and Uniform Versus Nonuniform Approximations. *Econometric Theory*, 19(1):100–142, 2003.

[14] H. Leeb and B. M. Pötscher. Model Selection and Inference: Facts and Fiction. *Econometric Theory*, 21(1):21–59, 2005.

[15] D. Danilov and J. R. Magnus. On the Harm That Ignoring Pretesting Can Cause. *Journal of Econometrics*, 122(1):27–46, 2004.

[16] T. Routtenberg and L. Tong. Estimation After Parameter Selection: Performance Analysis and Estimation Methods. *IEEE Transactions on Signal Processing*, 64(20):5268–5281, 2016.

[17] Federal Aviation Administration. Technical Standard Order C-145e: Airborne Navigation Sensors Using the Global Positioning System Augmented by the Satellite Based Augmentation System (SBAS). Technical report, 2017.

[18] T. Cozzens. uAvionix receives FAA order for certified drone GPS receiver, 2021. GPS World, August, 2021. [Online].

[19] European Union Agency for the Space Programme. Report on Aviation and Drones: User Needs and Requirements. Technical report, 2023.

[20] S. Geyer, I. Papaioannou, and D. Straub. Cross-Entropy-Based Adaptive Importance Sampling Using Gaussian Densities Revisited. *Structural Safety*, 76:15–27, 2019.

[21] N. Kurtz and J. Song. Cross-Entropy-Based Adaptive Importance Sampling Using Gaussian Mixture. *Structural Safety*, 42:35–44, 2013.

[22] Z. Wang and J. Song. Cross-Entropy-Based Adaptive Importance Sampling Using von Mises-Fisher Mixture for High Dimensional Reliability Analysis. *Structural Safety*, 59:42–52, 2016.

[23] I. Papaioannou, S. Geyer, and D. Straub. Improved Cross-Entropy-Based Importance Sampling with Flexible Mixture Model. *Reliability Engineering and System Safety*, 191:1–11, 2019.

[24] F. Uribe et al. Cross-Entropy-Based Importance Sampling with Failure-Informed Dimension Reduction for Rare Event Simulation. *Journal of Uncertainty Quantification*, 9(2):818–847, 2021.

Acknowledgments

This dissertation marks the end of my Ph.D. journey, which was made possible through the financial support of the Dutch Research Council (NWO) under Grant 18305 "I-GNSS Positioning for Assisted and Automated Driving". I also gratefully acknowledge the computational resources provided by the Delft High Performance Computing Centre and the Dutch National e-Infrastructure-SURF Cooperative under grant no. EINF-7002, which supported parts of this research. This journey involved not only research, but also the contributions of many people along the way. I would like to take this opportunity to acknowledge those whose contributions—whether academic, professional, or personal—helped shape the work presented here.

I would like to begin by expressing my gratitude to my promotor, Prof.dr.ir. Peter Teunissen, for his supervision, scientific insights, and objective feedback. These were instrumental throughout my research, enabling progress that ultimately led to results. Furthermore, among the many things I have learned from him, one stands out that I will carry forward: *the value of maintaining focus.*

I am also grateful for the supervision, support, and thoughtful engagement with my research by my co-promotor, Dr.ir. Christian C.J.M. Tiberius. His support and encouragement throughout the course of this research were invaluable, particularly in times of difficulty and while exploring new directions. A lasting lesson, among many others, that I take from working with him is one I will carry forward: *the importance of supporting those around you while remaining persistent in your own efforts.*

Next, I would like to thank my colleagues from the Geoscience and Remote Sensing (GRS) department for creating a positive and enjoyable working environment. In particular, I would like to thank Chengyu Yin, Carlos Fortuny Lombraña, Lotfi Massarweh, Bob van Noort, Serge Kaplev, Alexandru Lăpădat, Yan Yuan, and Lucas Alvarez Navarro for the many engaging discussions—whether about research, world events, or anything in between. It was a pleasure working with you and being your colleague. I am also grateful to Hayden Dorahy from u-blox AG for insightful conversations on numerical simulation. I also wish to thank Natascha Libanon, Debbie Rietdijk, and Cindy van Rheenen for their administrative support and promptness in times of need.

My sincere appreciation goes to the members of the doctoral committee for their time and evaluation.

I would also like to take this opportunity to thank my former professors, supervisors, mentors, and colleagues prior to my Ph.D. journey, in the countries where I have lived, studied, or worked—Romania, France, Spain, Germany, and the Netherlands. I am grateful

to Dr.ir. Vlad Gabriel Olteanu, Prof.dr.ir Alexandru Badea, Assoc.Prof.Dr.ir. Doru Mihai for their guidance and support during my bachelor studies in Romania. The lessons and experiences from those years have played a lasting role in shaping the path I continue to follow.

Finally, I wish to express my deepest gratitude to my parents. To my mother Maria, for her ongoing support throughout all the years. And to the memory of my father, Simion, whose values, ambition, and unshaken integrity continue to inspire me, even in his absence. Moreover, it was thanks to my wife Claudia's patience, understanding, and encouragement that I was able to make it through the most challenging moments of the Ph.D. I feel truly fortunate to have her by my side—together with our son Victor and our cat Leia, they make life richer.

Curriculum Vitæ

Sebastian Ciuban

7^{th} of March, 1992 — Born in Baia Mare, Romania

Experience

06/2025 - Present — **R&D Navigation/PNT Engineer**
Science & Technology (S&T) B.V., Defence and Security Unit, Delft, The Netherlands

03/2021 - 05/2025 — **Ph.D. Researcher**
Delft University of Technology, Delft, The Netherlands

01/2019 - 02/2021 — **GNSS Engineer**
CGI Nederland B.V., Rotterdam, The Netherlands

10/2017 - 12/2018 — **Navigation System Engineer**
European Space Agency (ESA)-ESA Graduate Trainee Programme in ESTEC, Noordwijk, The Netherlands

03/2017 - 09/2017 — **PNT Researcher**
German Aerospace Centre (DLR)-M.Sc. Graduation Project, Oberpfaffenhofen, Germany

07/2016 - 10/2016 — **PNT Researcher**
Acorde Technologies S.A.-Horizon Europe E-Knot Programme, Santander, Spain

Education

03/2021 - 05/2025 — **Ph.D. Researcher**
Delft University of Technology, Delft, The Netherlands

09/2015 - 09/2017 **M.Sc. Aerospace Systems-Navigation and Telecommunications**
École Nationale de l'Aviation Civile, Toulouse, France

08/2011 - 07/2015 **B.Eng. Geodetic Engineering**
Faculty of Land Reclamation and Environmental Engineering, Bucharest, Romania

Awards

12/2018 **First Place - Galileo Masters: GNSS Living Lab Prize**
European Satellite Navigation Competition (ESNC)

06/2018 **First Place - 1st Edition of ESA Galileo App Competition (2017/2018)**
European Space Agency (ESA)

09/2015 **M.Sc. Scholarship for Academic Excellence**
European Union Agency for the Space Programme (former European GNSS Agency-GSA)

07/2014 **First Place - International ESA/JRC Summer School on GNSS**
European Space Agency (ESA) and the European Commission's Joint Research Centre (JRC)

Patent

06/2022 **Method for detecting potential tampering with satellite navigation signals and/or for determining a position**
Authors: A. Vroom, T. van den Oever, A. van den Berg, **S. Ciuban**
Granted by: European Patent Office

List of publications and presentations

The following list includes research contributions made during the Ph.D. (2021–2025) as well as prior to its start (before 2021).

Peer-reviewed Journal Papers

1. **S. Ciuban**, P.J.G. Teunissen, and C.C.J.M. Tiberius. "*A Method to Compute the Probability of Positioning Failure for Vehicles in the Context of Dependence Between Parameter Estimation and Statistical Hypothesis Testing*", IEEE Transactions on Vehicular Technologies, 74(10):15238 - 15253, 2025.

2. **S. Ciuban**, P.J.G. Teunissen, and C.C.J.M. Tiberius. *"Dependence Between Parameter Estimation and Statistical Hypothesis Testing: Positioning Safety Analysis for Automated/Autonomous Vehicles"*, IEEE Transactions on Intelligent Transportation Systems, 26(4):5509 - 5521, 2025.

3. **S. Ciuban**, C. Yin, P.J.G. Teunissen, and C.C.J.M. Tiberius. *"Probability of Positioning Failure for UAVs in Multiple Authorized European Airspace Regions"*, IEEE Transactions on Vehicular Technologies, Submitted.

4. **S. Ciuban**, P.J.G. Teunissen, and C.C.J.M. Tiberius. *"DIA-Estimator and Multidimensional Model Misspecifications: GNSS-based Positioning Safety Analysis for UAVs"*, GPS Solutions, Submitted.

Conference Papers

1. **S. Ciuban**, P.J.G. Teunissen, and C.C.J.M. Tiberius. "*GNSS Positioning Safety: Probability of Positioning Failure and Its Components*", 37th International Technical Meeting of the Satellite Division of The Institute of Navigation (ION GNSS+), 2024.

2. P.J.G. Teunissen, **S. Ciuban**, C. Yin, B. van Noort, S. Zaminpardaz and C.C.J.M. Tiberius. "*The DIA-Estimator for Positional Integrity: Design and Computational Challenges*", International Association of Geodesy Symposia, 2024.

3. **S. Ciuban**, M. Krainski, D. Perz, and M. Burba. "*GNSS Compare: Performance assessment of real-time PVT algorithms using raw GNSS measurements on an Android*

smartphone", 9th Edition of European Space Agency's-ESTEC NAVITEC Conference, 2018.

4. M. Krainski, **S. Ciuban**, D. Perz, and M. Burba. "*GNSS Compare: a novel software framework for processing raw GNSS measurements on an Android smartphone"*, 9th Edition of European Space Agency's-ESTEC NAVITEC Conference, 2018.

5. **S. Ciuban** and V.G. Olteanu. "*MATLAB based student oriented platform for processing and analyzing GNSS data"*, GeoPreVi Conference organized by Technical University of Civil Engineering Bucharest, 2015.

6. **S. Ciuban** and V.G. Olteanu. "*Estimating the GNSS broadcast ephemeris error"*, International Student Symposium organized by Faculty of Land Reclamation and Environmental Engineering, 2014.

Articles in Professional Magazines

1. **S. Ciuban**, P.J.G. Teunissen, and C.C.J.M. Tiberius. "*Positioning Safety for Safety-Critical Applications via Probability of Positioning Failure*," *Inside GNSS*, November/December, 2025.

2. **S. Ciuban**, M. Krainski, D. Perz, and M. Burba. "*GNSS Compare: Real-time Algorithms with Raw GNSS Measurements on Android Smartphones*," *Inside GNSS*, February, 2020.

Book Chapter

1. **S. Ciuban**, C. Fortuny-Lombraña, B. van Noort, C. Yin, . "*Exploring Applications of the DIA-Estimator Framework. In: Navigating the Geodetic Landscape: A Tribute to 45 Years of Excellence*," Chapter 22, Editors A. Khodabandeh and S. Verhagen, Springer International Publishing AG, ISBN 9783031992735, 2025.

Selected Presentations

1. **S. Ciuban**, P.J.G. Teunissen, and C.C.J.M. Tiberius. "*Approaching GNSS Positioning Safety Analysis for Autonomous Vehicles via Rare Event Simulation"*, 11th Edition of European Space Agency's-ESTEC NAVITEC Conference, 2024.

2. **S. Ciuban**, P.J.G. Teunissen, and C.C.J.M. Tiberius. Presentation of "*GNSS Positioning Safety: Probability of Positioning Failure and Its Components"*, 37th International Technical Meeting of the Satellite Division of The Institute of Navigation (ION GNSS+), 2024.

3. **S. Ciuban**, P.J.G. Teunissen, and C.C.J.M. Tiberius. "*Parameter Estimation, Statistical Hypothesis Testing, and Rare Events in Positioning Safety Analyses*", Nederlands Centrum voor Geodesie en Geo-informatica (NCG) Symposium, 2024.

4. **S. Ciuban**, M. Krainski, D. Perz, and M. Burba. Presentation of "*GNSS Compare: Performance assessment of real-time PVT algorithms using raw GNSS measurements on an Android smartphone*", 9th Edition of European Space Agency's-ESTEC NAVITEC Conference, 2018.

5. **S. Ciuban** and V.G. Olteanu. Presentation of "*MATLAB based student oriented platform for processing and analyzing GNSS data*", GeoPreVi Conference organized by Technical University of Civil Engineering Bucharest, 2015.

6. **S. Ciuban** and V.G. Olteanu. Presentation of "*Estimating the GNSS broadcast ephemeris error*", International Student Symposium organized by Faculty of Land Reclamation and Environment Engineering, 2014.